Exploration of Nuclear-Structure Effects on Averaged Decay Quantities in the Quasicontinuum

TECHNISCHE
UNIVERSITÄT
DARMSTADT

Department of Physics
Institut für Kernphysik
AG Pietralla

Exploration of Nuclear-Structure Effects on Averaged Decay Quantities
in the Quasicontinuum
Untersuchung von Kernstruktureffekten auf gemittelte Zerfallsgrößen
im Quasikontinuum

Accepted doctoral thesis by Oliver Papst

Date of submission: 2024-06-25
Date of thesis defense: 2024-07-15

Darmstadt, Technische Universität Darmstadt

Erklärungen laut Promotionsordnung

§ 8 Abs. 1 lit. d PromO

Ich versichere hiermit, dass zu einem vorherigen Zeitpunkt noch keine Promotion versucht wurde. In diesem Fall sind nähere Angaben über Zeitpunkt, Hochschule, Dissertationsthema und Ergebnis dieses Versuchs mitzuteilen.

§ 9 Abs. 1 PromO

Ich versichere hiermit, dass die vorliegende Dissertation – abgesehen von den in ihr ausdrücklich genannten Hilfen – selbstständig verfasst wurde und dass die „Grundsätze zur Sicherung guter wissenschaftlicher Praxis an der Technischen Universität Darmstadt" und die „Leitlinien zum Umgang mit digitalen Forschungsdaten an der TU Darmstadt" in den jeweils aktuellen Versionen bei der Verfassung der Dissertation beachtet wurden.

§ 9 Abs. 2 PromO

Die Arbeit hat bisher noch nicht zu Prüfungszwecken gedient.

Darmstadt, 25. Juni 2024

_____

Oliver Papst

Abstract

In this work, the decay behavior of dipole strength of ^{96}Mo and ^{150}Nd after excitation with high-energy photons was investigated. For this purpose, multiple experiments at the γ^3 setup and clover array setup at the High-Intensity γ-ray Source (HIγS) at Duke University and at the Darmstadt High-Intensity Photon Setup (DHIPS) of the superconducting Darmstadt electron linear accelerator (S-DALINAC) at Technische Universität Darmstadt were performed. For the ^{150}Nd experiment at HIγS, the laser-Compton backscattering photon beam was operated in a new high-resolution mode, with an energy resolution of $\Delta E/E \approx 2\%$. The high energy resolution allowed, for the first time, the spectral separation of different decay components into the ground state band for a heavy deformed nucleus. Between 4 MeV and 7 MeV, an almost constant average branching ratio of 0.481(17) between the decay to the 2_1^+ state and the ground state was observed. By introducing an internal fluctuation ratio s, the statistical distribution of partial transition widths was deduced. The observations are consistent with χ^2-distributed transition widths with degree of freedom $\nu = 1.82(10)$, and inconsistent with the Porter-Thomas distribution ($\nu = 1$). Additionally, in combination with the DHIPS experiment, properties of individual states and the photon-scattering cross section were determined. For the ^{96}Mo experiment, utilizing $\gamma\gamma$-coincidence measurements in combination with a linearly polarized quasi-monochromatic photon beam, the photon strength functions (PSFs) were determined that are built on top of excited 2^+ states, which were then combined into a single downward PSF. The general shape and slope of the determined PSF agree very well with experiments using complementary probes, however, it is much smoother and exhibits fewer fluctuations in comparison to the literature values. This deviation indicates a possible violation of the Brink-Axel hypothesis for the studied energy range.

Zusammenfassung

Im Rahmen dieser Arbeit wurde das Zerfallsverhalten der Dipolstärke von ^{96}Mo und ^{150}Nd infolge von Anregung mittels hochenergetischer Photonen untersucht. Hierzu wurden mehrere Experimente am γ^3-Aufbau sowie Clover-Array-Aufbau an der High-Intensity γ-ray Source (HIγS) an der Duke University sowie am Darmstadt High-Intensity Photon Setup (DHIPS) des supraleitenden Darmstädter Elektronenlinearbeschleunigers (S-DALINAC) an der Technischen Universität Darmstadt durchgeführt. Für das ^{150}Nd Experiment an HIγS wurde der Laser-Compton-rückgestreute Strahl in einem weiterentwickelten hochauflösenden Modus mit einer Energieauflösung von $\Delta E/E \approx 2\,\%$ betrieben. Durch diese hohe Energieauflösung ist erstmals die spektrale Unterscheidung verschiedener Zerfallskomponenten in die Grundzustandsbande für einen schweren deformierten Kern möglich. Zwischen $4\,\mathrm{MeV}$ und $7\,\mathrm{MeV}$ wird ein nahezu konstantes mittleres Verzweigungsverhältnis von $0.481(17)$ beobachtet. Es wird das interne Fluktuationsverhältnis eingeführt, das von der statistischen Verteilung der partiellen Übergangsbreiten abhängt. Die Beobachtungen sind konsistent mit χ^2-verteilten Übergangsbreiten mit Freiheitsgrad $\nu = 1.82(10)$ und passen nicht zur Porter-Thomas-Verteilung ($\nu = 1$). Des Weiteren wurden in Kombination mit dem DHIPS-Experiment die Eigenschaften einzelner Zustände sowie der Photonenstreuwirkungsquerschnitt bis zur maximalen Strahlenergie unterhalb der Neutronenseparationsenergie bestimmt. Für das ^{96}Mo-Experiment wurden mittels $\gamma\gamma$-Koinzidenzmessungen in Kombination mit einem linear polarisierten quasimonochromatischen Photonenstrahl Photonenstärkefunktionen (PSFs) gemessen, die auf angeregten 2^+-Zuständen aufgebaut sind, und zu einer abregenden PSF kombiniert. Die Form und Steigung der bestimmten PSF stimmen gut mit Experimenten mit komplementären Sonden überein, im Vergleich zur Literatur ist der Verlauf allerdings deutlich glatter, mit weniger Fluktuationen. Dies deutet auf eine Verletzung der Brink-Axel Hypothese für den untersuchten Energiebereich hin.

Acknowledgements

This work would not have been possible without the support and assistance of many people. Specifically, I wish to express my gratitude to

… **Professor Dr. Dr. h. c. mult. Norbert Pietralla** for the opportunity to pursue a PhD in his group and study interesting problems in nuclear physics since my bachelor's thesis. I am grateful for the instructive physics discussions, his unwavering support, his ability to see through complex problems and critically point out potential issues and challenges, and for allowing me to attend several international conferences, summer schools, and experiments at world-class facilities.

… **Dr. Johann Isaak** for closely supervising my work and providing me with insightful feedback and guidance at every step. His encouragement and critical advice were essential in pushing me forward, while his enthusiasm for nuclear physics kept me motivated. He managed to keep an eye on the details of my work without losing sight of the big picture, pointing me in the right direction whenever necessary. I am also grateful for his extensive proofreading of the thesis.

… **Dr. Volker Werner** for guidance and help, both for the analysis of my data and interpretation of the results, as well as for any lab-related work and thesis proofreading.

… **Jörn Kleemann** for the close and productive collaboration during our studies and work, and his help and encouragement. I also thank him together with …

… my former office colleagues **Dr. Udo Friman-Gayer** and **Dr. Tobias Beck** for the pleasant atmosphere at work. They made every day in the office enjoyable and fun, but also educational, not only with respect to physics. I miss the frequent and extensive discussions that kept us distracted. In addition, Udos comprehensive collection of self-developed codes have benefited not only me but a whole generation of students analyzing NRF experiments. Furthermore, with great personal commitment, Udo took care of my own experiment on-site at HIγS when I was restricted from traveling there myself. The success of the experiment is thanks to his efforts.

… **Katharina E. Ide** for carefully proofreading and correcting the first draft of this thesis.

Contents

List of Figures

List of Tables

Abbreviations

ADC Analog-to-digital converter

AGB Asymptotic giant branch, a region of the Hertzsprung–Russell diagram that characterizes the temperature and luminosity of stars

BGO Bismuth germanate ($Bi_4Ge_3O_{12}$), a scintillator material used in BGO detectors for γ-ray detection

BSFG Back-shifted Fermi gas

CeBr$_3$ Cerium(III) bromide, a type of scintillation material used in CeBr$_3$ detectors for γ-ray detection

CFD Constant fraction discriminator

CI Configuration interaction, also known as interacting shell model or configuration interaction shell model

CT Constant temperature

DAQ Data acquisition system

DEP Double-escape peak

DHIPS Darmstadt High-Intensity Photon Setup

EDF Energy-density functional

ELBE Elektronen Linearbeschleuniger für Strahlen hoher Brillanz und niedriger Emittanz, an electron accelerator at HZDR

EoS Equation of state

EWSR Energy-weighted sum rule

FEL Free-electron laser

FEP Full-energy peak

FWHM Full width at half maximum

GOE Gaussian orthogonal ensemble

GSE Gaussian symplectic ensemble

γSF γ strength function, *see* PSF

GUE Gaussian unitary ensemble

HFB Hartree-Fock-Bogoliubov

HIγS The High-Intensity γ-ray Source, located at TUNL, Duke University

HMC Hamiltonian Monte Carlo, also known as hybrid Monte Carlo, a MCMC algorithm

HPGe High-purity germanium, a type of semiconductor used in HPGe detectors for γ-ray detection

HZDR Helmholtz-Zentrum Dresden-Rossendorf

ISGMR Isoscalar giant monopole resonance

ISGQR Isoscalar giant quadrupole resonance

IVGDR Isovector giant dipole resonance

IVGQR Isovector giant quadrupole reso-

nance

IVS$M1$ Isovector spin-$M1$

KSW Krane-Steffen-Wheeler multipole mixing ratio convention

LaBr$_3$ Lanthanum(III) bromide doped with cerium, a type of scintillation material used in LaBr$_3$(Ce) detectors for γ-ray detection

LCB Laser-Compton backscattering

LEE Low-energy enhancement

LMD List-mode data format

MAW Moving-average window

MBS Multi-branch system, a digital DAQ system developed at GSI

MCMC Markov chain Monte Carlo

MDA multipole decomposition analysis

MLE Maximum likelihood estimation

NaI Sodium iodide doped with thallium, a type of scintillation material used in NaI(Tl) detectors for γ-ray detection

NDE Nuclear data ensemble, a dataset of neutron resonance widths

NIM Nuclear instrumentation standard

NLD Nuclear level density

NNS Nearest-neighbor spacing

NRF Nuclear resonance fluorescence

NUTS No U-Turn Sampler, a type of HMC sampler

OCL The Oslo Cyclotron Laboratory, located at the University of Oslo

OMP Optical model potential

OSCAR The Oslo Scintillator Array

PDF Probability density function

PDR "Pygmy" dipole resonance

PMT Photomultiplier tube, a type of detector highly sensitive to (near-)visible light

PSF Photon strength function

PT Porter-Thomas, referring to the Porter-Thomas distribution

QDC Charge-to-digital converter

QPM Quasiparticle phonon model

QRPA Quasiparticle random-phase approximation

RCNP Research Center for Nuclear Physics, located in Osaka, Japan

RF Radio frequency

RMT Random-matrix theory

SCP Standard charge-integrating preamplifier

S-DALINAC The superconducting Darmstadt linear accelerator, located at TU Darmstadt

SEP Single-escape peak

SLO Standard Lorentzian, which is a relativistic Breit-Wigner distribution used to model the IVGDR

SMLO Simplified modified Lorentzian, a PSF model

TCP Transmission control protocol

TFA Timing filter amplifier

TSC Two-step cascade

TUNL Triangle Universities Nuclear Laboratory, located at Duke University

UDP User datagram protocol

UTR Upstream target room, an experimental site housing (among others) nuclear resonance fluorescence experiments at HIγS

VME Versa Module Eurocard-bus, also referred to as VMEbus

1. Introduction

1.1. Stellar nucleosynthesis

The atomic nucleus is a basic constituent of complex matter. It consists of protons and neutrons – the nucleons. Their interaction is mediated by the nuclear force, a remnant of the strong interaction that acts between the fundamental particles called quarks that form the nucleons. The way these components work together gives rise to a complex many-body quantum system that features a wide variety of excitation and interaction modes.

Only the lightest nuclei up to ^{4}He (neglecting minuscule amounts of ^{7}Li) were formed during the first few minutes after the Big Bang (*primordial nucleosynthesis*) [1]. Heavier elements began to emerge much later in stars (*stellar nucleosynthesis*) [2, 3], where the environmental conditions necessary for the fusion of light nuclei into heavier ones are found. A variety of fusion reactions and interaction chains contribute to this process. For a detailed overview, refer to Refs. [3, 4].

Nuclear fusion is energetically favored up to the $A \approx 60$ mass region around ^{56}Fe. Several other processes describe the synthesis of heavier elements by accumulation of additional protons or neutrons. One of these nucleosynthesis processes is the slow neutron-capture process (*s* process) [5]. It takes place in an environment with comparatively low temperatures (10^8 K to 4×10^8 K) and low neutron densities (10^7 cm^{-3} to 10^8 cm^{-3}). A stable nucleus successively captures neutrons in (n, γ) reactions, eventually resulting in an unstable nucleus. The unstable nucleus undergoes β^--decay back to the valley of stability before the process repeats. Multiple astrophysical sites provide sufficient neutron fluxes for the *s* process to occur [6]. For example, He burning in massive stars sustains the weak *s* process through (α, n) reactions, producing elements in the mass region between Fe and Sr [7]. The main *s* process takes place in

low-mass asymptotic giant branch (AGB) stars and synthesizes elements up to ^{209}Bi. Repeated neutron-capture reactions on unstable nuclei can generally not be sustained because of the low neutron flux present during the *s* process. Branch-point nuclei provide opportunities for the *s* process to also reach stable nuclei separated by a single unstable nucleus if the β^--decay rate is sufficiently low [6].

In contrast to the *s* process, the rapid neutron-capture process (*r* process) [8–10] takes place in environments with a larger temperature (10^9 K to 2×10^9 K) and a much larger neutron flux, allowing for repeated neutron-capture reactions in quick succession. It involves a large region of the nuclear chart, spanning from the valley of stability almost all the way to the neutron drip line, and produces elements up to Pu and beyond (for a short time). The nucleus accumulates neutrons in rapid succession until an equilibrium between (n, γ) neutron-capture and (γ, n) photodisintegration reactions is reached at the so-called *waiting point*. After some time, the nucleus β^--decays, the atomic number *Z* of the nucleus increases, and the process repeats.

Multiple astrophysical sites have been suggested that could host the *r* process, including neutrino-driven winds and mass ejection following core-collapse supernovae [9]. Multi-messenger observations of binary neutron star mergers [11] allowed for the first direct astronomical observations consistent with *r*-process predictions.

Neutron-induced fission reactions (n, f) can recycle heavy nuclei into lighter fragments, reintroducing them to the *r* process. It has been proposed [12] that this recycling weakens the dependency on the exact environmental conditions like temperature and density at the astrophysical site and instead strengthens the sensitivity of the *r* process on nuclear properties and models. Several nuclear data inputs are required [13], including the equation of state (EoS) of nuclear matter, and properties of neutron-rich nuclei. For *r*-process network simulations such as WinNet [14], neutron-capture, photodissociation and β-decay rates, and fission rates and yields are required. Neutron-capture and photodissociation rates for a particular decay channel are directly related to each other using detailed balance [15].

The *r*-process path runs through a region of the nuclear chart with a large neutron excess, which is, for the most part, not accessible experimentally for the foreseeable future. Therefore, theoretical models are required to describe these nuclei. The models have to be verified with or extrapolated from nuclear data for nuclei that are accessible experimentally. For neutron densities in between the *s* and *r* process, the intermediate neutron-capture process (*i* process) [16] has been suggested. Its existence is supported

by various observations (see Ref. [17] and references therein), but its astrophysical site is still under discussion. The *i* process traverses a region of the chart of nuclides a few nucleons away from the valley of stability. Finally, the *p* process [18] should be mentioned, which is the process responsible for the nucleosynthesis of proton-rich nuclei. Originally attributed to proton-capture reactions [2], it is now associated with photodisintegration reactions [18].

Stable nuclei are particularly well-suited for experiments. These are usually available in macroscopic quantities without requiring particle accelerators or nuclear reactors for production. With the method of isotopic enrichment, even samples of isotopes with a low natural abundance can be obtained. Thus, stable nuclei can be studied using processes with low cross sections, such as high-energy photon interactions. This thesis focuses on the experimental study of the nuclear photoresponse, which can be directly measured in photonuclear reactions and reactions involving the emission of photons (nuclear resonance fluorescence (NRF) experiments, (γ, γ')) for stable and long-lived isotopes.

1.2. Nuclear photoresponse

One of the essential properties of an atomic nucleus is its probability to absorb and emit photons with different energies. This so-called photon strength function (PSF) encodes the nuclear photoresponse of an atomic nucleus, a key ingredient of *r*-process calculations. This response can be separated into the different multipolarities λL, with radiation character $\lambda \in \{E, M\}$ (*E*: electric, *M*: magnetic) and angular momentum quantum number *L*. For transitions between two states with total angular momentum quantum numbers J_1 and J_2, and parity quantum numbers π_1 and π_2, the following selection rules apply [21]:

$$|J_1 - J_2| \leq L \leq J_1 + J_2, \qquad \pi_1 \pi_2 = \begin{cases} (-1)^L & \Leftrightarrow \lambda = E, \\ (-1)^{L+1} & \Leftrightarrow \lambda = M. \end{cases} \tag{1.1}$$

Because photons carry angular momentum, no (single-photon) transitions of type $E0$ or $M0$ are possible. Consequently, electromagnetic transitions between two states with $J_1 = J_2 = 0$ are forbidden. Other probes or internal conversion of electrons can induce $E0$ transitions.
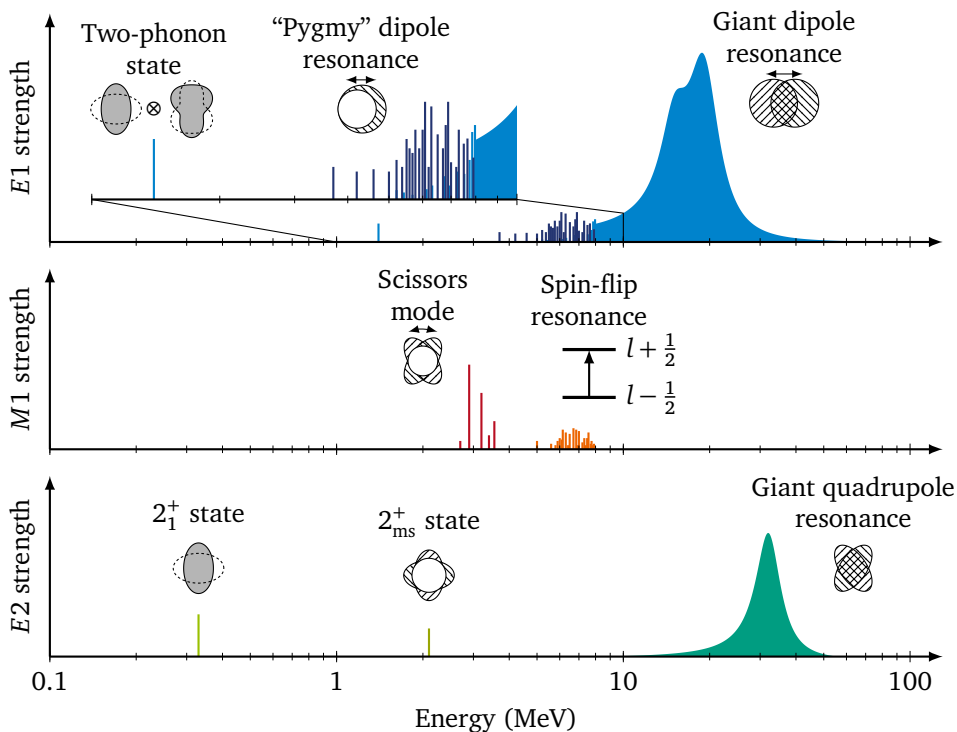
Figure 1.1.: Simplified illustration of the main modes of excitation observed in NRF experiments for a heavy deformed nucleus using MeV-ranged photons. Similar overview figures have been shown in various publications and talks, e.g., see Refs. [19, 20].

Lower multipole orders L dominate, and electric multipole transitions EL are usually more probable than magnetic multipole transitions ML. Because of the low angular momentum transfer of real photons , NRF reactions predominantly induce $E1$ and $M2$ transitions, while $E2$ transitions occur with significantly suppressed probability.

The transfer of angular momentum λL is described in terms of the transition operator $T(\lambda L)$. Following the notation of the reduced matrix element according to the Wigner-

Eckart theorem, it can be related to the reduced transition probability [21]

$$B(\lambda L; J_j^{\pi_j} \to J_k^{\pi_k}) = \frac{1}{2J_j+1} \left| \left\langle \Psi_k \left\| T(\lambda L) \right\| \Psi_j \right\rangle \right|^2, \qquad (1.2)$$

for transitions from state J_j to state J_k, which relates experimental and theoretical quantities. Upward $B(\lambda L)\uparrow$ and downward $B(\lambda L)\downarrow$ reduced transition probability, corresponding to the excitation and deexcitation process, respectively, are related by

$$B\left(\lambda L; J_i \to J_j\right) \equiv B(\lambda L)\uparrow = g \cdot B(\lambda L)\downarrow \equiv g \cdot B\left(\lambda L; J_j \to J_i\right), \qquad (1.3)$$

with the spin-statistical factor $g = (2J_j+1)/(2J_i+1)$. Reduced transition probabilities are given in units of MeVfm^{2L+1} in the SI system of units [22]. In the literature, Gaussian CGS units [23, pp. 775–784] of μ_N^2fm^{2L-2} for $B(ML)$ values and e^2fm^{2L} for $B(EL)$ values are commonly found. A conversion to Gaussian CGS units is possible using the relation

$$\left[1\,\text{MeVfm}^{2L+1}\right]_{\text{SI}} = \left[62.805\,\mu_N^2\text{fm}^{2L-2}\right]_{\text{CGS}} = \left[0.694\,46\,e^2\text{fm}^{2L}\right]_{\text{CGS}}. \qquad (1.4)$$

A quantity closely related to the reduced transition probability is the partial transition width $\Gamma_{j\to k}$, which is expressed as

$$\Gamma_{j\to k} = 8\pi \sum_{\lambda L} \left(\frac{E_\gamma}{\hbar c}\right)^{2L+1} \cdot \frac{L+1}{L\left[(2L+1)!!\right]^2} \cdot B(\lambda L)\downarrow. \qquad (1.5)$$

By expanding $\Gamma_{j\to k} = \sum_{\lambda L} \Gamma_{j\to k}^{\lambda L}$ and rearranging Eq. (1.5) with respect to $B(\lambda L)\downarrow$, one obtains

$$B(\lambda L)\downarrow = \frac{1}{8\pi} \cdot \left(\frac{\hbar c}{E_\gamma}\right)^{2L+1} \cdot \frac{L\left[(2L+1)!!\right]^2}{L+1} \cdot \Gamma_{j\to k}^{\lambda L}. \qquad (1.6)$$

In the following, an introduction to the relevant excitation modes and resonances will be given. For $E1$ radiation, it is primarily based on Refs. [24, 25], for $M1$ radiation on Ref. [26]. For a depiction of all discussed excitation modes and their respective energies, refer to Fig. 1.1.

1.2.1. Electric dipole strength

An estimate for the total $E1$ strength is obtained using the so-called Thomas-Reiche-Kuhn [27, 28] energy-weighted sum rule (EWSR) [29]

$$\int_0^\infty \sigma_{E1}\left(E_\gamma\right) \mathrm{d}E_\gamma \approx \frac{2\pi^2 e^2 \hbar c}{m_\mathrm{N} c^2} \frac{NZ}{A} \approx 60 \frac{NZ}{A} \,(\mathrm{MeV\,mb}). \tag{1.7}$$

Here, σ_{E1} refers to the $E1$ photoabsorption cross section, N, Z, and A refer to the neutron, proton, and mass number of the nucleus, and m_N is the nucleon mass. A majority of this sum rule is exhausted by a single resonance, the isovector giant dipole resonance (IVGDR) [24, 30]. Depending on the nucleus, its centroid energy E_c is at around 13 MeV to 25 MeV, with lower centroid energies corresponding to higher mass numbers. In a geometric picture, it corresponds to a collective out-of-phase oscillation of a proton fluid against a neutron fluid [31]. For heavy spherical nuclei, it is approximated by a Lorentzian curve:

$$\sigma_{\mathrm{IVGDR}}(E_\gamma) = \frac{\sigma_0}{1 + \left[(E_\gamma^2 - E_\mathrm{c}^2)/(E_\gamma^2 \Gamma^2)\right]}, \tag{1.8}$$

with peak cross section σ_0 and resonance width Γ.

For neutron-rich nuclei, a further contribution to $E1$ strength is situated on the low-energy tail of the IVGDR in the vicinity of the neutron-separation threshold. This concentration of $E1$ strength is commonly referred to as "pygmy" dipole resonance (PDR) [25, 32]. In contrast to the exclusive isovector character of the IVGDR, the PDR can be probed using both isovector and isoscalar probes [33].

Although the PDR has been studied extensively in the past years and decades, its origin and systematics are still heavily debated [34]. The most common macroscopic models attribute it to an oscillation of a neutron skin against an isospin-saturated ($N = Z$) core [35]. The neutron skin thickness is defined as the difference of the neutron and proton root-mean-square radii, i.e., $r^{\mathrm{n\text{-}skin}} = r_\mathrm{rms}^\mathrm{n} - r_\mathrm{rms}^\mathrm{p}$. It is expected [36] to be closely correlated to the electric dipole polarizability [37, 38]

$$\alpha_\mathrm{D} = \frac{8\pi}{9} \int_0^\infty \frac{\mathrm{d}B\left(E1, E_\gamma\right)}{\mathrm{d}E_\gamma} \frac{\mathrm{d}E_\gamma}{E_\gamma} = \frac{\hbar c}{2\pi^2} \int_0^\infty \frac{\sigma_\gamma^{E1}(E_\gamma)}{E_\gamma^2} \,\mathrm{d}E_\gamma, \tag{1.9}$$

with the reduced transition probability per unit excitation energy $dB(\lambda L, E_\gamma) / dE_\gamma$ and the photoabsorption cross section $\sigma_\gamma^{\lambda L}(E_\gamma)$ for electric dipole radiation, i.e., $\lambda L = E1$. See also Eq. (1.6) and Eq. (2.3). In contrast to the EWSR, the electric dipole polarizability is significantly more sensitive to low-lying electric dipole strength because of the inverse energy-weight. Equation (1.9) is especially useful because it does not require a separation of PDR and IVGDR strength to extract information about the neutron-skin thickness from PDR observations [25]. The electric dipole polarizability is expected to be sensitive to the symmetry energy of the nuclear EoS [36, 39, 40], which in turn impacts astrophysical calculations. Additionally, information about the neutron skin has further implications on the properties of neutron-star crusts [41].

An in-depth review of current (microscopical) models for the $E1$ strength distribution with a focus on the PDR region is found in Ref. [34]. The most successful descriptions have been achieved by microscopic self-consistent mean field models [34]. Another approach is the quasiparticle phonon model (QPM) that also takes into account one-particle one-hole (1p-1h) excitations [42]. The authors of Ref. [43] combine the QPM with energy-density functional (EDF) calculations and nuclear reaction theory, which reproduces the degree of fragmentation of the experimentally observed spectroscopic strength and NRF cross sections sufficiently well.

A further contribution to $E1$ strength observed for ground-state excitations is the two-phonon 1^- state. It is part of a five-state multiplet primarily formed by the coupling $\left[2_1^+ \otimes 3_1^-\right]$ [44] with additional IVGDR admixtures [45]. It is located at $E(1_1^-) \approx E(2_1^+) + E(3_1^-)$.

1.2.2. Magnetic dipole strength

Another feature of the nuclear dipole response for deformed nuclei is the scissors mode [46, 47], which results in orbital $M1$ strength [26]. For ground-state excitations of rare-earth nuclei, it is located at approximately $3\,\mathrm{MeV}$. It was first predicted by Lo Iudice and Palumbo [48] and Iachello [49] before being discovered in (e, e') experiments by Bohle *et al.* [46]. In a macroscopic picture, it is attributed to an out-of-phase oscillation of a neutron and proton fluid on top of an inert core. An overview over collective models (e.g., the geometric two-rotor model [48] or the

algebraic interacting boson model [49]) and microscopic models based on shell-model calculations is given in Ref. [26].

Usually, the scissors mode built on the ground state fragments into several states. Especially for transitions at higher temperature between states of the quasicontinuum at higher excitation energies and nuclear level densitys (NLDs), it results in a resonance-like structure that is also referred to as scissors resonance. The total integrated $M1$ transition strength of the scissors mode excited from the ground state is $\sum B(M1)\uparrow \approx 3\,\mu_\mathrm{N}^2$ [50]. In Oslo-method and two-step cascade (TSC) experiments, transitions between states in the quasicontinuum at excitation energies above the ground-state scissors mode were probed [51–53]. These experimental methods are not sensitive to the multipolarity of the observed strength, however, a resonance-like enhancement is apparent in the γ-decay spectra at around 3 MeV that was interpreted as the $M1$ quasicontinuum scissors resonance. The strength of this resonance was determined to be about twice as strong as the ground-state scissors mode.

A further characteristic of the $M1$ response involves spin-flip transitions, which form the so-called isovector spin-$M1$ (IVS$M1$) resonance typically found at energies between 5 MeV and 10 MeV [26]. In a shell-model picture, they correspond to single-particle transitions between spin-orbit partner shells with the same orbital angular momentum l that were split into two levels with $j = l \pm 1/2$ by the spin–orbit interaction. Evidence for the systematic occurrence of the expected spin-flip resonance is, however, weak until now.

1.2.3. The low-energy enhancement of strength

At low γ-ray energies, an enhancement of dipole strength referred to as low-energy enhancement (LEE) or *upbend* has been claimed [54, 55] for various nuclei [56]. First observations were obtained using the Oslo method and later confirmed using complementary probes [57]. The systematics, origin and electromagnetic character of this upbend are under discussion. While experiments have verified [58, 59] the dipole character of this enhancement, theoretical models for both $E1$ [60] and $M1$ [61] character have been proposed. Indications for a small bias towards $M1$ radiation were found in proton-scattering experiments. The presence of this upbend has considerable influence [62] on neutron-capture cross sections. Hartree-Fock-Bogoliubov (HFB)+quasi-particle random-phase approximation (QRPA) calculations

suggest [63] a strong sensitivity of neutron-capture cross sections of neutron-rich nuclei and proton-capture cross sections of neutron-deficient nuclei on a LEE of $M1$ strength.

The PSF of ^{153}Sm was probed in both Ref. [59] and Ref. [64] using the Oslo method for slightly different energy regions. The LEE is only observed for Ref. [59]. The authors of Ref. [64] attribute the lack of LEE contributions in their data to their comparatively higher energy cutoff at 1 MeV instead of 0.5 MeV, however, deviations are already observed for photon energies below 2 MeV (see Fig. 4c in Ref. [64]).

1.2.4. Electric quadrupole strength

To a certain extent, but weaker than dipole excitations, electric quadrupole ($E2$) transitions can be induced by resonantly absorbed photons. The $E2$ response of even-even nuclei consists of a variety of 2^+ states such as the rotational or vibrational excitation of the 0^+ ground-state ($K = 0$), which is almost always the first excited 2^+_1 state, or the mixed-symmetry 2^+_{ms} state. In the energy range of the IVGDR, isoscalar giant quadrupole resonance (ISGQR) is found, and for higher excitation energies, the isovector giant quadrupole resonance (IVGQR) [31].

1.2.5. Nuclear deformation

The shape of the strength distributions of the aforementioned excitation modes is altered significantly if the atomic nucleus is deformed. Most prominently, it results in the splitting of the IVGDR into several parts. For axially deformed nuclei, the IVGDR begins to broaden with the onset of nuclear deformation and eventually splits into two parts for well-deformed nuclei [65, 66]. For heavy nuclei, it can be approximated as a sum over two Lorentzian distributions (compare Eq. (1.8)). In a hydrodynamic model, the two parts correspond to oscillations along and perpendicular to the symmetry axis of the nucleus [31]. Based on the K-quantum number, which is the projection of the angular momentum quantum number J onto the nucleus' symmetry axis, this splitting is also referred to as K-splitting. The excitation modes are characterized by $K^\pi = 0^-$ for the parallel and $K^\pi = 1^-$ for the two orthogonal oscillations with respect to the nuclear symmetry axis.

An indication for the presence of nuclear deformation is the $R_{4/2} = E(4_1^+)/E(2_1^+)$ value, which takes on $R_{4/2} = 2.0$ for spherical nuclei (vibrator), $R_{4/2} = 2.5$ for γ-soft nuclei and $R_{4/2} = 3.33$ for an axially symmetric rotor [67]. A further characterization of the nuclear (quadrupole) deformation is possible using the Bohr deformation parameters β_2 (quadrupole deformation parameter) and γ (asymmetry deformation parameter). The former yields a direct estimate for the strength of nuclear deformation, ranging from $\beta_2 = 0$ for spherical to $\beta_2 \approx 0.3$ for prolate nuclei [67]. All β_2 values in this work are taken from Pritychenko *et al.* [68]. The latter is equal to $\gamma = 0°$ and $\gamma = 60°$ for axially prolate and oblate deformed nuclei, respectively. For $0° < \gamma < 60°$, the nucleus is triaxially deformed. The maximum triaxial deformation occurs at $\gamma \approx 30°$ [67].

Motivated by the similarities between the IVGDR and PDR in a geometric picture, a similar *K*-splitting has been proposed for the PDR. Calculations [69–71] based on the microscopic QRPA indicate a slight splitting of strength. Multiple experiments have been performed in an attempt to find observational evidence for a *K*-splitting of the PDR. In (γ, γ') experiments performed by Goddard *et al.* [72], the low-energy dipole response of the strongly-deformed ^{76}Se ($\beta_2 = 0.3133^{+0.0055}_{-0.0020}$) was probed. Even though a splitting of the IVGDR has been observed [73] for this nucleus, no obvious evidence for a splitting of the PDR was found. Further (γ, γ') experiments were performed in the $A \approx 160$ mass region, that also contains axially deformed nuclei. An experimental challenge in this mass region for (γ, γ') experiments is the low energy of the first 2^+ state. Tamkas *et al.* [74] with ^{156}Gd ($\beta_2 = 0.3399(40)$) and Papst *et al.* [75] with ^{164}Dy ($\beta_2 = 0.3486(21)$) studied two of the most-deformed stable nuclei in the rare-earth region. In both cases, the total photoabsorption cross section was not accessible because of the low $E(2_1^+)$ value. With the limited observational data, no indication for a splitting of the PDR was found.

A text-book example of nuclear deformation for the IVGDR is the Nd isotopic chain [31], which broadens with increasing mass number and apparently splits [76] into two parts for ^{150}Nd. However, recent proton-inelastic scattering experiments [77] were unable to reproduce this splitting into two well-separated parts for ^{150}Nd. The nucleus ^{150}Nd ($\beta_2 = 0.2825(16)$) is located in the transitional region close to the $X(5)$ critical point [78], so no pronounced splitting is expected. In comparison to all other stable deformed neutron-rich rare-earth nuclei, ^{150}Nd has a comparatively high energy of the 2_1^+ state of $E(2_1^+) \approx 130\,\text{keV}$, much larger than, e.g., ^{164}Dy (73 keV), ^{154}Sm (82 keV), or ^{156}Gd (89 keV). The larger energy gap is beneficial as it allows for the separation of unresolved decays to the 0_1^+ and 2_1^+ state. Thus, ^{150}Nd is not only an excellent

candidate to study the evolution of the PDR with increasing axial deformation but also suitable for refining the experimental method and pushing the limits of the latest generation of MeV-ranged photon beams.

1.3. Statistical model

Statistical model calculations are used to model nuclear reactions, even in the absence of detailed nuclear data, by employing simplifying assumptions and sophisticated models for the behavior of the nuclei. One of these models is the statistical Hauser-Feshbach approach [79]. It simplifies the reaction process by modeling the incoming and outgoing channels independently [80], with a compound nucleus in thermodynamic equilibrium formed as an intermediate step, assuming high level-densities and thus excitation energies. Its main ingredients are NLDs and the transmission coefficients for the entrance and exit channels, which are related to optical model potentials (OMPs) [81]. The OMP describes the interactions of a particle (such as a nucleon or α particle) with the target nucleus. For γ rays, photon strength functions (PSFs), also referred to as γ strength functions (γSFs), are needed instead. Examples for codes that rely on the Hauser-Feshbach formalism for the simulation of nuclear reactions are talys [82–84] and empire [85].

1.3.1. Nuclear level density

The nuclear level density (NLD) $\rho(E, J, \pi)$ describes the number of levels $\Delta N(E, J, \pi)$ per energy interval ΔE. It is the inverse of the average level spacing $D(E, J, \pi)$:

$$\lim_{\Delta E \to 0} \frac{\Delta N(E, J, \pi)}{\Delta E} = \frac{\mathrm{d} N(E, J, \pi)}{\mathrm{d} E} = \rho(E, J, \pi) = \frac{1}{D(E, J, \pi)}. \qquad (1.10)$$

In first order, the NLD increases exponentially with the level energy E [86–88]. Only for sufficiently high NLDs and thus level energies E, the limit in Eq. (1.10) applies and the NLD is approximated by a continuous function. At low energies, NLDs are determined by simply counting the number of observed levels, given the availability of sufficient experimental data.
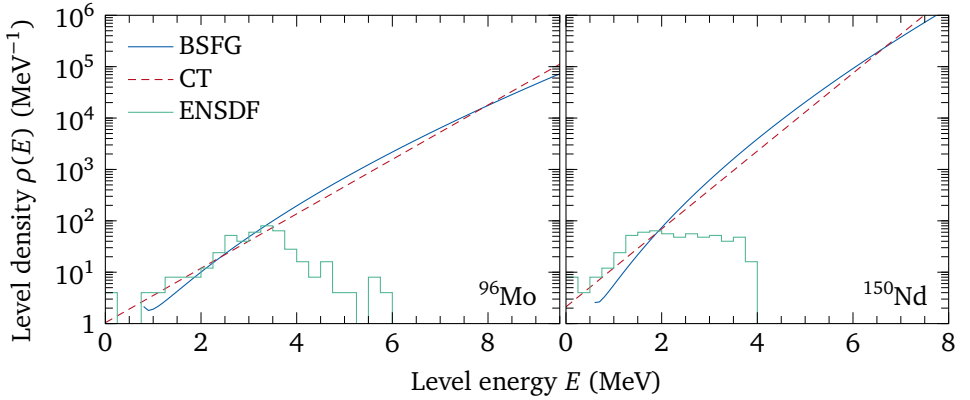
Figure 1.2.: Total NLDs for ^{96}Mo and ^{150}Nd. The parameters for the back-shifted Fermi gas (BSFG) and constant temperature (CT) NLDs are taken from Ref. [89]. For ^{96}Mo, experimental model parameters are used, whereas for ^{150}Nd, model parameters based on a global fit are used. In addition, the NLDs based on experimentally known levels taken from ENSDF [90] (see Refs. [91, 92]) are shown.

Usually, the NLD is assumed [89, 93] to be separable into a total NLD $\rho(E)$ and a spin-distribution function $f(J)$ [94], i.e.,

$$\rho(E,J) = f(J)\rho(E), \qquad f(J) = \exp(-J^2/(2\sigma^2)) - \exp(-(J+1)^2/(2\sigma^2)), \quad (1.11)$$

with spin-cutoff parameter σ, and neglecting any parity quantum number (π) dependency. Two widely-used semi-empirical models are the back-shifted Fermi gas (BSFG) model [86, 88] and the constant temperature (CT) model [88, 94]:

$$\rho_{\text{BSFG}}(E) = \frac{\exp\left[2\sqrt{a(E-E_1)}\right]}{12\sqrt{2}\sigma a^{1/4}(E-E_1)^{5/4}}, \qquad \rho_{\text{CT}}(E) = \frac{1}{T}\exp\left(\frac{E-E_0}{T}\right), \qquad (1.12)$$

with the free parameters a, the temperature T, and the energy parameters (back-shifts) E_1 and E_0. An overview of parametrizations for the spin-cutoff parameter σ and tabulated values for the aforementioned free parameters is found in Ref. [89]. A detailed comparison of six NLD models (also including models based on microscopical calculations) included in the TALYS reaction code is given in Ref. [95]. In Fig. 1.2, the

total BSFG and CT NLDs of ^{96}Mo and ^{150}Nd are depicted, in addition to NLDs from spectroscopically resolved levels at low energies.

1.3.2. Photon strength function

To determine a nucleus' probability of interacting with photons of multipolarity λL, one sums over the partial transition widths $\Gamma_{i\to j}^{\lambda L}$ of all states with spin and parity quantum number J_j^π within an energy range centered around $E_j = E_\gamma$. Alternatively, this quantity can be expressed as a product of the average partial transition width $\langle \Gamma_{i\to j}^{\lambda L} \rangle$ and NLD $\rho(E,J)$, yielding the photon strength function (PSF) [96]

$$f_{i\to j}^{\lambda L}(E_\gamma) = \frac{\langle \Gamma_{i\to j}^{\lambda L} \rangle}{E_\gamma^{2L+1}} \rho(E_\gamma, J).$$
(1.13)

The PSF applies to transitions from groups of states J_i^π around energy E_i to groups of states J_j^π around energy E_j. It is motivated by Fermi's golden rule, which explains the additional energy-dependent factor of $1/E_\gamma^{2L+1}$ in analogy to Eq. (1.6).

One can distinguish the upward $\overrightarrow{f}^{\lambda L}(E_\gamma)$ and downward $\overleftarrow{f}^{\lambda L}(E_\gamma)$ PSFs that correspond to the excitation (photoabsorption) and deexcitation (photoemission) process, respectively. The PSF can also be expressed as a function of the average photoabsorption cross section $\langle \sigma^{\lambda L} \rangle$:

$$\overrightarrow{f}_{i\to j}^{\lambda L}(E_\gamma) = \frac{1}{(\pi \hbar c)^2} \frac{\langle \sigma^{\lambda L} \rangle}{g \cdot E_\gamma^{2L+1}}, \qquad g = \frac{2J_j + 1}{2J_i + 1},$$
(1.14)

with the spin-statistical factor g. For typical ground-state excitations, $i = 0$.

A database containing experimental and theoretical PSF data has been compiled by Goriely *et al.* [97]. In Ref. [98], the authors discuss the influence of NLDs and PSFs on reaction cross sections relevant for astrophysical rates and nucleosynthesis processes (see Section 1.1). They find that the elemental abundance patterns for the i and r process show significant sensitivity to NLD and PSF properties, depending on the mass region and ejection direction. Conversely, the p process is determined to be less sensitive to NLD and PSF models.

1.3.3. Statistical fluctuations

The statistical fluctuations of individual partial transition widths around their average value can be addressed in the framework of random-matrix theory (RMT), developed by Wigner [99] and Dyson [100–102] (see also Ref. [103] and references therein). A recent review is found in Ref. [104]. Assuming that the matrix elements of the Hamiltonian matrices H are randomly distributed following some probability distribution, insights into fluctuations of partial transition widths and the distribution of nearest-neighbor spacings (NNSs) can be gained. For the application in nuclear physics, the matrix should be unitary ($H^\dagger H = \mathbb{1}$), resulting in the Gaussian unitary ensemble (GUE) [100], with random Hamiltonian matrix H^{GUE}. The real and imaginary parts of the complex-valued matrix elements are statistically independent Gaussian-distributed random variables [104]. If invariance under time-reversal is required as an additional restriction, the Gaussian orthogonal ensemble (GOE) [100] is obtained, which is the standard ensemble to model chaotic systems [104]. As a consequence, the Hamiltonian H^{GOE} is orthogonal ($H^T H = \mathbb{1}$) and real-valued. Other random-matrix ensembles include the Gaussian symplectic ensemble (GSE) [100] for systems with half-integer spin or ensembles constructed from invariance requirements [105], but these ensembles do not directly apply to nuclear physics. The canonical ensembles are characterized by the Dyson index β [100], which takes on values of $\beta^{\mathrm{GOE}} = 1, \beta^{\mathrm{GUE}} = 2$, and $\beta^{\mathrm{GSE}} = 4$.

The fluctuation $s := \Delta E / D$ of the actual level spacing ΔE around the average D is given by the Wigner surmise [99, 103, 106, 107], also referred to as Wigner distribution,

$$P(s) = c_\beta s^\beta \exp(-a_\beta s^2), \tag{1.15}$$

with the parameters a_β and c_β fixed by the normalization $\int P(s)\,\mathrm{d}s = \int sP(s)\,\mathrm{d}s = 1$. For Dyson index $\beta = 1$, the values $a_{\beta=1} = \pi/4$ and $c_{\beta=1} = \pi/2$ are obtained. Independent random energy levels characteristic of a Poisson process yield an exponential distribution [108]. In comparison to this exponential distribution, the factor s^β in Eq. (1.15) suppresses small level spacings, resulting in a repulsion of levels. For small s, it is linear for a GOE-Hamiltonian and quadratic for a GUE-Hamiltonian. The repulsion of energy levels was observed experimentally by Rosenzweig and Porter [109].

Similarly, one can study the distribution of partial transition widths $\Gamma_{j \to k}$ around their average $\langle \Gamma_j \rangle$. This distribution was discussed by Porter and Thomas [110], who studied
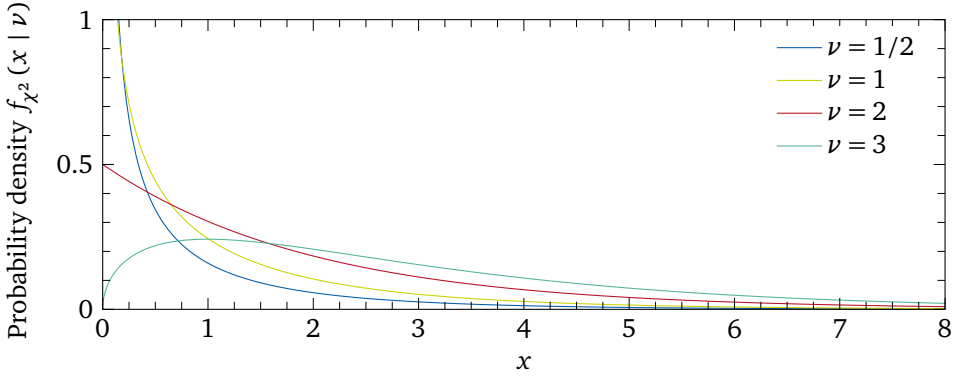
Figure 1.3.: Probability density functions (PDFs) $f_{\chi^2}(x \mid \nu)$ of the χ^2 distribution, depicted for several degrees of freedom ν.

the distribution of reduced neutron widths in the vicinity of the neutron-separation threshold S_{n}. Assuming χ^2-distributed partial transition widths

$$x := \Gamma_{j \to k} / \langle \Gamma_j \rangle, \qquad f_{\chi^2}(x \mid \nu) = \frac{1}{2^{\frac{\nu}{2}} \Gamma\left(\frac{\nu}{2}\right)} x^{\frac{\nu}{2}-1} \exp\left(-\frac{x}{2}\right), \qquad (1.16)$$

with the Gamma function $\Gamma(z)$, they performed a maximum likelihood estimation (MLE) to infer the degree of freedom ν. The χ^2 distribution for different degrees of freedom ν is shown in Fig. 1.3. From the data, they concluded that the reduced transition widths follow a χ^2 distribution with $\nu = 1$, which is now referred to as Porter-Thomas (PT) distribution. Within the framework of RMT, this distribution emerges if the matrix elements of the Hamiltonian are distributed according to a GOE. For a GUE-Hamiltonian, a χ^2 distribution with $\nu = 2$ emerges [111], which is equivalent to an exponential distribution. This distribution was excluded in the study by Porter and Thomas [110].

If time-reversal invariance is only partially broken, the Hamiltonian can be described by an interpolation [112, 113] between GOE and GUE. In this scenario, the degree of freedom ν takes on values between $\nu = 1$ and $\nu = 2$. For $\nu < 1$, because of the strong increase of the χ^2 distribution close to zero, the majority of transitions are small, but

the number of transitions significantly larger than the average value also increases compared to $\nu = 1$. For $\nu > 1$, the system behaves more chaotically, and the partial transition strengths become more homogeneous. For $\nu > 2$, the χ^2 distribution no longer permits arbitrarily small transition widths as it goes down to $f_{\chi^2}(x \mid \nu > 2) = 0^+$ for $x \to 0^+$.

Other degrees of freedom have been under discussion [111, 114–125]. A large dataset of neutron resonances referred to as nuclear data ensemble (NDE) was analyzed [114] to validate the PT distribution. The authors find a good agreement between GOE-predictions and experimental data. In Refs. [115, 116], experimental data for reduced transition probabilities of transitions below 8 MeV for ^{26}Al and ^{30}P was analyzed. A significant deviation from PT predictions is found, but not quantified. In a study by Koehler *et al.* [119], data from neutron-resonance spacings of Pt isotopes was used to determine a degree of freedom of $\nu \approx 0.5$ of the χ^2 distribution, significantly smaller than $\nu = 1$. A subsequent reanalysis of the NDE by Koehler [121] finds a degree of freedom of $\nu = 0.80(5)$ and rejects the validity of the PT distribution with high confidence. This disagreement is attributed to *p*-wave contaminations of the data, which was assumed to contain purely *s*-wave contributions. After correcting for the *p*-wave contaminations by introducing thresholds, a degree of freedom of $\nu = 1.22(9)$ is found, still deviating significantly, but in the opposite direction. In another experiment, for ^{147}Sm, an abrupt change of ν from $\nu = 1.04^{+0.33}_{-0.31}$ to $\nu = 2.7(6)$ was observed [117, 118, 123] for neutron-resonance widths within a narrow energy region slightly above the neutron-separation threshold. In Ref. [124], it is shown that a coupling to other decay channels, such as non-statistical γ decays, can result in a significant modification of width distributions. The resulting effective Hamiltonian consists of a GOE term and an additional coupling term that is not invariant under orthogonal transformations.

The fluctuations of the PSF itself depend on the NLD, as larger numbers of levels average out the effects of individual strong transitions. Thus, assuming χ^2-distributed partial transition widths, an uncertainty

$$\delta f = f \sqrt{2\nu / M} \tag{1.17}$$

for the PSF f can be assigned [96], which depends on the number of considered states M.

1.3.4. The Brink-Axel hypothesis

An assumption that is commonly used for Hauser-Feshbach calculations is the Brink-Axel hypothesis [126, 127]. It was initially proposed by Brink [126], stating that "the energy dependence of the photo effect is independent of the detailed structure of the initial state so that, if it were possible to perform the photo effect on an excited state, the cross section for absorption of a photon of energy E would still have an energy dependence given by (15)" [126]. The mentioned Eq. (15) of Ref. [126] suggest a relativistic Breit-Wigner shape for the IVGDR, which is often referred to as the standard Lorentzian (SLO) distribution. In other words, the IVGDRs built on top of the ground state and excited states are the same, only shifted upward in energy [96, 126]. Later, this hypothesis was generalized [127] and applied to the quasicontinuum region. Nowadays, the hypothesis is interpreted to be applicable to the complete PSF, including the $E1$ and $M1$ distributions for transitions below particle-separation thresholds. This (generalized) Brink-Axel hypothesis states, that the PSF is independent of properties such as level energies, spin, and parity quantum numbers of initial and final states and depends on the γ energy only (e.g., see Refs. [128–130]), except for the obvious multipolarity selection rules. As a consequence, upward $\overrightarrow{f}^{\lambda L}(E_\gamma)$ and downward PSF $\overleftarrow{f}^{\lambda L}(E_\gamma)$ for multipolarity λL are expected to be the same, which is a special case of the detailed-balance principle [131].

Evidently, this hypothesis conflicts with nuclear structure and shell-model perspectives when applied to the transition between individual levels. It requires sufficient NLDs such that multiple levels contribute to the PSF and nuclear-structure related effects average out over many possible transitions. Correspondingly, wave functions of participating levels are expected to contain contributions from numerous possible configurations [96]. This idea can be illustrated through the concept of a compound nucleus. In a compound nucleus reaction [21], the excitation and deexcitation channels, corresponding to the formation and decay of the compound nucleus, can be separated and are independent of each other. The compound nucleus is the result of extensive configuration mixing with many participating (one-particle) states. Thus, the nucleus "forgets" how it was excited, justifying the independence of incoming and outgoing reaction channel.

Several experiments have been performed to ascertain the limits of the applicability of the Brink-Axel hypothesis. Oslo-method experiments detected no violation of the generalized Brink-Axel hypothesis for the quasicontinuum [128]. However, the

Oslo method inherently assumes the validity of this hypothesis, casting doubt on the generalizability of these findings. Experiments in the mass region around $A \approx 60$ also found no violation in proton- and deuteron-scattering experiments [132, 133]. Similarly, other experiments probing the PSF by analyzing two-step cascades in radiative proton-capture experiments [134] found no evidence of a violation of the Brink-Axel hypothesis [135, 136]. All of these experiments only probe the downward PSF. In other experiments, indications were found that the PDR cannot be adequately described with a single PSF [137–139], resulting in a violation of the Brink-Axel hypothesis. In neutron-capture experiments, an energy-dependency of the spreading width of the IVGDR was observed and interpreted as a partial violation of the Brink-Axel hypothesis [140].

The authors of Ref. [141] discuss the applicability of the Brink-Axel hypothesis to the PDR energy region using the microscopic configuration interaction (CI) approach, also known as interacting shell model. They find that the PDR of Ne isotopes is significantly stronger for ground-state excitations, breaking the assumption of the Brink-Axel hypothesis. Also using CI calculations, Johnson [142] draws similar conclusions for the same mass region based on the dependency of the evolution of sum rules on the energy of the initial state.

The nucleus ^{96}Mo was most extensively studied with multiple different probes. The PSF was probed in (γ, γ') experiments using bremsstrahlung [143] (upward PSF extracted from deexcitations), in relativistic proton-scattering experiments at extreme forward angles [144] (upward PSF), and in $(^3\text{He}, ^3\text{He}'\gamma)$ [55] and $(p, p'\gamma)$ [146] experiment using the Oslo method (downward PSF). An overview of all data published to date is shown in Fig. 1.4, including results above the neutron-separation threshold $S_\text{n} = 9.15\,\text{MeV}$ from (γ, n) [145] and $(\gamma, x\text{n})$ [147] experiments.

The Oslo-method results for $(^3\text{He}, ^3\text{He}'\gamma)$ published in Ref. [55] use the s-wave neutron resonance parameters given in RIPL-1 [148] for normalization purposes. In particular, the normalization procedure depends on the s-wave resonance spacing D_0 and the average, total radiative width $\langle \Gamma_\gamma \rangle$. These Oslo-method results were updated in Ref. [145] using preliminary results for the s-wave neutron resonance parameters D_0 and $\langle \Gamma_\gamma \rangle$, later published by Koehler [149], for normalization purposes. The preliminary parameters used in Ref. [145] differ significantly from the final published parameters in Ref. [149]. Both Ref. [55] and Ref. [145] use a version of the Oslo-method analysis code that was later found to contain a coding error in the normalization procedure [146, 150]. In addition, Oslo-method results for $(p, p'\gamma)$ data
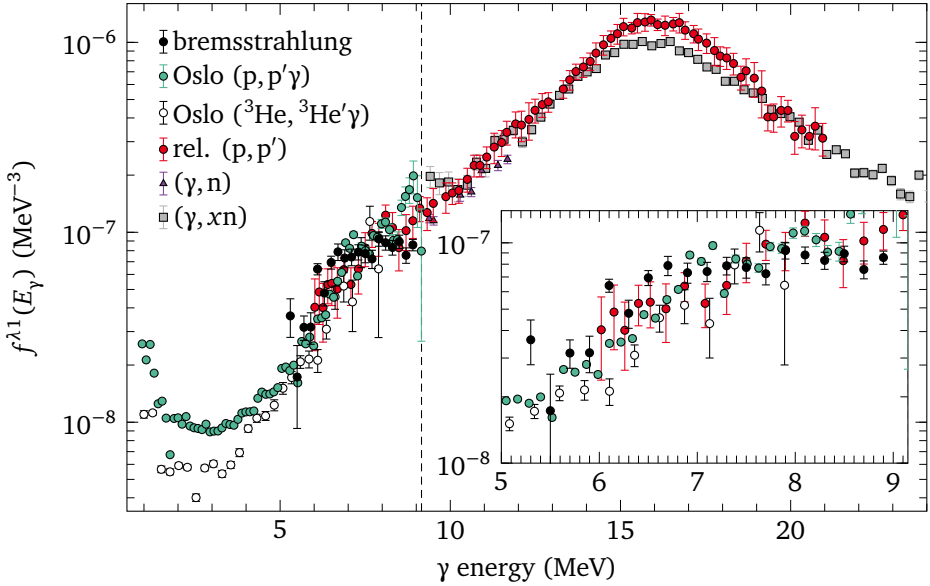
Figure 1.4.: PSF of ^{96}Mo from bremsstrahlung [143], relativistic (p,p') [144], (^{3}He,^{3}He'γ) [55] (with the updated results from Ref. [145]), (p,p'γ) [146], (γ,n) [145], and (γ,xn) [147] experiments. Except for the Oslo-method data (^{3}He,^{3}He'γ) and (p,p'γ), the data are taken from Ref. [97]. The dashed line indicates the neutron-separation threshold.

are reported. Because of the different normalization and the issues in the old Oslo-method code, the (^{3}He, ^{3}He'γ) and the (p,p'γ) dataset differ significantly, especially at low energies.

At low-energies between 5 MeV to 7 MeV, significant discrepancies were found [144] between the bremsstrahlung data, the relativistic proton-scattering data, and the updated (^{3}He, ^{3}He'γ) from Ref. [145]. The bremsstrahlung data yields a PSF that is approximately twice as strong as the PSF inferred from the Oslo-method data, with the proton-scattering data being in between the two, agreeing with both (within uncertainties). At higher energies between 8 MeV to 9 MeV, the (γ,γ') data deviates significantly from the (p,p') data by a factor of up to two for three data points.

Deviations could be explained, at least partially, by the model dependency of all three models. With the most-recent normalization [146] of the (^{3}He, ^{3}He$'\gamma$) Oslo-method data based on results from Ref. [149], a good agreement with the relativistic proton-scattering data is found (not depicted in Fig. 1.4). The same is the case for the (p, p$'\gamma$) Oslo-method results. Still, there is a discrepancy between the results of those three methods and the (γ, γ') bremsstrahlung data. For a discussion of the limitations of the bremsstrahlung method, refer to Section 2.3.5.

A new experimental method based on ($\vec{\gamma}$, $\gamma'\gamma''$) experiments with quasi-monochromatic MeV-ranged photon beams was introduced by Isaak *et al.* [129]. It enables the simultaneous, model-independent determination of upward and downward PSF in a single ($\vec{\gamma}$, $\gamma'\gamma''$) experiment. This method was first demonstrated for ^{128}Te [129]. The experiment found that for the studied energy range of 4 MeV to 8 MeV, the ansatz of the statistical model is insufficient to describe the observed data. Within uncertainties, no unique single PSF is consistent with the data for both absorption and emission, indicating a violation of the Brink-Axel hypothesis.

Until recently, the PSF of ^{128}Te was not yet measured using complementary probes. In 2024, experiments to probe the NLD and PSF of ^{128}Te using the Oslo method in (p, p$'\gamma$) reactions were performed both at the Oslo Cyclotron Laboratory (OCL) and at the IFIN-HH 9 MV tandem accelerator in Bucharest. Thus, it is not yet possible to compare the results with other experimental data. Given the plethora of data that is available for ^{96}Mo and the observed deviations between them, this nucleus is an excellent candidate for further experiments with the ($\vec{\gamma}$, $\gamma'\gamma''$)-based approach. Such an experiment will yield further insights into the limitations of the Brink-Axel hypothesis below particle-separation thresholds, and allow for a verification and further refinement of the experimental method.

The nucleus ^{96}Mo is located in a region of the chart of nuclides where spherical shapes dominate ($R_{4/2} = 2.09$). While still close to sub-shell closures, its proton valence shell ($1g_{9/2}$, two protons) and neutron valence shell ($2d_{5/2}$, two neutron-holes) are both partially filled. This region of the chart of nuclides was already studied extensively in NRF experiments. With respect to the PDR, the effects of adding two protons (in comparison to ^{94}Zr [151]) or two neutrons (in comparison to ^{94}Mo [152]) are of further interest.

1.4. Nuclear resonance fluorescence

PSFs describe the average probability of a nucleus to absorb or emit photons for a given photon energy. Evidently, photonuclear reactions are well-suited for their investigation: An atomic nucleus resonantly absorbs a real photon, resulting in the population of an excited state. The nucleus can then decay via the subsequent emission of potentially multiple particles or γ rays, or via fission, depending on the energy of the excited state. In case of emitted γ radiation, a (γ, γ') reaction takes place, also referred to as nuclear resonance fluorescence (NRF) [153–155].

In analogy to actual particle scattering experiments, this process is also referred to as *photon scattering*, even though the atomic nucleus fully absorbs the exciting photon. Similarly, decays back to the original state (usually the ground state) and via intermediate states are distinguished as *elastic* and *inelastic* photon scattering, respectively.

The photon interacts purely (ignoring gravity) via electromagnetic interaction, which is well-understood and does not introduce dependencies on interaction models. Only limited angular momentum can be transferred from the exciting photon to the nucleus, resulting in a very selective spin-window that allows for $E1$, $M1$, and (to some extent) $E2$ transitions, exclusively. For even-even nuclei, only $J \in \{1^{\pm}, 2^{+}\}$ states can be excited from the $J = 0^{+}$ ground state. Using a beam of photons for excitation, the distinct angular distributions of the corresponding ground-state transitions allow for a direct assignment of angular momentum quantum numbers J. Additionally, for a linearly polarized photon beam, parity quantum numbers π can also be assigned to excited states. Alternatively, instead of restricting (or measuring) the polarization of the incoming photon, the polarization of the outgoing photon can be measured in Compton polarimetry to determine parity quantum numbers.

Because of the low probability for the photon to interact resonantly with the nucleus, significant amounts of material (typically around $\sim 10^{22}$ atoms, $\sim 1\,\mathrm{g}$ to $10\,\mathrm{g}$ for heavy nuclei) have to be amassed for practical NRF experiments. As a consequence, only stable or long-lived isotopes that can be provided with sufficient enrichment $\gtrsim 95\,\%$ in large quantity are suitable NRF targets. The region of the nuclear chart traversed by the r process is completely inaccessible.

PSFs can be extracted separately for the excitation (upward PSF) and deexcitation (downward PSF) process, as described in Section 2.3. NLDs are not directly accessible,

however, for low NLDs, the number of observed levels can simply be counted, assuming that all existing levels are excited and resolved.

1.5. Objectives of this work

The previous sections discuss the most pressing open questions regarding the photoresponse of heavy nuclei for intermediate excitation energies below particle separation thresholds. This work seeks to address some of these questions by providing new experimental data. The main objectives of this work can be summarized as follows:

1. Study the statistics of the decay of the PDR with respect to the excitation energy for a heavy deformed nucleus.

2. Measure the downward PSF built on excited states for a heavy nucleus from $\gamma\gamma$ coincidences in unprecedented detail (uncertainty and covered energy range).

3. Obtain insights into the applicability and limitations of the Brink-Axel hypothesis.

Objective 1 is achieved by measuring the (average) branching of photoexcited states in the PDR-energy region into the ground state band. The average branching ratio can be related to statistical properties of the distribution of partial transition widths of excited states. The study of this quantity for the PDR region, i.e., distributed unresolved strength, has so far been prevented for heavy deformed nuclei in the rare-earth mass region by the low excitation energy of the first excited 2^+ state. Utilizing the latest-generation laser-Compton backscattering (LCB) beams will allow for the spectral resolution of the individual decay branches to the first two states of the ground-state band 0_1^+ and 2_1^+. With the two decay branches resolved, the statistical properties of excited states in the PDR-energy region and their energy dependency can be inferred. The nucleus that was chosen to accomplish this objective is ^{150}Nd, a transitional nucleus at the onset of nuclear deformation, with a comparatively (for this mass region) high energy of the 2_1^+ state at 130 keV.

Objective 2 is achieved by applying the method developed by Isaak *et al.* [129] using the upgraded NRF setup at the High-Intensity γ-ray Source (HIγS), the clover array setup. By considering the PSF built on top of several low-lying states, and covering

a large photon beam energy range, the low-energy cutoff of the measured PSF is reduced in comparison to the previous experimental limit of around 3.5 MeV for ^{128}Te. The measurement of the PSF at low energies will allow addressing open questions such as the LEE observed in multiple experiments.

Finally, objective 3 is achieved by comparing the obtained PSF with results from complementary probes. The atomic nucleus with the most thoroughly investigated PSF, ^{96}Mo, was selected to fulfill this purpose. By comparing the individual PSFs, crucial information about the limitations of the Brink-Axel hypothesis will be obtained, depending on their agreement or disagreement with each other.

2. Experimental methods

In the following chapter, the foundations for the experimental method of NRF are introduced, along with an overview of the angular correlation formalism for γ-ray emission. In addition, several methods for the determination of PSFs are described, including the one used for this work.

2.1. Nuclear resonance fluorescence

Nuclear resonance fluorescence (NRF) describes the resonant absorption and subsequent emission of electromagnetic radiation by an atomic nucleus. Experimentally, this process is observed as a resonance at resonance energy E_r. For a description of the scattering process itself, the complex-valued scattering amplitude $a^{\mathrm{NRF}}(E)$ has to be examined.

The NRF scattering amplitude for a $J_i \rightarrow J_j \rightarrow J_k$ transition is given as [156]

$$
\begin{aligned}
a^{\mathrm{NRF}}(E) &= \sqrt{\sigma_0} \frac{\sqrt{\Gamma_{i \rightarrow j}} \sqrt{\Gamma_{j \rightarrow k}}/2}{(E_r - E) - \mathrm{i}\Gamma_j/2} w(\vartheta, \varphi) \\
&\equiv \sqrt{2\pi \left(\frac{\hbar c}{E}\right)^2 \frac{2J_j + 1}{2J_i + 1}} \frac{\sqrt{\Gamma_{i \rightarrow j}} \sqrt{\Gamma_{j \rightarrow k}}/2}{(E_r - E) - \mathrm{i}\Gamma_j/2} w(\vartheta, \varphi),
\end{aligned}
\tag{2.1}
$$

with resonance energy $E_r = E_j - E_i$, resonance width (total transition width)

$$
\Gamma_j = \sum_k \Gamma_{j \rightarrow k} = \sum_{k, \lambda, L} \Gamma_{j \rightarrow k}^{\lambda L},
\tag{2.2}
$$

partial (transition) widths $\Gamma_{i\to j}, \Gamma_{j\to k}$, their multipole decomposition $\Gamma_{i\to j}^{\lambda L}$, and angular distribution coefficient $w(\vartheta, \varphi)$. The notation for the transition widths in this thesis differs from the conventional notation found in the literature, which omits the index j of the originating state.

The NRF scattering cross section for the cascade $J_i \to J_j \to J_k$ without non-resonant contributions can be calculated from Eq. (2.1) as (c.f. Ref. [156])

$$
\begin{aligned}
\frac{\mathrm{d}\sigma(E)}{\mathrm{d}\Omega} &= 2\pi \left(\frac{\hbar c}{E}\right)^2 \underbrace{\frac{2J_j+1}{2J_i+1}}_{g} \left|\frac{\sqrt{\Gamma_{i\to j}}\sqrt{\Gamma_{j\to k}}/2}{(E_\mathrm{r}-E)-\mathrm{i}\Gamma_j/2}\right|^2 \frac{W(\vartheta,\varphi)}{4\pi} \\
&= 2\pi \left(\frac{\hbar c}{E}\right)^2 g \frac{\Gamma_{i\to j}\Gamma_{j\to k}/4}{(E-E_\mathrm{r})^2+\Gamma_j^2/4} \frac{W(\vartheta,\varphi)}{4\pi} \\
&= \frac{\sigma_0}{1+\left[(E-E_\mathrm{r})/(\Gamma_j/2)\right]^2} \frac{W(\vartheta,\varphi)}{4\pi} \equiv \sigma(E)\frac{W(\vartheta,\varphi)}{4\pi}.
\end{aligned}
\tag{2.3}
$$

This type of cross section $\sigma(E)$ is referred to as the (non-relativistic) Breit-Wigner cross section [157]. By integrating Eq. (2.3) over all possible decays to lower-lying states J_k, one obtains the photoabsorption cross section $\sigma_\mathrm{a}(E)$ [153], replacing $\Gamma_{j\to k}$ with Γ_j in Eq. (2.3).

Usually, resonance widths Γ_j in NRF experiments are of the order of meV, many orders of magnitude smaller than available photon beam bandwidths [155]. Thus, one considers the energy-integrated differential cross section [154]

$$
\begin{aligned}
\frac{\mathrm{d}I_{i\to j\to k}}{\mathrm{d}\Omega}\,\mathrm{d}\Omega &= \int_0^\infty \frac{\mathrm{d}\sigma(E)}{\mathrm{d}\Omega}\,\mathrm{d}E\,\mathrm{d}\Omega = g\pi^2\left(\frac{\hbar c}{E_\mathrm{r}}\right)^2 \Gamma_{i\to j}\frac{\Gamma_{j\to k}}{\Gamma_j}\frac{W(\vartheta,\varphi)}{4\pi}\,\mathrm{d}\Omega \\
&\equiv I_{i\to j}\frac{\Gamma_{j\to k}}{\Gamma_j}\frac{W(\vartheta,\varphi)}{4\pi}\,\mathrm{d}\Omega \equiv I_{i\to j\to k}\frac{W(\vartheta,\varphi)}{4\pi}\,\mathrm{d}\Omega,
\end{aligned}
\tag{2.4}
$$

which is experimentally accessible in NRF experiments, assuming that the spectral distribution of the photon beam can be approximated by a linear function within the range of the resonance energy [155].

Besides NRF, high-energy photons can interact with matter by several other processes [158], including coherent and incoherent scattering from electrons and nuclei,

and the interaction with their respective Coulomb fields. At much higher photon energies ($\gtrsim 100\,\text{MeV}$) than used for typical NRF experiments, further contributions from interactions with the nucleus' internal degrees of freedom start to become relevant. Table 1 in Ref. [158, pp. 38–39] gives an overview over the most important processes and their energy ranges.

Of particular importance are coherent scattering processes that result in scattered radiation that has the same energy as NRF ground-state transitions. Their cross sections could mistakenly be attributed to nuclear reactions with the atomic nucleus, including Rayleigh and Delbrück scattering on electrons, and Thomson scattering on the atomic nucleus [159].

Rayleigh scattering is primarily relevant for lower photon energies below 1 MeV, with its cross section diminishing rapidly at higher energies [160]. Similarly to Delbrück scattering, its differential cross section peaks at small scattering angles ($\lesssim 60°$) [159]. The same behavior is observed for Compton scattering. Hence, NRF experiments are typically performed with detectors placed at larger scattering angles (90° to 135°).

The Thomson-scattering process is the low-energy limit of Compton scattering. Its cross section is independent of the photon energy E. The scattering amplitude as a function of (azimuthal and polar) scattering angles (ϑ, φ) is given by [161]

$$a^{\text{Th}}(\vartheta, \varphi) = -\frac{1}{(4\pi\epsilon_0)} \frac{Z^2 e^2}{(Mc^2)} w^{\text{Th}}(\vartheta, \varphi), \tag{2.5}$$

with nuclear charge Z, nuclear mass (Mc^2), electron charge e, and angular distribution coefficient $w^{\text{Th}}(\vartheta, \varphi)$. A modified variant is given in Ref. [160], extending the Thomson-scattering amplitude with higher-order terms. Squaring the scattering amplitude yields the differential Thomson-scattering cross section [162]

$$\frac{d\sigma^{\text{Th}}}{d\Omega} = \left|a^{\text{Th}}(\vartheta, \varphi)\right|^2 = \frac{1}{(4\pi\epsilon_0)^2} \frac{Z^4 e^4}{(Mc^2)^2} \frac{W^{\text{Th}}(\vartheta, \varphi)}{4\pi}, \tag{2.6}$$

with the angular distribution $W^{\text{Th}}(\vartheta, \varphi)$ normalized to 4π. The total Thomson-scattering cross section can be calculated using [158]

$$\sigma^{\text{Th}} = \frac{8\pi}{3} \frac{1}{(4\pi\epsilon_0)^2} \frac{Z^4 e^4}{(Mc^2)^2}. \tag{2.7}$$

For the two nuclei studied in this work, the nuclear Thomson cross sections are 0.068 mb (^{96}Mo) and 0.115 mb (^{150}Nd).

The angular distribution $W^{\mathrm{Th}}(\vartheta, \varphi)$ is identical to the angular distribution of $0^{\pm} \rightarrow 1^{\pm} \rightarrow 0^{\pm}$ NRF transitions. Thus, one has to consider the coherent interference between both the NRF process and Thomson scattering. For the analysis of individual NRF transitions, the Thomson-scattering contributions are already accounted for by the background fit.

The combined cross section of both processes can be obtained using

$$\frac{\mathrm{d}\sigma}{\mathrm{d}\Omega} = \left| a^{\mathrm{Th}} + a^{\mathrm{NRF}} \right|^2. \tag{2.8}$$

Both terms interfere destructively and constructively on the low- and high-energy side of the NRF resonance, respectively. When integrating over the whole resonance, the constructive and destructive parts cancel each other out. Thus, for low NLDs without overlapping resonances, the interference can be ignored and the Thomson-scattering cross section can simply be subtracted from the total cross section to obtain the NRF cross section.

The energy-integrated cross section for a resonance at energy E_{r} is directly accessible in NRF experiments from the number of observed reactions

$$A = \iiiint \mathrm{d}x\,\mathrm{d}y\,\mathrm{d}z\,\mathrm{d}\Omega\, n_{\mathrm{T}}(x,y,z)\, n_{\gamma}(E_{\mathrm{r}},x,y)$$
$$\times I_{i\rightarrow j\rightarrow k}\, \frac{W(\vartheta,\varphi)}{4\pi}\, \varepsilon(E_{\mathrm{r}},x,y,z,\vartheta,\varphi) \tag{2.9}$$

in the full-energy peak (FEP), with the target density $n_{\mathrm{T}}(x,y,z)$, the time- and energy-integrated photon flux density $n_{\gamma}(E_{\mathrm{r}},x,y)$, and the FEP efficiency for a thin, stable target of finite size, $\varepsilon(E_{\mathrm{r}},x,y,z,\vartheta,\varphi)$, assuming a parallel photon beam. The variables x, y, and z are the Cartesian coordinates, the x axis is parallel to the ground, and the photon beam is aligned with the z axis. For thick targets, the attenuation of the photon beam by resonant and non-resonant scattering processes has to be taken into account [163, 164], resulting in an energy-dependent reduction of the photon flux with increasing penetration depth of the photon beam. Often, including in this work, the position dependency of the photon beam energy distribution is neglected for practical purposes. At the outer parts of the beam, the energy distribution of

the photon beam is shifted to slightly lower energies compared to its central part because of the scattering-angle dependency of the Compton-back-scattered beam. This approximation holds if the point of origin of the photon beam is far away and the beam is sufficiently collimated, which is the case for all experiments presented in this work.

Another quantity of interest is the fraction of all decays that occur for a particular decay channel. For NRF experiments below particle-separation thresholds, photoemission is the only probable decay channel. The ratio of the partial transition width $\Gamma_{j \to k}$ to a lower-lying state in comparison to the total transition width $\Gamma_j = \sum_j \Gamma_{j \to k}$ is called the decay-intensity ratio

$$b = \frac{\Gamma_{j \to k}}{\Gamma_j}. \tag{2.10}$$

Sometimes, it is more instructive to directly compare two decay channels. For the study of deformed nuclei, the ratio

$$R_{\text{exp}} = \frac{B(\lambda L; J_j^{\pi_j} \to J_k^{\pi_k})}{B(\lambda L; J_j^{\pi_j} \to J_l^{\pi_l})} = \frac{\Gamma_{j \to k}}{\Gamma_{j \to l}} \cdot \frac{E_{\gamma, j \to l}^{2L+1}}{E_{\gamma, j \to k}^{2L+1}} \tag{2.11}$$

is of particular importance, as it can be directly related to ratios of Clebsch-Gordan coefficients $\langle J_j, K_j, L, \Delta K | J_k, K_k \rangle$ for angular momentum coupling using the Alaga rules [165]

$$R_{\text{Alaga}} = \frac{B(\lambda L; J_j^{\pi_j} \to J_k^{\pi_k})}{B(\lambda L; J_j^{\pi_j} \to J_l^{\pi_l})} = \left| \frac{\langle J_j, K_j, L, K_k - K_j | J_k, K_k \rangle}{\langle J_j, K_j, L, K_k - K_j | J_l, K_k \rangle} \right|^2. \tag{2.12}$$

They apply to axially-deformed nuclei, and assume a perfect separation of rotational and vibrational degrees of freedom. In NRF experiments for even-even nuclei, they can be applied [155] to the ratio of reduced transition probabilities from excited $J_{K_j} = 1_{K_j}$ states to the 0_1^+ and 2_1^+ states of the $K_k = 0$ ground state band, yielding

$$\frac{B(\lambda 1; 1_{K_j} \to 2_{K_k=0}^+)}{B(\lambda 1; 1_{K_j} \to 0_{K_k=0}^+)} = \left| \frac{\langle 1, 1, 1, -K_j | 2, 0 \rangle}{\langle 1, 1, 1, -K_j | 0, 0 \rangle} \right|^2 = \begin{cases} 2.0 & \text{for } K_j = 0, \\ 0.5 & \text{for } K_j = 1. \end{cases} \tag{2.13}$$

Assuming that *K* is a good quantum number, a value for the *K* quantum number can be assigned based on observed branching ratios.

2.2. Angular correlations

In general, an atomic nucleus with a non-random orientation, i.e., a non-uniform population of magnetic substates (e.g., from application of an external magnetic field or some interaction process such as photoexcitation), emits γ radiation anisotropically. Thus, the consecutive absorption and emission of photons results in an angular correlation between the absorption and emission directions that can be measured and has to be taken into account for γ-ray spectroscopy experiments. As a consequence, the observed angular distribution of the emitted radiation(s) can be used to assign angular momentum and parity quantum numbers to the involved states. The formalism for the calculation of angular correlations, on which the following description is based, is presented in detail in Ref. [166]. This work uses the KSW convention for the multipole mixing ratio δ established by Krane, Steffen, and Wheeler [167]. All angular distributions and correlations are given for emitted photons. To adapt the formalism, at it is described in this work, to NRF reactions, a time-reversal operator has to be applied to the first transition in the cascade, resulting in a sign reversal for the first multipole mixing ratio $\delta(\gamma_0)$.

This formalism allows for the description of angular correlations by summing over several coefficients that describe individual steps in the γ cascade. By fixing the direction (z axis) and polarization (xz plane) of the first photon, the angular distribution of emitted radiation for any subsequent step in the γ cascade can be derived. For excitation by an incident photon beam with a degree of linear polarization $P_{\vec{\gamma}}$ (1: horizontal, -1: vertical), the angular distribution of the *N*-th subsequent step in the decay cascade can be expressed by (adapted from Ref. [166], eq. 12.245)

$$
\begin{aligned}
W(\vartheta, \varphi) = \quad & \sum_{\nu=0,2,4} B_\nu(\vec{\gamma}_0) U_\nu(\gamma_1) \cdots U_\nu(\gamma_{N-1}) A_\nu(\gamma_N) P_\nu(\cos\vartheta) \\
& \left(\pm_{\vec{\gamma}_0}\right) P_{\vec{\gamma}} \sum_{\nu=0,2,4} B_\nu^\perp(\vec{\gamma}_0) U_\nu(\gamma_1) \cdots U_\nu(\gamma_{N-1}) A_\nu(\gamma_N) P_\nu^{(2)}(\cos\vartheta) \cos(2\varphi).
\end{aligned}
$$

$$(2.14)$$
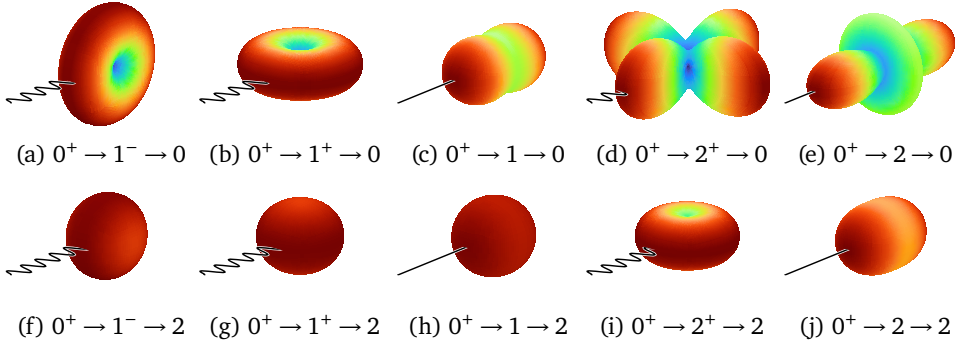
Figure 2.1.: Angular distributions for various NRF transitions excited with polarized (sinusoidal line in plane of polarization) and unpolarized (straight line) photon beams. Only the leading multipole order is assumed to contribute, i.e., $\delta = 0$. The color and amplitude with respect to the zero point at the center depict the relative emission probability for that direction.

Here, $\pm_{\vec{\gamma}_0}$ takes on a positive (negative) sign for electric (magnetic) radiation character of the leading multipole order of the exciting radiation $\vec{\gamma}_0$, $P_\nu(x)$ is the Legendre polynomial, and $P_\nu^{(2)}(x)$ the associated Legendre polynomial of order 2. The coefficients $B_\nu^{(\perp)}$ (orientation coefficient[1]), U_ν (deorientation coefficient[2]), and A_ν (angular distribution coefficient[3]), correspond to the individual steps of the probed cascade, i.e., the excitation, unobserved intermediate decay(s), and the final (observed) decay, respectively. For an unpolarized beam ($P_{\vec{\gamma}} = 0$), the second term in Eq. (2.14) vanishes. The angular distribution is normalized to $\iint W(\vartheta, \varphi) \sin(\vartheta) \, \mathrm{d}\vartheta \, \mathrm{d}\varphi = 4\pi$.

For the angular distributions relevant for the even-even nuclei studied in this work, an

---

[1] See Ref. [166], eqs. (12.228), (12.246).
[2] See Ref. [166], eq. (12.209).
[3] See Ref. [166], eq. (12.185).

$$\delta(\gamma_1) = -1 \qquad \delta(\gamma_1) = 0 \qquad \delta(\gamma_1) = 1 \qquad \delta(\gamma_1) = \infty$$

(a) $0^+ \to 1^+ \to 2$

(b) $0^+ \to 2^+ \to 2$
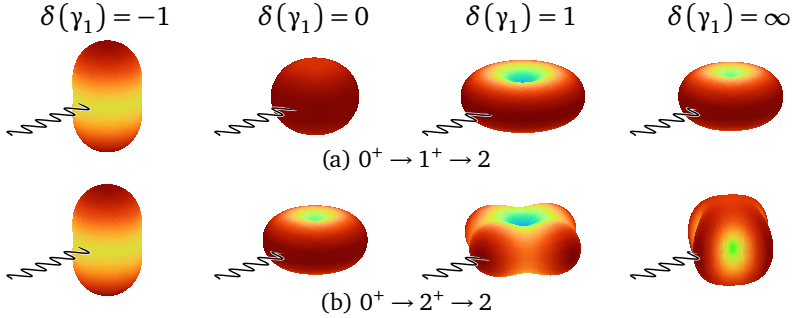
Figure 2.2.: Angular distributions for NRF transitions with different multipole mixing ratios $\delta(\gamma_1) = 0, \pm 1, \pm\infty$. The direction of the exciting linearly polarized photon beam is fixed (sinusoidal line in plane of polarization). The color and amplitude with respect to the zero point at the center depict the relative emission probability for that direction.

even simpler general expression is possible (refer also to eq. (119) in Ref. [155]):

$$W(\vartheta, \varphi) = 1 + \frac{1}{1+\delta(\vec{\gamma}_0)} \frac{1}{1+\delta(\gamma_1)} \left\{ \left[p_2 P_2(\cos\vartheta) + p_4 P_4(\cos\vartheta) \right] \right. \tag{2.15}$$
$$\left. \left(\pm_{\vec{\gamma}_0} \right) P_{\vec{\gamma}} \frac{1}{2} \cos(2\varphi) \left[p_2' P_2^{(2)}(\cos\vartheta) + p_4' P_4^{(2)}(\cos\vartheta) \right] \right\},$$

with the ordinary and associated Legendre polynomials

$$P_2(\cos\vartheta) = \frac{1}{2}(3\cos^2\vartheta - 1), \qquad P_4(\cos\vartheta) = \frac{1}{8}(35\cos^4\vartheta - 30\cos^2\vartheta + 3), \tag{2.16}$$

$$P_2^{(2)}(\cos\vartheta) = 3(1 - \cos^2\vartheta), \qquad P_4^{(2)}(\cos\vartheta) = -\frac{15}{2}(1 - 8\cos^2\vartheta + 7\cos^4\vartheta). \tag{2.17}$$

Figures 2.1 and 2.2 depict the angular distributions encountered in NRF experiments studying even-even nuclei. Refer to Table 2.1 for a set of coefficients relevant to this work. A more extensive table of coefficients p_i can be found in Ref. [155]. In contrast to this work, the authors of Ref. [155] have already applied the time reversal operator to the exciting photon to explicitly describe NRF reactions. Thus, the sign reversal of $\delta(\vec{\gamma}_0)$, which is required for the angular correlations calculated with the formalism

Table 2.1.: The most important angular distribution coefficients for Eq. (2.15) relevant for transitions of even-even nuclei studied in this work.

Transition	$p_2 = p'_2$	p_4	p'_4
$0^+ \xrightarrow{\bar{\gamma}_0} 1^\pm \xrightarrow{\gamma_1} 0$	$\frac{1}{2}$	0	0
$0^+ \xrightarrow{\bar{\gamma}_0} 1^\pm \xrightarrow{\gamma_1} 2$	$\frac{1}{20} + \frac{3}{2\sqrt{5}}\delta(\gamma_1) + \frac{1}{4}\delta^2(\gamma_1)$	0	0
$0^+ \xrightarrow{\bar{\gamma}_0} 2^\pm \xrightarrow{\gamma_1} 0$	$\frac{5}{14}$	$\frac{8}{7}$	$-\frac{4}{21}$
$0^+ \xrightarrow{\bar{\gamma}_0} 2^\pm \xrightarrow{\gamma_1} 2$	$\frac{1}{4} + \frac{1}{2}\sqrt{\frac{15}{7}}\delta(\gamma_1) - \frac{15}{196}\delta^2(\gamma_1)$	$\frac{16}{49}\delta^2(\gamma_1)$	$-\frac{8}{147}\delta^2(\gamma_1)$

described above, is already incorporated. As a consequence, the orientation coefficient $B_\nu^{(\perp)}$ is substituted by another angular distribution coefficient $A_\nu^{(\perp)}$ in Eq. (37) in Ref. [155]. Because the exciting transition for even-even nuclei is of pure multipole character, the direction of time for the first transition is not relevant for Table 2.1.

For $(\vec{\gamma}, \gamma'\gamma'')$ coincidence measurements, the triple angular correlation between all three involved photons can be simplified to the double correlation between the two emitted photons by fixing the direction of the exciting photon as it was done for Eq. (2.14). It is given by (adapted from Ref. [166], eq. 12.204)

$$
W(\vartheta_1, \varphi_1, \vartheta_N, \varphi_N) = \sum_{\substack{\nu_0, q_0, \nu_1, q_1, \nu_N, q_N \\ \nu_0, \nu_1, \nu_2 = 0,2,4}} \frac{(-1)^{\nu_1 + \nu_N}}{\sqrt{2\nu_N + 1}} \overbrace{\begin{pmatrix} \nu_N & \nu_1 & \nu_0 \\ q_N & q_1 & q_0 \end{pmatrix}}^{\equiv \frac{(-1)^{\nu_N - \nu_1 - q_0}}{\sqrt{2\nu_0 + 1}} \langle \nu_N q_N \nu_1 q_1 | \nu_0 (-q_0) \rangle}
$$
$$
\times\, B_{\nu_0, q_0}(\vec{\gamma}_0) A_{\nu_1}^{\nu_2, \nu_0}(\gamma_1) U_{\nu_2}(\gamma_1) \cdots U_{\nu_2}(\gamma_{N-1}) A_{\nu_2}(\gamma_N)
$$
$$
\times\, Y_{\nu_1, q_1}(\vartheta_1, \varphi_1) Y_{\nu_N, q_N}(\vartheta_N, \varphi_N),
$$

$$(2.18)$$

with the 3×2 symbol in round braces referring to the Wigner-$3j$ symbol, and the spherical harmonics $Y_{l,m}(\vartheta, \varphi)$. Again, several coefficients B_{ν_0, q_0} (orientation coefficient[4]), $A_{\nu_1}^{\nu_N, \nu_0}$ (generalized angular distribution coefficient[5]), U_ν (deorientation

---

[4] See Ref. [166], eqs. (12.228) and (12.232) to (12.234).
[5] See Ref. [166], eq. (12.205).

$(\vartheta_2, \varphi_2) =$
$(90°, 180°)$ $(90°, 135°)$ $(90°, 90°)$ $(135°, 180°)$ $(135°, 135°)$ $(135°, 90°)$

(a) $0^+ \rightarrow 1^- \rightarrow 2 \rightarrow 0$

(b) $0^+ \rightarrow 1^+ \rightarrow 2 \rightarrow 0$

(c) $0^+ \rightarrow 2^+ \rightarrow 2 \rightarrow 0$

(d) $0^+ \rightarrow 1^- \rightarrow 2 \rightarrow 2$

(e) $0^+ \rightarrow 1^+ \rightarrow 2 \rightarrow 2$

(f) $0^+ \rightarrow 2^+ \rightarrow 2 \rightarrow 2$
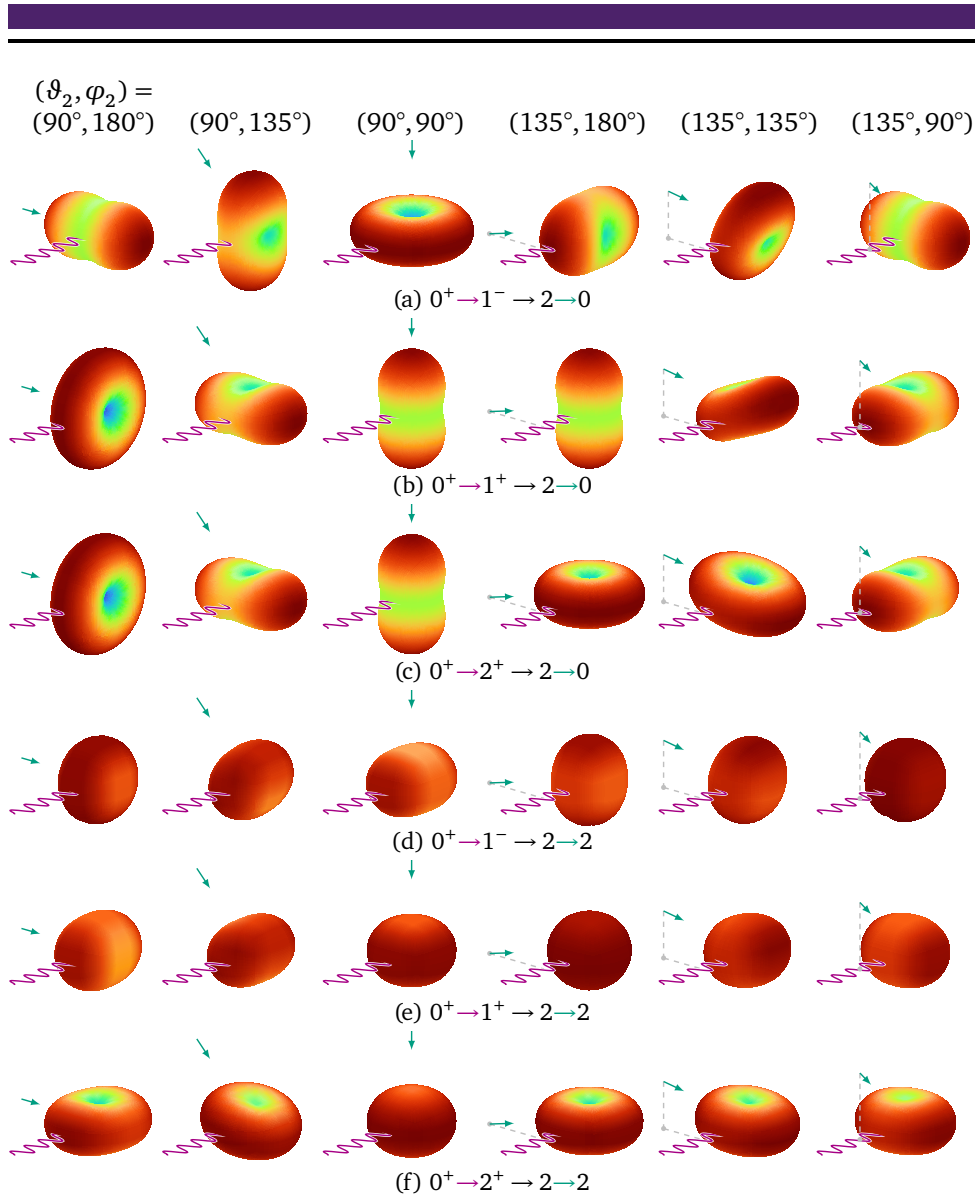
Figure 2.3.: Angular distributions for triple γ cascades ($\delta = 0$). Following excitation by a linearly polarized photon beam (sinusoidal line), the plots depict the angular distribution of the first decay, assuming that the second photon is emitted in the direction (ϑ_2, φ_2) (arrow). See also caption of Fig. 2.1.

$\delta(\gamma_1) = -1 \qquad \delta(\gamma_1) = 0 \qquad \delta(\gamma_1) = 1 \qquad \delta(\gamma_1) = \pm\infty$

(a) $(\vartheta_2, \varphi_2) = (90°, 180°)$

(b) $(\vartheta_2, \varphi_2) = (90°, 135°)$

(c) $(\vartheta_2, \varphi_2) = (90°, 90°)$

(d) $(\vartheta_2, \varphi_2) = (135°, 180°)$

(e) $(\vartheta_2, \varphi_2) = (135°, 135°)$

(f) $(\vartheta_2, \varphi_2) = (135°, 90°)$
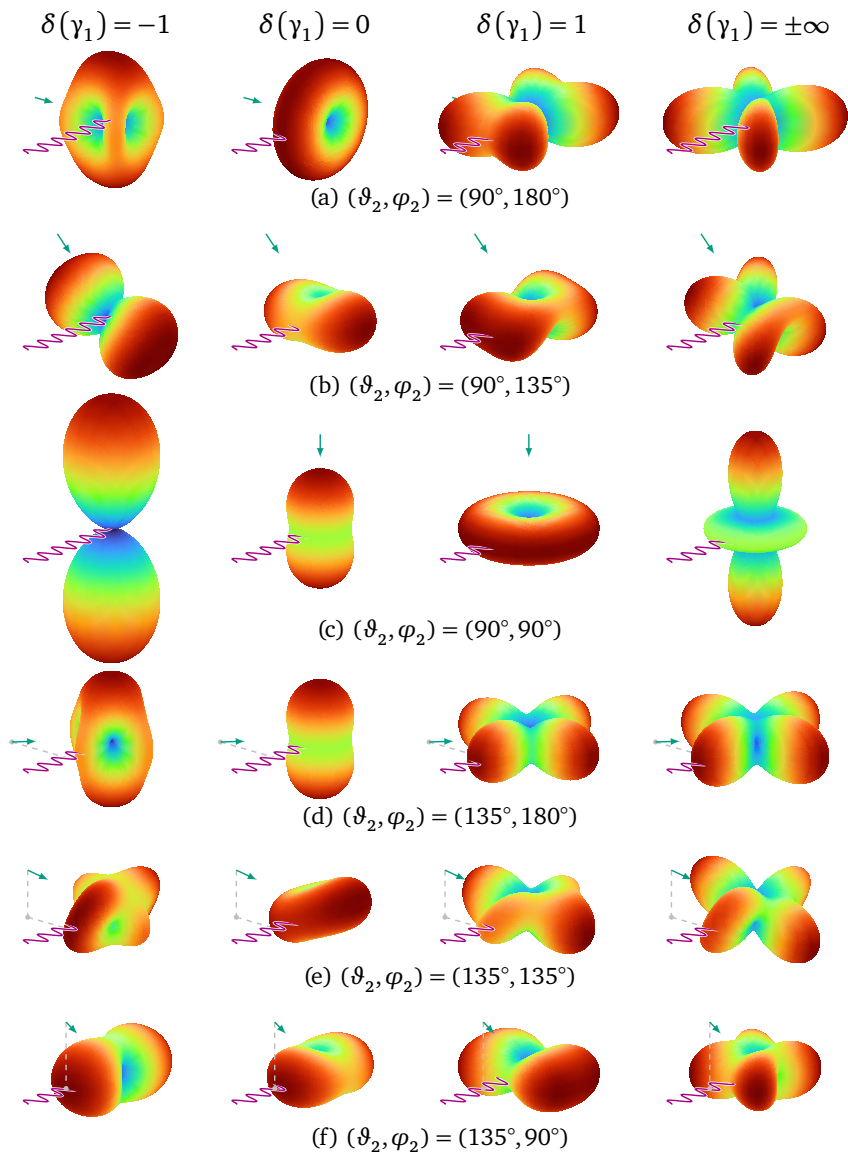
Figure 2.4.: Angular distributions for the triple γ cascade $0^+ \rightarrow 1^+ \rightarrow 2 \rightarrow 0$ for different multipole mixing ratios $\delta(\gamma_1) = 0, \pm1, \pm\infty$. The angular distribution of the first emitted photon is shown. The directions of the exciting photon (purple sinusoidal line) and the second emitted photon (green arrow) are fixed. See also caption of Fig. 2.3.

coefficient[6]), and A_ν (angular distribution coefficient[7]), are used to describe the individual steps of the cascade. The angular correlation applies if the first and last emitted photons of the decay cascade are observed. If no intermediate photons are emitted, i.e., $N = 2$, the U_ν coefficients vanish. The angular correlation is normalized to $\iiiint W(\vartheta_1, \varphi_1, \vartheta_N, \varphi_N) \sin(\vartheta_1) \sin(\vartheta_N) \, d\vartheta_1 \, d\varphi_1 \, d\vartheta_N \, d\varphi_N = 4\pi$.

A fundamental building block of the B_ν, B_{ν_0,q_0}, A_ν, $A_{\nu_1}^{\nu_N,\nu_0}$, and U_ν coefficients are the ordinary (F_ν) and generalized ($F_\nu^{\nu_1 \nu_0}$) F-coefficients,

$$
\begin{aligned}
F_\nu(LL'J_2J_1) = (-1)^{J_1+J_2-1} & \begin{pmatrix} L & L' & \nu \\ 1 & -1 & 0 \end{pmatrix} \begin{Bmatrix} L & L' & \nu \\ J_1 & J_1 & J_2 \end{Bmatrix} \times \\
& [(2J_1 + 1)(2L + 1)(2L' + 1)(2\nu + 1)]^{\frac{1}{2}},
\end{aligned} \tag{2.19}
$$

$$
\begin{aligned}
F_\nu^{\nu_1 \nu_0}(LL'J_1J_0) = (-1)^{L'+\nu_1+\nu_0+1} & \begin{pmatrix} L & L' & \nu \\ 1 & -1 & 0 \end{pmatrix} \begin{Bmatrix} J_1 & L & J_0 \\ J_1 & L' & J_0 \\ \nu_1 & \nu & \nu_0 \end{Bmatrix} \times \\
& [(2J_0 + 1)(2J_1 + 1)(2L + 1)(2L' + 1)(2\nu_0 + 1)(2\nu_1 + 1)(2\nu + 1)]^{\frac{1}{2}}.
\end{aligned} \tag{2.20}
$$

The 3×2 symbols in round and curly braces correspond to Wigner-3j and -6j symbols, respectively, the 3×3 symbol in curly braces is the Wigner-9j symbol.

2.3. Extraction of photon strength functions

Two approaches can be used to extract the PSF from NRF experiments using quasi-monochromatic MeV-ranged photon beams. They can be used to measure both the upward PSF (from the ground-state) and downward PSFs in a single experiment utilizing $\gamma\gamma$ coincidences. Both methods are illustrated in Fig. 2.5. The following descriptions of both methods are based on Ref. [129].

---

[6]See Ref. [166], eq. (12.209).
[7]See Ref. [166], eqs. (12.185).
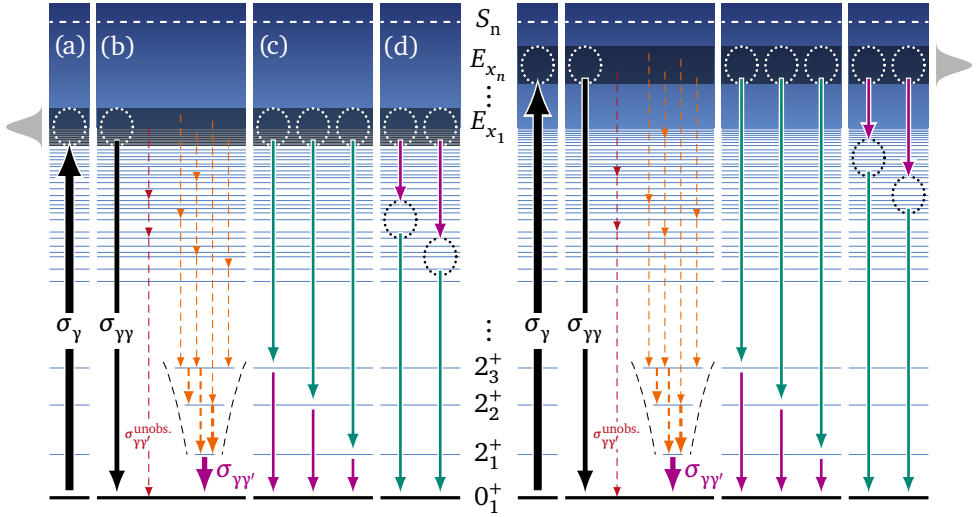
Figure 2.5.: Extraction of upward and downward PSF from a single NRF experiment. (a) A quasi-monochromatic photon beam excites nuclear states in a narrow energy region. (b) The direct ground-state decay ($\sigma_{\gamma\gamma}$) and the decay of the 2_1^+ state (approximately $\sigma_{\gamma\gamma}$) are observed. Similar to a funnel, the 2_1^+ state is expected to collect most of the decay cascades via intermediate states. A fraction of decays bypasses the 2_1^+ state ($\sigma_{\gamma\gamma'}^{\text{unobs.}}$). (c) By gating on transition energies of the decays of low-lying states in $\gamma\gamma$-coincidence measurements, the average branching ratio is determined for each primary-decay branch. (d) Similarly, one can also gate on the continuum of states at energies without corresponding low-energy transitions. This type of measurement is repeated for multiple photon beam energies E_x.

2.3.1. Measurement of the photoabsorption process

After excitation by a quasi-monochromatic photon beam, the excited states decay either via the elastic or the inelastic decay channel. To obtain a measure for the photoabsorption cross section σ_γ, which is directly related to the upward PSF using Eq. (1.14), all contributions to both the elastic ($\sigma_{\gamma\gamma}$) and inelastic ($\sigma_{\gamma\gamma'}$) decay channel have to be measured. Because of the quasi-monochromatic photon beam, elastic decays only occur in a narrow energy range given by the width of the photon beam.

Non-resonant background contributions vanish in this energy region. After applying the detector response correction, both resolved and unresolved strength is obtained by integrating over the excited energy range. Resolved strength is attributed to individual lines that can be separated in experimental spectra (state-to-state analysis). For higher NLDs, the resolution of the detectors is no longer sufficient to separately resolve individual spectral lines. This unresolved strength cannot be attributed to observed transitions, but allows for the analysis of average quantities in integral spectroscopy.

To account for the inelastic decay channel, the selectivity of the NRF reaction is used, which primarily excites $J = 1$ states for even-even nuclei. Most of the decay cascades via intermediate states decay dominantly via dipole and quadrupole transitions that end up populating one of the first few excited states. Thus, these low-lying states act like a "funnel" [168], and by observing their decay, one can obtain an estimate for the missing inelastic decay channel. The combination of both contributions results in a measurement of the full photoabsorption cross section $\sigma_\gamma = \sigma_{\gamma\gamma} + \sigma_{\gamma\gamma'}$ for the excitation energy region of the photon beam.

The validity of this assumption is discussed in Ref. [169] and has been applied to numerous nuclei [25, 72, 75, 138, 152, 170, 171]. Statistical model simulations indicate that, for typical NLD and PSF models, the observed decay of the 2_1^+ state, populated by feeding contributions, typically accounts for more than 90 % of all non-ground state transitions. For ^{164}Dy, a good agreement between the population of low-lying states and statistical model simulations was found [75].

2.3.2. Measurement of the photoemission process

The measurement of the downward PSF using NRF experiments with quasi-mono-chromatic photon beams has been first described by Isaak *et al.* [129]. It is based on the ratio method introduced by Wiedeking *et al.* [57] for particle-induced reactions, which was later independently generalized to the shape method [172].

The ratio method introduces a ratio of the PSF for two energies

$$R = \frac{f_{j \to k}^{\lambda L}(E_j - E_k)}{f_{j \to l}^{\lambda L}(E_j - E_l)} = \frac{N_{jk}}{N_{jl}} \cdot \frac{(E_j - E_l)^{2L+1}}{(E_j - E_k)^{2L+1}}, \qquad (2.21)$$

that is related to the decay intensities N_{jk}, N_{jl} of primary γ-decays to two low-lying states J_k and J_l, respectively. Isaak *et al.* [129] adapted this to the NRF reaction with quasi-monochromatic photon beams, introducing σ_{jk} to denote the cross section for the excitation into the energy region E_j and the subsequent decay to the low-lying state J_k. This quantity R can be obtained in a γγ-coincidence measurement by gating on the decay of a low-lying state to select the primary decays of excited states into it. Using Eq. (2.21), it is directly related to the PSF via

$$f_{j \to k}^{\lambda L}(E_j - E_k) = s_j \frac{\sigma_{j,k}}{(E_j - E_k)^{2L+1}}. \tag{2.22}$$

The arbitrary scaling factor s_j is the same for all low-lying states J_k for a particular photon beam energy E_j. Thus, by gating on the decay of multiple low-lying states, one can obtain the downward PSF at the excited energy region E_j, in arbitrary units, for photon energies corresponding to the energy differences $E_j - E_k$.

The same experiment is repeated for different photon beam energies in close-meshed intervals. For each beam energy, the energy difference between the excited energy region and low-lying states $E_j - E_k$ is different, and thus, one obtains the PSF $f_{j \to k}^{\lambda L}(E_j - E_k)$ at different energies. Assuming the validity of the Brink-Axel hypothesis, all of these PSFs for individual photon beam energies should correspond to a single downward PSF $\overleftarrow{f}^{\lambda L}(E_\gamma)$ that is unique for the probed nucleus.

To obtain this downward PSF, an iterative process can be used, which is illustrated in Fig. 2.6. Starting from the highest photon beam energy, the PSF for this energy is interpolated using a model, such as linear interpolation between each data point. The data points for the next-lower beam-energy setting are scaled to this PSF, minimizing the (quadratic) differences between the data points and the interpolation of the PSF, taking into account the uncertainties of the data points. Using this newly-determined combination of PSF for two different photon beam energies, the process is repeated for each beam-energy setting. This way, one obtains the overall downward PSF $\overleftarrow{f}_{\text{exp}}^{\lambda L,\text{p}}(E_\gamma)$ in arbitrary units (i.e., with an unknown overall scaling factor s) for primary decays (superscript "p"). Finally, this PSF can be scaled to existing PSF data from other experimental probes, or, ideally, from the results obtained to determine the upward PSF in the same NRF experiment as described in Section 2.3.1.

To evaluate the limits of the Brink-Axel hypothesis, one can study the spread of the individual data points $\overleftarrow{f}_{\text{exp}}^{\lambda L,\text{p}}(E_\gamma)$ around a moving-average window (MAW) $\overleftarrow{f}_{\text{MAW}}^{\lambda L,\text{p}}(E_\gamma)$.
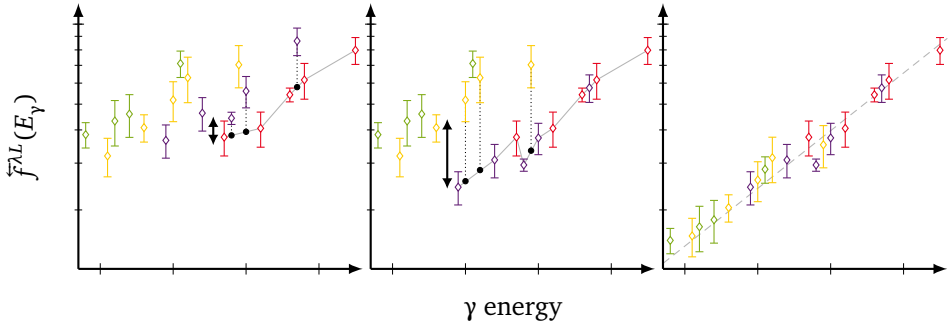
Figure 2.6.: Iterative scaling process applied to the downward PSF for a synthetic dataset. Data points with the same color belong to the same photon beam energy, and constitute one PSF measurement. Each data point of a PSF corresponds to primary decays to a different low-lying state. The combined PSF dataset is initialized with the PSF obtained using the highest photon beam energy (red). In the first step (left panel), the PSF for the next-lower photon beam energy (purple data points) is scaled to the PSF dataset. The procedure minimizes the (squared) differences (dashed black lines) between the purple data points and a linear interpolation of the points in the dataset (gray line), i.e., the red data points. The scaled purple data points are inserted into the combined dataset. In the next step (middle panel), the process is repeated for the PSF for the next-lower photon beam energy (yellow data points). The scaling process is iteratively repeated for all photon beam energies, resulting in a combined dataset that contains the scaled PSF data points for all photon beam energies (right panel).

Assuming PT-distributed partial transition widths in combination with a NLD model, one can calculate the PT-related uncertainty of the PSF using Eq. (1.17). Furthermore, deviations between upward and downward PSF can be studied.

2.3.3. Bremsstrahlung-based method

In the past, a further approach has been used to extract PSF data from NRF experiments using bremsstrahlung [143]. A single NRF bremsstrahlung measurement was performed with an electron-beam energy exceeding the neutron-separation threshold

S_n to ensure a high photon flux up to S_n. Because of increasing NLDs, the spectroscopic resolution of individual transitions is no longer possible for high excitation energies.

The resulting γ-ray spectra have to be analyzed taking into account several additional effects that have to be modeled using simulations: The bremsstrahlung photon beam results in contributions from atomic scattering of the beam on the target. In addition, it has to be considered that nuclear states can simultaneously either be populated directly by the incident photon beam or by decays from higher-lying states. Inelastic NRF transitions in between nuclear states result in further contributions to the γ-ray spectra at lower energies. Furthermore, to obtain the photoabsorption cross section σ_γ, one has to correct for the branching to intermediate states due to non-ground state transitions.

Rusev *et al.* [143] employ a combination of multiple simulations to account for the individual contributions. The spectral profile of the photon beam and the atomic background are described by particle transport simulations. Statistical model simulations account for inelastic transitions, feeding effects, and the missing contributions from branchings to intermediate states. Overall, this approach results in a rather strong model-dependency.

Depending on the studied nucleus, large deviations in comparison to other methods are observed. For example, for ^{100}Mo, the bremsstrahlung measurement [143] results in a very flat PSF that differs significantly from (p, p′) data [146] results obtained both using the Oslo method and the shape method, which exhibit a much steeper PSF. The same can be observed for ^{96}Mo, although to a lesser extent.

2.3.4. The Oslo method

Another method referred to as Oslo method [173] was developed by the Oslo Cyclotron [174] group. It allows for the extraction of PSF data from (p, p′γ), (^{3}He, αγ), and (^{3}He, ^{3}He′γ) reactions. To measure both the emitted γ radiation and the scattered particle, the current setup at the Oslo Cyclotron makes use of two detection systems. The silicon ring ("SiRi") particle-telescope system [175], consisting of two layers of silicon detectors, performs a ($\Delta E - E$)-type measurement of the scattered particles. Additionally, the Oslo Scintillator Array (OSCAR) array [176], consisting of 30 cerium-doped lanthanum(III) bromide (LaBr$_3$) detectors, is used to detect the γ

radiation emitted in the subsequent decay cascade. Earlier experiments made use of the CACTUS array, consisting of 28 thallium-doped sodium iodide (NaI) detectors.

After correcting the observed γ-ray energy spectra for the detector response, the excitation energy vs. γ-ray energy matrix is adjusted to only include the primary (or "first-generation") γ rays emitted in each cascade using the first-generation method [177, 178]. It relies on the assumption that the states directly populated in the particle-scattering reaction decay in exactly the same way as the states populated by decays from higher-lying excited states later on in the decay cascade. The excitation reaction has to populate the same set of states as those populated by decays from higher-lying states. This assumption is valid if the NLD is sufficiently high, such that a compound nucleus is formed. It is implemented as an iterative process, with an initial guess for the first-generation γ-ray spectrum that is iteratively updated in subsequent iterations until the process converges.

Based on the first-generation matrix $P(E_i, E_\gamma)$, the unnormalized NLD and PSF are extracted. Assuming the validity of the Brink-Axel hypothesis, the first-generation matrix is factorized as [55]

$$P(E_i, E_\gamma) = \mathcal{T}(E_\gamma)\rho(E_i - E_\gamma). \qquad (2.23)$$

Here, $\mathcal{T}(E_\gamma)$ depicts the radiative transmission coefficient. Both $\mathcal{T}(E_\gamma)$ and $\rho(E_i - E_\gamma)$ are determined simultaneously by performing a minimization procedure. The results are unnormalized and contain an unknown slope parameter [173]. For normalization purposes, two data points for the NLD $\rho(E)$ are used: (1) At low energies $E \rightarrow 0\,\mathrm{keV}$, $\rho(E)$ is determined by counting the known discrete levels. (2) At the neutron-separation energy S_n, the NLD $\rho(E = S_n)$ can be obtained from s-wave neutron-resonance-spacing data [173]. The normalization has to take into account the spin-selectivity of the excitation mechanism used for Oslo-method experiments, which is model-dependent. For the normalization of $\mathcal{T}(E_\gamma)$, experimental data for the average total radiative width $\langle \Gamma_\gamma \rangle$ of neutron resonances at S_n is used. Both normalizations require experimental data from neutron-absorption experiments. Thus, to apply the Oslo method to a nucleus $^A_Z X$, both $^A_Z X$ and $^{A-1}_Z X$ have to be sufficiently long-lived to allow for the production of suitable enriched targets for Oslo-method experiments and neutron-absorption experiments, respectively.

Assuming that only dipole radiation $L = 1$ contributes, the PSF is calculated from the

normalized radiative transmission coefficient $\mathcal{T}(E_\gamma)$ using

$$f^{\lambda 1}(E_\gamma) = \frac{1}{2\pi} \frac{\mathcal{T}(E_\gamma)}{E_\gamma^3}. \tag{2.24}$$

2.3.5. Relativistic inelastic proton scattering

A further method [179] allows for the determination of the upward PSF and the NLD using relativistic $(\vec{p}, \vec{p}')$ reactions measured at extreme forward angles [180]. This method has been used at the Grand Raiden spectrometer [181] located at the Research Center for Nuclear Physics (RCNP) in Osaka, Japan, to study the PSF of ^{96}Mo [144] and ^{208}Pb [179]. In both experiments, 295 MeV-proton beams were used to excite nuclear states in the excitation energy region of about 5 MeV to 25 MeV via Coulomb excitation, which dominates for small scattering angles.

Two methods can be used to separate contributions from different multipolarities. In the first method, polarization transfer observables are measured [182] in terms of the total spin transfer at $0°$. These observables allow for the distinction between spin-flip ($\Delta S = 1$) and non-spin-flip ($\Delta S = 0$) contributions, which are assumed to correspond to isovector $M1$ spin-flip transitions and the $E1$ IVGDR, respectively. In the second method, multipole decomposition analysis (MDA) [182, 183] can be performed to separate $E1, M1, E2$, and nuclear background contributions, each. The transfer of angular momentum ΔL increases for larger scattering angles. Because the isoscalar giant monopole resonance (ISGMR) is located at higher energies, and isoscalar monopole transitions are only weakly excited in proton scattering [183], $E0$ contributions can be neglected. Nuclear states are excited via virtual photons exchanged between the scattered protons and the nucleus. The $E1$ PSF can be extracted by converting the Coulomb excitation cross sections into equivalent photoabsorption cross sections using the virtual photon method [184]. For the extraction of $M1$ strength using the so-called unit cross section method [185, 186], refer to Refs. [187, 188].

The NLD is extracted by performing a fluctuation analysis [189–191] of the observed spectra, which requires a sufficient energy resolution (~ 20 keV for the discussed experiments).

3. Experimental details

The experiments discussed in this work used three different experimental setups located at two facilities, each providing high-energy MeV-ranged photon beams. This section describes the facilities and the related γ-ray production mechanisms, the experimental setups, detector configurations, and target geometries, and the data acquisition (DAQ) systems of the experimental setups used at HIγS and DHIPS.

3.1. Experimental facilities and setups

Several facilities exist that provide intense high-energy photon beams in the MeV-energy region relevant for nuclear structure applications [155]. For the present work, three experiments were performed at two facilities. Bremsstrahlung-based photon beams were used at the DHIPS setup at the S-DALINAC to perform experiments with ^{150}Nd. Free-electron laser (FEL)-based photon beams were used at HIγS for experiments with both ^{150}Nd and ^{96}Mo. The present study utilizes both facilities to benefit from the unique properties of each radiation source.

3.1.1. Bremsstrahlung at the S-DALINAC

The superconducting Darmstadt electron linear accelerator (S-DALINAC) is an electron accelerator located at Technische Universität Darmstadt in Darmstadt, Germany. It consists of an injector that provides electron beam energies in the range of 2 MeV to 10 MeV and a main accelerator that can increase this energy to up to 130 MeV in up to four passes. A detailed description of the S-DALINAC can be found in Ref. [192]. For the study of photonuclear reactions, the unpolarized electron beam, with a maximum

current of up to 60 μA [192], is extracted from the injector without passing through the main accelerator. It is directed to the DHIPS setup.

3.1.2. Darmstadt High-Intensity Photon Setup (DHIPS)

A detailed overview of the Darmstadt High-Intensity Photon Setup (DHIPS) can be found in Ref. [193]. After exiting the evacuated beam pipe of the S-DALINAC through a 100 μm aluminum exit window, water-cooled radiator targets stop the impinging electron beam, resulting in the emission of a continuous bremsstrahlung spectrum. This spectrum contains γ-ray energies up to the endpoint energy, which corresponds to the kinetic energy of the impinging electron beam. The electron beam can be accelerated to up to 10 MeV by the injector.

Depending on the beam energy, up to two radiator targets have to be used to fully stop the electron beam. For the ^{150}Nd experiment, two radiator targets made from Au ($Z = 79$) with thicknesses of 2.5 mm and 0.5 mm were used. In addition, an optional beam hardener can be added to reduce the photon flux at low photon beam energies. The beam hardener significantly reduces the amount of low-energy radiation scattered on the target, allowing for higher beam currents and thus a higher photon flux in the high-energy region without overwhelming the γ-ray detectors. The ^{150}Nd experiment used a 10 mm copper beam hardener mounted directly in front of the collimator entrance.

Next, the photons pass through a 1480 mm collimator consisting of 14 copper blocks (10×100 mm $+ 4 \times 120$ mm). The radii of the collimator holes increase from 6 mm (upstream) to 12 mm (downstream). The last copper block has an additional circular recess with a depth of 98 mm and a radius of 17.5 mm, corresponding to the final opening of the collimator at its exit. The successive widening of the collimator hole decreases small-angle scattering off the collimator walls.

Table 3.1.: Configuration of the HPGe detectors, including absorbers placed in front of the detectors, for the ^{150}Nd experiment at DHIPS.

Position φ	Detector	Thickness (mm)	
		Cu filter	Pb filter
90°	HPGe80	10	30
−90°	HPGePol	10	30
−130°	HPGe2	10	20

An aluminum plate, located 162 mm behind the end of the collimator, holds the scattering target in place. The aluminum plate is shaped like an annulus with a cutout on one side to allow the photon beam to pass through its center without interaction with the aluminum frame. Two types of target holders are commonly used: One uses two orthogonal strings, while the other employs a set of plastic screws to attach the scattering target or calibration source.

A set of three high-purity germanium (HPGe) detectors placed at azimuthal angles of $\varphi = \pm 90°$ and $-130°$ with respect to the beam axis and a distance of 225 mm (detector end cap to target center) detect the γ-ray radiation emitted from the target position. Bismuth germanate (BGO) anti-Compton shields encompass each HPGe detector. They detect radiation scattered from the HPGe detectors and thus allow for the suppression of events related to photons that only deposit a fraction of the photon energy into the HPGe crystal. Extensive lead shielding blocks the detectors from each other, prevents radiation from directly entering the BGO shields and protects the setup from the high-radiation environment in the accelerator hall, in which DHIPS is located.

A circular 25 mm-radius collimator hole in the lead shielding surrounding each detector allows radiation to reach the HPGe detector crystal from the target position. These collimator holes also hold circular discs, referred to as filters, which decrease the amount of low-energy γ radiation reaching each detector. Typically, a combination of copper and lead filters is employed, with copper filters positioned between the lead filters and the detector end cap. The copper absorbs characteristic X-rays generated by the photoelectric effect, which have comparatively high energies because of the high atomic number of lead ($Z = 82$). For a detailed overview of detector positions and filters used for the experiment discussed in the present work, refer to Table 3.1.

3.1.3. High-Intensity γ-ray Source (HIγS)

The High-Intensity γ-ray Source (HIγS) is located at the Triangle Universities Nuclear Laboratory (TUNL) at Duke University in Durham, NC, USA. It utilizes an FEL to provide quasi-monochromatic linearly or circularly polarized photon beams [194, 195]. A combination of a linear accelerator and subsequent booster ring feed discrete electron bunches with energies of up to 1.2 GeV into an electron storage ring. On a straight section of the storage ring, wiggler magnets force the electrons on a sinusoidal

path, resulting in the emission of optical synchrotron radiation primarily in the direction of the electron beam. A set of optical mirrors backreflects this radiation onto the electron beam. At the interaction point between photons and electron beam, the photons Compton-back scatter off the next electron bunch in the storage ring. This head-on collision takes place in the rest frame of the highly-relativistic electrons ($\beta \approx 1$). The corresponding Lorentz transformations from laboratory frame into rest frame and back result in an energy boost of the photon energy by a factor of $\gamma(1 + \beta)$ for each transformation. This allows for the production of photons in the energy range of 1 MeV to 100 MeV.

The Compton-back scattered photons pass through a circular collimator located about 53 m from the interaction point [195]. Smaller collimator radii decrease the energy bandwidth and spatial extension of the photon beam and the photon flux. An evacuated beam pipe connects the collimator and the experimental setups in the upstream target room (UTR). A special high-resolution mode of the FEL enables a further improvement of the photon beam resolution at the expense of photon flux [194]. This is achieved by detuning the FEL to reduce the energy spread of the electron beam.

Two different experimental setups were used for the two HIγS experiments presented in this work: The ^{150}Nd experiment performed in 2018 made use of the γ³ setup [196]. This setup was superseded by the clover array setup [197] used for the ^{96}Mo experiment in 2021.

3.1.4. γ³ setup at HIγS

In 2001, Pietralla *et al.* [198] performed the first NRF experiments in the UTR at the HIγS facility. The initial setup consisted of four 60 % HPGe detectors used for measurements of parity quantum numbers [198, 199]. HPGe detectors have a high energy resolution compared to other common detector types, such as LaBr$_3$ detectors, of about 3 keV to 5 keV in the relevant energy range. This results in large peak-to-background ratios and enables the resolution of individual lines even for high level densities.

The γ³ setup [196, 200] expands this initial setup with four 3 in × 3 in LaBr$_3$ detectors, resulting in a total of 8 detectors placed around the target position. The LaBr$_3$ detectors provide high detection efficiencies, good time resolution, and can easily

handle rates in excess of $100\,kHz$ or more. A mechanical construction provides mounting points at $\vartheta = 90°$ and $135°$. For the γ^3 and clover array setup, ϑ and φ denote the azimuthal and polar angles. For the detector configuration used for the ^{150}Nd experiment, refer to Table A.1.

A further HPGe detector is located several meters behind the target position. For beam-profile measurements (i.e., measurements of the spectral distribution the photon beam), a motor swivels this $0°$-HPGe detector into the attenuated photon beam.

3.1.5. Clover array setup at HIγS

In 2021, the commissioning of an upgraded mechanical mounting structure referred to as clover array significantly expanded the capabilities of the NRF setup at HIγS. In addition to the large $3\,in \times 3\,in$ LaBr$_3$ detectors, smaller $1.5\,in \times 1.5\,in$ cerium(III) bromide (CeBr$_3$) detectors, standard coaxial (HPGe) detectors, and clover (HPGe) detectors can be mounted. Up to nine CeBr$_3$ detectors are available, providing a slightly reduced energy resolution, similar timing properties and a significantly reduced efficiency (due to the reduced size) in comparison to the LaBr$_3$ detectors. The segmented clover detectors consist of four individual HPGe crystals (called *leaves*) and provide better angular resolution and higher maximum rates than the coaxial single-crystal detectors. By applying an add-back procedure (see Section 4.2.3), the signals of the individual clover leaves can be combined to achieve an efficiency that exceeds the sum efficiency of the individual crystals. Up to eight clover detectors are available. If required and available, the setup can support further coaxial HPGe detectors. For the detector configuration and filters used for the ^{96}Mo experiment, refer to Table A.2.

3.2. Data acquisition systems

3.2.1. γ^3 DAQ

The γ^3 setup combines two complementary and independent DAQ systems: The analog GENIE DAQ records single spectra for the HPGe detectors with a good energy-

resolution. In addition, a digital multi-branch system (MBS)-based [201] DAQ, hereafter referred to as *mbsdaq*, records synchronous event data from all detectors [200] using two Struck SIS3316 digitizer modules [202] with 14 bit and 16 bit resolution, respectively. An advanced trigger-logic with several low- and high-energy thresholds reduces the trigger rate to limit the dead time while still enabling the analysis of coincidences. The mbsdaq also includes additional scaler branches and timestamp information, e.g., for the beam pick-up or the accelerator radio-frequency (RF) signal.

3.2.2. Clover array DAQ

A synchronous DAQ system triggers all channels simultaneously, such that an increase in detector numbers also increases the dead time. The trigger rate of the synchronous mbsdaq already exhausted the limitations of that system. For the first clover array campaign in 2021, a commercial DAQ system from Mesytec called mvme [203] replaced the existing mbsdaq. Though still trigger-based, this so-called *mvmedaq* enables about an order of magnitude higher trigger rates in comparison to the mbsdaq.

The clover array DAQ system consisted of multiple Mesytec MDPP-16 digitizer modules. One digitizer module utilized the charge-to-digital converter (QDC) firmware [204], suitable for signal processing of fast photomultiplier (PMT) signals from scintillator detectors without preamplifier. All other modules employed the standard charge-integrating preamplifier (SCP) firmware [205] suitable for signal processing of signals from HPGe detectors with preamplifiers. When triggered, the MDPP-16 synchronously reads out all of its channels. Each channel supports a single threshold that determines if a channel is read out, depending on the pulse height of a detected pulse (implemented internally using a timing filter amplifier (TFA) and constant fraction discriminator (CFD)). The MDPP-16 also includes several trigger outputs. As a read-out controller, the Mesytec MVLC Versa Module Eurocard-bus (VME) controller [206] was used. It collects, processes, and distributes all the LEMO trigger signals, and performs the initialization and readout of the VME modules using the VMEbus. It communicates with the DAQ control software via User Datagram Protocol (UDP) [207] over Ethernet or via USB.

The add-back procedure applied to clover detectors is most effective when recording signals from all leaves of a detector. Usually, the incident photon deposits most of its

energy into a single clover leaf, with the other clover leaves receiving no or only a small amount of energy. To properly reconstruct the total energy of the incident photon, the add-back algorithm takes the sum of all clover leave energies, which requires the digitizer to record all signals (above noise level) of all clover leaves. However, when setting the internal threshold of the MDPP-16 to the lowest energy possible, the resulting trigger rate would be excessively high. Because all channels (of all digitizer modules) are read out synchronously, the low thresholds would result in excessive dead times and data rates exceeding the capabilities of the DAQ system.

Instead, a more complex trigger system was implemented by including spare MDPP-16 and Struck SIS3316 modules for additional trigger signals. In the following description of the trigger logic, all HPGe detectors are treated as clover detectors. The preamplifiers of each detector had comparable amplification settings for all leaves of each clover detector. By plugging the clover leaf signals into a fan-in/fan-out nuclear instrumentation standard (NIM) module, a sum energy signal for each clover detector was obtained. A single SIS3316-250 module generated two additional triggers (outputs TO, UO) for the scintillators. In total, seven trigger signals were available with different energy thresholds:

- `c_90`: $\gtrsim 70\,\text{keV}$ for clover leaves at $\vartheta = 90°$ (MDPP-16)
- `c_135`: $\gtrsim 70\,\text{keV}$ for clover leaves at $\vartheta = 135°$ (MDPP-16)
- `c_le`: $\gtrsim 300\,\text{keV}$ for clover sum energies (fan-in/fan-out + MDPP-16)
- `c_he`: $\gtrsim 560\,\text{keV}$ for clover sum energies (fan-in/fan-out + MDPP-16)
- `s_to`: $\gtrsim 70\,\text{keV}$ for scintillators at $\vartheta = 135°$ (SIS3316 TO)
- `s_le`: $\gtrsim 300\,\text{keV}$ for scintillators at $\vartheta = 135°$ (MDPP-16)
- `s_uo`: $\gtrsim 1300\,\text{keV}$ for scintillators at $\vartheta = 135°$ (SIS3316 UO)

The thresholds for `c_90`, `c_135` and `s_le` correspond to the internal thresholds of the MDPP-16 modules used for data recording. The clover sum MDPP-16 modules and SIS3316 modules did not take any data but only provided trigger information. A GSI VULOM4A[1] universal logic module collected all trigger signals and combined them using the following trigger conditions:

- `s_uo`: High-energy scintillator singles

---

[1]prototype version of VULOM4B

- `c_he`: High-energy Clover detector singles

- `c_90` $\wedge$ `c_135`: Low-energy clover-clover coincidences (only in between detectors with different ϑ)

- `s_le` $\wedge$ `c_le`: Low-energy scintillator-clover coincidences

The VULOM4A emitted a trigger signal if any of the trigger conditions applied. Because the DAQ system triggered all channels simultaneously, the high-energy single triggers also recorded all channels with coincident low-energy signals. The implemented trigger system did not allow for low-energy coincidences between two scintillators or between two HPGe detectors.

A separate VME crate, operated independently of the mvmedaq crate, contained the SIS3316, the VULOM4A (operated using the TRLO II firmware [208] and related control programs), and a CES RIO4 single board computer. The RIO4 initialized the other two modules over the VMEbus. A control program provided by B. Löher was used to configure the SIS3316 and read out per-channel scalers for the `s_to` trigger threshold.

The lowest γ-ray energies of photons emitted from low-lying states in ^{96}Mo constrained the energies of the trigger thresholds. Low-energy thresholds at 300 keV allowed for the observation of the $0_2^+ \rightarrow 2_1^+$ decay branch at 370 keV in coincidences, and high-energy thresholds at 560 keV allowed for the observation of the $3_1^- \rightarrow 2_3^+$ decay branch at 609 keV.

3.2.3. DHIPS DAQ

For the present work, a new digital DAQ system was implemented for DHIPS and commissioned during the 2020 spring beamtime. It utilizes VME electronic modules to implement the trigger logic and convert the detector signals, resulting in a binary stream in the list-mode data (LMD) format that contains energy and timing information of the detector signals and scaler values.

A single Mesytec MDPP-16 digitizer module operated using the SCP firmware [205] is used to convert signals from both the HPGe detectors and the BGO shields. Because the SCP firmware is optimized for standard charge-integrating preamplifiers, the BGO signal is first amplified using a TFA before entering the digitizer. A VULOM4B module

(operated using the TRLO II firmware [208]) is used to create the trigger signal. It accounts for conversion- and readout-related dead time, keeps track of trigger-related scalers, records trigger timestamps, and optionally provides additional pulser signals. To control and readout the VME modules, a PowerPC-based RIO4-8072 single-slot VME board produced by Mercury Systems is used. It runs a custom Linux distribution with a PREEMPT_RT real-time kernel and includes a gigabit Ethernet interface for network access.

Most of the software used for the readout of the data acquisition system was originally developed for the R^{3}B setup [209] at GSI/FAIR as part of the NUSTAR DAQ. To implement the readout and data transportation pipeline, *drasi* [210] is used. It serves the same purposes as MBS and can be used as a drop-in replacement, but enables higher data rates, provides additional features, is under active development (as of 2024), and available under a GNU LGPL v2.1 license.

The initialization and readout of the modules is performed using the nurdlib library [211, 212], which was extended to provide additional features for the SCP [205] and QDC [204] firmware of the MDPP-16 digitizer. This library is used by the user-provided readout program, referred to as f_user.c. This program provides experiment-specific functions for initialization and readout that are called by drasi ("glue code"). Instead of developing the readout program from scratch, the f_user.c program called r3bfuser [213] developed by the R^{3}B collaboration [209] was used, which was adapted with DHIPS-specific modifications to optimize scaler readout and provide absolute timestamps without a dedicated timestamp source.

The readout is performed using event counting in combination with multi-event readout, shadow readout and early dead-time release [214]. Instead of synchronously reading out every event processed by the MDPP-16 digitizer separately (single-event readout), multiple events are read out at once (multi-event readout), which amortizes the overhead introduced by the readout process. For shadowed multi-event readout, this readout process is also performed in the background, without introducing any additional dead time. Thus, dead time is only introduced for synchronization checks, which are required regularly to make sure that the event counters are still synchronized. Early dead-time release allows the digitizer to convert further events while (event) data are still being transferred, further reducing the introduced dead time. A ucesb [215]-based unpacker for the generated data was created to convert the recorded lmd files into ROOT [216, 217] files.

For data-analysis purposes, an analysis toolkit named *dhips2spec* was created that can be used as a general purpose tool to create spectra and rate plots for DHIPS data. It also allows for the creation of coincidence matrices, timestamp selection, dead-time determination, and to segment runs into time periods with and without active photon beam based on the trigger rate.

For online-monitoring purposes, the nupeline [218] data transport framework was utilized. It provides the foundation for a modular data analysis pipeline. Individual programs that perform different tasks of the data analysis, the so-called boxes, are chained together, communicating via network (Transmission Control Protocol (TCP)) to exchange event data, histograms, and other control parameters and flags. The first box in the pipeline runs the DHIPS-specific unpacker that directly communicates with the DAQ system to populate the analysis pipeline with the online data. Several DHIPS-specific boxes were created to perform tasks such as histogram creation, energy calibration, Compton suppression, dead-time determination, and rate monitoring. Determined metrics can be exported to time-series databases such as InfluxDB [219] or VictoriaMetrics [220] using an adapter box that was created for this purpose. The database collects metrics used for online-monitoring purposes, and is populated from other data sources as well. The Grafana [221] observability platform is used to visualize the recorded metrics, and accessed by the responsible physicist on experimental shift. A generic plugin was created for hdtv [222] to make it possible to view online histograms created by nupeline boxes.

For an in-depth description of the DHIPS DAQ system, refer to the DHIPS DAQ manual [223]. It includes detailed information about the cabling, its various subsystems, the readout process, online monitoring, the data format and processing, and instructions for experiment preparation and detector optimizations.

4. Analysis

This chapter presents the methodology for analyzing the experimental data. It is split into two sections. The first section describes the analysis of the ^{150}Nd data, consisting both of the HIγS and DHIPS experiments. The second section describes the analysis of the ^{96}Mo experiment performed at HIγS. Analysis steps that are equivalent are described in detail in the first section.

The analysis made use of several data analysis tools and libraries. Analysis code was written in C++ and Python. The C++ analysis primarily made use of the ROOT [216, 217] data analysis framework. For the Python analysis, a variety of libraries were utilized, including NumPy [224], Sympy [225], SciPy [226], Matplotlib [227], Pandas [228, 229], Jupyter [230], PyMC [231–233], uproot [234], and ArviZ [235]. In addition, an angular correlation code was written in Julia [236]. Spectral analysis was performed using the hdtv spectrum analysis tool [222]. Visualizations for this work use the TikZ library [237] for LaTeX.

4.1. ^{150}Nd experiments

The ^{150}Nd analysis comprises the DHIPS and HIγS experiments that complement each other. The continuous bremsstrahlung spectrum of the DHIPS-experiment covers the whole energy range up to 6.7 MeV and allows for the determination of absolute energy-integrated cross sections of individual levels relative to well-known cross sections of ^{27}Al. The linearly polarized quasi-monochromatic LCB photon beam of HIγS, on the other hand, can be used to selectively probe the strength in a very narrow energy range.

4.1.1. Simulation of experimental setups

The probability for a detector to interact with γ-ray radiation depends on a variety of factors, such as crystal and scintillator size, detector shielding, and direction of irradiation. For analysis purposes, this interaction probability, referred to as *detector response*, had to be calibrated using a combination of experimental calibration measurements and calculations. A Monte-Carlo particle-tracking simulation based on the GEANT4 toolkit [238–240] was used to model the detector response, which was then scaled using calibration measurements. The geometries of the setups were replicated digitally, including the materials and their physical properties. Particles (in this case, photons) were created in the simulation, and their interaction with the geometry of the setup and detectors was simulated and tracked.

If the detector crystal shape (including dead crystal layers), the geometry of detector housings and shielding, target geometry, and the respective positions and orientations were known exactly, the simulation would be sufficient to completely characterize the detector response. Because these parameters were not known exactly, the results of the simulation were scaled to experimental efficiency-calibration measurements to account for differences between observed and simulated absolute efficiencies.

The simulations for the ^{150}Nd experiments at HIγS and DHIPS were performed using the *utr* code[1] [241]. It makes use of the GEANT4 toolkit[238–240]. For the simulation of electromagnetic interactions such as the photoelectric effect, Rayleigh and Compton scattering, and pair production, the polarized variant of the (phenomenological) *Livermore* physics model provided by GEANT4 was used. For a detailed overview of interaction processes, refer to Ref. [242]. The NRF process itself was not implemented, because the excitation of nuclear levels and subsequent γ-ray emission was not part of the simulation. Other elastic or coherent scattering processes such as Delbrück scattering, which could be mistaken for NRF reactions (especially in a continuum of unresolved transitions), have been demonstrated to be negligible [243].

Detector response simulations with non-isotropic angular distributions for the ^{150}Nd experiments made use of a customized particle source based on an accept-reject sampling algorithm (e.g., refer to section 2.3.2 in Ref. [244]). The utr code provides a hard-coded list of angular distributions for several transitions relevant for typical

---

[1]Originally implemented for simulations of the UTR at HIγS, the utr code was later expanded to also include the DHIPS geometry (and other setups).
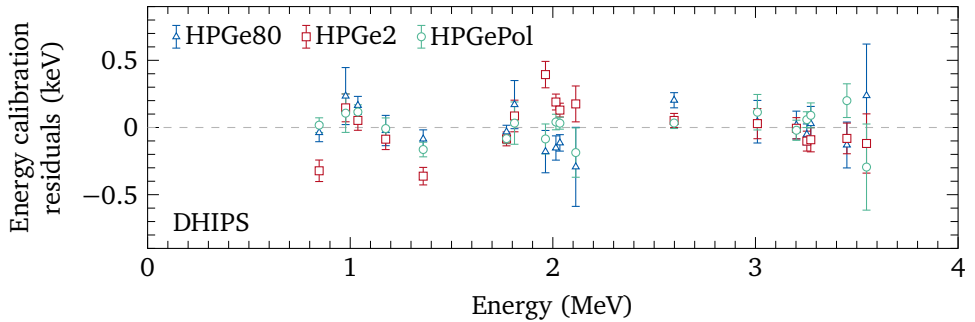
Figure 4.1.: Energy calibration residuals for HPGe detectors at DHIPS. All residuals are smaller than 0.5 keV, indicating that the linear model is sufficient to precisely calibrate the energy spectra.

NRF experiments. The angular distributions were calculated using the angcorrwat code [245], which can automatically generate suitable C++ code, which was then integrated into the utr code.

4.1.2. Detector calibrations

Energy calibration

The analog-to-digital converters (ADCs) provide pulse-height information for individual events (event-based digital DAQs) or in form of prebinned histograms (analog GENIE DAQ). Known spectral lines from natural background radiation, radioactive calibration sources and contaminants were used to associate pulse-heights of the detector signals and γ-ray energies of the incident photons. Lots of spectral lines emitted by radioactive sources were identified in background spectra. For example, in DHIPS background spectra, lines originating from ^{40}K, ^{60}Co, ^{124}Sb, ^{207}Bi, ^{208}Tl, ^{212}Bi, ^{214}Bi, ^{214}Pb, ^{228}Ac, and ^{234}Pa were found. These lines are present up to energies of 2615 keV.[2] Furthermore, radioactive calibration sources with known activity were placed at the target position and provide additional spectral lines up to 3612 keV

---

[2]A background line of ^{214}Bi at 2695 keV exists but is usually below the sensitivity limit.
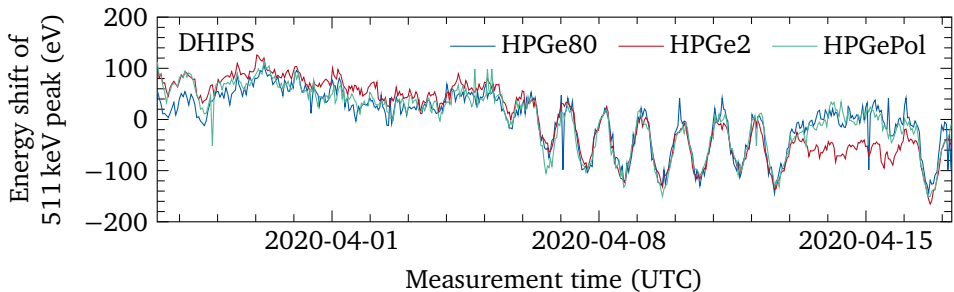
Figure 4.2.: Energy-dependent shift of 511 keV peak relative to its average position in HPGe detectors for DHIPS measurements. From April 6 to April 13, pronounced oscillations with a 24 h period were observed. The absolute scale of the oscillations is negligible in comparison to the peak width and uncertainty of the energy calibration.

(in case of ^{56}Co). Known states of other elements contained in the target that were excited via NRF reactions by the photon beam provide further calibration lines at even higher energies.

For HPGe detectors, a linear model is usually sufficient to describe the relationship between pulse height and γ-ray energy. The resulting residuals are shown in Fig. 4.1. For scintilllator detectors such as the LaBr$_3$ detectors used for the experiment, saturation effects in PMTs result in non-linearities that require polynomials of higher order for a sufficient description of the relationship. For this work, polynomials of degree three were used for the energy-calibration of LaBr$_3$ and CeBr$_3$ detectors.

The non-linear terms result in large uncertainties when extrapolating to higher energies. Because radioactive calibration sources only provide detectable calibration lines up to around 3.5 MeV for scintillator detectors, but measurements were performed with photon beam energies up to almost 10 MeV, large uncertainties are expected if the energy calibration is exclusivey based on the measured calibration lines.

Additionally, the relationship between pulse height and γ-ray energy is not stable but can be influenced by a variety of internal and external factors, such as detection rate, temperature, magnetic fields, or voltage fluctuations. The fluctuations are illustrated for the HPGe detectors of the DHIPS setup in Fig. 4.2. The shift of the 511 keV peak from its mean positions was tracked over time by splitting the data into individual time

slices. The photon beam intensity and detector rates were approximately constant throughout the shown time frame. A strong correlation between the data in the three detectors can be seen. In the second half of the depicted time frame, a sinusoidal wave with a 24 h period emerged. When comparing the data to outside-temperature measurements, it was found that the sinusoudal shift emerges when the maximum temperature of the day exceeded approximately 10 °C. However, it is unclear how the outside temperature could affect detectors located in an underground facility under meters of concrete and lead. The absolute and relative scale ($\lesssim 100\,\text{eV}$) of the observed shifts for the HPGe detectors was insignificant in comparison to other factors and was therefore neglected for the analysis.

However, especially scintillator detectors are sensitive to these influences. For the LaBr$_3$ detectors during the ^{150}Nd HIγS experiment, the position of the ground-state decays (observed as a single bump resembling the shape of the photon beam profile) deviated from the known centroid energy of the photon beam by up to $\pm 20\,\text{keV}$, in some cases even $\pm 30\,\text{keV}$, when using a single energy calibration for all runs. Therefore, the ground-state decay bump was used as an additional data point to create individual energy calibrations for each run.

Width calibration

Natural line widths of typical transitions observed in NRF reactions are in the meV range. Doppler-broadening due to thermal motion increases the width to the eV range. However, the intrinsic resolution of γ-ray detectors is much lower, and determines the energy width of observed spectral lines. The typical experimental resolution of HPGe detectors is several keV, and of scintillator detectors several tens of keV, depending on the transition energy and detector properties. Factors that influence the resolution are, among others, uncertainties from electron-hole pair production and charge collection in the detector, and electronic noise during signal processing [246].

The model

$$\omega^2 = e + p^2 E + c^2 E^2 \tag{4.1}$$

describes the relationship between peak width ω and energy E. The coefficients p, c, and e related to electronic, production, and collection noise [246] were determined from calibration lines. However, similar to the energy calibration, the peak widths of the detectors are also sensitive to influences such as the rate of incident γ rays.

High rates result in a shift of the baseline of the energy signal of the detector, and the overlap of signals from successive pulses can result in a lowered resolution. For the HPGe detectors used at DHIPS, laboratory tests indicate that the peak width at 1332 keV increases by 0.1 keV to 0.7 keV (or 4 % to 13 %), depending on the detector, when the (free) γ-ray rate increases from 1 kHz to 20 kHz. Therefore, peak widths were calibrated using spectral lines from NRF reactions and natural background lines present in runs with active LCB photon beam and not from calibration runs.

If the peak width and the number of counts of the continuous γ-ray background are known, one can define an energy-dependent spectroscopic sensitivity limit for the identification of spectral lines. However, because of the high NLDs of ^{150}Nd, the assumptions of non-overlapping peaks and a continuous background were not fulfilled, especially for higher excitation energies. Already at 5 MeV, the average level spacing for 1^- states is around 2 keV for ^{150}Nd according to CT and BSFG NLD models. Therefore, no sensitivity limit is given in the present work. Instead, the width calibration was used to distinguish individual spectral lines from concentrations of transition strength that originated from clusters of adjacent nuclear states that could not be resolved individually.

Efficiency calibration

The detection efficiency of γ-ray detectors was measured using radioactive calibration sources with known activity. Phenomenological multi-parameter models such as the ones by Knoll [242] or Jäckel, Westmeier, and Patzelt [247] can interpolate the detection efficiency in between the measured data points. Radioactive calibration sources provide calibration lines below 3.6 MeV, however, the experiments performed for this work covered an energy range up to 9.5 MeV. Because of the non-linear (exponential) terms of these models, reliable extrapolations from the decay energies of available calibration sources to the energy ranges studied in this work were not feasible.

Instead, GEANT4 simulations were performed to not only obtain the detection efficiency for FEP events, but the complete detector-response matrix. The simulated energies range from 50 keV to 8000 keV in steps of 50 keV. As a trade-off between the statistical uncertainty and computational costs, 5×10^7 events were simulated per energy setting,
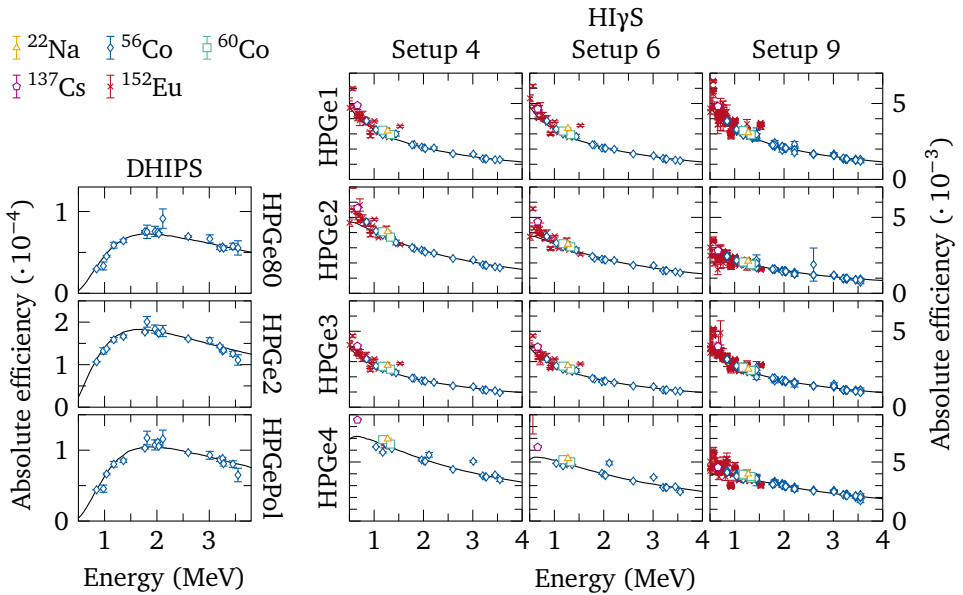
Figure 4.3.: Absolute efficiency calibration for DHIPS and HIγS HPGe detectors for the ^{150}Nd experiment. The efficiency data points of up to five calibration sources are shown, in addition to the simulated curve obtained from GEANT4 simulations, which were scaled to the calibration measurements.

resulting in a relative statistical uncertainty for the number of counts in the FEP of 1 %.

By linear interpolation between the simulated energies, the resolution of the detector-response matrix increases from 50 keV to 1 keV. The FEP position was shifted according to the energy difference between simulated and interpolated energy. The shifted interpolation results in unphysical shifts of the 511 keV and 1022 keV peaks. However, the present work only relies on detector-response matrices above energies of 2 MeV. For a suitable interpolation of detector-response matrices at lower photon energies, see Sec. 5.1.5 in Ref. [248].

The general shape of the energy dependency of the efficiency was sufficiently well-

described by the GEANT4 simulation. Differences in the thickness of the detector shielding or dead regions around the inner core of the detectors [249] resulted in different absolute efficiencies for the simulated and measured detector efficiencies. These deviations were accounted for by scaling the detector-response matrices, such that the experimentally observed efficiencies obtained using calibration measurements with radioactive calibration sources [250–254] were reproduced. For most detectors, the scaling factor was slightly smaller than one, i.e., the simulated efficiencies tended to overestimate the real detection efficiencies. For the HIγS experiment, experimental and simulated efficiencies deviated below 600 keV. At those energies, the efficiency is highly sensitive to even minor deviations in the thickness of detector shields. However, the experiment discussed in the present work only concerns higher energies, and for the scaling of the detector-response matrices, only calibration data points above 1 MeV were taken into account. The observed efficiencies between 1 MeV to 4 MeV were well-reproduced by the GEANT4 simulation, and a good extrapolation across the entire studied energy range up to 7.5 MeV was expected. To interpolate the efficiency for FEP events between simulated data points, a continuous spline was used instead of a linear interpolation for more accurate results. Figure 4.3 depicts the resulting simulated efficiencies and calibration data points both for the DHIPS and HIγS ^{150}Nd measurement for the used HPGe detectors.

4.1.3. Recoil correction

Absorption of the exciting photon and the subsequent emission of radiation result in the transfer of momentum to and from the nucleus. For this reason, for a nucleus at rest, the energy E_γ required to excite a nuclear level is slightly larger than the level energy E_j. Likewise, the energy of the emitted photon is also shifted, depending on angle of emission ϑ with respect to the incident photon. Using the conservation of momentum and energy, and the law of cosines, one obtains the change in energy

$$\Delta E_{\text{Absorption}} = E_{\gamma, i \to j} - E_{\text{r}} = +\frac{E_{\text{r}}^2}{2Mc^2}, \tag{4.2}$$

$$\Delta E_{\text{Emission}} = E_{\gamma, j \to i} - E_{\text{r}} = -\frac{E_{\text{r}}^2}{2Mc^2}\left(1 - 2\cos\vartheta\right) + \mathcal{O}\left(E_{\text{r}}^3\right). \tag{4.3}$$

The energy dependency of the recoil is illustrated in Fig. 4.4, including the energy of a photon emitted from a nucleus at rest.
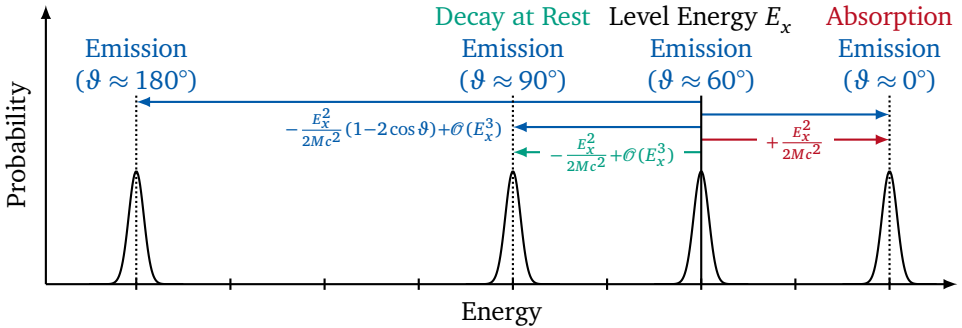
Figure 4.4.: Energy of the absorbed (red) and emitted (blue) photon for an (elastic) NRF scattering process compared to the level energy E_x (black) and to the decay at rest (teal). For the excitation of the nuclear level, the energy of the absorbed photon has to be higher compared to the level energy because of the conservation of energy and momentum. The additional energy is converted into recoil energy of the nucleus. Except for metastable states, excited levels are short-lived. Thus, a nucleus emitting γ radiation is usually in motion from the recoil of the preceding populating reaction and not at rest. The energy of the photon emitted during the subsequent γ decay of the excited nucleus, as observed in the laboratory frame, depends on the emission angle ϑ relative to the incident photon. Additional energy and momentum are transferred to the nucleus.

4.1.4. Photon-flux calibrations

Bremsstrahlung photon-flux calibration at DHIPS

The number of observed scattering events from NRF reactions depends on the number of incident photons N_γ impinging on the target. To calibrate the photon flux for a bremsstrahlung photon beam experiment, one possible method is the simultaneous placement of a reference target in the beam with known energy-integrated cross sections. From the areal density of target nuclei in the reference target, the photon flux per area can be determined.

The ^{150}Nd DHIPS measurement used a so-called sandwich target. The ^{150}Nd target was layered in between two ^{27}Al metal pieces with the same diameter as the target
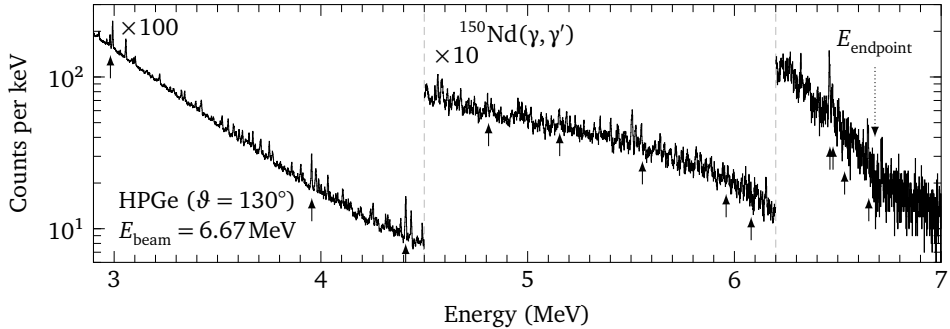
Figure 4.5.: Compton-suppressed spectrum of the ^{150}Nd experiment at DHIPS for the HPGe detector at $\vartheta = 130°$. Arrows mark transitions of ^{27}Al, which was used to calibrate the photon flux. As indicated, the regions from 2.9 MeV to 4.5 MeV and 4.5 MeV to 6.2 MeV are scaled down by factors of 100 and 10, respectively. The dashed arrow indicates the endpoint energy of the electron beam of 6.67 MeV.

material (inner target container dimensions), and masses of 679.5 mg (front of target) and 689.4 mg (back of target), respectively. Placing reference targets on either side ensures that the mean photon flux received by the ^{27}Al is comparable to the one that the ^{150}Nd target experiences.

From the well-known energy-integrated transition strengths of ^{27}Al [255], the time-integrated photon flux of the photon beam was determined. Effects of the geometry of the sandwich target and the angular distribution of the emitted photons (with non-zero multipole mixing ratios δ) were simulated and taken into account using GEANT4 simulations.

The phenomenological Schiff formula [256] approximates the spectral distribution of the bremsstrahlung photon-flux spectrum assuming a thin target. It depends on two parameters, the atomic number of the radiator target and an energy parameter that is slightly larger than the energy of the incident e^- beam but has no physical meaning. Thus, it is not possible to obtain an estimate of a bremsstrahlung spectrum for a given e^--beam energy without further calibration data points. More advanced models use the Born approximation with a higher-order Coulomb correction [257, 258], but require more advanced codes for calculation [259].
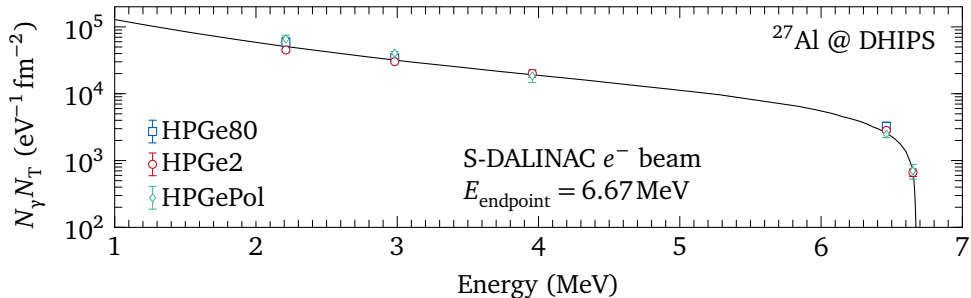
Figure 4.6.: Bremsstrahlung photon beam flux of the ^{150}Nd experiment at DHIPS. The data points, obtained using the ^{27}Al reference target, are rescaled to the number of target nuclei N_{T} of ^{150}Nd to allow for a direct comparison with Fig. 4.10. The curve depicts the photon flux obtained by fitting the Schiff formula to the data points.

For the interpolation of the bremsstrahlung in between the experimental ^{27}Al data points, however, the Schiff formula sufficed. Some data points overlap with ground-state transitions from ^{150}Nd that are observed at HIγS. The area of the ^{27}Al transition at 3956 keV is corrected for the area of the ^{150}Nd ground-state transition at the same energy using the observed ratio of the energy-integrated cross sections of the ^{150}Nd transitions at 3956 keV and 3888 keV at HIγS. The relevant energy range for HPGe spectra of ^{150}Nd taken at DHIPS and HIγS is pictured in Fig. 4.7.

Figure 4.6 shows the bremsstrahlung flux of the ^{150}Nd measurement and the ^{27}Al calibration data points. For easier comparison with the HIγS experiment, where only the product between photon flux N_γ and number of target nuclei N_{T} was measured, the depicted photon flux and ^{27}Al calibration data points were scaled to the number of ^{150}Nd nuclei N_{T}.

The energy spectrum of the HPGe detector placed at backward angles for the DHIPS experiment is depicted in Fig. 4.5. The energies of known ^{27}Al lines are indicated by arrows. Some ^{27}Al lines were overlapping with ^{150}Nd lines and excluded from the analysis. In addition, the spectral lines for transition of ^{150}Nd are visible.
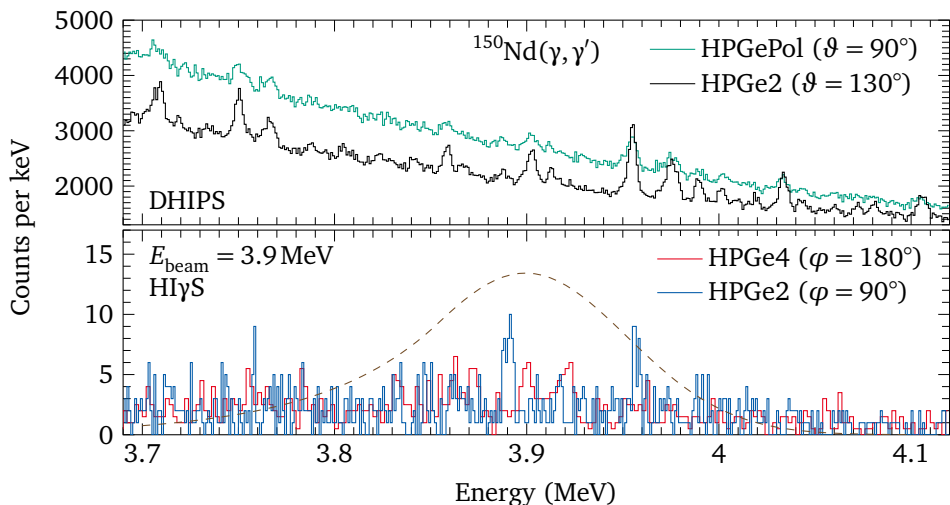
Figure 4.7.: Comparison of DHIPS (top) and HIγS (bottom) spectra for ^{150}Nd. In both cases, the spectra of two HPGe detectors at different angles are depicted. All histograms have bin widths of 1 keV per bin, except for HPGe4, which has a bin width of 2 keV per bin to account for the lower detector resolution. The bin values were scaled down accordingly. The detector names HPGe2 at HIγS and DHIPS refer to two different detectors. The dashed line in the bottom panel indicates the spectral distribution of the quasi-monochromatic photon beam with a nominal energy of 3.9 MeV. There is a ^{27}Al calibration line at 3.956 MeV in the DHIPS spectrum.

Photon flux from atomic background at HIγS

It has been shown [74, 75, 243] that the atomic background, which is dominating the γ-ray spectra at low energies, can be used to calibrate the time- and energy-integrated photon flux for HIγS NRF experiments. In preparation for the photon-flux calibration, a GEANT4 simulation was performed. A polarized photon beam with the diameter of the used collimator was directed at the simulated target. The detector-response-corrected photon beam spectrum was used to define the energy distribution of the simulated photon beam. Spectra were created for detector multiplicities of $m = 1, 2, 3$.

The number of counts within a certain energy range in the spectra of the detectors in
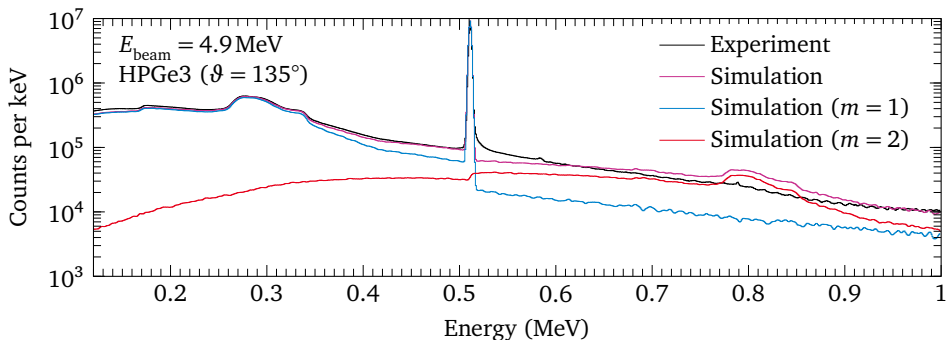
Figure 4.8.: HIγS photon flux calibration using radiation from atomic scattering. The experimental spectrum of HPGe3 is depicted for a photon beam energy of $E_{beam} = 4.9\,\text{MeV}$, in addition to the GEANT4 simulation of the incident photon beam, which was scaled to the experimental spectrum. Its decomposition into events with multiplicities $m = 1$ and $m = 2$ is shown. A convolution with a Gaussian kernel was applied to account for the finite detector resolution. the Compton-scattered photon beam can be seen at around 280 keV, and the e^+e^- annihilation peak at 511 keV.

the setup is proportional to the number of incident photons of the beam. Thus, the ratio of the number of counts in experiment and simulation (normalized to the number of simulated photons) is proportional to the time- and energy-integrated photon flux. Pile-up has to be taken into account [243], which required a more sophisticated fitting procedure that also took into account events with multiplicities to reproduce the experimental spectrum and resulted in additional systematic uncertainties.

A fit was performed to scale the simulated spectra with different multiplicities to the experimental spectrum (see Fig. 4.8). To account for the detector resolution and Doppler broadening of the 511 keV peak, a convolution with a Gaussian kernel was applied to the simulated spectra. The experimental and simulated spectrum agreed very well, especially for energies up to the 511 keV peak. At 511 keV, the simulated spectra contained a step that is not present in the experimental spectra. Events with higher multiplicities (also included in the simulation) compensated for the step. In addition, the tail on the high-energy side of the 511 keV peak also obscured the observed step.

A distinct structure is visible at around 280 keV for the depicted photon beam energy. It is attributed to Compton scattering of the photon beam on the target. The energy range of the structure is directly related to the relative angle of the detector with respect to the beam axis of $\vartheta = 135°$, and its width is determined by the solid angle of the detector. By comparing the spectra of pure background runs to the spectra of runs with active LCB photon beam, it was found that the 511 keV peak was dominated by events that were correlated with the photon beam. The contribution of 511 keV photons from background-related sources was smaller than 0.02 % to 0.2 %, depending on collimator, photon beam energy, beam intensity and detector. Hence, those contributions were neglected, and it was assumed that the 511 keV peak exclusively originates from on-beam events.

Because the scattering cross section for small scattering angles is larger, and the detectors at backwards angles are placed further away from the target, the number of 511 keV photons observed at backward angles was about 12 % to 20 % lower in comparison to detectors placed at 90° with respect to the beam, depending on detector and γ-ray energy.

The results for the energy-integrated photon flux in $\gamma\,s^{-1}$ are depicted in Fig. 4.9. The method was applied to detectors HPGe1, HPGe2, and HPGe3 separately, and combined into a single mean value per photon beam energy setting. The increase in photon flux for higher photon beam energies and the decrease in photon flux for decreasing collimator sizes canceled each other out, such that the photon flux stayed approximately constant throughout the experiment. The individual values obtained for each detector scattered around the mean value by around $\pm 2\%$, which was used to quantify the uncertainty of the method.

To determine the absolute scale of the photon flux, the energy-integrated cross sections of observed transitions were scaled to their known values using a single scaling factor that is the same for all photon beam energies. The energy-integrated cross sections from the DHIPS experiment (above 4 MeV) and from Ref. [260] (below 4 MeV) were used for calibration purposes. The resulting spectral distributions of the photon beam for each photon beam energy setting are depicted in Fig. 4.10. Not the entire target was exposed to the photon beam. As the collimator radius was reduced for higher photon beam energies, the number of target nuclei that could interact with the beam decreases, which was accounted for by adjusting the radius of the photon beam in the GEANT4 simulation. In addition to the photon-flux distributions, Fig. 4.10 also shows the data points that were used for calibration purposes. A good agreement between
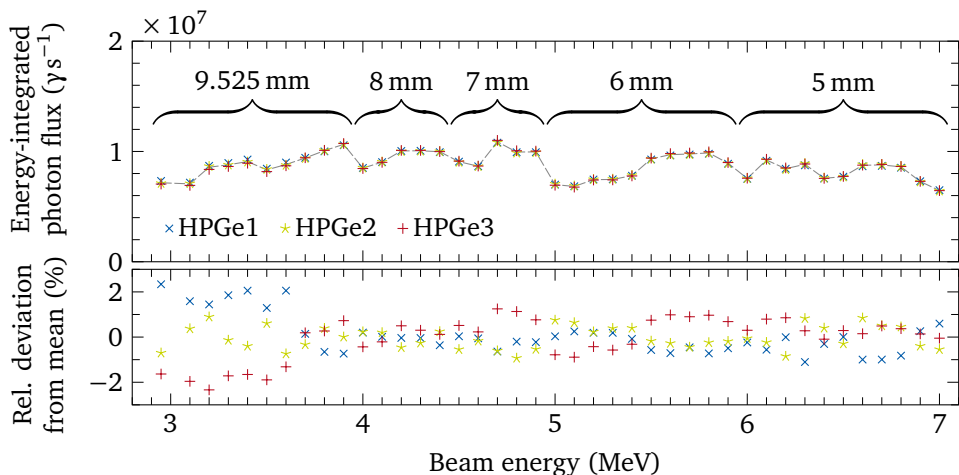
Figure 4.9.: Energy-integrated photon flux for the ^{150}Nd experiment at HIγS. The flux was determined by comparing the area of the 511 keV peak in different detectors with GEANT4 simulations of the photon beam. The dashed line connects the mean value for each photon beam energy setting. The bottom panel shows the relative deviation of the flux values determined independently for each detector from the mean value of all detectors. The annotation in the top panel gives the collimator radius used for each photon beam energy setting.

the calibrated photon-flux distributions and the data points was found for the entire energy range for which transitions were observed.

4.1.5. Analysis of decay behavior

For the ^{150}Nd experiment, the LCB photon beam of HIγS was operated in high-resolution mode (see Section 3.1.3). The collimator radii were carefully selected to maximize the photon flux while keeping the full width at half maximum (FWHM) of the beam below $E_{2_1^+} \approx 130\,\text{keV}$. Below 4 MeV, the high-flux mode was used because it still provided sufficient resolution using a standard $3/8\,\text{in} = 9.025\,\text{mm}$ radius collimator. For higher energies, the high-resolution mode was used in combination
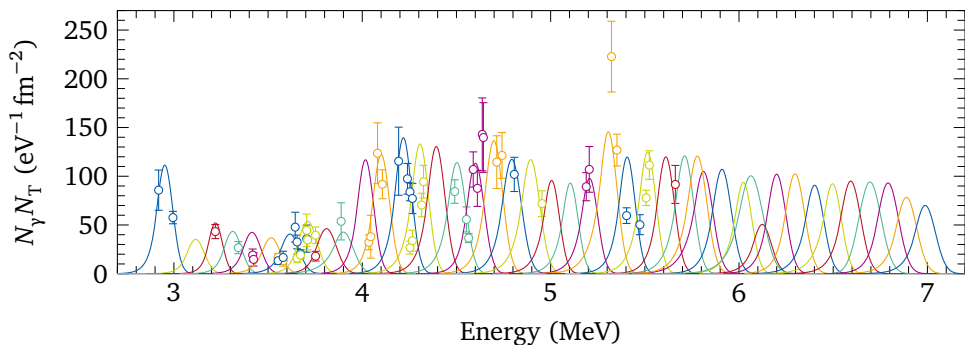
Figure 4.10.: Normalized photon-flux distributions for all photon beam energies of the ^{150}Nd experiment at HIγS. Data points are calibrated using experimental energy-integrated cross sections from DHIPS for energies above 4 MeV and from Ref. [260] for energies below 4 MeV.

with 8 mm, 7 mm, 6 mm, and 5 mm collimator radii. Figure 4.11 shows the FWHM of the LCB photon beam for each energy setting. In almost all cases, the photon beam FWHM stayed below 130 keV.

The accomplished resolution was sufficient to separate both decay branches to the ground-state band. However, there was still significant overlap between the bumps associated with decays to the 0_1^+ and 2_1^+ states. An elaborate fitting procedure was developed to extract and separate the four different contributions from NRF reactions: Decay radiation both from excited 1^- and 1^+ states to both the 0_1^+ ground state and the first excited 2_1^+ state.

The fits were based on several assumptions:

- The NLD in the excited energy region is high.

- The dipole strength is distributed uniformly among excited states.

- Contributions from $E2$ transition strength can be neglected.

As a consequence of the first two assumptions, each decay branch takes on a shape that resembles the shape of the incoming photon beam. For low excitation energies, nuclear-structure effects dominate the properties and distribution of nuclear states,
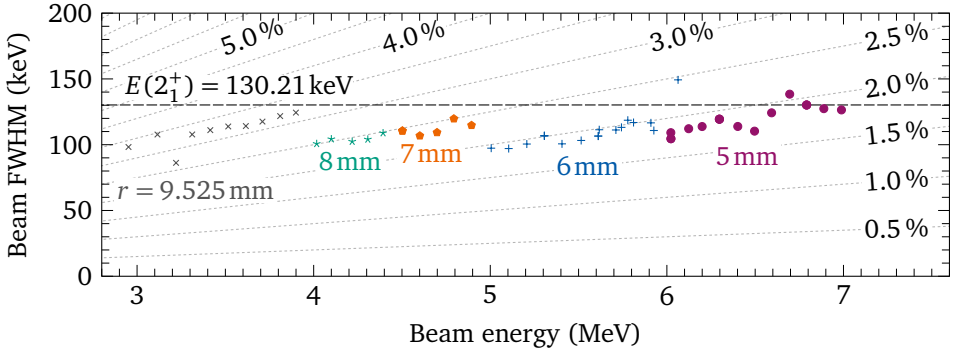
Figure 4.11.: FWHM of the HIγS photon beam for different collimator radii and beam energies. The gray dashed lines indicate different relative widths of the photon beam. The resolution should stay below the black horizontal line corresponding to the energy of the 2_1^+ state to ensure that decays to the 0_1^+ and 2_1^+ states can be distinguished in integral spectroscopy.

consisting of a few strong states only. As the NLD increases with excitation energy, the strength is also distributed more uniformly and is usually described by the χ^2-distribution. Thus, the fit should be able to sufficiently reproduce the experimental spectra for high excitation energies but might fail to reproduce the observed spectra for low excitation energies, especially if single strongly-excited states are present. The absence of observed 2^+ states in the DHIPS spectra supports the last assumption.

The fit took into account several contributions to the resulting nuclear spectra:

- The four possible decay branches, each resembling the shape of the incident photon beam.

- Background radiation. For the HPGe detectors, a separate background measurement was performed, which was combined with a constant-background model (with a single scaling parameter) to account for background observed at higher energies in the detected spectra. For the LaBr$_3$ detectors, background spectra were generated from the online spectra (i.e., runs with beam) by selecting off-beam events using time gates.

- Atomic scattering of the photon beam on the target. The scattered radiation resulted in a tail that increased exponentially towards lower energies (at least locally close to the excitation energy).

- Contributions from NRF reactions on other elements in the target, mainly ^{12}C at an energy of 4439 keV and ^{16}O at an energy of 6915 keV.

The photon beam profile was obtained from a separate measurement involving the 0°-detector. A normal distribution with an exponential tail λ_l on its low-energy side was used to model the spectral distribution of the photon beam. The shape was parametrized by the distribution $\mathcal{T}\left(\mu, \sigma^2, \lambda_l, \lambda_r\right)$, which also includes a right tail λ_r (which was not used here, i.e., $\lambda_r \rightarrow \infty$). The exponential tails $t_i \equiv \sigma \lambda_i$ (with $i \in \{l, r\}$, $t_i \in (0, \infty)$) account for a slower (exponential) decline of the beam intensity far from its center. The PDF (normalized to 1) is defined as

$$
f_{\mathcal{T}}\left(x \,\middle|\, \mu, \sigma^2, \lambda_l, \lambda_r\right) = \nu_{\mathcal{T}} \cdot \exp\left(\left\{\begin{array}{lll} \frac{1}{2}\left(\frac{t_l}{\sigma}\right)^2 + \frac{t_l}{\sigma}\left(\frac{x-\mu}{\sigma}\right) & \text{for} & x - \mu \leq -t_l \\ -\frac{1}{2}\left(\frac{x-\mu}{\sigma}\right)^2 & \text{for} & -t_l < x - \mu < t_r \\ \frac{1}{2}\left(\frac{t_r}{\sigma}\right)^2 - \frac{t_r}{\sigma}\left(\frac{x-\mu}{\sigma}\right) & \text{for} & t_r \leq x - \mu \end{array}\right\}\right),
$$
(4.4)

with the normalization constant

$$
\nu_{\mathcal{T}}^{-1} = \sum_{i \in \{l,r\}} \underbrace{\frac{\sigma^2}{t_i} \exp\left(-\frac{t_i^2}{2\sigma^2}\right)}_{=0 \text{ for } t_i \rightarrow \infty} + \sqrt{\frac{\pi}{2}}\sigma\left(\sum_{i \in \{l,r\}} \underbrace{\mathrm{erf}\left(\frac{t}{\sqrt{2}\sigma}\right)}_{=1 \text{ for } t_i \rightarrow \infty}\right).
$$
(4.5)

At the position where the Gaussian core switches to the exponential tail, the function and its first derivative are continuous. For $\lambda_l \rightarrow \infty \wedge \lambda_r \rightarrow \infty$, the $\mathcal{T}$ distribution reduces to the normal distribution $\mathcal{N}(\mu, \sigma^2)$.

For several reasons, a simple background subtraction combined with a subsequent detector-response correction of the nuclear spectra is not desirable. In the original nuclear spectrum, each bin content corresponds to a Poisson-distributed random variable. Taking the difference of two Poisson-distributed random variables results in a random variable that is no longer Poisson-distributed but instead contains Bessel function terms [261], severely complicating the proper treatment of uncertainties. Performing a detector-response correction of the nuclear spectra is also questionable,
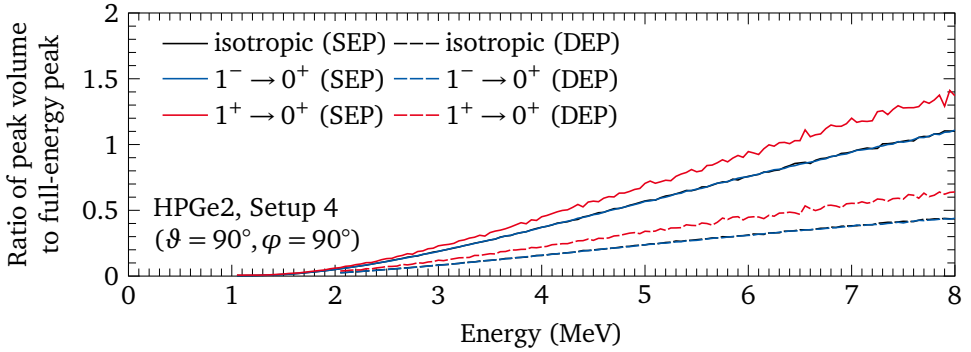
Figure 4.12.: Ratio of single-escape peak (SEP) and double-escape peak (DEP) volume to FEP volume obtained from GEANT4 simulations. The results for detector HPGe2 for the detector distances used for setup 4 are shown.

because the different contributions listed above correspond to different detector-response matrices. No single detector-response matrix can be used for all of them.

The background radiation is known from separate measurements, detector-response correction is neither necessary nor possible (unknown spatial origin of radiation). The four observed decay branches correspond to different angular distributions of the cascades $0^+ \to 1^\pm \to 0^+$ and $0^+ \to 1^\pm \to 2^+$. Depending on the detector, the angular distribution results in a significant deviation of the ratio of escape peaks to the FEP in comparison to isotropically emitted radiation (see Fig. 4.12). Assuming isotropically emitted radiation corrected by a scalar angular distribution factor results in systematic deviations of the order of up to 10 %, depending on energy, detector, and decay branch. For the depicted detector, the number of counts in the escape peaks of 1^+ ground-state transitions is 10 % larger than the number of counts in the escape peaks of 1^- ground-state transitions, assuming identical FEP volumes.

The angular distribution of 2^+ ground-state decays is less pronounced, but also has to be taken into account for the decay of excited states of ^{12}C and ^{16}O, which are also found in the target, and have to be corrected for. Finally, the atomic background radiation from scattering of the photon beam on the target, with an angular distribution described by the Klein-Nishina formula [262], has to be considered. For the
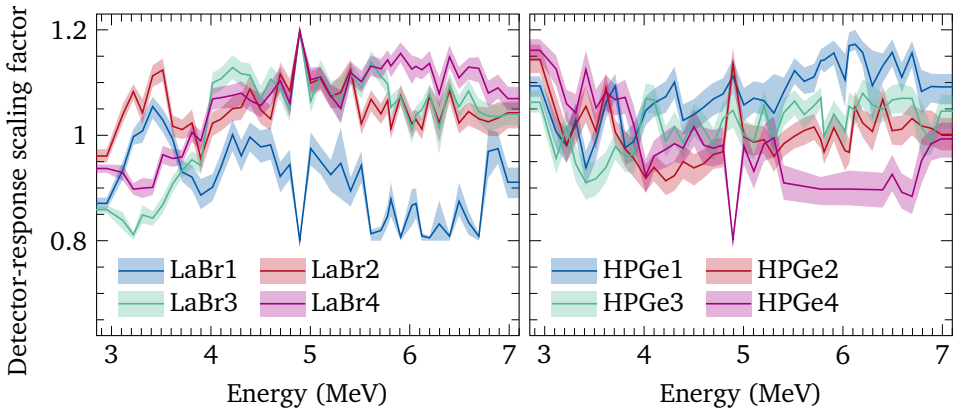
Figure 4.13.: Energy-dependency of the scaling factor of the detector-response matrix for each detector. The deviation of the scaling factor from unity is especially large for the problematic fit at 4.9 MeV.

atomic background radiation, which is detector-response corrected, isotropic emission is assumed, because the detectors are not located at extrema of the corresponding angular distribution.

To account for shifts of the energy calibration in between different runs (see Section 4.1.2), the model included an energy-shift parameter that allowed energy shifts of ± 40 keV for the $LaBr_3$ detectors and ± 3 keV for the HPGe detectors. This shift parameter could also account for potentially asymmetric strength distributions that deviated from the Gaussian shape of the photon beam. To favor the original energy calibration, a (truncated) Gaussian distribution was chosen as the prior probability distribution. The Gaussian prior distribution in a Bayesian model is equivalent to L_1 regularization (LASSO regression) [263, 264] in a frequentist approach. The standard deviation was set to 0.1 keV and 4 keV for the HPGe and $LaBr_3$ detectors, respectively, because deviations of that size were expected.

Similarly, to allow for deviations of the observed detector efficiency (and thus asymmetries introduced in Section 6.1.2, see Eq. (5.2)), the model included an efficiency scaling factor for each detector. The prior distribution of this factor was modeled as a truncated Gaussian distribution centered at 1, with a standard deviation of 4 %

and bounds at 0.8 and 1.2. Figure 4.13 shows the fit results for the scaling factor for each run. When comparing the experimental results for fits with and without the scaling factor, it was found that the scaling factor caused larger uncertainties, but no significant deviation of the experimental results.

The fits were performed using Bayesian inference in combination with a Markov chain Monte Carlo (MCMC) method implemented in the PyMC [231–233] python package. A detailed introduction into the relevant concepts can be found, e.g., in Refs. [244, 265]. A Metropolis-Hastings algorithm [266, 267] was used, which approximates the posterior distribution by performing a random walk starting from some point in the parameter space. At each step in the Markov chain, a proposal for a jump (generated by a proposal function) to another sample point in the parameter space is made, which is accepted or rejected. The probability for acceptance/rejection depends on the ratio of the prior distribution and likelihood at both the original and the proposed point. The next sample in the Markov chain is either the accepted proposal or the same sample again (if the proposal was rejected). The process then repeats.

The efficiency of the Metropolis-Hastings algorithm depends on the choice of proposal function. A Hamiltonian Monte Carlo (HMC) algorithm [268] was used to generate proposals, which is motivated by Hamiltonian dynamics in physics and introduces a momentum vector to improve mixing and convergence, taking into account gradient information. An extension of this algorithm referred to as No U-Turn Sampler (NUTS) [269] was used. It adaptively sets the jump length to avoid U-turns in the random walk, resulting in low autocorrelation times (i.e., the correlation between subsequent draws in the Markov chain) and thus improved computational efficiency.

The samples from the Markov chain converge to the posterior distribution of the model. It is a robust method particularly suited for high-dimensional parameter spaces, which cannot be efficiently explored using typical optimization algorithms. Even complicated posterior distributions can be sampled reliably, allowing for a detailed analysis of uncertainties.

Figure 4.14 shows the resulting fit-based decomposition of the observed spectra of the two LaBr$_3$ detectors in the cross at $\vartheta = 90°$ for $E_{\text{beam}} = 5.1\,\text{MeV}$. The reconstruction of the incident spectra is in good agreement with the observation.

The decompositions of all spectra of all detectors for all photon beam energies are shown in the supplementary material [270]. At low excitation energies below 4 MeV, the fit was sometimes not able to correctly reproduce the incident spectrum, because
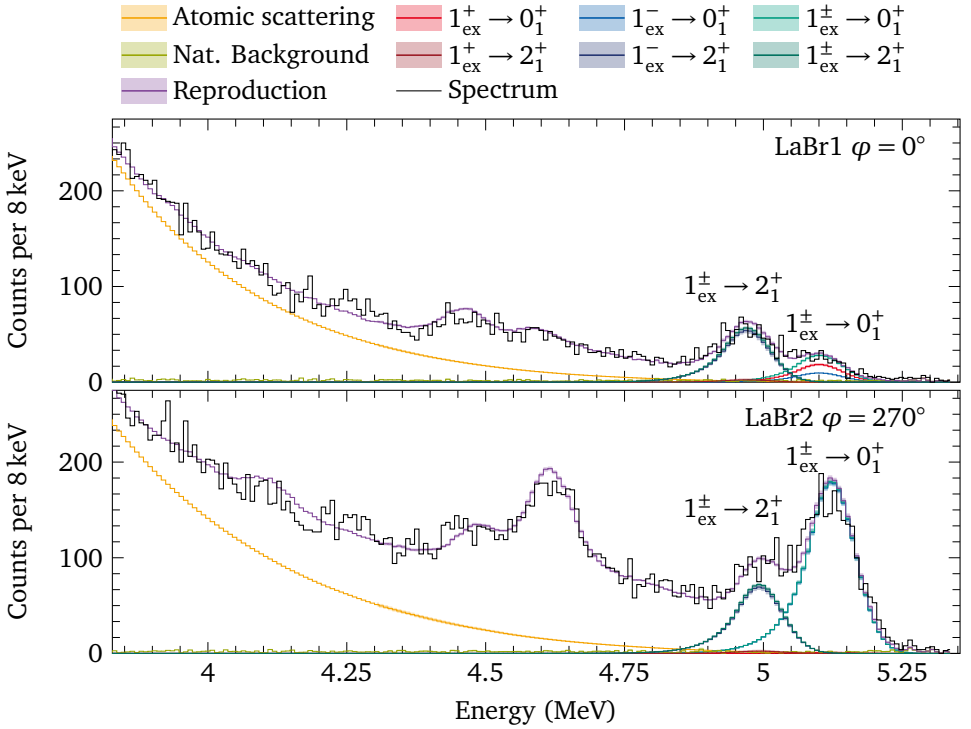
Figure 4.14.: LaBr$_3$ spectra and fits for average decays at $E_{\text{beam}} = 5.1\,\text{MeV}$. For an overview of all involved detectors (fitted simultaneously), see the supplementary material [270]. The reproduced spectrum is the sum of all individual contributions multiplied with the respective detector-response matrices.

the transition strength was not distributed evenly across the excited energy range. At $E_{\text{beam}} = 4.9\,\text{MeV}$ depicted in Fig. 4.15, the fit failed to separate $E1$ and $M1$ ground state transitions, which resulted in strong correlations between the two contributions. The reconstruction overestimated the total area of both contributions for LaBr1 at $\varphi = 0°$ and underestimated it for LaBr2 at $\varphi = 270°$. However, for the LaBr3 and LaBr4 at backward angles, the fit sufficiently reproduced the observed spectra, indicating that the sum of both contributions was still correctly determined. Thus, while $E1$
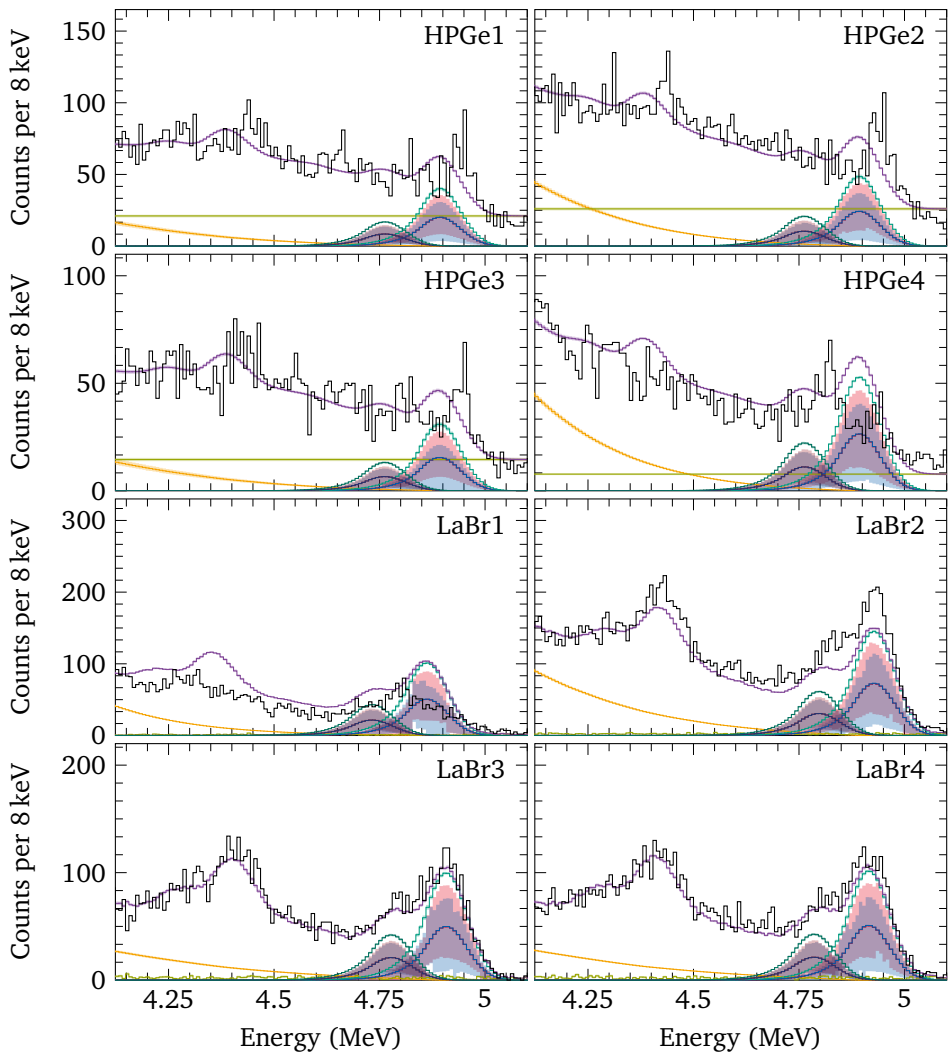
Figure 4.15.: LaBr$_3$ spectra and fits for average decays at $E_{\mathrm{beam}} = 4.9\,\mathrm{MeV}$. The fit fails to separate $E1$ and $M1$ contributions. The reproduced spectrum is the sum of all individual contributions multiplied with the respective detector-response matrices. For the legend, see Fig. 4.14.

and $M1$ contributions could not be sufficiently distinguished and have large relative uncertainties, their fit values were strongly correlated, and the relative uncertainty of their sum was comparable to the relative uncertainty for other photon beam energies. In an attempt to obtain better results, the fit for this photon beam energy was repeated with different start parameters, but always converged to the same result. In the HPGe spectra, it can be seen that the distribution of excited states is highly asymmetric in the excited energy range. Hence, because the assumptions of the fit were not fulfilled, the fit failed to reproduce the observed spectra.

4.2. ^{96}Mo experiment

The ^{96}Mo experiment was performed at HIγS. This work focuses on the analysis of the γγ coincidences required to extract the downward PSF.

4.2.1. Simulation of detection efficiency and angular correlations

Similarly to the ^{150}Nd experiment (refer to Section 4.1.1), GEANT4 simulations were performed to understand the interaction of the experimental setup with γ radiation for the ^{96}Mo experiment. For this purpose, the *nutr* code[3] [271] was used both to extrapolate detection efficiencies to high detection energies not accessible by calibration sources, and to obtain detector-response matrices.

For the ^{96}Mo experiment, the correction of the detector response for γγ-coincidence spectra was necessary. In principle, it is possible to directly simulate angular correlations involving the emission of several photons in an NRF cascade using the nutr code. However, for the creation of detector-response matrices for coincidence measurements, the simulated photons have to be detected by two detectors simultaneously. In comparison, for single measurements, only one detector has to detect the photon. Because of the limited absolute efficiency of approximately 0.1 % for the least-sensitive detector, the ratio of detected to simulated photons is approximately three order of magnitude smaller. Thus, the number of photons that have to be simulated to obtain the desired relative uncertainty of about 1 % is about 1000 times higher than for the

---

[3]*New utr*, a modernized reimplementation of the utr code.

[150]Nd experiment, for which only singles data were analyzed. Furthermore, separate detector-response matrices are required for each decay channel of [96]Mo that is being studied, i.e., each low-lying state that is gated in. Consequently, a different approach has to be adopted to better utilize available computing resources.

An optimized simulation algorithm was developed that can be used to resample GEANT4 simulations performed with an arbitrary angular distribution into any other angular distribution (one emitted photon) or correlation (several emitted photons). Only a single GEANT4 simulation has to be performed for this purpose, with enough photons detected in each detector to achieve the desired accuracy. For this GEANT4 simulation, in addition to the initial photon energy and the energy deposited into each detector crystal, the emission direction of the initial photon is recorded. The simulated angular distribution of the simulation does not matter as long as enough photons are emitted in the direction of each detector. An isotropic angular distribution is a sensible choice for the present experiment, which contains detectors in all directions except for extreme forward-scattering angles.

Instead of using GEANT4 to separately simulate the interaction of each sampled photon with the setup, the isotropic angular distribution simulation results are used instead. For each sample of the emission direction, the simulated GEANT4 event is selected that most closely matches the emission direction. Using a k-d tree [272] to partition and organize the GEANT4 simulation data, a simple search operation can be used that is several orders of magnitude faster than performing an actual physics simulation. It was estimated that the necessary computation time was reduced by a factor of almost 100 000 due to this algorithm.

Two versions of the optimized simulation algorithm were implemented in C++ and Python. The nanoflann library [273] implementation of the k-d tree algorithm was used in combination with the pynanoflann [274] Python bindings for the Python version. Additional optimizations in the Python implementation significantly reduced the number of necessary k-d tree searches by performing the creation of detector-response matrices for multiple γ energies at once, which allows reusing angular distribution samples and k-d tree searches. By selecting the n closest events during the k-d tree search instead of just selecting the best match ($n = 1$), the required computation time is further reduced by approximately $\sqrt{n}$. The statistical accuracy of the resulting detector response simulation for each detector converges to the accuracy of the underlying isotropic GEANT4 simulation, depending on the number of resampled events.

Similarly to the sampling of angular distributions directly in the GEANT4 simulation as described in Section 4.1.1, accept-reject sampling was used to sample the emission direction of photons according to arbitrary angular distributions or correlations (one or multiple emitted photons). The nutr code can make use of the alpaca code [275] to sample angular distributions based on the formalism by Biedenharn [276]. While alpaca can calculate both angular distributions and correlations, the sampling only works reliably for the first emitted photon. Therefore, a new sampling algorithm was created for this work that can be used to sample any arbitrary angular distribution or correlation correctly. This code, named AngularCorrelation.jl [277], is written in the high-performance language Julia [236] aimed at scientific computing, and is based in part on prior work for the angcorrwat code [245]. It follows the multipole mixing ratio convention by Krane, Steffen and Wheeler (KSW) [167]. For angular distributions, it was verified that the AngularCorrelation.jl code produces the same results as the angcorrwat code. For angular correlations of three photons (with the first photon performing the initial excitation), by marginalizing the two variables associated with the second photon, angular distributions were obtained, that could then be compared to the angcorrwat results. The central part of the angular distribution and correlation code is fully covered by unit tests.

4.2.2. Data unpacking

The mvme [203] DAQ software records data in the form of *mvlclst* files. It is a low-level file format that contains a list of various control sequences, the most important one being the readout of data from the VME modules. The mvme program supports the export of data as ROOT files [216, 217] in the form of TTrees, the standard file format used for event-based nuclear- and particle-physics data.

During the processing of the exported TTrees several issues were encountered, necessitating a more thorough analysis of the original mvlclst files to ensure that all data were exported properly. For this purpose, an unpacker was created from scratch for the mvlclst file format using the ucesb [215] unpacker framework. This unpacker framework is typically used for the creation of experiment-specific unpackers using the LMD file format produced by MBS-derived DAQ systems. A complete implementation of the mvlclst file format was necessary to parse the file contents.

During the development of the ucesb-based unpacker for the mvlclst file format, various issues in the stored files were encountered: Some events were only partially recorded, i.e., the beginning or end of the events were missing, such that only some detectors were read out. In some cases, longer blocks of data containing up to a few hundred contiguous events were missing from the mvlclst files, with the last and first events on either side of this data hole only partially recorded. From the structure of the file format, it was inferred that the missing data were lost because of intermittent network connectivity issues such as package loss. The mvlc controller was read out via Ethernet using a UDP-based transmission protocol. UDP [207] is stateless and, unlike the more complex TCP [278], makes no guarantee of packet delivery or ordering. For direct connections between two clients, such as it is the case for the DAQ used for the experiment, these limitations of UDP are usually not a problem, though.

Further issues were found in the data returned by some digitizer modules. Data are transmitted as a series of 32 bit words. Occasionally, bits at certain (but not all) positions in the data words were flipped, pointing at hardware defects in the used digitizers. The flipped bits result in some bins containing a much larger number of counts than their direct neighbors in the resulting energy histograms. In affected runs, at low energies, a comb-like structure was observed. Furthermore, during the initialization of the modules, sometimes, for certain registers of the digitizers used for the scintillators, the modules were not initialized correctly. In particular, the register for the energy threshold was not written correctly, such that data were recorded with the wrong threshold settings for some detectors. As a consequence, for affected runs, depending on the change in threshold, the trigger rate was either significantly larger than for the correct threshold settings, resulting in very high dead times, or important data were no longer recorded. Usually, this problem was immediately noticed by the responsible physicist on experimental shift, and fixed by reinitializing the DAQ and starting a new run. However, some runs had to be discarded because of this issue. In all instances, a sufficient number of runs with proper threshold settings was available for each photon beam energy, except for optional calibration measurements.

In addition to erroneous energy- and time signals, in some cases, the data format itself was corrupted because of the bit flips. For example, time signals were reported as energy signal or vice versa, or the number of reported events was inconsistent with the number of events actually present in the data. The unpacker relies on the integrity of data for unpacking and can not easily handle inconsistencies within the data stream. As soon as any errors in the structure of the processed file are being encountered, the

unpacker reports the error and is terminated. Typically, the proactive reporting of errors is desirable, because any issues with the setup of the DAQ system are noticed immediately and can be fixed during the experiment itself, proactively preventing any further loss of data. However, this approach results in problems if one wants to unpack corrupted data files.

Most of the described issues can be worked around, however, the wrongly reported event sizes caused issues with buffer sizes that could not be easily fixed. If this problem exists in the data, the ucesb-based unpacker cannot easily recover, discard the affected event, and proceed with the next valid event. In the end, it was decided to use the ROOT files exported by mvme for the further data analysis. However, the ucesb-based unpacker allowed for the examination of the extent of observed corruptions. It was found, that only a few runs were affected, most affected runs were calibration runs without any beam, and the number of corrupted or missing events was less than 1 %. Thus, using the information obtained from the ucesb-based unpacker, some problematic runs were excluded from the analysis, with only minor loss in data that did not impair the results of the analysis.

For each trigger, the mvme DAQ provides a single event, containing all hits for each signal that occurred within the configured time window before and after the trigger pulse. A duration of 3000 ps and 400 ps was chosen for the digitizers with HPGe and scintillator detectors, respectively, to account for the different rise times of the detector pulses. The scintillator detector signals are fast enough for multiple hits to occur within the time window of interest. The version 3.4.1 of the mvme software which was used to export ROOT files did not support the export of multiple hits per event. Using the ucesb-based unpacker, it was verified that less than 1 % of all events contained multiple hits (primarily the two LaBr$_3$ detectors at $\vartheta = 90°$ with the highest rates).

Each digitizer recorded an absolute timestamp for the time of the trigger signal for each event, synchronized using the built-in 16 MHz clock of the VME crate. It was found that the digitizers did not maintain a consistent timestamp synchronization. After some time had passed after the beginning of a run, events would no longer only contain data corresponding to the same trigger for all digitizers. This could have prevented the analysis of coincidences. Because absolute timestamps were available, it was possible to resort all the data, ensuring that all events only contained hits recorded for the same trigger signal. For unknown reasons, for a small (negligible) number of cases, subsequent events of the same module contained the same timestamp.
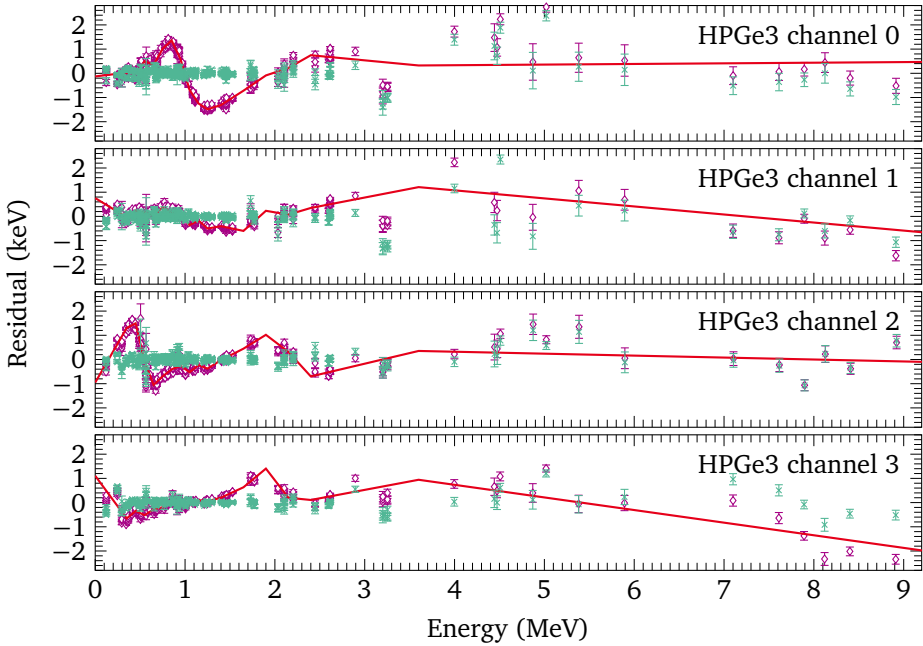
Figure 4.16.: Spline-based energy calibration residuals for clover detector HPGe3 at HIγS. A $k = 1$ spline (red) is used to model and correct for the non-linear residuals of a linear energy calibration (purple diamonds). The teal-colored crosses show the residuals after applying the correction.

4.2.3. Detector calibrations

Energy calibration

The same considerations as described in Section 4.1.2 apply for the ^{96}Mo experiment. Similarly, ^{22}Na, ^{56}Co, ^{60}Co, ^{137}Cs, ^{152}Eu, as well as an AmBe source were for calibration purposes. The LaBr$_3$ detectors were calibrated equivalently.

For the HPGe clover detectors used for the ^{96}Mo experiment, a more sophisticated energy calibration was required. An add-back procedure was performed, which

combined the energies recorded for the individual crystals (leaves) of the same clover detector. The add-back procedure assumes that the energy that is deposited into multiple crystals of the same clover detector at the same time corresponds to a single incoming photon, which deposits energy into multiple crystals because of scattering. By summing over the energies of all leaves of a clover detector, the original energy of the incoming photon is reconstructed. Illustratively, events that would otherwise be part of the SEP, DEP, or Compton continuum are *added back* to the FEP, resulting in an effective increase of FEP efficiency.

For clover detectors, even minuscule deviations in the energy calibration for the individual clover leaves result in a significant degradation of resolution. For events with multiplicities larger than one, the deviations get amplified with each additional non-zero clover leaf energy signal. This results in a degraded resolution for events with add-back-multiplicities larger than one. In most cases, a majority of a photon's energy is deposited into a single crystal. For example, following pair creation, one or two of the photons created by the subsequent annihilation of the formed positron could escape and be absorbed by one of the other crystals of the clover detector. If only one annihilation photon escapes into another crystal, the first crystal detects the energy of the incident photon minus 511 keV, and the second crystal detects the energy of the escaped 511 keV annihilation radiation. To lessen the loss of resolution during add-back of the (low-energy) signals from the other clover leaves, a good energy calibration at low energies is required. Furthermore, for the analysis of coincidences, a high energy resolution at low energies allows for well-defined energy gates on low-lying states with a larger peak-to-background ratio.

After applying a linear energy calibration to the individual clover-detector leaves, a non-linear jitter of approximately ± 2 keV around the calibrated energy is found that cannot be accounted for with a polynomial energy calibration. This jitter is modeled using a univariate linear ($k = 1$) spline. The positions of the 18 spline knots are chosen to account for the density of available energy calibration points in each energy range. The energy calibration is corrected with the resulting spline, effectively being equivalent to a piecewise linear energy calibration. Figure 4.16 depicts the spline, and the residuals of the energy calibration before and after correcting for the non-linear jitter. The correction significantly reduces the size of the residuals and improves the energy resolution substantially, especially at low energies.

Because of crosstalk between the individual clover-leaf channels somewhere during signal processing, peak positions were shifted towards higher energies for events with
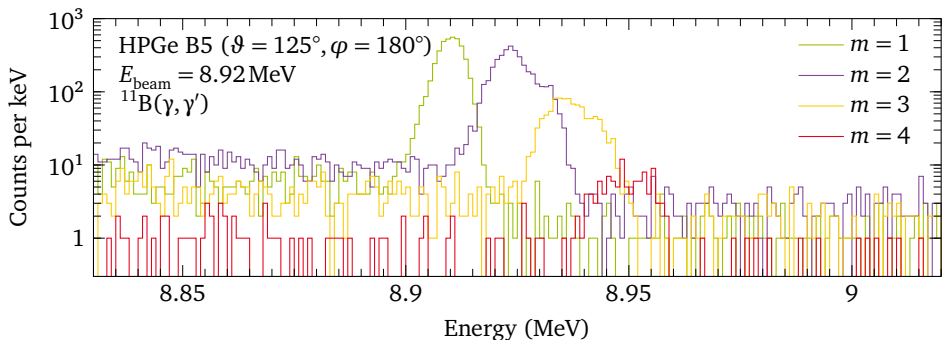
Figure 4.17.: Multiplicity-dependent shift of the detected energy for the add-back signal of the HPGe clover detector B5 before the multiplicity-shift correction was applied. The $3/2^- \rightarrow 5/2^- \rightarrow 3/2^-$ transition at 8920 keV for a ^{11}B calibration run is shown. For higher multiplicities m, the peak energy is shifted to higher values, and the peak width increases.

add-back multiplicity larger than one (see Fig. 4.17). The magnitude of this effect was proportional to the energy and resulted in energy shifts of up to 10 keV for multiplicity $m = 2$, depending on the detector. For the energy shift, no rate dependency was observed. The magnitude of the effect was calibrated using high-energy transitions during an ^{11}B target run and were corrected for.

Finally, low-energy events just above 0 keV, occurring in coincidence with events from other leaves of the same clover detector, also contributed significantly to the degradation of the energy resolution. In the digitizers, low-energy thresholds for the energy signals of the clover leaves were set at 80 keV to 90 keV, depending on the detector and clover leaf. The threshold was determined by the internal TFA of the ADCs and is thus not a hard cutoff but spans over several keV. To filter out any low-energy noise, a hard cutoff at 100 keV was applied during the analysis before correcting for add-back.
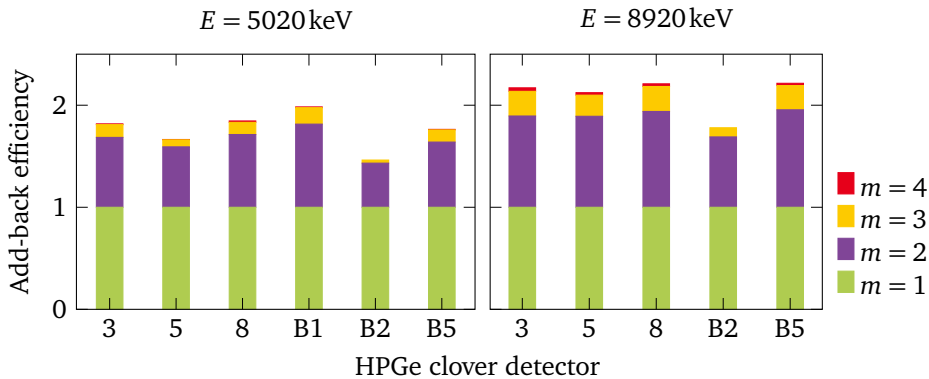
Figure 4.18.: Add-back efficiency of the clover detectors, decomposed into the contributions of different multiplicities m, i.e., the number of clover crystals that simultaneously triggered. The efficiencies are normalized to the sum of the efficiencies of the individual crystals, which corresponds to events with add-back multiplicity $m = 1$.

Efficiency calibration

The efficiency calibration of the LaBr$_3$ detectors and the coaxial HPGe detector was equivalent to Section 4.1.2 and will not be discussed any further. For the efficiency calibration of the clover detectors, the add-back-corrected spectra were used. The add-back procedure creates a virtual detector of the combined size of all four crystals. An identical procedure was applied to the GEANT4 simulation, such that it can be used for extrapolation purposes. In analogy to the experimental data, a low-energy cutoff at 100 keV was applied to the efficiency simulation, ensuring consistency between simulation and experiment.

The internal preamplifier of detector B1 was saturated starting at an energy of around 7.2 MeV to 7.5 MeV (depending on the clover leaf). At higher energies, the correspondence between the pulse height of the detector pulse and the energy deposited in the crystal was lost, and no useful spectral information was obtained.

As an additional quantity, the efficiency of the add-back procedure was determined. The add-back efficiency corresponds to the ratio of peak volumes in the add-back-corrected spectrum to the FEP volumes in the sum spectrum of all four individual clover

leaves without any add-back procedure applied. It quantifies the relative increase in efficiency due to the add-back procedure.

In Fig. 4.18, the add-back efficiency is shown for all clover detectors for two ^{11}B transitions at energies of 5020 keV and 8920 keV. The efficiency gain is broken down into the multiplicities of the observed events. Only including events with multiplicity $m = 1$ is equivalent to taking the sum spectrum of all clover leaves (assuming low count rates, i.e., only a single photon is detected per event). The add-back efficiency is normalized to the sum-spectrum efficiency such that it quantifies the additional gain in efficiency due to the add-back procedure. The average add-back efficiency of all clover detectors was 176 % at 5020 keV and 210 % at 8920 keV. The average contribution of events with a multiplicity of $m = 2$ was 65 percentage points and 87 percentage points for the respective energies. For higher energies, a larger number of events with multiplicities of $m = 3$ or $m = 4$ were observed.

Time-gates for background suppression

Additional conditions were imposed to filter out undesirable events. Events originating from background radiation rather than reactions induced by the photon beam within the target were filtered out for the scintillator detectors. The LaBr$_3$ energy spectra contained significant contributions from natural background radiation at γ-ray energies of about 1.5 MeV to 2.5 MeV. The increased background radiation occurred because of the so-called self-contamination of the LaBr$_3$ detectors, which originates from α decays of ^{211}Bi, ^{215}Po, ^{219}Rn, ^{223}Ra, and ^{227}Th that are part of the actinium decay chain. The contaminations were present because of the chemical similarity between Lanthanum and Actinium, which complicates the production of crystals with a high degree of (chemical) purity.

The pulsed time structure of the HIγS photon beam, in combination with the high time resolution of scintillator detectors, enabled the suppression of off-beam events originating solely from background radiation. As a time reference, the RF signal of HIγS was connected to one of the trigger inputs of the digitizer with the scintillator detector signals. The RF frequency was 2.79 MHz = 358.4 ns^{-1}, but the electron storage ring contained two equally spaced electron bunches, such that the photon beam was pulsed with a frequency of 5.58 MHz = 179.2 ns^{-1}. Sometimes, the digitizer did not pick up an individual RF pulse, such that the time of the next pulse was stored
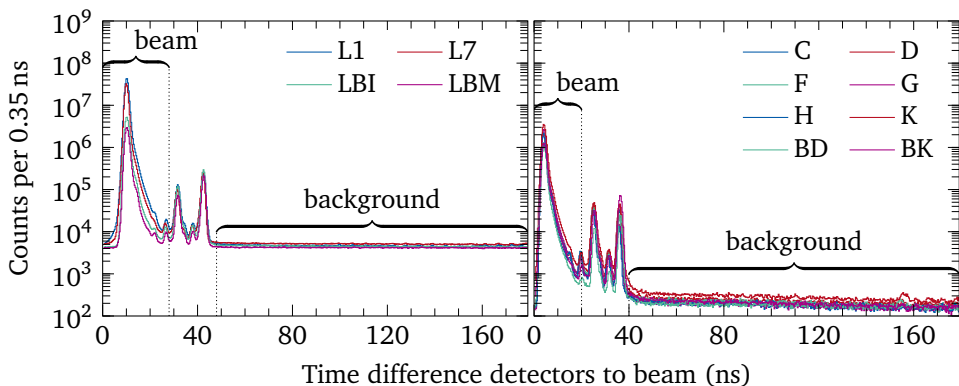
Figure 4.19.: Time-difference spectra between detector pulse and beam for $E_{beam} = 7$ MeV. Left and right panel show $LaBr_3$ and $CeBr_3$ detectors, respectively. The braces indicate time gates for beam- and background-correlated events. The different curves show the signals for the different detectors (see legend). The $CeBr_3$ spectra contain fewer counts than the $LaBr_3$ spectra, because of the smaller physical size and thus reduced absolute efficiency of the detectors. In addition, the $LaBr_3$ detectors observe more background radiation because of their intrinsic radioactivity.

instead. Because all beam pulses are equally spaced in time, a (floating point) modulo operation for a period of 179.2 ns was applied to the time difference between detector signal and RF pulse, resulting in values between 0 ns to 179.2 ns. An additional time offset was applied to each detector individually, to shift the beam-correlated peak to the same time.

The results can be seen in Fig. 4.19 for both $LaBr_3$ and $CeBr_3$ detectors. A large peak sits on top of a constant background, which corresponds to events generated by the photon beam hitting the target. Following the main beam pulse, several smaller pulses can be seen with a delay of around 20 ns to 30 ns. The smaller pulses correspond to photons scattered back from various objects traversed by the photon beam downstream of the target position, such as the exit window of the beam pipe, or the beam dump. The inclusion of those events results in undesirable low-energy artifacts in the energy spectra, hence, the time gate was chosen to exclude these events.
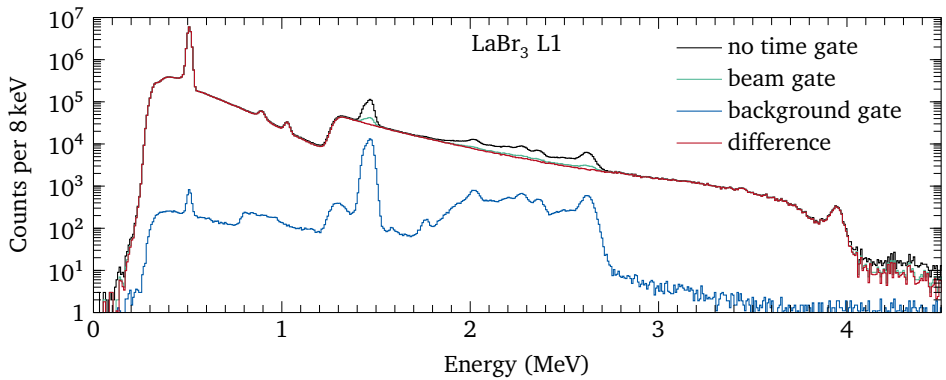
Figure 4.20.: Energy spectrum of LaBr$_3$ detector L1 with different time gates for $E_{\text{beam}} = 3.9\,\text{MeV}$. Beam and background correspond to the time gates depicted in the left panel of Fig. 4.19. The background-gated spectrum was scaled to match the live time of the beam-gated spectrum. For the difference spectrum, the background-gated spectrum (with live-time correction) was subtracted from the beam-gated spectrum to create a spectrum that only shows beam-correlated events. The energy threshold of the ADC for single events is visible at around 1300 keV. The energy threshold for coincidences is located at around 300 keV.

The resulting spectra can be seen for the case of LaBr$_3$ detector L1 in Fig. 4.20. By applying the beam-correlated time gate, a significant background reduction was possible. The non-beam-correlated background contributions can be eliminated completely by subtracting the background-gated spectrum from the beam-gated spectrum. Before subtraction, the background-gated spectrum has to be scaled by the ratio of the widths of the time gates. Above 2.6 MeV, natural background contributed only very little and thus, the background subtraction is primarily useful to reduce the background at lower energies.

For the HPGe detectors at $\vartheta = 90°$, the RF signal cable was disconnected for photon beam energies up to including 6.5 MeV. The time resolution of HPGe detectors is significantly lower than for scintillator detectors. While some correlation between the HPGe trigger time and RF signal was found, the overall benefit of time gates is small, also considering the lower natural background for HPGe detectors. To keep the analysis consistent for all runs, no time gates were applied.

4.2.4. Generation of γγ-coincidence matrices and energy-gated spectra

The determination of downward PSFs required the quantification of the strength of primary decays into low-lying 2^+ states in γγ coincidences. For the analysis of γγ coincidences, γγ-coincidence matrices were created for all possible pairs of detectors, with the two dimensions of such a 2-dimensional matrix corresponding to the energies observed by the two detectors. If both detectors of such a matrix registered hits in short succession, a count was added to the corresponding bin of the matrix. The mvme DAQ already created events that contained hits from all detectors that registered a signal within a configured time window. During the experiment preparation, a suitable time window was configured to include all *true* coincidences while avoiding excessive dead time. Here, true coincidences refer to events occurring within the same beam pulse, in contrast to those occurring between successive beam pulses.

A further analysis of the time difference spectra between two detectors, comparable to the one described in Section 4.2.3, can be used to suppress random coincidences by gating on the corresponding peak in the time-difference spectrum. In addition, the contributions from random coincidences originating from multiple beam-induced reactions occurring for the same beam pulse can be examined by gating on the following beam pulse in the time-difference spectrum. However, these contributions were orders of magnitude smaller than the true coincidences. Hence, to achieve the level of background-suppression required for the present experiment, only the beam-correlated time gate described in Section 4.2.3 was applied. In combination with the strong suppression of random coincidences because of the coincidence criterion itself, a sufficient reduction of background radiation was achieved.

Next, an energy range was selected for one of the two detectors also referred to as *energy gate* or *energy cut*, cropping the matrix to the extent of the selected energy range. Afterwards, a projection onto the other dimension was performed to obtain the energy spectrum of all events of the other detector that occurred in coincidence with events within the selected energy range of the first detector.

As a first step of the further analysis, to assess which low-lying states were populated by direct decays, an energy region at high energies corresponding to primary decays of excited states was selected. The restriction to high-energy primary decays was used simply to reduce the background at low energies, resulting in an increased sensitivity
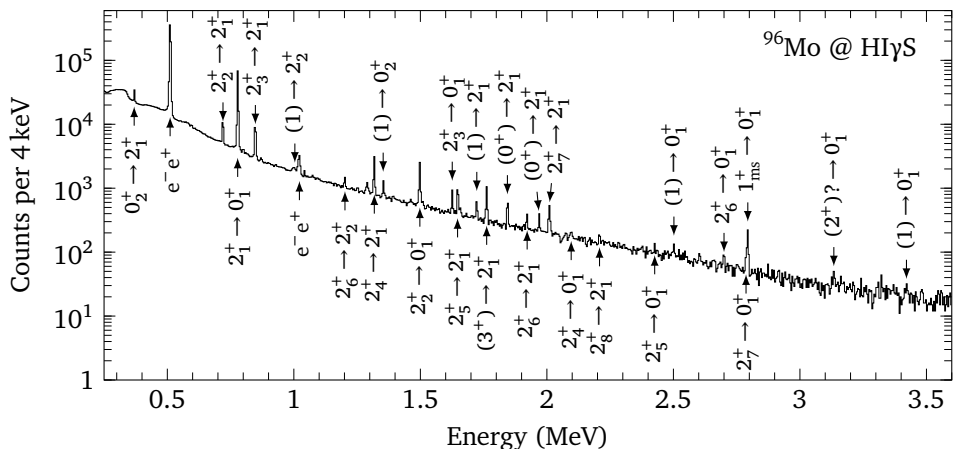
Figure 4.21.: Decays of low-lying states in γγ coincidences for ^{96}Mo. A sum spectrum for all HPGe detectors is shown, gating on the energy range 3.0 MeV to 0.5 MeV below the beam energy for all HPGe and LaBr$_3$ detectors. The depicted sum spectrum contains data from five measurements with photon beam energies ranging from 8 MeV to 9 MeV to maximize the statistics.

to low-lying transitions. An energy gate ranging from 3.0 MeV to 0.5 MeV below the beam energy was selected, applied to all HPGe and LaBr$_3$ detectors. The resulting γγ-coincidence spectrum for all HPGe detectors, depicted in Fig. 4.21, shows the sum spectrum of five measurements with photon beam energies spanning from 8 MeV to 9 MeV to maximize statistics. Numerous decays of low-lying states are visible, including decays of the eight lowest-lying 2^+ states, and decays of several 0^+, 1, and 3^+ states. A level scheme with low-lying states of ^{96}Mo that depicts the transitions observed in coincidence with primary decays is shown in Fig. 4.22.

Based on the results of the initial assessment of low-lying transitions observed in coincidences, a more thorough investigation of coincidences was performed, examining each decay of a low-lying state separately. Thus, it was possible to specifically choose a high-energy gate that only included the energy range for which the SEP and FEP of primary decays into the specific low-lying state were expected. The more restrictive energy-gate resulted in a significant reduction of background radiation
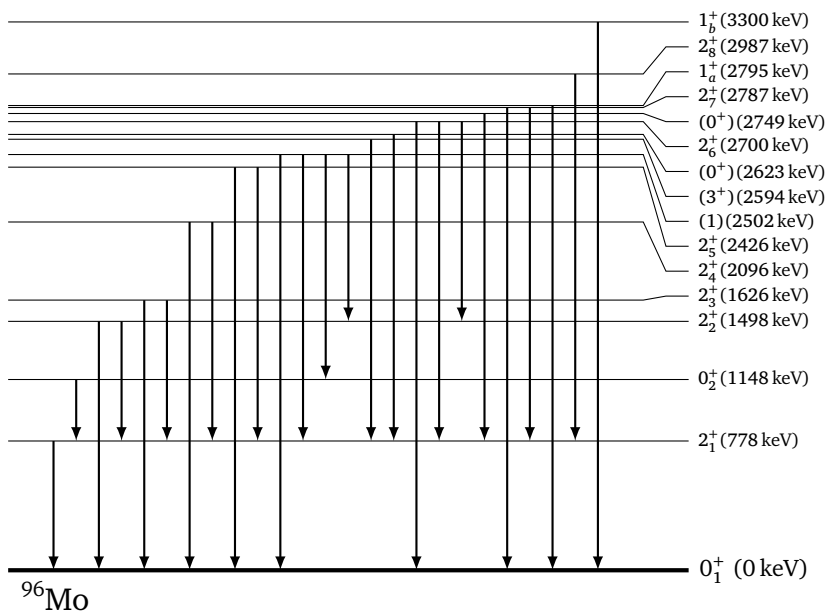
Figure 4.22.: Low-lying level scheme of ^{96}Mo with the most important transitions observed in coincidence with primary decays, i.e., direct decays from states excited by the photon beam.

around the low-energy transition. As the next step, an energy gate was selected around this low-energy transition, to systematically study the primary decays into the corresponding low-lying state. For the LaBr$_3$ detectors, the energy-gate was shifted in comparison to the nominal peak position, accounting for non-linearities of the detector not accounted for by the polynomial energy calibration. In addition, two (and in some cases, three) background gates on either side of the transition were selected to account for background radiation in the high-energy spectrum. The background gates were selected to be as close as possible to the low-lying transition without overlapping with other decays. To prevent gating on Compton-scattered radiation associated with the low-lying transition itself, a more narrow energy range was selected for the background gate on the low-energy side of the transition.

There were several overlapping low-lying transitions because of the large number of lines and the limited resolution of the detectors, especially the LaBr$_3$ detectors. The 2_3^+ state at 1626 keV is located adjacent to the 4_1^+ state at 1628 keV, which could not be resolved by either the HPGe or the LaBr$_3$ detectors. It can be populated by $0^+ \to 2^+ \to 4^+$ cascades in two successive $E2$ transitions. The ground-state decays of the 2_7^+ state at 2787 keV and a 1_{ms}^+ state [279] at 2794 keV could be barely separated in the HPGe detectors. For the LaBr$_3$ detectors, multiple other decays were overlapping as well. For example, the ground-state transition of the 2_1^+ state at 778 keV is right next to the $2_3^+ \to 2_1^+$ transition at 848 keV. However, because the 2_3^+ state is at 1626 keV, the primary decays of the two low-lying transitions are separated by 848 keV, such that it was possible to resolve both bumps individually. The SEPs and DEPs of primary decays to the 2_1^+ state overlapped with the FEPs of primary decays to the 2_3^+ state, though. Thus, the partial overlap of the transitions could still cause problems when performing a deconvolution of the corresponding primary spectra. The $2_5^+ \to 2_1^+$ transition at 1648 keV is close to the ground-state decay of the 2_3^+ state at 1626 keV, which could not be resolved for the LaBr$_3$ detectors. Again, there is an energy difference between the two corresponding primary decays. The 2_7^+ state at 2787 keV is very close to a (0^+) state at 2749 keV. The energy difference of only 38 keV could be resolved for the HPGe detectors, however, for the LaBr$_3$ detectors, the decays of the low-lying state overlap and primary decays were also expected for the same energy. (e.g., see Fig. 1.521 in the ^{96}Mo supplementary material of this work [280]). Thus, a systematic increase of the corresponding branching ratios is expected. The large density of (strong) transitions also complicates the gating on transition-free regions to create suitable background gates. By considering the spectra of the HPGe detectors, which have a higher energy resolution and improved peak-to-background ratio, transition-free energy regions in the LaBr$_3$ spectra were identified. In several cases, it was difficult to find suitable transition-free energy regions.

4.2.5. Detector-response correction and integration

For each low-lying transition and detector pair, two γγ-coincidence spectra were generated in the previous subsection, Section 4.2.4: one peak-gated spectrum gating on the low-lying transition, and another background-gated spectrum gating on the transition-free regions next to the peak (see Figs. 4.23 to 4.25). It was taken into account that the energy gate of the background-gated spectrum had a different width.

Depending on the number of detectors that allowed for a clean energy gate, $\gamma\gamma$-coincidence spectra were available for up to $11 \times 10 = 110$ detector pairs (4 LaBr$_3$ detectors + 7 HPGe detectors). The CeBr$_3$ detectors did not provide sufficient statistics and were excluded from the analysis.

For each photon beam energy and low-lying state of interest, the intensity of the corresponding decay branch had to be determined, i.e., quantity

$$r_{j,k} := s_j \sigma_{j,k} \tag{4.6}$$

in Eq. (2.22), by integrating over the corresponding primary-transition bump. Similar to the method described in Section 4.1.5, a global fit was performed, taking into account the spectra from all detector pairs simultaneously. This fit extracted $r_{j,\pi,k,y}$, distinguishing between the parity quantum number π of excited states and resolving individual energy bins y. Three different approaches can be taken:

The radiation emitted by the decay of 1^+ or 1^- states has a distinct angular correlation (refer to Section 2.2), depending on the parity quantum number of excited states. By fitting the spectrum of each detector pair at the same time (first model), the fraction of excited states with either parity quantum number can be determined. The fitting procedure minimizes the difference between the observed and reproduced spectrum. Alternatively, the data from all detectors can be combined into a single sum spectrum (second model). The latter approach benefits from a huge reduction in computational effort as the number of output parameters of the fit that are optimized simultaneously is reduced by a factor of 110 (see above). Likewise, the relative uncertainty of the number of counts of each energy bin in the sum spectrum is reduced by a factor of more than 10. As a result, the numerical stability of the fit procedure is greatly improved. The improved numerical stability is accompanied by a loss of sensitivity on the parity quantum number of the excited states. In turn, the number of fit input parameters is reduced by a factor of two, as contributions from strength corresponding to the decay of 1^+ and 1^- states can no longer be treated separately. Assumptions must be made about the ratio of contributions from 1^+ and 1^- states. A third model, which combines both approaches, is discussed in the outlook (Section 7.1).

First model: Separate *E*1 and *M*1 strength

Analogous to Eq. (2.9), the first model, which considered each detector individually, is defined as follows:

$$A_{j,k,l,\text{det-pair},x} = \sum_{\pi \in \{-1,+1\}} \frac{\Gamma_{k \to l}}{\Gamma_k} \varepsilon_{\text{det-pair},x,y}^{0^+ \to 1^\pi \to J_k \to J_l} r_{j,k,\pi,y} + u_{j,k,l,\text{det-pair}} A_{j,k,l,\text{det-pair},x}^{\text{bg}}. \quad (4.7)$$

Here, $A_{j,k,l,\text{det-pair},x}$ represents the number of counts in a detector pair identified by index "det-pair" in energy bin x of the $\gamma\gamma$-coincidence spectrum generated by gating on the low-lying transition $J_k \to J_l$ for beam-energy E_j. The detector response for detector pair "det-pair" is denoted by the symbol $\varepsilon_{\text{det-pair},x,y}^{0^+ \to 1^\pi \to J_k \to J_l}$, with the energy bin y of the incident spectrum. The number of counts per energy x of the corresponding background-gated spectrum is represented by $A_{k,l,\text{det-pair}x}^{\text{bg}}$, with an additional factor $u_{j,k,l,\text{det-pair}}$ to account for the different widths of the energy gates.

The model contains two input quantities, with their estimators denoted as $\hat{r}_{j,\pi,k,y}$ and $\hat{A}_{j,k,l,\text{det-pair},x}^{\text{bg}}$ to distinguish them from the measured values. Both quantities are known to be positive, and thus, their prior distribution in this Bayesian approach are modeled as (improper) non-negative uniform distributions over the interval $[0,\infty)$. Alternative choices of prior distributions, such as an exponential distribution were also explored, and yielded consistent results (within model uncertainties). The two measurands are the number of counts of the energy- and background-gated spectra $A_{j,k,l,\text{det-pair},x}$ and $A_{j,k,l,\text{det-pair},x}^{\text{bg}}$, respectively.

The fit has a high dimensionality: There are 110 detector pairs, two parities of excited states, and (for the chosen binning) 72 energy bins, covering an energy range of up to 4 MeV to 5 MeV. Up to three decay branches $k \to l$ of low-lying states are gated on and fitted simultaneously (with the same k, but different l). In this example with three observed decay branches for a state k, the detector response tensor $\varepsilon_{\text{det-pair},x,y}^{0^+ \to 1^\pi \to J_k \to J_l}$ has a total size of $110 \times 3 \times 2 \times 72 \times 72 = 3\,421\,440$, and, analogously, the two estimators $\hat{r}_{j,\pi,k,y}$ and $\hat{A}_{j,k,l,\text{det-pair},x}^{\text{bg}}$ have a size of 432 and 23 760, respectively. Monte-Carlo samples for their posterior distributions are obtained using an MCMC algorithm (see also Section 4.1.5).

Second model: Only *E*1 strength

The second model used to fit the coincidence spectra does not distinguish between different parity quantum numbers π, summing over the spectra of all detectors, i.e.,

$$A_{j,k,l,x} := \sum_{\text{det-pair}} A_{j,k,l,\text{det-pair},x}, \qquad A_{j,k,l,x}^{\text{bg}} := \sum_{\text{det-pair}} u_{j,k,l,\text{det-pair}} A_{j,k,l,\text{det-pair},x}^{\text{bg}}. \qquad (4.8)$$

Any information about angular distributions is discarded, greatly simplifying Eq. (4.7):

$$A_{j,k,l,x} = \frac{\Gamma_{k \to l}}{\Gamma_k} \varepsilon_{x,y}^{0^+ \to 1 \to J_k \to J_l} r_{j,k,y} + A_{j,k,l,x}^{\text{bg}}. \qquad (4.9)$$

The size of the two estimators $\hat{r}_{j,k,y}$ and $\hat{A}_{j,k,l,x}^{\text{bg}}$ for three low-energy gates is reduced to 216, each, and the detector response tensor $\varepsilon_{x,y}^{0^+ \to 1 \to J_k \to J_l}$ has a size of $15\,552$. Especially the size of $\hat{A}_{j,k,l,x}^{\text{bg}}$ is significantly reduced. Prior distributions equivalent those used for the first model are chosen.

Fit results and spectra

To obtain $r_{j,k,\pi}$ from $r_{j,k,\pi,y}$, summing over the energy range of the photon beam for index y is necessary. Because of the non-negative priors, the number of counts in each bin y for $r_{j,k,\pi}$ tend to favor larger values. Bins of the incident spectrum with a low number of counts (located far from the centroid of the spectral distribution of the photon beam), or with a large relative uncertainty (because of low statistics) cannot fluctuate to negative values. When the prior distribution is applied during an intermediate analysis step, this bias towards non-negative values can accumulate, leading to systematically overestimated values. Therefore, in Bayesian analysis, the prior distribution should only be applied in the last step of the analysis, i.e., after summing over the energy range of the photon beam. Thus, the total number of counts in the primary bump is restricted to positive values, but individual bin values can be negative. To accommodate this restriction, an unbounded uniform distribution is selected as a prior for the fit, which does not prevent negative numbers of counts in intermediate steps of the analysis.

Two issues were observed for the first model: The use of an informative prior that prevents negative number of counts resulted in bin values that are systematically too large compared to the observed experimental spectra for certain decay branches and photon beam energies. This deviation becomes apparent when comparing the reproduction of the sum spectrum for all detectors with the experimental data (see the ^{96}Mo supplementary material to this thesis found in Ref. [280], e.g., Fig. 1.508). The resulting FEP bump for 1^- states $r_{j,-1,k}$ is significantly larger than the same bump in the experimental spectrum. The visualization in Figs. 4.23 to 4.25 depicts the sum over all detectors, but the actual fit is applied to the spectra of the individual detectors. In the individual coincidence spectra, the number of counts per energy bin is extremely low, typically only around one count per bin for most detector pairs. Consequently, while the fit successfully reproduces the spectra of the individual detector pairs within their uncertainties, it also introduces a slight bias for higher count numbers because of the non-negative prior distribution. This bias accumulates and becomes apparent in the sum spectrum for all detector pairs. Hence, the resulting prior distribution for $r_{j,\pi,k}$ is suitable for a qualitative assessment of the ratio of 1^- and 1^+ states that contribute to the observed strength, but it does not allow for a quantitative analysis.

The bias towards higher count numbers does not arise when using a noninformative prior, which does not constrain the number of counts to non-negative numbers. However, with the additional freedom that the noninformative prior enables, the fitting algorithm fails to adequately reproduce the spectra for individual detector pairs. This instability of the model is attributed to the high number of parameters in the model. Several attempts were made to address the poorly converged fit result: Multiple other prior distributions were tested, such as a uniform prior that restricts the estimator to values larger than some number smaller than zero, or a Laplace distribution for regularization purposes. Other combinations of hyperparameters of the MCMC algorithm, such as increasing the target acceptance for improved numerical stability, were also explored. Attempts were made to initialize the noninformative-prior fit with the results of the informative-prior fit. However, none of these attempts resulted in a significantly improved convergence. The fit results for both 1^+ and 1^- states showed fluctuations around zero, with a large variance that increased towards lower energies, and no discernibile beam-related bump was observed.

Still, a qualitative assessment of the ratio of $M1$ to $E1$ transition strength is possible using the results of the informative-prior fit. The Figs. 4.23 to 4.25 depict the fits for the primary decays to three low-lying states. In each figure, the middle panel
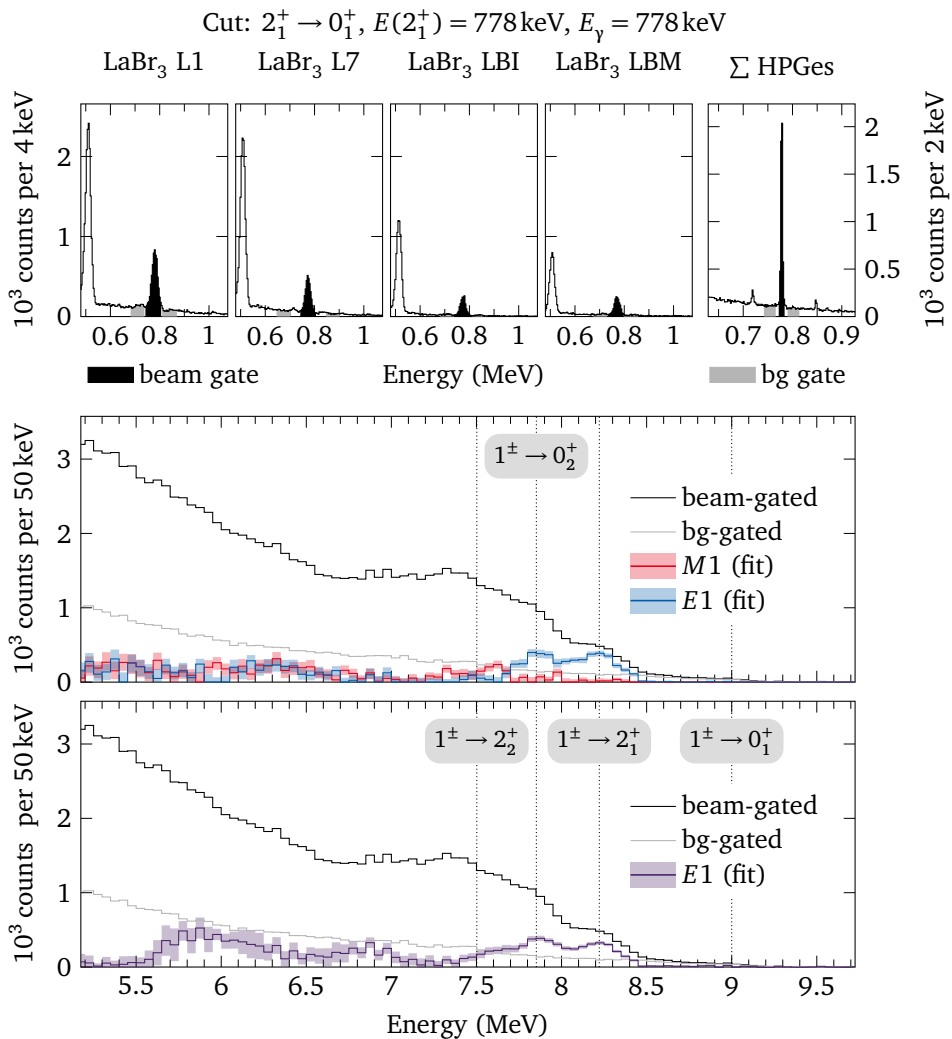
Figure 4.23.: Fit using both methods (see Section 4.2.5) to extract primary decays to the 2_1^+ state for $E_{\text{beam}} = 9\,\text{MeV}$. Top row: Beam (black) and background (gray) gates on low-lying transitions. Bottom two panels: Beam- (black) and background-gated (gray) spectra. Middle panel: Simultaneous fit of $E1$ (blue) and $M1$ (red) contributions. Bottom panel: Fit assuming pure $E1$ radiation (purple). Dotted lines with labels indicate energies of primary transitions.
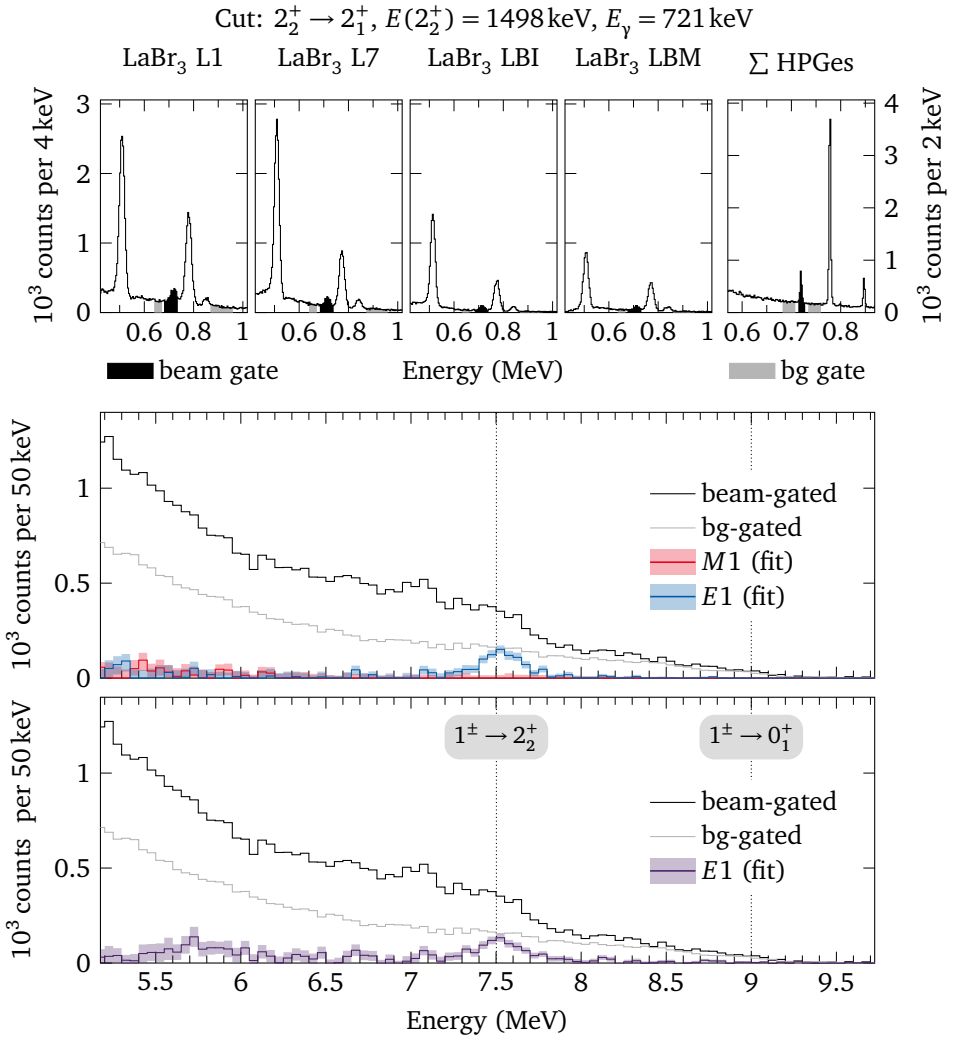
Figure 4.24.: Fit using both methods (see Section 4.2.5) to extract primary decays to the 2_2^+ state gating on $2_2^+ \to 2_1^+$ for $E_{\text{beam}} = 9\,\text{MeV}$. Top row: Beam (black) and background (gray) gates on low-lying transitions. Bottom two panels: Beam- (black) and background-gated (gray) spectra. Middle panel: Simultaneous fit of $E1$ (blue) and $M1$ (red) contributions. Bottom panel: Fit assuming pure $E1$ radiation (purple). Dotted lines with labels indicate energies of primary transitions.
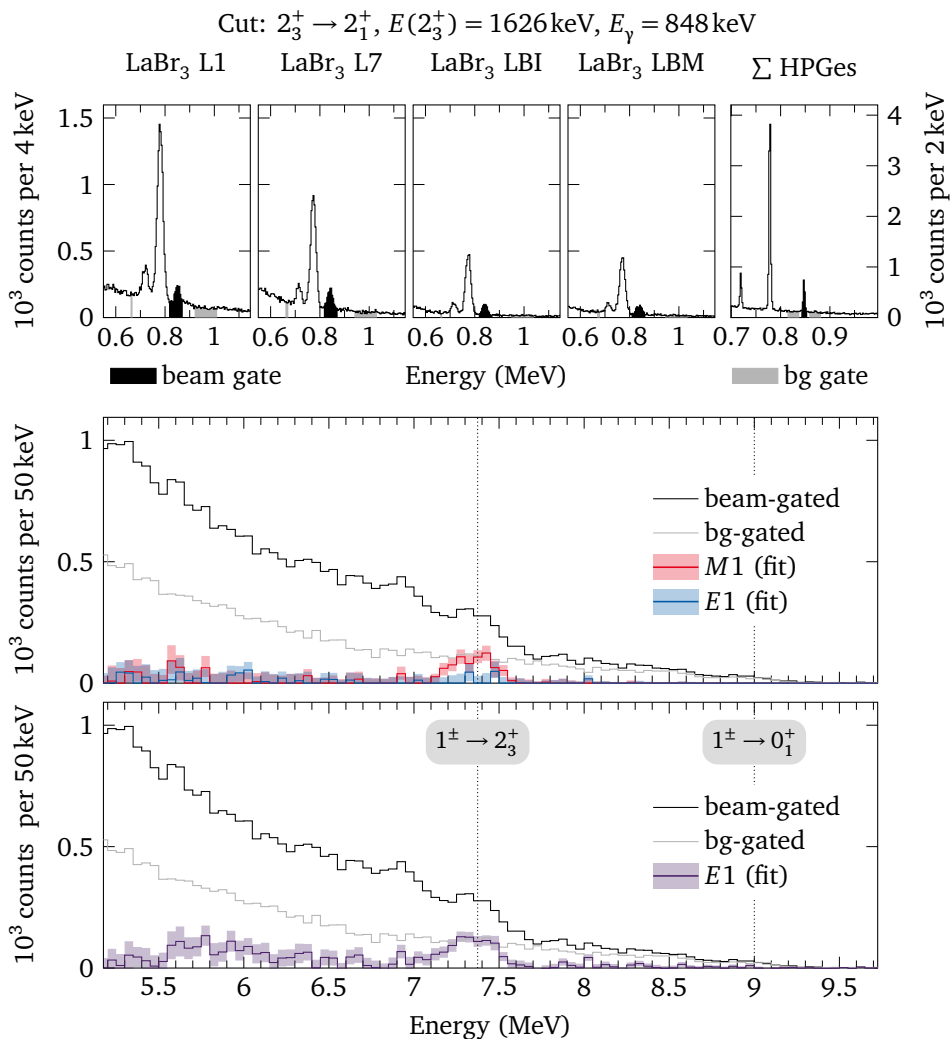
Figure 4.25.: Fit using both methods (see Section 4.2.5) to extract primary decays to the 2_3^+ state gating on $2_3^+ \rightarrow 2_1^+$ for $E_{\text{beam}} = 9\,\text{MeV}$. Top panels: Beam (black) and background (gray) gates on low-lying transitions. Bottom two panels: Beam- (black) and background-gated (gray) spectra. Middle panel: Simultaneous fit of $E1$ (blue) and $M1$ (red) contributions. Bottom panel: Fit assuming pure $E1$ radiation (purple). Dotted lines with labels indicate energies of primary transitions.

shows the informative fit distinguishing $E1$ and $M1$ radiation, while the bottom panel shows the noninformative fit, assuming pure $E1$ radiation. In Fig. 4.23, for the decay $1^{\pm} \rightarrow 2_1^+$ at $E_{\text{beam}} = 9\,\text{MeV}$, it is evident that $E1$ radiation strongly dominates the distribution, while contributions from $M1$ radiation are consistent with zero within their uncertainties. The same conclusion applies to primary decays to the 2_2^+ and 2_4^+ state. However, the results indicate a significant presence of $M1$ radiation for decays to the 2_3^+ state (see Fig. 4.25). This contribution of $M1$ radiation contrasts with all other primary transitions to 2_1^+ states and direct ground-state decays, which are strongly dominated by $E1$ transitions. The dominance $E1$ radiation for all other observed primary decays suggests that 1^+ states contribute little to the observed transition strength. The $2_3^+ \rightarrow 2_1^+$ transition at $E_\gamma = 848\,\text{keV}$ is the only low-energy transition of the 2_3^+ state that is being gated on, and it is located right next to the $4_1^+ \rightarrow 2_1^+$ transition $E_\gamma = 850\,\text{keV}$. In addition, the $2_3^+ \rightarrow 2_1^+$ transition has a comparatively large $M1/E2$ multipole mixing ratio of $\delta = -1.05^{+0.09}_{-0.10}$ [281], which could not be considered by the used method (See Section 7.1 for a discussion of alternative methods). Both effects could result in an incorrect assignment of radiation character for the primary transition. For decays to higher-lying 2^+ states, the statistics are not sufficient for a conclusive distinction of $E1$ and $M1$ strength. It can be concluded that $E1$ strength is strongly dominating for the studied energy range. Thus, for the second method, it was assumed that $E1$ strength contributes to the PSF exclusively.

Because of the funnel-like nature of the 2_1^+ state (refer to Section 2.3.1), the γγ-coincidence spectrum when gating on the decay of this state not only contains primary decays into the 2_1^+ state. Primary decays into every other low-lying state that depopulates via the 2_1^+ state can also be identified. Decaying via the 2_1^+ state is the most probable decay path for the majority of low-lying 2^+ states. The 0_2^+ state can only decay via the 2_1^+ state, such that $100\,\%$ of the strength that decays via the 0_2^+ state at $E(0_2^+) = 1148\,\text{keV}$ will end up in the γγ-coincidence spectrum, when gating on the decay of the 2_1^+ state. Thus, several bumps are visible in the γγ-coincidence spectrum, each shifted by the energy difference between the corresponding low-lying state and the 2_1^+ state (see Fig. 4.23). Primary decays to the 0_2^+ state are only 370 keV lower in energy in comparison to primary decays to the 2_1^+ state. The spectral width of the photon beam is sufficiently small to resolve both bump individually. However, for higher photon beam energies, there is an overlap between both bumps, which complicates integrating over the 2_1^+-primary bump exclusively.

Instead of integrating over the whole bump, it is also possible to integrate only over

a portion of it. For the primary decay into the level with energy E_k, an adaptive integration range of

$$\left[\max\left(0.98 \cdot E_{\text{beam}}, 1.02 \cdot E_{\text{beam}} - \left(E\left(0_2^+\right) - E\left(2_1^+\right)\right)\right) - E_k, 1.02 \cdot E_{\text{beam}} - E_k\right] \quad (4.10)$$

was chosen, which assumes a width of the photon beam of 4 %. For high beam energies, it cuts off the low energy portion of the bump, which contains the high-energy tail of the primary decays into the 0_2^+ state when gating on the decay of the 2_1^+ state. This integration range is used to integrate over the bumps of *all* primary decays into low-lying states J_k, such that the factor s_j in Eq. (2.22) remains the same for all decay branches.

Detector gain shifts (by zeroth order) only result in an energy offset of the primary bump, which is consistent for all γγ-coincidence spectra. Thus, they do not affect the applicability of the method, but slightly reduce the statistics. For the primary decay to the 2_1^+ state, gain shifts could result in undesirable contributions from primary decays into the 0_2^+ state. With typical energy shifts of less than 30 keV, no significant impact on the results is expected.

4.2.6. Determination of downward PSF

Using the results of the previous section and Eq. (2.22), one can calculate the downward PSF

$$f_{j \to k}^{\lambda L}(E_j - E_k) \propto \frac{r_{j,k,\pi}}{(E_j - E_k)^{2L+1}} \quad (4.11)$$

for one particular beam energy E_j. When analyzing decays into the states 2_1^+ up to 2_7^+, the seven data points for the PSF per photon beam energy cover an energy range with an extent of around 2 MeV. Applying the Brink-Axel hypothesis, one can combine them into a single downward PSF $\overleftarrow{f}_{\text{exp}}^{\lambda L, \text{p}}(E_\gamma)$.

An iterative approach illustrated in Fig. 2.6 was used to combine multiple PSFs into a single downward PSF: The process begins with the PSF for the highest beam energy. Data points and their uncertainties are pairwise interpolated using a linear spline to connect all data points. Subsequently, the PSF for the next lower beam energy is considered. A least-squares minimization is performed to minimize the quadratic

difference to the interpolated PSF, accounting for the uncertainties of both the data points and the PSF. After applying the scaling factor determined by the minimization procedure to the combined PSF dataset, the process is repeated until the PSFs for all beam energies have been combined into a single dataset. The resulting dataset contains the downward PSF in arbitrary units, ranging from approximately 1.1 MeV to 8.5 MeV.

Uncertainties introduced by the scaling method are not considered. As each step introduces a further scaling factor, starting with the highest beam energy results in small scaling-related uncertainties for high beam energies, but large scaling-related uncertainties for low beam energies. The large increase of uncertainties towards lower photon beam energies would be misleading. Instead, there is a correlation between neighboring scaled data points that could influence the overall shape and slope of the combined PSF.

A moving average was calculated for the combined dataset, henceforth referred to as moving-average window (MAW). To prevent an unphysical flattening out of the MAW at the boundaries of the dataset, a normalization in form of a coordinate transformation was performed before applying the MAW. As further discussed in Section 6.2, the PSF has an approximately exponential shape. By subsequently applying a logarithmic transformation and linear transformation in succession, the data points were normalized to be approximately equal to unity. After calculating the MAW, the inverse coordinate transformation was performed.

On a densely-spaced energy grid, the MAW of the PSF was calculated by taking the average of all data points of the combined PSF $\overleftarrow{f}_{\mathrm{exp}}^{\lambda L,\mathrm{p}}(E_\gamma)$ within a certain energy range around the grid point. Instead of using a boxcar filter (i.e., a rectangular function), a Gaussian distribution around the grid point with a FWHM of 200 keV was used. This approach results in a "smooth" MAW PSF, i.e., its first derivative exists. Uncertainties were taken into account. For the value of one MAW grid point $\overleftarrow{f}_{\mathrm{MAW}}^{\lambda L,\mathrm{p}}(E_\gamma)$, the following general formula was used, derived from Eq. (1) in Ref. [282] with additional arbitrary filter weights w_i:

$$\overline{x} \pm \delta\overline{x} = \frac{\sum_i \frac{x_i w_i}{(\delta x_i)^2}}{\sum_i \frac{w_i}{(\delta x_i)^2}} \pm \left(\frac{\sum_i \frac{w_i^2}{(\delta x_i)^2}}{\left(\sum_i \frac{w_i}{(\delta x_i)^2}\right)^2} \right)^2 . \tag{4.12}$$

Here, $\overline{x} \pm \delta\overline{x}$ refers to the MAW mean value and standard deviation, x_i and δx_i are

the data points and their 1σ-uncertainty, and w_i are the (unnormalized) filter weights of the MAW.

5. Results

In this chapter, the experimental results for the ^{150}Nd and ^{96}Mo experiments are listed. The given quantities are described briefly. For a discussion, refer to Chapter 6.

5.1. Photon scattering off ^{150}Nd

Table 5.1: Identified states of ^{150}Nd from DHIPS and HIγS experiments. All states above 3.9 MeV are newly observed. For lower energies, results by Pitz *et al.* [260] should take precedence because of possible feeding from higher-lying states in the DHIPS experiment.

E^* (keV)	J^π	$\Gamma_{0_1^+}^*$ (meV)	$\Gamma_{2_1^+}^*$ (meV)	I^* (eVb)	R_exp	$B(E1)\downarrow^*$ ($10^{-5}e^2\mathrm{fm}^2$)	$B(M1)\downarrow^*$ ($10^{-3}\mu_\mathrm{N}^2$)
2269.15(25)‡	1	4.8(7)		10.7(15)		39(5)	35(5)
2413.20(12)‡	1	29.4(23)	27(4)	30.3(19)	1.09(11)*	200(16)	181(14)
2494.98(28)‡	1	9.4(11)		17.5(20)		58(7)	53(6)
2569.9(16)‡	1, 2$^+$	9(5)		16(9)		52(29)	47(26)
2587.70(30)‡	1	11.0(14)		18.9(24)		60(8)	55(7)
2680.22(29)‡	1	9.4(11)		15.1(18)		47(6)	42(5)
2894.43(26)	1$^+$	26.2(28)	16(5)	22.3(17)	0.71(14)†		93(10)
2919.44(35)	1$^-$	9.2(10)		12.5(14)		35(4)	
2992.79(6)	1$^+$	88.5(31)	51(4)	72.3(21)	0.66(4)		285(10)

Table 5.1:   (Continued)

E^* (keV)	J^π	$\Gamma_{0_1^+}{}^*$ (meV)	$\Gamma_{2_1^+}$ (meV)	I^* (eVb)	$R_{\exp}$	$B(E1)\downarrow^*$ $(10^{-5}e^2\mathrm{fm}^2)$	$B(M1)\downarrow^*$ $(10^{-3}\mu_\mathrm{N}^2)$
3056.62(9)	$1^{+\S}$	53.8(29)	34(4)	40.7(18)	0.72(6)		163(9)
3094.0(5)	1	12.6(13)		15.2(16)		41(4)	37(4)
3102.03(28)	1	18.3(15)		21.9(18)		58(5)	53(4)
3185.0(4)‡	1	4.6(10)		5.2(11)		13.5(29)	12.2(26)
3219.95(23)	1^+	19.8(23)	5.7(19)	17.1(17)	0.32(8)†		51(6)
3287.9(7)	1	9.8(15)		10.5(16)		26(4)	24(4)
3325.6(4)	1	14.1(16)		14.7(17)		37(4)	33(4)
3340.52(26)	1	15.7(15)		16.2(16)		40(4)	36(4)
3394.88(21)‡	1	15.7(14)		15.7(14)		38.3(34)	34.7(31)
3417.0(7)	1^-	9.1(18)		9.0(18)		22(4)	
3514.8(6)‡	1	8.5(13)		7.9(12)		18.6(28)	16.8(26)
3551.3(4)	1^-	38(6)	52(15)	14.5(16)	1.53(27)	80(12)	
3579.88(21)	1	12.9(13)		11.6(12)		26.8(28)	24.3(25)
3652.82(27)	1^-	31(4)	43(12)	11.1(12)	1.55(25)	60(9)	
3670.90(21)	1^-	27(6)	20(13)	13.6(12)	0.8(4)†	53(11)	
3706.01(23)	1^-	25(4)	29(9)	9.7(10)	1.30(26)	47(7)	
3710.7(4)	1^-	19.8(35)	20(8)	8.3(11)	1.11(27)	37(7)	
3750.49(27)	1^+	43(4)	36(8)	19.0(14)	0.94(13)		70(7)
3766.36(33)	1	15.4(15)		12.5(12)		27.5(26)	24.9(24)
3858.8(4)‡	1	13.9(15)		10.8(12)		23.2(26)	21.0(23)
3887.8(6)	1^-	5.9(13)		4.5(10)		9.6(21)	
3989.5(5)	1^-	20(4)	20(8)	7.3(12)	1.09(25)†	30(6)	
4002.5(5)‡	1	8.8(15)		6.3(11)		13.0(23)	11.8(21)
4033.21(26)	1^-	40(6)	61(15)	11.2(14)	1.68(22)	58(9)	
4043.3(7)	1^-	16(6)	36(22)	3.6(11)	2.4(8)*	24(9)	
4071.9(9)	1	4.9(14)		3.4(10)		6.9(20)	6.3(18)
4080.4(6)	1^-	7.1(16)		4.9(11)		9.9(22)	
4105.3(6)	1^-	30(5)	12.2(32)	14.5(21)	0.45(8)	41(6)	

Continued on next page

Table 5.1:   (Continued)

E^* (keV)	J^π	$\Gamma_{0_1^+}^*$ (meV)	$\Gamma_{2_1^+}$ (meV)	I^* (eVb)	R_{exp}	$B(E1)\!\downarrow^*$ ($10^{-5}e^2\text{fm}^2$)	$B(M1)\!\downarrow^*$ ($10^{-3}\mu_N^2$)
4193.1(8)	1^-	6.6(17)		4.3(11)		8.5(22)	
4239.5(7)	1^-	19.6(35)	9(5)	8.7(11)	0.49(20)†	25(4)	
4251.63(31)	1^-	29.8(24)	7.0(17)	15.4(11)	0.26(5)	37.0(30)	
4265.4(7)	1^-	22(5)	21(11)	7.1(10)	1.03(35)†	27(6)	
4312.8(5)	1^-	21.1(33)	11(5)	8.5(10)	0.59(18)*	25(4)	
4322.7(5)	1^-	11.7(16)		7.2(10)		13.8(19)	
4332.9(7)‡	$1,2^+$	8.1(13)		5.0(8)		9.6(15)	8.6(14)
4490.34(27)	1^-	17.8(16)		10.2(9)		18.8(17)	
4552.4(7)	1^-	11.1(16)		6.2(9)		11.3(16)	
4564.40(24)	1^-	34.0(18)		18.8(10)		34.1(18)	
4589.6(7)	1^-	16.8(22)		9.2(12)		16.6(22)	
4610.5(6)	1^-	12.4(17)		6.7(9)		12.0(16)	
4626.6(6)‡	1	3.9(11)		2.1(6)		3.8(11)	3.4(10)
4637.30(35)	1^-	19(4)	26(10)	4.1(6)	1.5(4)*	17.7(35)	
4643.1(4)	1^-	19(4)	25(10)	4.5(7)	1.42(33)*	18(4)	
4662.5(8)	1	7.4(17)		3.9(9)		6.9(16)	6.3(14)
4675.62(28)‡	1	21.6(17)		11.4(9)		20.2(16)	18.3(14)
4701.3(6)	1	6.1(17)		3.2(9)		5.6(16)	5.1(14)
4714.0(4)	1^-	45(11)	1.7(6)	5.0(9)	4.0(8)*	41(10)	
4742.78(29)	1^-	12.9(20)		6.6(10)		11.5(17)	
4805.7(7)	1^-	33(5)	30(8)	8.6(10)	0.98(16)†	28(4)	
4821.7(5)‡	1	19.0(20)		9.4(10)		16.1(17)	14.6(16)
4830.9(8)‡	1	12.6(20)		6.2(10)		10.6(17)	9.6(16)
4869.3(5)‡	1	10.5(19)		5.1(9)		8.7(15)	7.9(14)
4919.4(18)‡	1	7.8(19)		3.7(9)		6.2(15)	5.6(14)
4926.5(11)‡	1	13.5(21)		6.4(10)		10.8(17)	9.7(15)
4952.21(31)	1^-	18.1(17)		8.5(8)		14.2(13)	
4972.5(7)‡	1	11.4(17)		5.3(8)		8.8(13)	8.0(12)

Continued on next page

E^* (keV)	J^π	$\Gamma_{0_1^+}^{\,*}$ (meV)	$\Gamma_{2_1^+}$ (meV)	I^* (eVb)	R_{exp}	$B(E1){\downarrow}^*$ $(10^{-5}e^2\mathrm{fm}^2)$	$B(M1){\downarrow}^*$ $(10^{-3}\mu_N^2)$
5053.7(5)‡	1	11.3(18)		5.1(8)		8.4(13)	7.6(12)
5090.5(9)‡	1	31(6)	41(14)	6.0(9)	1.43(27)*	23(4)	20(4)
5114.5(7)	1	12.0(18)		5.3(8)		8.6(13)	7.8(12)
5124.0(6)	1,2⁺	13.0(20)		5.7(9)		9.2(15)	8.3(13)
5188.2(4)	1⁻	22.2(26)		9.5(11)		15.2(18)	
5205.5(5)	1⁻	13.2(19)		5.6(8)		8.9(13)	
5229.68(35)‡	1	10.2(17)		4.3(7)		6.8(11)	6.2(10)
5273.2(4)‡	1	10.1(19)		4.2(8)		6.6(13)	6.0(11)
5323.6(6)	1⁻	19.7(25)		8.0(10)		12.4(16)	
5351.1(4)	1⁻	33.5(27)		13.5(11)		20.9(17)	
5401.56(35)	1⁻	40.0(30)		15.8(12)		24.2(18)	
5438.6(4)‡	1	34.6(28)		13.5(11)		20.5(17)	18.6(15)
5475.0(10)	1⁻	26.0(29)		10.0(11)		15.1(17)	
5505.85(20)	1⁻	86(6)		32.6(22)		49.0(33)	
5523.6(5)	1⁻	36.8(32)		13.9(12)		20.8(18)	
5662.1(6)	1⁻	34.5(33)		12.4(12)		18.1(18)	
5690.0(9)‡	1	23.9(31)		8.5(11)		12.4(16)	11.2(14)
5717.42(31)‡	1	36.0(31)		12.7(11)		18.4(16)	16.6(14)
5745.4(6)‡	1	58(10)	90(28)	8.0(11)	1.65(29)*	29(5)	27(5)
5773.7(5)‡	1	80(14)	1.9(6)	8.1(11)	2.6(4)*	39(7)	36(6)
5816.5(5)‡	1	50(4)		16.9(14)		24.1(20)	21.8(18)
5838.4(5)‡	1	46(4)		15.4(13)		21.8(18)	19.8(17)
5865.6(12)‡	1	34(4)		11.4(14)		16.1(20)	14.6(18)
5885.1(8)‡	1	51(5)		17.0(15)		23.9(21)	21.7(19)
5998.5(7)‡	1	25(4)		8.1(12)		11.2(17)	10.1(15)
6037.2(5)‡	1	28.1(35)		8.9(11)		12.2(15)	11.0(14)
6055.22(33)‡	1	37.8(35)		11.9(11)		16.3(15)	14.7(14)

Table 5.1: (Continued)

E^* (keV)	J^π	$\Gamma_{0_1^+}{}^*$ (meV)	$\Gamma_{2_1^+}$ (meV)	I^* (eVb)	R_{exp}	$B(E1)\downarrow^*$ $(10^{-5}e^2\text{fm}^2)$	$B(M1)\downarrow^*$ $(10^{-3}\mu_N^2)$
6322.3(16)‡	1	49(11)		14.2(32)		19(4)	17(4)

* Only includes DHIPS data.
† Only includes HIγS data.
‡ Only observed at DHIPS.
§ Parity taken from Ref. [283].

The results of the state-to-state analysis can be found in Table 5.1. The table includes level energies, spin, and parity quantum numbers J^π, transition widths to the 0_1^+ and 2_1^+ states, energy-integrated cross sections I, branching ratios R_{exp}, and reduced transition probabilities [$B(E1)\downarrow$, $B(M1)\downarrow$]. Out of 93 observed levels in total, 39 states were assigned as $J = 1^-$ and 4 states as $J = 1^+$. 56 states were observed both at HIγS and DHIPS, the other 37 states were exclusively observed at DHIPS. In three cases, it was not possible to determine the angular momentum quantum number J.

The results of the analysis of average quantities are listed in Table 5.2. For each beam-energy setting, characterized by a centroid energy E_{beam} and FWHM, the photon-scattering cross section $\sigma_{\gamma\gamma} = \sigma_{\gamma\gamma}^{E1} + \sigma_{\gamma\gamma}^{M1}$ is given, including its decomposition into $E1$ and $M1$ strength. The average branching ratios

$$\langle R_{\text{exp}} \rangle = \frac{\left\langle \frac{\Gamma_2 \Gamma_0}{\Gamma} \right\rangle}{\left\langle \frac{\Gamma_0 \Gamma_0}{\Gamma} \right\rangle} \cdot \frac{E_\gamma(0_1^+)^3}{E_\gamma(2_1^+)^3} = \frac{\sum_i \Gamma_{0,i} \frac{\Gamma_{2,i}}{\Gamma_i}}{\sum_i \Gamma_{0,i} \frac{\Gamma_{0,i}}{\Gamma_i}} \cdot \frac{E_\gamma(0_1^+)^3}{E_\gamma(2_1^+)^3} \tag{5.1}$$

defined in analogy to Eq. (2.11) are given both for $E1$ and $M1$ transition strength. In addition, the table lists the experimentally observed asymmetry $\langle \epsilon \rangle$ between $E1$ and $M1$ radiation (which is corrected for any effects related to the finite detector size and efficiency), i.e.,

$$\langle \epsilon \rangle = \frac{\left\langle \frac{\Gamma_0 \Gamma_0}{\Gamma} \right\rangle^{M1} - \left\langle \frac{\Gamma_0 \Gamma_0}{\Gamma} \right\rangle^{E1}}{\left\langle \frac{\Gamma_0 \Gamma_0}{\Gamma} \right\rangle^{M1} + \left\langle \frac{\Gamma_0 \Gamma_0}{\Gamma} \right\rangle^{E1}}. \tag{5.2}$$

Table 5.2: Elastic cross sections $\sigma_{\gamma\gamma}$, including a decomposition into $E1$ and $M1$ transition strength, average branching ratios $\langle R_{\mathrm{exp}}^{E1}\rangle$, and $\langle R_{\mathrm{exp}}^{M1}\rangle$, and the average efficiency-corrected asymmetry $\langle\epsilon\rangle$ of ^{150}Nd for different excitation energy ranges.

E_{beam} (MeV)	FWHM (keV)	$\sigma_{\gamma\gamma}$ (mb)	$\sigma_{\gamma\gamma}^{E1}$ (mb)	$\sigma_{\gamma\gamma}^{M1}$ (mb)	$\langle R_{\mathrm{exp}}^{E1}\rangle$	$\langle R_{\mathrm{exp}}^{M1}\rangle^{\star}$	$\langle\epsilon\rangle$
2.95	100	0.66(6)	0.088(17)	0.57(4)	$1.3^{+0.6}_{-1.0}$	<0.73	0.732(32)
3.11	109	0.47(5)	0.031(14)	0.434(34)	5.0(28)	<0.42	0.87(5)
3.22	87	0.306(33)	0.068(15)	0.238(19)	1.1(5)	<0.40	0.56(6)
3.31	109	0.272(30)	0.064(15)	0.207(18)	0.6(4)	<0.30	0.53(7)
3.41	112	0.209(25)	0.075(15)	0.133(11)	$0.4^{+0.2}_{-0.4}$	<0.63	0.28(7)
3.52	115	0.194(24)	0.080(17)	0.114(11)	2.0(4)	<0.67	0.18(8)
3.62	116	0.42(4)	0.310(34)	0.113(11)	$0.56^{+0.10}_{-0.08}$	<0.89	−0.46(4)
3.71	119	0.56(5)	0.35(4)	0.205(17)	$1.10^{+0.11}_{-0.08}$	<0.50	−0.263(31)
3.81	124	0.255(29)	$0.079^{+0.018}_{-0.015}$	0.175(16)	1.2(7)	<0.98	0.38(7)
3.90	128	0.307(33)	0.164(23)	$0.142^{+0.012}_{-0.015}$	$0.10^{+0.05}_{-0.10}$	<0.32	−0.07(6)
4.02	102	0.41(4)	0.318(33)	0.090(9)	$0.81^{+0.15}_{-0.11}$	<1.62	−0.557(30)
4.10	106	0.39(4)	0.254(29)	0.137(12)	1.34(12)	<0.65	−0.30(4)
4.22	104	0.311(34)	0.225(27)	0.086(8)	0.69(9)	<0.76	−0.45(4)
4.31	108	0.33(4)	0.245(28)	0.089(9)	0.64(6)	<0.43	−0.46(4)
4.39	110	0.325(35)	0.150(22)	0.174(16)	0.66(8)	<0.15	0.08(6)
4.50	114	0.286(31)	0.217(26)	0.069(8)	$0.65^{+0.17}_{-0.13}$	<1.67	−0.52(4)
4.60	109	0.35(4)	0.300(33)	0.052(6)	0.59(6)	<1.20	−0.704(28)
4.70	113	0.307(33)	0.237(28)	0.070(8)	0.78(6)	<0.46	−0.54(4)
4.79	122	0.293(32)	0.235(28)	0.058(6)	0.94(8)	<0.77	−0.602(35)
4.89	117	0.35(4)	0.11(10)	$0.23^{+0.08}_{-0.23}$	$0.9^{+2.7}_{-0.9}$	<5.04	0.3(6)
5.00	100	0.40(4)	0.34(4)	0.056(7)	0.59(5)	<0.90	−0.718(27)
5.10	98	0.42(4)	0.37(4)	0.056(7)	0.75(4)	<0.75	−0.735(26)
5.21	103	0.54(5)	0.49(5)	0.045(6)	0.468(32)	<1.02	−0.831(20)
5.31	109	0.52(5)	0.47(5)	0.049(6)	0.484(32)	<0.97	−0.810(19)
5.40	104	0.59(5)	0.54(5)	0.050(7)	0.597(30)	<0.87	−0.830(19)

Continued on next page

Table 5.2:   (Continued)

E_{beam} (MeV)	FWHM (keV)	$\sigma_{\gamma\gamma}$ (mb)	$\sigma_{\gamma\gamma}^{E1}$ (mb)	$\sigma_{\gamma\gamma}^{M1}$ (mb)	$\langle R_{\mathrm{exp}}^{E1}\rangle$	$\langle R_{\mathrm{exp}}^{M1}\rangle^{\star}$	$\langle\epsilon\rangle$
5.51	106	0.90(8)	0.85(8)	0.046(7)	$0.396^{+0.027}_{-0.021}$	<1.52	−0.897(15)
5.61	109	0.71(6)	0.66(6)	0.052(7)	0.606(25)	<0.67	−0.852(17)
5.71	115	0.76(7)	0.72(6)	0.038(6)	$0.519^{+0.026}_{-0.021}$	<1.13	−0.899(16)
5.78	125	0.89(8)	0.83(7)	0.053(7)	0.432(15)	<0.50	−0.881(13)
5.81	120	0.99(8)	0.94(8)	0.044(9)	0.316(20)	<1.26	−0.910(17)
5.91	120	0.81(7)	0.76(7)	0.053(7)	0.564(22)	<0.69	−0.869(16)
6.02	109	0.98(9)	0.92(8)	0.061(9)	0.424(22)	<1.01	−0.876(16)
6.06	154	1.13(10)	1.05(9)	0.082(11)	0.366(20)	<0.58	−0.855(16)
6.12	115	0.93(8)	0.85(7)	0.078(9)	0.459(20)	<0.46	−0.832(16)
6.20	118	0.77(7)	0.70(6)	0.070(8)	0.519(21)	<0.37	−0.818(17)
6.30	121	0.74(7)	0.69(6)	0.054(7)	0.486(23)	<0.70	−0.853(16)
6.40	117	0.56(5)	0.50(5)	0.064(8)	0.687(31)	<0.34	−0.772(21)
6.50	114	0.65(6)	0.61(6)	0.045(7)	0.471(26)	<0.72	−0.862(20)
6.59	128	0.66(6)	0.60(6)	0.058(8)	0.502(25)	<0.49	−0.824(20)
6.69	141	0.52(5)	0.48(5)	0.042(6)	0.602(32)	<0.52	−0.840(21)
6.79	134	0.54(5)	0.47(5)	0.065(8)	0.544(31)	<0.47	−0.758(22)
6.89	130	0.57(6)	0.45(5)	0.11(4)	0.45(4)	<0.33	−0.60(11)
6.99	131	0.45(4)	0.39(4)	0.057(9)	0.63(5)	<0.96	−0.74(4)

* Given as 2σ upper limits.

5.2. Downward PSF of ^{96}Mo

Using the $\gamma\gamma$-coincidence method described in Section 4.2.6, the downward PSFs of ^{96}Mo were determined. The results are given in Tables 5.3 to 5.6. The PSF data are normalized to the $(\mathrm{p,p'}\gamma)$ Oslo-method data from Ref. [146]. The results for decays to 1^+ states in Table 5.4 are further scaled to match the scale of the 2^+ PSF as discussed in Section 6.2.3.

Table 5.3: PSF of ^{96}Mo for all observed decays to low-lying $J^\pi = 2^+$ states from $\gamma\gamma$ coincidences. The table lists the energy of the primary transition E_γ to the state J_k^π at $E(J_k^\pi)$, the photon beam energy E_{beam}, and the PSF value $\overleftarrow{f}^{E1}(E_\gamma)$.

E_γ (MeV)	E_{beam} (MeV)	J_k^π	$E(J_k^\pi)$ (MeV)	$\overleftarrow{f}^{E1}(E_\gamma)$ $(10^{-8}\,\mathrm{MeV}^{-3})^\star$
1.113	3.9	2_7^+	2.787	5(4)
1.313	4.1	2_7^+	2.787	1.6(20)
1.474	3.9	2_5^+	2.426	2.6(27)
1.513	4.3	2_7^+	2.787	2.2(32)
1.674	4.1	2_5^+	2.426	1.3(17)
1.713	4.5	2_7^+	2.787	0.4(4)
1.804	3.9	2_4^+	2.096	0.4(4)
1.874	4.3	2_5^+	2.426	1.1(9)
1.913	4.7	2_7^+	2.787	0.9(9)
2.004	4.1	2_4^+	2.096	0.7(6)
2.074	4.5	2_5^+	2.426	0.5(5)
2.113	4.9	2_7^+	2.787	0.5(4)
2.204	4.3	2_4^+	2.096	0.5(5)
2.274	4.7	2_5^+	2.426	1.2(9)
2.274	3.9	2_3^+	1.626	10.0(31)
2.313	5.1	2_7^+	2.787	1.0(10)
2.402	3.9	2_2^+	1.498	3.3(19)
2.404	4.5	2_4^+	2.096	0.24(21)
2.474	4.9	2_5^+	2.426	0.17(15)
2.474	4.1	2_3^+	1.626	3.0(8)

Continued on next column/page

E_γ (MeV)	E_{beam} (MeV)	J_k^π	$E(J_k^\pi)$ (MeV)	$\overleftarrow{f}^{E1}(E_\gamma)$ $(10^{-8}\,\mathrm{MeV}^{-3})^\star$
2.513	5.3	2_7^+	2.787	0.6(6)
2.602	4.1	2_2^+	1.498	4.5(8)
2.604	4.7	2_4^+	2.096	1.3(10)
2.674	4.3	2_3^+	1.626	5.2(10)
2.674	5.1	2_5^+	2.426	0.6(5)
2.713	5.5	2_7^+	2.787	0.8(7)
2.802	4.3	2_2^+	1.498	2.8(8)
2.804	4.9	2_4^+	2.096	0.4(4)
2.874	4.5	2_3^+	1.626	2.5(5)
2.874	5.3	2_5^+	2.426	0.7(8)
2.963	5.8	2_7^+	2.787	0.20(17)
3.002	4.5	2_2^+	1.498	1.9(6)
3.004	5.1	2_4^+	2.096	1.1(7)
3.074	4.7	2_3^+	1.626	2.4(6)
3.074	5.5	2_5^+	2.426	0.5(4)
3.122	3.9	2_1^+	0.778	0.25(19)
3.202	4.7	2_2^+	1.498	2.5(4)
3.204	5.3	2_4^+	2.096	0.7(5)
3.213	6.0	2_7^+	2.787	0.61(30)
3.274	4.9	2_3^+	1.626	0.84(31)
3.322	4.1	2_1^+	0.778	0.63(12)
3.324	5.8	2_5^+	2.426	0.36(29)
3.402	4.9	2_2^+	1.498	0.68(26)
3.404	5.5	2_4^+	2.096	0.8(4)
3.463	6.2	2_7^+	2.787	0.38(33)

Continued on next column/page

E_γ (MeV)	E_{beam} (MeV)	J_k^π	$E(J_k^\pi)$ (MeV)	$\overleftarrow{f}^{E1}(E_\gamma)$ $(10^{-8}\,\text{MeV}^{-3})^\star$
3.474	5.1	2_3^+	1.626	2.9(6)
3.522	4.3	2_1^+	0.778	0.45(13)
3.574	6.0	2_5^+	2.426	0.8(4)
3.602	5.1	2_2^+	1.498	2.7(9)
3.654	5.8	2_4^+	2.096	0.46(19)
3.674	5.3	2_3^+	1.626	3.1(5)
3.713	6.5	2_7^+	2.787	0.8(4)
3.722	4.5	2_1^+	0.778	1.14(14)
3.802	5.3	2_2^+	1.498	2.0(5)
3.824	6.2	2_5^+	2.426	0.88(29)
3.874	5.5	2_3^+	1.626	2.0(4)
3.904	6.0	2_4^+	2.096	1.20(23)
3.922	4.7	2_1^+	0.778	0.94(13)
3.963	6.8	2_7^+	2.787	1.05(31)
4.002	5.5	2_2^+	1.498	2.4(5)
4.074	6.5	2_5^+	2.426	1.1(4)
4.122	4.9	2_1^+	0.778	1.30(10)
4.124	5.8	2_3^+	1.626	1.13(14)
4.154	6.2	2_4^+	2.096	0.46(12)
4.213	7.0	2_7^+	2.787	1.7(4)
4.252	5.8	2_2^+	1.498	1.48(17)
4.322	5.1	2_1^+	0.778	0.97(15)
4.324	6.8	2_5^+	2.426	0.74(25)
4.374	6.0	2_3^+	1.626	1.54(15)
4.404	6.5	2_4^+	2.096	0.67(20)
4.463	7.2	2_7^+	2.787	1.6(6)
4.502	6.0	2_2^+	1.498	1.83(16)
4.522	5.3	2_1^+	0.778	1.05(14)
4.574	7.0	2_5^+	2.426	1.2(4)
4.624	6.2	2_3^+	1.626	1.47(17)
4.654	6.8	2_4^+	2.096	1.34(21)
4.713	7.5	2_7^+	2.787	1.5(6)
4.722	5.5	2_1^+	0.778	1.36(14)
4.752	6.2	2_2^+	1.498	1.28(15)
4.824	7.2	2_5^+	2.426	0.75(34)
4.874	6.5	2_3^+	1.626	3.27(22)
4.904	7.0	2_4^+	2.096	1.69(28)
4.963	7.8	2_7^+	2.787	2.0(7)
4.972	5.8	2_1^+	0.778	1.68(7)
5.002	6.5	2_2^+	1.498	2.21(19)
5.074	7.5	2_5^+	2.426	1.5(5)
5.124	6.8	2_3^+	1.626	2.00(17)
5.154	7.2	2_4^+	2.096	1.08(28)
5.213	8.0	2_7^+	2.787	2.2(5)
5.222	6.0	2_1^+	0.778	1.78(7)
5.252	6.8	2_2^+	1.498	2.19(16)
5.324	7.8	2_5^+	2.426	1.2(5)
5.374	7.0	2_3^+	1.626	2.55(18)
5.404	7.5	2_4^+	2.096	1.6(4)
5.463	8.2	2_7^+	2.787	3.6(6)

Table 5.3: (Continued)

E_γ (MeV)	E_{beam} (MeV)	J_k^π	$E(J_k^\pi)$ (MeV)	$\overleftarrow{f}^{E1}(E_\gamma)$ $(10^{-8}\,\text{MeV}^{-3})^\star$
5.472	6.2	2_1^+	0.778	2.39(8)
5.502	7.0	2_2^+	1.498	2.63(17)
5.574	8.0	2_5^+	2.426	1.6(6)
5.624	7.2	2_3^+	1.626	2.79(25)
5.654	7.8	2_4^+	2.096	2.8(4)
5.713	8.5	2_7^+	2.787	4.4(13)
5.722	6.5	2_1^+	0.778	2.52(10)
5.752	7.2	2_2^+	1.498	3.20(23)
5.824	8.2	2_5^+	2.426	2.6(7)
5.874	7.5	2_3^+	1.626	3.00(23)
5.904	8.0	2_4^+	2.096	2.5(4)
5.963	8.8	2_7^+	2.787	4.0(11)
5.972	6.8	2_1^+	0.778	2.97(9)
6.002	7.5	2_2^+	1.498	2.60(23)
6.074	8.5	2_5^+	2.426	2.5(9)
6.124	7.8	2_3^+	1.626	3.28(27)
6.154	8.2	2_4^+	2.096	2.8(5)
6.213	9.0	2_7^+	2.787	6.3(13)
6.222	7.0	2_1^+	0.778	3.49(10)
6.252	7.8	2_2^+	1.498	3.55(30)
6.324	8.8	2_5^+	2.426	3.2(15)
6.374	8.0	2_3^+	1.626	3.59(29)
6.404	8.5	2_4^+	2.096	4.3(6)
6.463	9.2	2_7^+	2.787	6.0(15)
6.472	7.2	2_1^+	0.778	4.25(14)

E_γ (MeV)	E_{beam} (MeV)	J_k^π	$E(J_k^\pi)$ (MeV)	$\overleftarrow{f}^{E1}(E_\gamma)$ $(10^{-8}\,\text{MeV}^{-3})^\star$
6.502	8.0	2_2^+	1.498	3.32(30)
6.574	9.0	2_5^+	2.426	5.2(14)
6.624	8.2	2_3^+	1.626	5.3(4)
6.654	8.8	2_4^+	2.096	4.1(9)
6.722	7.5	2_1^+	0.778	4.87(13)
6.752	8.2	2_2^+	1.498	5.3(4)
6.824	9.2	2_5^+	2.426	4.7(23)
6.874	8.5	2_3^+	1.626	5.1(4)
6.904	9.0	2_4^+	2.096	4.4(11)
6.972	7.8	2_1^+	0.778	5.62(16)
7.002	8.5	2_2^+	1.498	6.2(5)
7.124	8.8	2_3^+	1.626	6.4(7)
7.154	9.2	2_4^+	2.096	4.1(16)
7.222	8.0	2_1^+	0.778	7.02(16)
7.252	8.8	2_2^+	1.498	6.1(6)
7.374	9.0	2_3^+	1.626	8.2(8)
7.472	8.2	2_1^+	0.778	8.11(23)
7.502	9.0	2_2^+	1.498	8.4(8)
7.624	9.2	2_3^+	1.626	12.5(14)
7.722	8.5	2_1^+	0.778	9.30(26)
7.752	9.2	2_2^+	1.498	9.8(15)
7.972	8.8	2_1^+	0.778	10.70(35)
8.222	9.0	2_1^+	0.778	11.9(4)
8.472	9.2	2_1^+	0.778	12.3(7)

* Normalized with data from Ref. [146]. The normalization results in an additional 1.5 % statistical uncertainty not accounted for in the listed values.

Table 5.4: PSF of ^{96}Mo for decays to low-lying $J^\pi = 1^+$ states from $\gamma\gamma$ coincidences. See Table 5.3.

E_γ (MeV)	E_{beam} (MeV)	J_k^π	$E(J_k^\pi)$ (MeV)	$\overleftarrow{f}^{E1}(E_\gamma)$ $(10^{-8}\,\text{MeV}^{-3})^\star$
2.200	5.5	1_b^+	3.300	1.1(11)
2.450	5.8	1_b^+	3.300	0.20(28)
2.700	6.0	1_b^+	3.300	0.5(5)
2.706	5.5	1_a^+	2.794	0.5(4)
2.950	6.2	1_b^+	3.300	0.22(22)
2.956	5.8	1_a^+	2.794	0.15(13)
3.200	6.5	1_b^+	3.300	0.29(25)
3.206	6.0	1_a^+	2.794	0.48(32)
3.450	6.8	1_b^+	3.300	0.20(22)
3.456	6.2	1_a^+	2.794	0.25(19)
3.700	7.0	1_b^+	3.300	0.7(6)
3.706	6.5	1_a^+	2.794	0.41(27)
3.950	7.2	1_b^+	3.300	0.9(9)
3.956	6.8	1_a^+	2.794	1.1(6)
4.200	7.5	1_b^+	3.300	0.5(5)
4.206	7.0	1_a^+	2.794	1.0(9)
4.450	7.8	1_b^+	3.300	1.4(13)
4.456	7.2	1_a^+	2.794	1.2(8)
4.700	8.0	1_b^+	3.300	1.2(10)
4.706	7.5	1_a^+	2.794	1.2(9)
4.950	8.2	1_b^+	3.300	1.7(16)
4.956	7.8	1_a^+	2.794	1.6(7)
5.200	8.5	1_b^+	3.300	1.7(13)

Continued on next column/page

Table 5.4: (Continued)

E_γ (MeV)	E_{beam} (MeV)	J_k^π	$E(J_k^\pi)$ (MeV)	$\overleftarrow{f}^{E1}(E_\gamma)$ $(10^{-8}\,\text{MeV}^{-3})^\star$
5.206	8.0	1_a^+	2.794	3.0(9)
5.450	8.8	1_b^+	3.300	1.6(14)
5.456	8.2	1_a^+	2.794	3.0(9)
5.700	9.0	1_b^+	3.300	2.2(24)
5.706	8.5	1_a^+	2.794	3.1(15)
5.950	9.2	1_b^+	3.300	6(5)
5.956	8.8	1_a^+	2.794	3.8(17)
6.206	9.0	1_a^+	2.794	3.5(20)
6.456	9.2	1_a^+	2.794	3.7(26)

* Normalized with data from Ref. [146]. The normalization results in an additional 1.5 % statistical uncertainty not accounted for in the listed values. To account for the unknown ground-state branching ratio Γ_0/Γ of each 1^+ state, the data were further scaled to a MAW interpolation of the 2^+ PSF.

Table 5.5: PSF of ^{96}Mo for all observed decays to the low-lying $J^\pi = 0_2^+$ state from $\gamma\gamma$ coincidences. See Table 5.3.

E_γ (MeV)	E_beam (MeV)	J_k^π	$E(J_k^\pi)$ (MeV)	$\overleftarrow{f}^{E1}(E_\gamma)$ $(10^{-8}\,\text{MeV}^{-3})^\star$
4.352	5.5	0_2^+	1.148	2.8(6)
4.602	5.8	0_2^+	1.148	0.85(23)
4.852	6.0	0_2^+	1.148	1.97(26)
5.102	6.2	0_2^+	1.148	1.38(27)
5.352	6.5	0_2^+	1.148	1.55(33)
5.602	6.8	0_2^+	1.148	1.29(23)
5.852	7.0	0_2^+	1.148	1.64(26)
6.102	7.2	0_2^+	1.148	2.26(34)
6.352	7.5	0_2^+	1.148	1.86(35)
6.602	7.8	0_2^+	1.148	2.4(4)
6.852	8.0	0_2^+	1.148	3.3(5)
7.102	8.2	0_2^+	1.148	3.3(7)
7.352	8.5	0_2^+	1.148	4.8(8)
7.602	8.8	0_2^+	1.148	4.8(9)
7.852	9.0	0_2^+	1.148	6.2(10)
8.102	9.2	0_2^+	1.148	10.9(21)

[*] Normalized with data from Ref. [146]. The normalization results in an additional 1.5 % statistical uncertainty not accounted for in the listed values.

Table 5.6: PSF of ^{96}Mo for decays to the low-lying $J^\pi = 3_1^+$ state from $\gamma\gamma$ coincidences. See Table 5.3.

E_γ (MeV)	E_beam (MeV)	J_k^π	$E(J_k^\pi)$ (MeV)	$\overleftarrow{f}^{E2}(E_\gamma)$ $(10^{-10}\,\text{MeV}^{-5})^\star$
2.960	5.5	3_1^+	2.540	12(10)
3.210	5.8	3_1^+	2.540	3.1(20)
3.460	6.0	3_1^+	2.540	7.3(25)
3.710	6.2	3_1^+	2.540	2.8(16)
3.960	6.5	3_1^+	2.540	6.3(27)
4.210	6.8	3_1^+	2.540	5.6(16)
4.460	7.0	3_1^+	2.540	6.3(11)
4.710	7.2	3_1^+	2.540	5.6(14)
4.960	7.5	3_1^+	2.540	3.5(14)
5.210	7.8	3_1^+	2.540	6.3(18)
5.460	8.0	3_1^+	2.540	7.0(13)
5.710	8.2	3_1^+	2.540	9.6(23)
5.960	8.5	3_1^+	2.540	12.3(26)
6.210	8.8	3_1^+	2.540	9(4)
6.460	9.0	3_1^+	2.540	12.8(30)
6.710	9.2	3_1^+	2.540	13(5)

[*] Normalized with data from Ref. [146]. The normalization results in an additional 1.5 % statistical uncertainty not accounted for in the listed values.

6. Discussion

In the following, the results of the ^{150}Nd and ^{96}Mo experiments are discussed. The first part of this chapter addresses the state-to-state analysis and average quantities of ^{150}Nd. In the second part, the determined PSF is discussed and compared to results obtained using complementary experimental probes.

6.1. Discussion for ^{150}Nd

In this section, the experimental results for both ^{150}Nd experiments are addressed. After a discussion of the state-to-state analysis, the extracted average quantities are discussed, including a geometrical and statistical interpretation of the data.

6.1.1. State-to-state analysis

Energy-integrated cross sections

In Fig. 6.1, the energy-integrated cross sections for ground-state transitions $I_{s,0}$ obtained at DHIPS are shown. Depicted parity quantum numbers are taken from the results of the HIγS experiment. In addition, the ratio between the experimental results for the presented experiment and the experiment performed by Pitz *et al.* [260] are shown. Similar to the DHIPS experiment, the Pitz experiment used a bremsstrahlung photon beam provided by the Stuttgart Dynamitron accelerator [284]. At higher excitation energies, there is no significant deviation between the experimental results for both works. For lower excitation energies, the results of the presented experiment are significantly larger. Feeding transitions from higher-lying states populate the
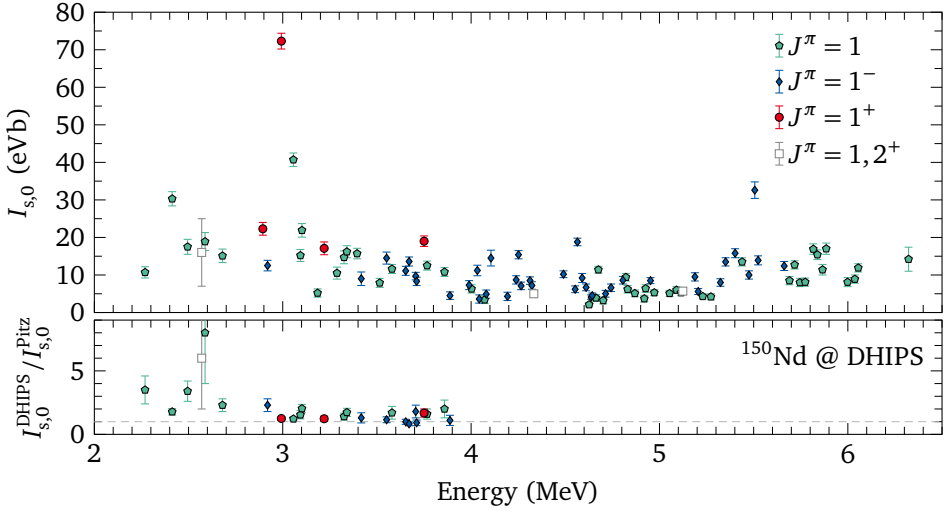
Figure 6.1.: Energy-integrated cross sections $I_{s,0}$ of ^{150}Nd states (top panel). The bottom panel shows the ratio of the present values to the values by Pitz *et al.* [260]. Above 3 MeV the ratio is close to one, indicating agreement of both experiments within their uncertainties. For lower excitation energies, larger cross sections in the present work suggest contributions from feeding transitions.

states at lower excitation energies, resulting in larger peak areas. The Pitz experiment used a lower e$^-$-beam energy of $E_{\text{endpoint}} = 4.1$ MeV, such that fewer contributions from feeding transitions are expected. In addition, the Pitz experiment had a higher photon flux, resulting in smaller statistical uncertainties. Therefore, below 4 MeV, the results of the Pitz experiment should take precedence over the results of this work for $I_{s,0}$.

Angular momentum quantum numbers

For the determination of the angular momentum of excited states, the intensity ratio

$$w = \frac{N(\vartheta = 90°)}{N(\vartheta = 130°)} \tag{6.1}$$
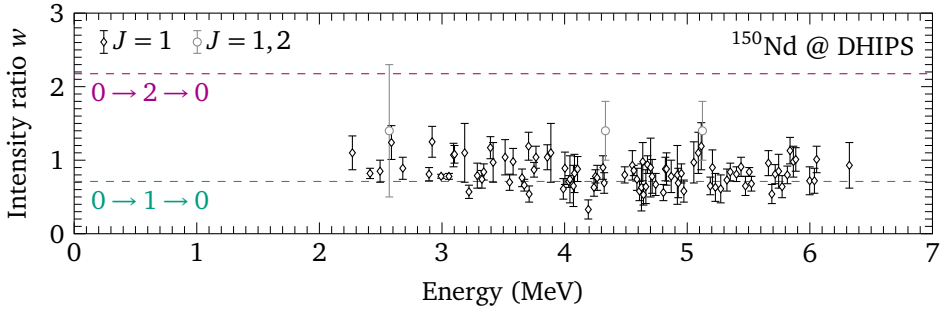
Figure 6.2.: Intensity ratios w (see Eq. (6.1)) of ^{150}Nd ground-state transitions at DHIPS. The dashed lines indicate the nominal values for $J = 1$ (teal) and $J = 2$ states (purple) obtained using GEANT4 simulations. For almost all observed transitions, a firm assignment of $J = 1$ is possible (black diamonds). In some cases (gray circles), the sensitivity is not sufficient to assign an angular momentum quantum number to the excited states.

was calculated, depicted in Fig. 6.2. Here, $N(\vartheta)$ refers to the efficiency-corrected peak volume observed with an HPGe detector at the azimuthal angle ϑ. In addition, simulation results for $0 \to 1 \to 0$ and $0 \to 2 \to 0$ cascades are shown, also taking into account geometrical effects because of the finite detector size. Without the geometrical effects (i.e., for point-like detectors), intensity ratios of approximately 0.71 and 2.26 are expected for $J = 1$ and $J = 2$ ground-state transitions, respectively. It can be seen that for almost all states, a firm assignment of $J = 1$ was possible. In some cases, the statistics were not sufficient to assign an angular momentum quantum number. Not a single state with a firm $J = 2$ assignment was observed.

Parity quantum numbers

For the analysis of parity quantum numbers, the linearly polarized HIγS beam was utilized. From the angular distribution of the decay of excited states, information about parity quantum numbers was inferred. Several factors complicated the identification and analysis of individual spectral lines at HIγS: Operating the FEL in high-resolution mode results in a reduction of photon flux and thus statistics by about one order of
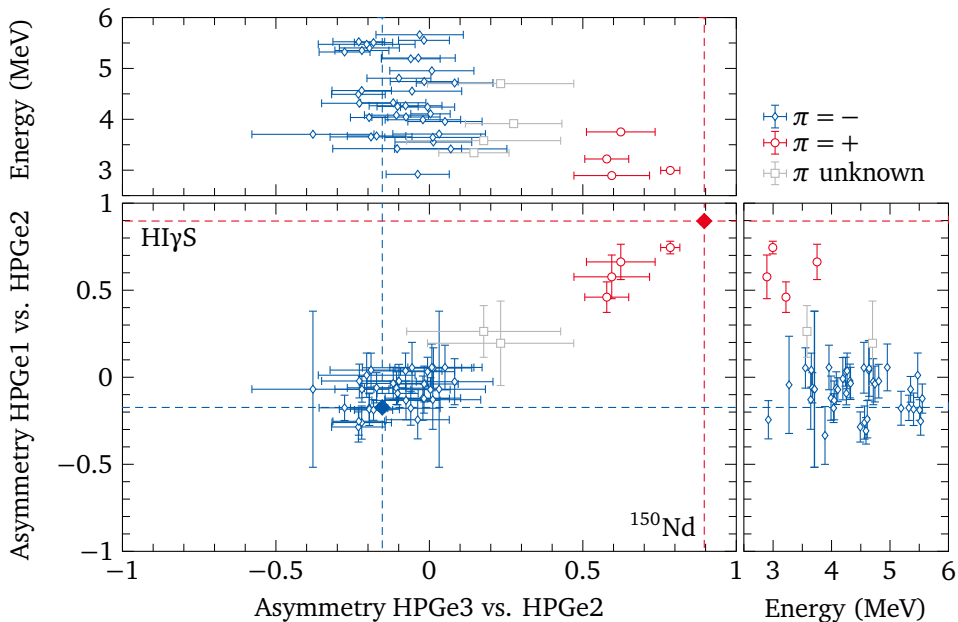
Figure 6.3.: Asymmetries ϵ of efficiency-corrected peak volumes for states identified at HIγS. The blue and red filled diamonds and dashed lines indicate the simulated asymmetries $q\Sigma$ for 1^- (parity quantum number $\pi = -$) and 1^+ ($\pi = +$) ground-state excitations, respectively. The color of the data points indicates the parity quantum number assignment of the respective state. For gray data points, no parity quantum number assignment was possible.

magnitude. Common NLD models provided by Capote *et al.* [81] indicate, that the low spacing of levels $\frac{1}{\rho}$ (see Section 1.3.1, especially Eq. (1.10)) for ^{150}Nd surpasses the detector resolution already at low energies. At 5 MeV, the average level spacing of 1^- states is around 2 keV. The low resolution of detector HPGe4 (approximately 15 keV instead of 5 keV observed for the other HPGe detectors), attributed to vacuum-leak issues, worsened this problem. Despite the expected NLD, individual peaks were still resolved. However, in multiple cases, non-Gaussian peak shapes and increased peak widths indicated that the observed concentration of excitation strength cannot be

attributed to single spectral lines but instead originates from a cluster of unresolved spectral lines.

Figure 6.3 depicts the asymmetry

$$\epsilon_{a,b} = \frac{N_a - N_b}{N_a + N_b} = q\Sigma \tag{6.2}$$

between two detectors a and b for ground-state transitions observed at HIγS, with the efficiency-corrected peak areas N_a, N_b. The analyzing power

$$\Sigma = \frac{W(\vartheta_a, \varphi_a) - W(\vartheta_b, \varphi_b)}{W(\vartheta_a, \varphi_a) + W(\vartheta_b, \varphi_b)} \tag{6.3}$$

is a measure of the sensitivity to the parity quantum number of excited states, excluding geometrical effects due to the finite detector size accounted for by the geometrical factor q. Preferably, the asymmetry ϵ is calculated for the two HPGe detectors parallel (a = HPGe4) and perpendicular (b = HPGe2) to the polarization plane at $\vartheta = 90°$, resulting in analyzing powers of $\Sigma = \pm 1$ for excited $1^\pm$ states. Because HPGe4 did not resolve individual transitions, asymmetries in comparison to detectors at backward angles ($\vartheta = 135°$) are shown instead. The product $q\Sigma$ is denoted by dashed lines and diamonds for $0^+ \to 1^\pm \to 0^+$ transitions in Fig. 6.3. In almost all cases, uncertainties allow for the assignment of parity quantum numbers, with most excited states having negative parity quantum numbers. A systematic deviation between the measured ϵ and expected asymmetry ($q\Sigma$) can be observed for the excited 1^+ states.

6.1.2. Average quantities

Elastic cross sections

The results of the analysis of average quantities are listed in Table 5.2. For each beam-energy setting, characterized by a centroid energy E_{beam} and FWHM, the photon-scattering cross section $\sigma_{\gamma\gamma} = \sigma_{\gamma\gamma}^{E1} + \sigma_{\gamma\gamma}^{M1}$ is given, including its decomposition into $E1$ and $M1$ strength. The experimental results for the elastic cross sections of ^{150}Nd $\sigma_{\gamma\gamma} = \sigma_{\gamma\gamma}^{E1} + \sigma_{\gamma\gamma}^{M1}$ are depicted in Fig. 6.4. To estimate the amount of the observed strength that originates from unobserved transitions, the energy-integrated cross
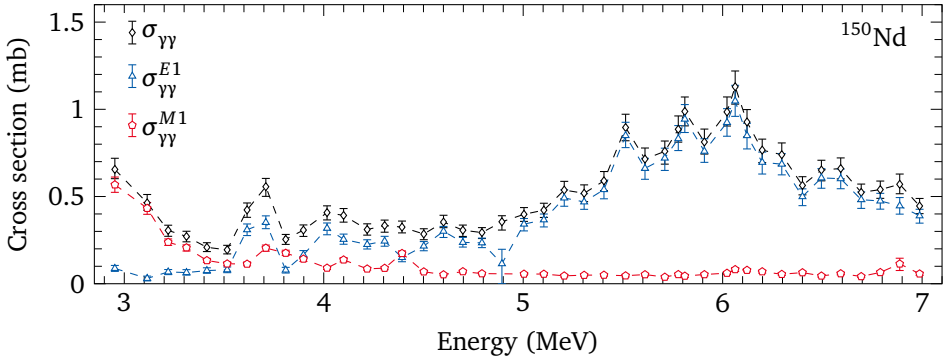
Figure 6.4.: Average photon-scattering cross sections for ^{150}Nd are shown, including a decomposition into $E1$ and $M1$ strength. The $E1$ strength has been corrected for Thomson-scattering contributions, such that only NRF is taken into account.

sections for all states listed in Table 5.1 were multiplied with the relative intensity of the photon beam for each beam energy. By summing over all intensity-weighted states for each beam energy, the elastic cross section from resolved states $\sigma_{\gamma\gamma}^{\text{peaks}}$ was extracted, shown in Fig. 6.5. The ratio of resolved to total strength decreases with excitation energy and increasing NLD. Still, between 5 MeV to 6 MeV, around a third of the total strength can be attributed to observed transitions. For higher excitation energies, the ratio of resolved strength drops to almost zero.

Average branching ratios

The average branching ratios as defined by Eq. (5.1) and listed in Table 5.2 are depicted in Fig. 6.6. For excitation energies above 4 MeV, $E1$ transition strength is found to dominate both the decay to the 0_1^+ state (see Fig. 6.5) and 2_1^+ state. Because of the limited statistics for $M1$ transition strength, corresponding to the decay of excited 1^+ states to both the 0_1^+ and 2_1^+ state, $\langle R_{\text{exp}}^{M1} \rangle$ values can only be given as 2σ-upper limits. For the average $E1$ branching ratios, there is no obvious relationship between the observed values and the excitation energy. Above 4 MeV, no distinct trend is discernible, and the $\langle R_{\text{exp}} \rangle$ values scatter around a value of approximately 0.5. For lower excitation energies, the determined $\langle R_{\text{exp}} \rangle$ values fluctuate strongly, and
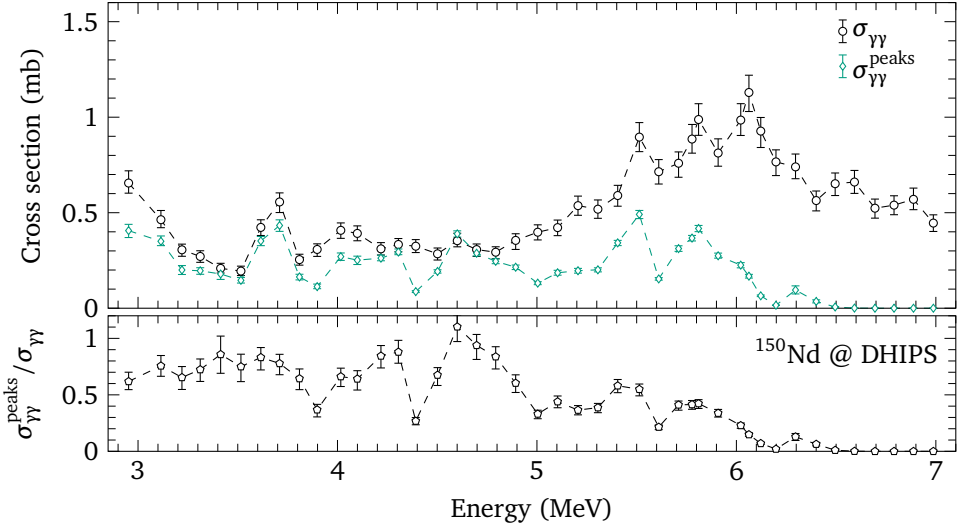
Figure 6.5.: Comparison of resolved and total average cross sections for ^{150}Nd. The top panel depicts the resolved and total elastic cross sections, the bottom panel depicts the ratio of the two values. At lower excitation energies, almost all the observed strength can be attributed to resolved transitions. Above 6 MeV, almost no transitions are resolved because of large NLDs and a strong fragmentation of strength.

the uncertainties are large. The fluctuations are an artifact of the used fit procedure (see Section 4.1.5), which assumes that the observed strength is distributed uniformly across the excited energy region. This assumption is violated because of the low level density at low excitation energies. Therefore, a reliable interpretation of these data points is not possible.

For energies above 4 MeV, an average value for R_{exp} was determined using a Bayesian approach. To account for the fluctuations, the variance σ^2 of the data points was assumed to be unknown and inverse-gamma distributed (which is the conjugate prior distribution of the normal-distributed variance). After integrating out σ^2, the Student's t-distribution with a degree of freedom ν was obtained (e.g., see Ref. [265], Appendix A). An average value of $\langle\langle R_{\mathrm{exp}}\rangle\rangle = 0.481(17)$ was determined.
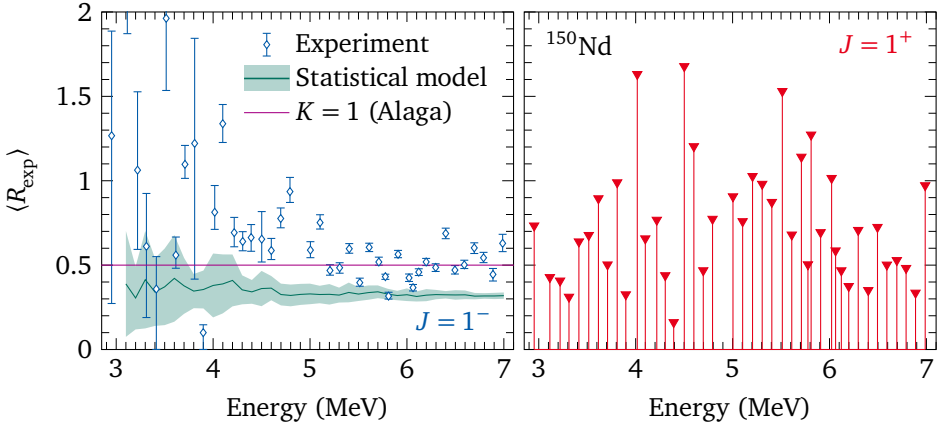
Figure 6.6.: Mean R_{exp} for ^{150}Nd. For $J = 1^-$ (left panel), strong fluctuations and large uncertainties are observed for lower excitation energies up to around 4 MeV because of limitations of the fit-based method. The data points above 4 MeV, $\langle R_{exp} \rangle$ fluctuate around a value of about 0.5. For comparison, the Alaga rule prediction for $K = 1$ and a DICEBOX statistical model simulation are shown. A good agreement between the experiment (green) and Alaga rule (purple) is observed above 5 MeV. For a discussion of the implications for the statistical model, see text. For $J = 1^+$ (right panel), only 2σ-upper limits are provided, because of a lack of statistics and sensitivity for $M1$ transition strength.

6.1.3. Geometrical interpretation

The resulting value for $\langle\langle R_{exp} \rangle\rangle$ is close to 0.5, which, according to Alaga rules, corresponds to $K = 1$, i.e., transversal vibrations with respect to the nucleus' symmetry axis. When only taking into account data points above 5 MeV, a value of $\langle\langle R_{exp} \rangle\rangle = 0.489(16)$ is obtained, which agrees with 0.5 within its 1σ-uncertainty. The experimental values scatter by about ± 0.2 around 0.5. No obvious energy dependency can be identified. For a K-splitting of the PDR, values for R_{exp} between 0.0 and 2.0 are expected, depending on the mixing between the two configurations [285, 286]. In a simplified picture not taking into account mixing, a transition from 0.5 to 2.0 would be expected. This is a simplified assumption, neglecting multi-shape mixing, which can alter the branching ratios. Hence, the experimental results indicate, that

no K-splitting of the PDR occurs below the neutron-separation threshold for ^{150}Nd.

Yoshida and Nakatsukasa [70, 71] performed theoretical calculations for ^{150}Nd. They used a non-empirical Skyrme EDF approach with a QRPA on top of HFB ground states to calculate the $E1$ response of Nd and Sm isotopes in the rare-earth shape-phase transitional region of the chart of nuclides. Their results for ^{150}Nd indicate that a majority of $K = 0$ $E1$ strength occurs above 7 MeV (c.f. Fig. 4 in Ref. [70]). For the energy range of 4 MeV to 7 MeV studied in the present work, the calculated $K = 1$ strength is found to dominate strongly because of the observed $\langle R_{\text{exp}} \rangle$ value of approximately 0.5. The observed lack of $K = 0$ strength for the theoretical calculation is in agreement with the results of this work.

6.1.4. Statistical interpretation

Instead of a geometrical interpretation, one can also discuss the statistics of the observed decays in the Hauser-Feshbach model [79]. For this purpose, a statistical model simulation was performed using a modified version of the DICEBOX [287] code adjusted for the NRF reaction. The simulation is performed in two stages: In the first stage, the level scheme is built. At low excitation energies, the level scheme is initialized using the energies and branching ratios known from the literature. For the present work, the twelve lowest-lying levels of ^{150}Nd were taken from Ref. [92]. On top of those levels, a level scheme is generated based on a NLD model. For the present work, a BSFG model with parameters $E_1 = -0.516$ MeV and $a = 16.275$ MeV^{-1} taken from Ref. [89] was used (depicted in Fig. 1.2). The generated level scheme takes into account the repulsion of levels described by the Wigner distribution [99, 107]. In the second stage, the NRF reaction is simulated. The excitation and subsequent decay of states in NRF reactions is simulated according to a PSF model, taking into account the PT distribution. For the present work, the sampled PSF consisted of the IVGDR, which was parametrized according to Ref. [76] as a SLO, the scissors and spin-flip resonance modeled according to Ref. [288] using the simplified modified Lorentzian (SMLO) model, and a small $E2$ contribution from single-particle interactions. The PDR was not part of the statistical model simulation.

The simulation was performed for each beam-energy setting for the energy range excited by the photon beam, and repeated for a total 30 realizations per beam-energy setting for uncertainty quantification related to PT fluctuations. The results of the

simulation were analyzed in the same way as the experimental results. In particular, the average branching ratio

$$\langle R_{\text{exp}}\rangle = \frac{\langle\Gamma_0\frac{\Gamma_2}{\Gamma}\rangle}{\langle\Gamma_0\frac{\Gamma_0}{\Gamma}\rangle}\frac{E_\gamma\left(0_1^+\right)^3}{E_\gamma\left(2_1^+\right)^3} \tag{6.4}$$

was determined. For $J = 1^-$ states, it is depicted in Fig. 6.6 (left panel), which shows the experimental results, the statistical model simulation, and the Alaga rule prediction for $K = 1$. The statistical model simulation predicts an approximately constant $\langle R_{\text{exp}}\rangle \approx 0.31$, with an uncertainty that decreases for higher energies. This value is significantly smaller than the experimental result of $\langle\langle R_{\text{exp}}\rangle\rangle = 0.481(17)$.

To investigate the discrepancy between the experimental result and the simulation, Eq. (6.4) must be examined more closely. The simulated value of ~ 0.31 for Eq. (6.4) deviates from the result that is obtained from the non-averaged definition of R_{exp} in Eq. (2.11). Because of the low energy of the 2_1^+ state of 130 keV, the energy difference between decays to the 0_1^+ and 2_1^+ state is small, i.e., $E_\gamma\left(0_1^+\right)^3 \approx E_\gamma\left(2_1^+\right)^3$. For the same reason, the average partial transition widths $\langle\Gamma_0\rangle$ and $\langle\Gamma_2\rangle$ are approximately equal, because they are determined by the PSF, which does not change significantly within 130 keV, at the respective γ-ray energy, Naively substituting Γ_0 with Γ_2 in Eq. (6.4) in analogy to Eq. (2.11), one expects $\langle R_{\text{exp}}\rangle$ to be equal to approximately unity, which conflicts with the results of the statistical model simulation. Next, the average branching ratio will be examined more carfully, incorporating the statistical correlation of partial transition widths from the underlying statistical distribution.

Internal fluctuation ratio

A closer look at the average ratio

$$\frac{\langle\Gamma_0\frac{\Gamma_2}{\Gamma}\rangle}{\langle\Gamma_0\frac{\Gamma_0}{\Gamma}\rangle} \equiv \frac{\sum_{i=0}^{M}\Gamma_{i\to0}\frac{\Gamma_{i\to2}}{\Gamma_i}}{\sum_{i=0}^{M}\Gamma_{i\to0}\frac{\Gamma_{i\to0}}{\Gamma_i}} \tag{6.5}$$

has to be taken, which is the average branching ratio $\langle R_{\text{exp}}\rangle$ from Eq. (6.4) without the energy-weighting factor. In other words, this quantity refers to the average ratio

of partial transition widths instead of reduced transition probabilities. The index i sums over all states J_i in the excited energy region. The quantities in angled brackets $\langle \Gamma_0 \rangle$, $\langle \Gamma_2 \rangle$, and $\langle \Gamma \rangle$, refer to the average partial transition widths to the ground state, the 2_1^+ state, and to the average total transition width, respectively. The quantities $\Gamma_{i\rightarrow 0}$, $\Gamma_{i\rightarrow 2}$, and Γ_i, are the corresponding partial and total transition widths of an individual state J_i. The values for individual transitions are assumed to fluctuate around the average value according to some distribution f_i and g_i:

$$\Gamma_{i\rightarrow 0} = \langle \Gamma_0 \rangle \cdot f_i, \qquad \Gamma_{i\rightarrow 2} = \langle \Gamma_2 \rangle \cdot f_i', \qquad \Gamma_i = \langle \Gamma \rangle \cdot g_i. \tag{6.6}$$

Inserting these relations into Eq. (6.5) yields

$$\frac{\sum_{i=0}^{M} \Gamma_{i\rightarrow 0} \dfrac{\Gamma_{i\rightarrow 2}}{\Gamma_i}}{\sum_{i=0}^{M} \Gamma_{i\rightarrow 0} \dfrac{\Gamma_{i\rightarrow 0}}{\Gamma_i}} = \frac{\sum_{i=0}^{M} \langle \Gamma_0 \rangle f_i \cdot \langle \Gamma_2 \rangle f_i' / \langle \Gamma \rangle g_i}{\sum_{i=0}^{M} \langle \Gamma_0 \rangle f_i \cdot \langle \Gamma_0 \rangle f_i / \langle \Gamma \rangle g_i} = \frac{\langle \Gamma_2 \rangle}{\langle \Gamma_0 \rangle} \frac{\sum_{i=0}^{M} f_i \cdot f_i' / g_i}{\sum_{i=0}^{M} f_i \cdot f_i / g_i} \equiv \frac{\langle \Gamma_2 \rangle}{\langle \Gamma_0 \rangle} \cdot s. \tag{6.7}$$

Assuming χ^2-distributed partial transition widths, the total transition widths are Gaussian-distributed, i.e.,

$$f_i \sim \chi^2(\nu), \quad f_i' \sim \chi^2(\nu), \quad g_i \sim \frac{1}{N}\sum_{j=0}^{N} \chi^2(\nu) \xrightarrow{N\rightarrow\infty} \mathcal{N}(\mu = \nu, \sigma^2 = 2\nu/N). \tag{6.8}$$

Here, N refers to the number of partial transition widths contributing to Γ_i. Thus, the statistical factor s only depends on the degree of freedom ν of the $\chi^2(\nu)$ distribution. In the following, a generalization of the χ^2 distribution for $\nu \in \mathbb{R}^+$ based on the gamma distribution is used. In its limit definition, g_i is statistically independent of f_i and f_i', which follows directly from the central limit theorem. Using (a) the central limit theorem and (b) the independence of f_i, f_i', and g_i for different i, its expectation value $\mathrm{E}[s]$ is calculated as

$$\mathrm{E}[s] \equiv \mathrm{E}\left[\frac{\sum_i f_i \cdot f_i'/g_i}{\sum_i f_i \cdot f_i/g_i}\right] \overset{\text{(a)}}{=} \frac{\sum_i \mathrm{E}[f_i \cdot f_i'/g_i]}{\sum_i \mathrm{E}[f_i \cdot f_i/g_i]} \overset{\text{(b)}}{=} \frac{M \,\mathrm{E}[f \cdot f'/g]}{M \,\mathrm{E}[f \cdot f/g]} = \frac{\mathrm{E}[f \cdot f'/g]}{\mathrm{E}[f \cdot f/g]}. \tag{6.9}$$

The contribution from $g \sim \mathcal{N}(\mu, \sigma^2)$, which is present in both the expectation value of the nominator and the denominator, is approximately constant, as its variance
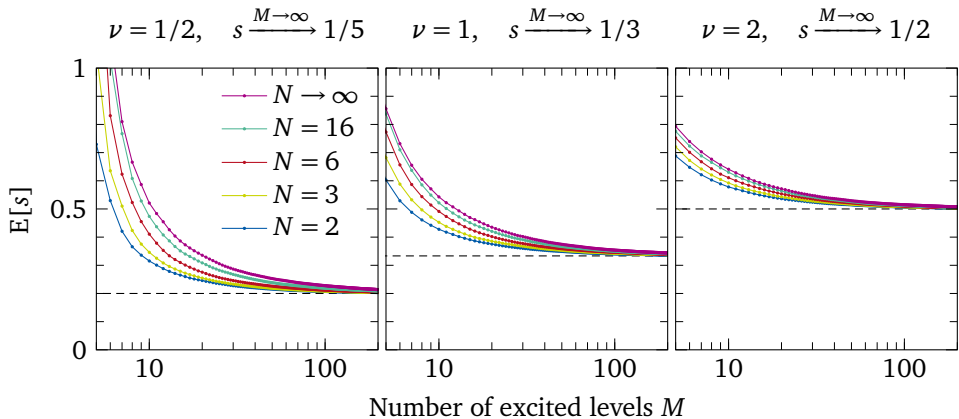
Figure 6.7.: Convergence of the expectation value E[s] of the internal fluctuation ratio s as a function of the number of excited levels M and the number of partial transition widths N that contribute to $\langle \Gamma \rangle$. The degree of freedom ν and the limit of the internal fluctuation ratio s for large M are given above each panel.

$\sigma^2 = 2\nu/N$ decreases with increasing number N of transitions to lower-lying states. Instead, the simplified expression

$$E[s] = \frac{E\left[f \cdot f'\right]}{E\left[f \cdot f\right]} \tag{6.10}$$

is calculated.

The nominator is a product of two independent random variables that can be separated, i.e., $E\left[f \cdot f'\right] = E[f] \cdot E[f'] = \nu^2$, using $E[f] = \nu$ for the χ^2 distribution. The denominator is the expectation value of the square of a random variable, which is (c) equivalent to its second moment. Given the PDF of the $\chi^2(\nu)$ distribution

$$f_{\chi^2}(x \mid \nu) = \frac{1}{2^{\nu/2}\Gamma(\nu/2)}x^{\nu/2-1}\exp(-\nu/2), \tag{6.11}$$

with the gamma function $\Gamma(x)$, the expectation value can be calculated using

$$\mathrm{E}\left[f\cdot f\right] \overset{(c)}{=} \int_0^\infty x^2 f_{\chi^2}(x\mid\nu)\,\mathrm{d}x \equiv \int_0^\infty x^2 \frac{1}{2^{\nu/2}\Gamma(\nu/2)} x^{\nu/2-1}\exp(-\nu/2)\,\mathrm{d}x \quad (6.12)$$

$$= \frac{4\Gamma(\nu/2+2)}{\Gamma(\nu/2)} \overset{(d)}{=} 2\nu(\nu/2+1) = \nu(\nu+2). \quad (6.13)$$

For (d), $\Gamma(z+1) = z\Gamma(z)$ is used. In conclusion,

$$s = \frac{\mathrm{E}\left[f\cdot f'\right]}{\mathrm{E}\left[f\cdot f\right]} = \frac{\nu^2}{\nu(\nu+2)} = \frac{\nu}{\nu+2} \qquad \Leftrightarrow \qquad \nu = \frac{2s}{1-s}, \quad (6.14)$$

with the following special cases:

$$s(\nu=0.5) = 1/5, \qquad s(\nu=1) = 1/3, \qquad s(\nu=2) = 1/2. \quad (6.15)$$

The convergence of the statistical factor for different numbers N of partial transition widths and different numbers M of states in the excitation energy region is illustrated in Fig. 6.7. The plot was generated by sampling from the individual probability distributions. If fewer transitions and thus partial transition widths N contribute to $\langle\Gamma\rangle$, the convergence is even faster than for the limit of $N\to\infty$. Thus, even if only $\Gamma = \Gamma_0 + \Gamma_2$, the expectation value $\mathrm{E}[s]$ for the statistical factor s converges for sufficiently large numbers of excited levels M.

As can be seen in Fig. 6.7, if the number of excited states M within an energy region is too small, the expectation value $E[s]$ is larger than its limit for large M. For ^{150}Nd, the internal fluctuation ratio is expected to be converged: Both CT and BSFG NLD model agree that the average level spacing for 1^- states is around $2\,\mathrm{keV}$ for $E = 5\,\mathrm{MeV}$ ($\rho^{1^-}(5\,\mathrm{MeV}) = 500\,\mathrm{MeV}^{-1}$), and decreases to about $0.1\,\mathrm{keV}$ for $E = 7\,\mathrm{MeV}$ ($\rho^{1^-}(7\,\mathrm{MeV}) = 10^4\,\mathrm{MeV}^{-1}$). The NLDs observed in Oslo-method experiments for ^{150}Nd [289] are slightly lower but confirm the order of magnitude. This ensures that s is converged. The statistical model simulation depicted in Fig. 6.6 also takes into account the NLD, such that this effect is already quantified by the simulation and its uncertainties. For higher excitation energies, the NLD increases, and the experimental values should get closer to the limit value for $E[s]$. However, no trend of the average branching ratios can be observed. Thus, this hypothesis can be rejected.

Applying Eq. (6.14) to the experimental result of $s = 0.480(16)$ (which is almost equal to $\langle R_{\mathrm{exp}}\rangle$), a degree of freedom of $\nu = 1.84(12)$ is obtained for ^{150}Nd above $5\,\mathrm{MeV}$.
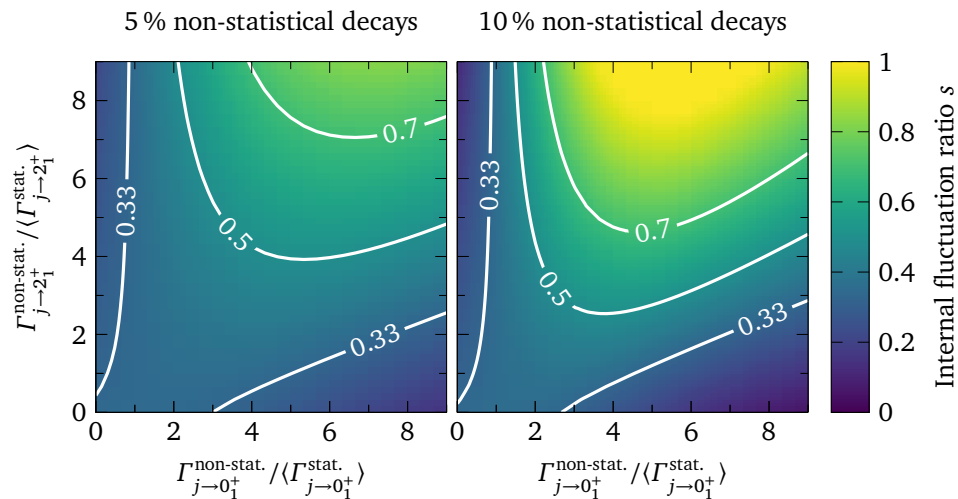
Figure 6.8.: Influence of non-statistical decays on the internal fluctuation ratio s. Depicted are non-statistical admixtures for 5 % (left) and 10 % (right) of all excited states. The partial transition widths of non-statistical decays to the 0_1^+ and 2_1^+ states (x and y axes) are given in comparison to the average value of partial transitions widths according to the PT distribution.

This value is significantly larger than $\nu = 1$ and does not agree with the PT distribution. It is much closer to the prediction of $\nu = 2$ for a GUE Hamiltonian than to the $\nu = 1$ prediction of a GOE Hamiltonian. However, the presumed violation of time-reversal symmetry for the GUE Hamiltonian seems unlikely, as it is in conflict with reciprocity and detailed balance, and would result in a different Γ_i for absorption and emission. Therefore, the GUE Hamiltonian is usually not considered to be applicable to nuclear physics, and also constrained by strong experimental upper limits (e.g., see Chap. 1-2c in Ref. [21] and references therein)

Instead of a modified degree of freedom ν of the χ^2 distribution, two other explanations for the deviation are possible: The assumption of large level densities could be violated, or strong non-statistical decays could skew the resulting distribution of partial transition widths in a way that cannot be described by the χ^2 distribution.

To study the influence of non-statistical decays, Monte-Carlo simulations were performed, sampling s as defined in Eq. (6.7) for modified variants of the χ^2 distribution. This modified distribution consisted of a statistical part, which followed the PT distribution, and a non-statistical part affecting 10 % of all states. The resulting fluctuation ratio s changes very little ($\lesssim 5\%$) if the non-statistical part assumes partial transition widths that are systematically smaller than the PT-distributed transition. The same behavior is observed if the non-statistical effect applies only to one of the Γ_0 or the Γ_2 transition width. Only if both the Γ_0 and Γ_2 transition width take on values that are systematically larger than the mean value of the χ^2 distribution, the internal fluctuation ratio s increases significantly. For example, if 10 % of all states take on values of $\Gamma_0 = 3\langle\Gamma_0\rangle$ and $\Gamma_2 = 3\langle\Gamma_2\rangle$, a fluctuation ratio of $s \approx 0.50$ is determined. In this case, the non-statistical partial transition widths contribute about 29 % to the sum of all partial transition widths for the transition to the 0_1^+ or 2_1^+ state, respectively. If instead $\Gamma_0 = 6\langle\Gamma_0\rangle$ is used, i.e., $\Gamma_2/\Gamma_0 = 1/2$, the resulting fluctuation ratio s is approximately 0.51. In Fig. 6.8, the internal fluctuation ratio s is depicted for different combinations of non-statistical partial transition widths Γ_0, and Γ_2, assuming that 5 % or 10 % of all states do not decay according to the PT distribution. It can be seen that the observed internal fluctuation ratio s can only be explained, if both the non-statistical decays to the 0_1^+ state and the 2_1^+ state are significantly stronger than the average of the distribution.

The results of the Monte-Carlo simulation highlight that a few (10 %) non-statistical decays can significantly alter the obtained internal fluctuation ratio s. One indication for non-statistical decays is the ratio of the elastic cross section of resolved peaks $\sigma_{\gamma\gamma}^{\text{peaks}}$ to the total elastic cross section $\sigma_{\gamma\gamma}$, shown in Fig. 6.5. As can be seen, above 6 MeV, almost no strength is attributed to individual transitions. However, the lack of observed individual transitions is primarily a result of the high NLDs for high photon beam energies. Thus, no conclusive assessment of the contribution of non-statistical transitions to the internal fluctuation ratio s is possible.

6.2. Photon strength function of ^{96}Mo

In the following section, the results for the downward PSFs of ^{96}Mo obtained using $\gamma\gamma$ coincidences are discussed. The extracted MAW interpolation is described, statistical

fluctuations are quantified, and the results are compared with literature data from experiments using complementary probes.

6.2.1. PSF data points

Figure 6.9 depicts the PSFs for each photon beam energy after applying the scaling procedure. The resulting combined PSF increases exponentially with γ-ray energy. This exponential increase is observed both for the individual PSFs, but especially for the combined PSF. For low beam energies of less than 5.5 MeV, the PSFs no longer exhibit the exponential shape and start to fluctuate strongly. The general lack of statistics for primary decays into most of the low-lying 2^+ states results in large statistical uncertainties for the data points. Still, especially decays into the 2_2^+ and 2_3^+ states contain significant statistics, and the primary decays into these states is larger than the observed branching into the 2_1^+ state for low beam energies.

These fluctuations could be explained if the assumption that primarily 1^- states are excited is violated. In a preliminary state-to-state analysis [290] of the dataset, a 2^+ state at 5096 keV was identified. A further concentration of 2^+ states was observed below 4.4 MeV. Depending on the strength of these states, which is yet to be determined, and the strength of potentially unobserved 1^+ and 2^+ states, the observed average branching ratios could be altered significantly.

At higher beam energies, it can be seen that some systematic effects are visible for decays to higher-lying 2^+ states. For example, decays into the 2_7^+ have a tendency to be consistently stronger than decays to other low-lying 2^+ states for the same photon beam energy. Conversely, decays to the 2_5^+ state tend to be smaller than average in comparison to decays to other low-lying 2^+ states. In both cases, the statistical uncertainties are large, however, the systematic deviation of all data points for decays to a particular low-lying 2^+ state hints at some underlying effect responsible for this discrepancy. A simple explanation could be problems with the energy gates that were used to extract the corresponding primary decays. Indeed, the $2_7^+ \rightarrow 2_1^+$ transition is only 38 keV higher in energy than the decay of a (0^+) state to the 2_1^+ state (see also the discussion in Section 4.2.4). Together with the increased PSF values, it is concluded that the LaBr$_3$-detector energy gate for the $2_7^+ \rightarrow 2_1^+$ transition also contains decays to the (0^+) state at 2749 keV. Another possibility for a systematic deviation arises if the branching ratio of the observed decay(s) of the low-lying 2^+ state, which is
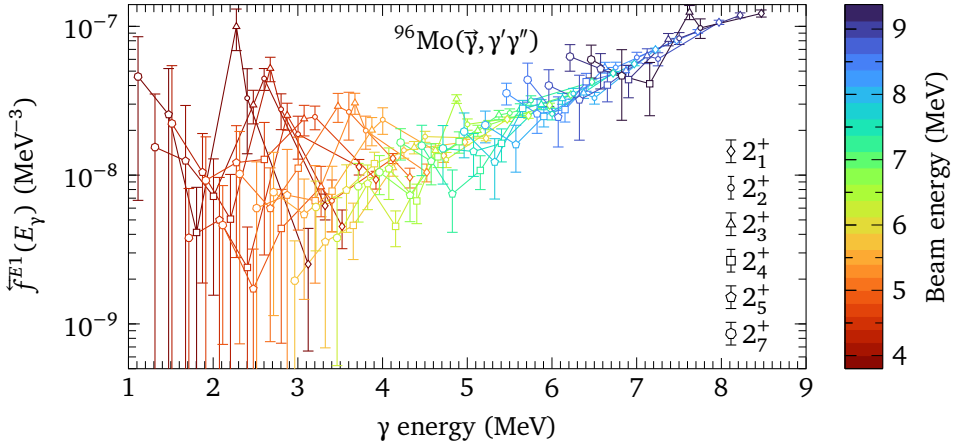
Figure 6.9.: PSFs of ^{96}Mo for each beam energy after the scaling procedure is applied. The marker shape indicates the low-lying 2^+ state the data point corresponds to. The absolute scale was determined by scaling an interpolation of the data for beam energies above 5.5 MeV to the ^{96}Mo(p,p'γ) Oslo-method data [146].

required for the normalization of the corresponding decays, is incorrect or incomplete. However, for both the 2_5^+ and 2_7^+ state, branching ratios with relative intensities of less than 5 % are reported in the literature [91], indicating that the knowledge of branching transitions is fairly complete, ruling out this explanation.

6.2.2. Interpolation of the PSF

The data was divided into two subsets of data: One containing the PSF data for all beam energies, and another one with the data restricted to beam energies of 5.5 MeV and above. A MAW interpolation as described in Section 4.2.6 was determined for both datasets, henceforth referred to as full MAW and restricted MAW. The results are shown in Fig. 6.10. For the restricted MAW, the PSF increases approximately exponentially with γ energy. The same behavior is observed for the full MAW above γ energies of 4 MeV. At lower energies, the full MAW deviates from the restricted MAW, and flattens out, before forming a pronounced peak around 2 MeV to 3 MeV. This peak
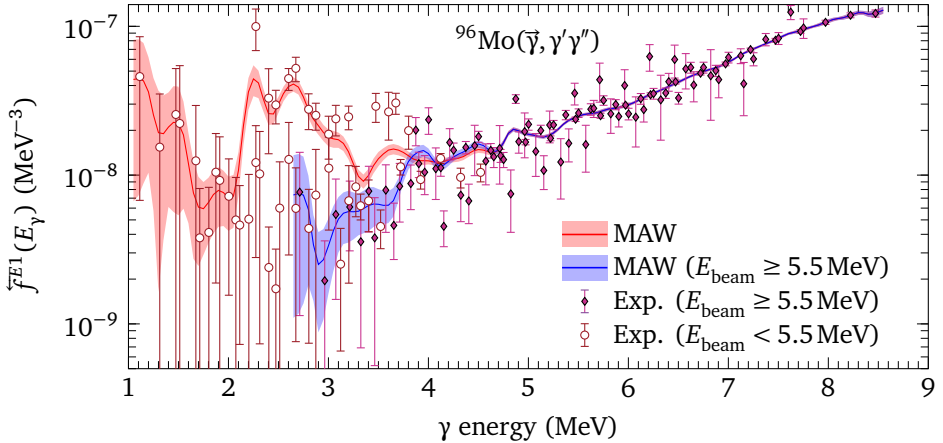
Figure 6.10.: MAW interpolations of the PSF of ^{96}Mo. The blue MAW curve was determined using data points for beam energies above 5.5 MeV (purple diamond data points). The red MAW curve takes into account all data points (green and purple diamond data points). The absolute scale was determined by scaling the blue MAW curve to the ^{96}Mo(p, p'γ) data from Ref. [146].

arises because of the strong primary transitions into the 2_2^+ and 2_3^+ states found in this energy region, but significantly deviates from the general downward trend observed for transitions into other low-lying 2^+ states. In contrast, for the restricted MAW, the data points scatter symmetrically around the curve, and the magnitude of the deviation of individual data points scales with the respective uncertainty. Therefore, in the following, only the restricted MAW (simply referred to as MAW) will be discussed.

6.2.3. PSFs for decays to 0^+, 1^+, and 3^+ states

Using the same scaling factors s_j as determined for the 2^+ PSFs, the primary decays to other low-lying states observed in coincidences can be scaled to obtain the PSFs built on top of further low-lying states. The results can be seen in Fig. 6.11 for the 0_2^+ and 3_1^+ states, and for two 1^+ states. The PSFs on top of 0^+ and 1^+ states are also dominated by $E1$ transition strength (and in case of 0^+, of pure $E1$ character).
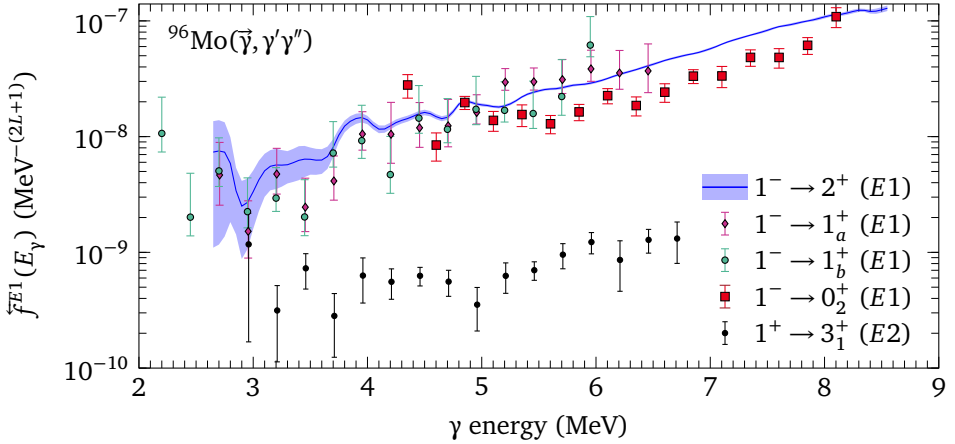
Figure 6.11.: Comparison of PSFs built on top of $0^+, 1^+, 2^+$ and 3^+ states. For observed decays into 2^+ states, the determined MAW is shown. In all cases, only beam energies above 5.5 MeV were taken into consideration. $E1$ PSFs are given in units of MeV^{-3}, the $E2$ PSF is given in units of MeV^{-5}. The absolute scale was determined by scaling the 2^+ MAW curve to the $^{96}\text{Mo}(\text{p},\text{p}'\gamma)$ data from Ref. [146]. The PSFs on top of 1^+_a at 2794 keV and on top of 1^+_b at 3300 keV were scaled to the 2^+ PSF to account for unknown branching transitions of the 1^+ states required for the normalization of the observed primary transitions.

Thus, according to the Brink-Axel hypothesis, the corresponding $E1$ PSFs should be equivalent to the $E1$ PSF determined for the 2^+ states.

PSF for decays to the 0^+_2 state

For the 0^+_2 PSF, the slope is consistent with the 2^+ PSF, except for two data points at low γ energies, and for the highest photon beam energy. However, the overall scale of the 0^+_2 PSF is reduced by a factor of about two. It was not possible to gate on the decay of the 0^+_2 state in LaBr_3 detectors because of limitations of the DAQ system. Thus, in contrast to the 2^+ PSF, LaBr_3-LaBr_3 coincidences could not be considered. The restriction on a subset of detectors could have resulted in systematic deviations.

Still, a scaling factor of almost two is surprisingly pronounced and can not be purely explained by systematic effects of the applied method.

The existence of low-lying 0^+ states in even-even nuclei is often interpreted as an indication for shape coexistence [291, 292]. For the Mo isotopic chain, the energy of the 0_2^+ state decreases with increasing mass number until ^{98}Mo. The implications for the Mo and Zr isotopic chains are discussed in Refs. [279, 293–295]. For ^{98}Mo and ^{100}Mo, Rusev *et al.* [294] observed the decay of $J = 1$ states with energies of 3 MeV to 4 MeV into both the 0_1^+ and 0_2^+ state with approximately equal intensities, which they attribute to the mixing of two 0^+ states with moderately different deformations. The authors assume positive parity quantum numbers, i.e., $J = 1^+$, for the observed states, however, they note that the model also holds for negative parity quantum numbers. Only one and two out of several observed $J = 1$ states decay into the 0_2^+ state for ^{98}Mo and ^{100}Mo, respectively. These observations highlight that overall, a reduced average branching into the 0_2^+ state is expected, even in the presence of strong configuration mixing. Ultimately, these nuclear-structure-related considerations are in conflict with the Brink-Axel hypothesis, which treats transitions as a purely statistical phenomenon.

PSFs for decays to 1^+ states

Similar observations as for the 0_2^+ PSF are made for decays to the two 1^+ states at 2794 keV (1_a^+) and 3300 keV (1_b^+) for the present work. The cross section for decays into these two states is small in comparison to decays to lower-lying states because of the small energy difference between the beam energy region and ~ 3 MeV. Thus, the PSFs for the two 1^+ states have much larger statistical uncertainties. Still, the overall shape of the two 1^+ PSFs agrees very well with the 2^+ PSF, but their scale is reduced. The PSFs for 1^+ states are depicted in Fig. 6.11, however, they are already scaled to the 2^+ PSF, so the different scale has been corrected for. In contrast to the decays to the 0_2^+ state, the observed difference in scale is not unexpected: The 0_2^+ state exclusively decays to the 2_1^+ state, and does not have to be corrected for any other branching transitions. The observed ground-state decay of the two 1^+ states, on the other hand, has to be corrected for the ground-state branching ratio $\Gamma_{j\rightarrow 0}/\Gamma_j$, which is unknown. Thus, the "missing" strength can be attributed to other decays of the 1^+ states to other intermediate states. Assuming the validity of the Brink-Axel hypothesis,

their PSFs should be equivalent to the 2^+ PSF. Thus, by scaling the 1^+ PSFs to the 2^+ PSF, the ground-state branching ratio of these two 1^+ states can be deduced from the scaling factor. Values of $\Gamma_{a\to 0}/\Gamma_a = 0.351(35)$ and $\Gamma_{b\to 0}/\Gamma_b = 0.224(18)$ for the two states 1_a^+ and 1_b^+ are determined, but should be interpreted with care. Figure 6.11 depicts the 1^+ PSFs after being scaled to the 2^+ PSF.

PSF for decays to the 3_1^+ state

Finally, primary decays to the 3_1^+ state are observed. This observation is unexpected, because it conflicts with the assumption used for the extraction of $E1$ PSFs, which assumes the absence of other multipole characters. However, the 3_1^+ state can only be populated directly by $E2$ or $M1$ transitions from 1^+ or 2^+ states. In relativistic proton-scattering experiments [144], an enhanced relative yield of spin-flip strength was observed for the excited energy region. Motivated by this observation and by the general lack of predicted $E2$ strength for the probed γ-ray energy region (see Section 1.2), it was assumed that the transitions into the 3_1^+ state originate exclusively from 1^+ states. Hence, the corresponding PSF is of $E2$ character. As can be seen in Fig. 6.11, its shape is comparatively flat, showing only a slight increase in strength across the probed energy range.

Comparison to literature data

In Fig. 6.12, a comparison of the MAW interpolation of the downward PSF for ^{96}Mo to literature data is shown. In general, a good qualitative agreement is found between the results of this work and the literature data. Between 4 MeV to 8.5 MeV, the slope and general trend of the (p, p′γ) Oslo data, which was used to normalize the results of the present work, is well reproduced. However, the (p, p′γ) Oslo data fluctuates significantly around the MAW, which has a very smooth exponential-like progression. Thus, the resonances identified at 7.04 MeV and 8.19 MeV on top of an extrapolation of the IVGDR in Ref. [146] cannot be reproduced in this work.

The smooth behavior of the MAW can be attributed to the energy width of the photon beams of approximately 4 %, and the widths of the MAW itself of 200 keV
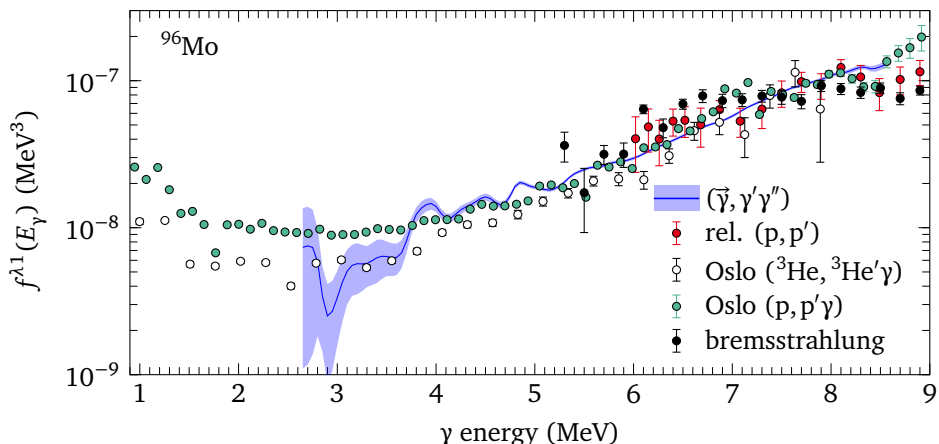
Figure 6.12.: Comparison of the $(\vec{\gamma}, \gamma'\gamma'')$ results for the downward ^{96}Mo PSF (MAW with 5.5 MeV cutoff) with data from relativistic proton-scattering experiments at extreme forward angles [144] (upward PSF), $(^3\text{He}, ^3\text{He}'\gamma)$ [55] and $(p, p'\gamma)$ [146] data obtained using the Oslo method (downward PSF), and bremsstrahlung data [143] (upward PSF),

(FWHM). For a photon beam energy of 7 MeV to 8 MeV, the combined width is approximately 350 keV, which is still significantly smaller than the widths of 1.0(1) MeV and 1.4(2) MeV of the resonances identified in Ref. [146].

Several other differences between the two experimental methods can also account for the observed deviation: The reaction mechanisms are different, which could result in a systematic difference between the properties of excited states. Also, the possible angular momentum quantum numbers of excited states ("spin window") are well-known for the NRF reaction, which primarily excites $J = 1$ states. In Oslo-method experiments, however, states with a wide range of angular momentum quantum numbers are populated. This spin window has to be modeled using the spin-cutoff parameter, resulting in additional uncertainties of the method. Finally, the Oslo-method PSF does not distinguish between an electric and a magnetic radiation character. In contrast, the PSF results of the present work were analyzed under the specific assumption that *only E1* radiation contributed significantly to the resulting PSF. It was found that *E1*

strength dominates for transitions to the 2_1^+ and 2_2^+ states, but the presence of $M1$ strength for other decay branches cannot be excluded.

The (p, p') data [144] allows for the (model-dependent) distinction between $E1$ and $M1$ contributions. Significant spin-flip $M1$ contributions were found around 8 MeV to 9 MeV. Overall, the slope and scale of the (p, p') upward PSF agrees reasonably well with the NRF and Oslo-method results. Again, it fluctuates more strongly than the $\gamma\gamma$-coincidence NRF PSF. In contrast, the bremsstrahlung-NRF measurement [143], which also determined the upward PSF (indirectly, from observations of decays) deviates significantly from the results of any other experimental method. The slope of the determined PSF of the bremsstrahlung measurement is significantly flatter, especially for high photon energies. An even flatter shape of the PSF is observed for other Mo isotopes [143] studied using the same bremsstrahlung method, which is also in conflict with the results for experiments using complementary probes [146]. The limitations and strong model dependency of this method are discussed in Section 1.3.4, which could lead to significant systematic deviations.

Statistical fluctuations of the PSF

A quantitative comparison of other experimental datasets using complementary probes to the MAW PSF of the present work is discussed below. For this purpose, the sum of the inverse-variance weighted squared differences between the two datasets

$$\chi_i^2 = \frac{\left(f_{\text{exp},i}^{\lambda L, \text{p}} - \bar{f}_{\text{MAW},i}^{\lambda L, \text{p}} \right)^2}{\sigma_i^2} \tag{6.16}$$

was calculated, with $\sigma_i^2 = \sigma_{\text{exp},i}^2 + \sigma_{\text{MAW},i}^2 + (\delta f)^2$. Here, $\sigma_{\text{exp},i}$ and $\sigma_{\text{MAW},i}$ are the uncertainties of the experimental and MAW PSF data point, respectively. The uncertainty because of PT fluctuations is taken into account by δf defined in Eq. (1.17). The total deviations are quantified by

$$\chi_{\text{red}}^2 = \frac{1}{N-1} \cdot \sum_i \chi_1^2, \tag{6.17}$$

with the total number of data points N. This method was also applied in Ref. [129]. When comparing two datasets that are normalized to each other, $N-2$ has to be used in the denominator instead.

Without accounting for PT fluctuations, a $\chi^2_{\text{red}} = 2.18$ is determined when comparing the experimental results for the PSF determined from decays to low-lying 2^+ states to the determined MAW PSF. When PT fluctuations are taken into account, this value reduces to $\chi^2_{\text{red}} = 1.11$. A value close to one indicates a reasonably good agreement between the experimental PSF dataset and its MAW interpolation. To estimate the magnitude of the PT fluctuations, Eq. (1.17) is used, which depends on the number of states and thus the NLD in the energy region excited by the photon beam. When more states are excited simultaneously, the fluctuations of average quantities decrease. The NLD was calculated using the CT model with parameters taken from Ref. [89]. The minor deviation can be explained by an underestimated NLD, or if the fluctuations of partial transition widths are stronger than predicted by the PT distribution. For a more thorough comparison, a full statistical model simulation would have to be performed.

When comparing the results of the $(p, p'\gamma)$ Oslo-method experimental data [146] to the MAW PSF in the energy range from around 3 MeV to 8 MeV, without taking PT fluctuations into account, a $\chi^2_{\text{red}} = 18.26$ is determined. The excitation mechanism of the Oslo method differs from NRF experiments, and the spin window is broader and has to be modeled. Consequently, Eq. (1.17) cannot be applied directly, and PT fluctuations can only be considered through statistical model simulations. Still, the large $\chi^2_{\text{red}} \gg 1$ indicates that the deviations between the $(p, p'\gamma)$ Oslo-method data and the MAW of this work cannot simply be explained by statistical uncertainties, even when taking into account PT fluctuations. The discrepancy between the PSF of the present work and the $(^3\text{He}, {}^3\text{He}'\gamma)$ Oslo-method data is attributed to the different normalization of the latter and an issue in the old Oslo-method analysis code (see Section 1.3.4).

In conclusion, the general shape and slope of the PSF of the present work agrees very well with the obtained results using other probes. For Oslo-method experiments, the resulting PSF fluctuates significantly more strongly compared to the MAW PSF of this work. The difference in the strength of the observed fluctuations of the PSF hints at a possible violation of the Brink-Axel hypothesis for the probed energy range. The (generalized) Brink-Axel hypothesis suggests that the PSF is the same regardless of excitation energy (see also Section 1.3.4). Thus, one would expect an agreement of the PSFs for the present work and the Oslo method within statistical uncertainties. A more conclusive statement will be possible once the upward PSF has been determined from the (γ, γ') dataset analyzed in this work (for the methodology, see Section 2.3.1).

7. Summary and outlook

In the first part of this chapter, a summary and outlook will be given for the experimental results for the ^{150}Nd and ^{96}Mo experiments presented in this work. In the second part, the further development of the DAQ systems used for the experiments performed for this work will be outlined, some of which has already been implemented during the 2022 and 2023 HIγS and the 2022 and 2024 DHIPS beamtimes.

7.1. Experimental results

In the present work, the nucleus ^{150}Nd was studied using NRF experiments to probe the influence of the onset of nuclear deformation on the PDR. Combining experiments performed at HIγS and the S-DALINAC, 93 states were observed, including 62 newly-observed states above 4 MeV. Level energies, angular momentum and parity quantum numbers, energy-integrated cross sections, and branching ratios were measured with high precision.

For the first time, average decays to the ground-state band, i.e., the 0^+_1 and 2^+_1 states, were resolved in integral spectroscopy for a heavy deformed nucleus. Integral spectroscopy refers to the analysis of experiments with quasi-monochromatic photon beams by integrating excited states for the extraction of average quantities instead of analyzing individual transitions. An approximately constant average branching ratio of $\langle\langle R_{\mathrm{exp}}\rangle\rangle = 0.481(17)$ was observed for ^{150}Nd. In a geometrical picture, the result was interpreted as a $K = 1$ oscillation, with no indication for a K-splitting of the PDR for the observed energy range. Using a statistical model approach, the average branching ratio was related to the distribution of partial transition widths, and the internal fluctuation ratio s was introduced. Assuming χ^2-distributed partial transition widths,

the degree of freedom ν of the χ^2 distribution could be inferred from the internal fluctuation ratio s. A result of $\nu = 1.84(12)$ was obtained, significantly larger than the commonly used PT distribution with $\nu = 1$. The possible influence of non-statistical decays on the internal fluctuation ratio s was discussed.

Experimental average branching ratio data already exists for other nuclei such as ^{128}Te [129] and ^{140}Ce [171], and, to a limited extend with large statistical and systematic uncertainties, for ^{156}Gd [74] and ^{164}Dy [75]. By determining the internal fluctuation ratio s, the degree of freedom ν of the χ^2 distribution can be calculated using the formalism developed in Section 6.1.4. With an increasing energy of the 2_1^+ state, the model dependency increases, as the PSF can no longer be expected to be the same for decays to the 0_1^+ and 2_1^+ states. With the further development of high-resolution LCB beams, it will be possible to expand the study of average ground-state-band branching ratios to strongly-deformed nuclei with 2_1^+ states with even lower excitation energies.

To further study the statistics of the decay of excited states and the validity of the Brink-Axel hypothesis, the PSF of ^{96}Mo was probed in $\gamma\gamma$-coincidence experiments using NRF. By gating on the decay of transitions between low-lying states, the primary decays to low-lying states could be determined and related to the PSF. A domination of $E1$ strength was observed. For the further quantitative analysis of the PSF, the absence of $M1$ radiation was assumed because of numerical instabilities when fitting both $E1$ and $M1$ contributions. The simplifying assumption allows summing up the spectra of all detectors instead of fitting the spectra of each detector separately.

For future experiments, this analysis method could be improved by grouping together and summing over the spectra of multiple detector pairs to maximize the statistics per spectrum. The selective creation of sum spectra would reduce computational complexity while retaining some sensitivity on the parity quantum number of excited states, allowing for a separation of $E1$ and $M1$ strength.

With the current approach, only the leading multipole order can be considered. For $M1$ radiation, small but non-zero $E2$ admixtures are expected, resulting in systematic deviations of the determined $M1$ strength. Using an approach similar to the one described in Ref. [296], it should be possible to decompose the angular correlation matrices into (generalized) F-coefficient matrices (see Eqs. (2.19) and (2.20)). The detector-response matrix can then be expressed as a function of (generalized) F-

coefficient matrices and the multipole mixing ratio δ, which can be considered as an additional free parameter during the fit procedure.

For the present experiment, a PSF was determined for each photon beam energy. Assuming the validity of the Brink-Axel hypothesis, a scaling procedure was applied to combine all PSFs into a single downward PSF for ^{96}Mo. It was normalized to the $(p, p'\gamma)$ Oslo-method dataset [146] and subsequently compared to experiments using complementary probes. Except for the bremsstrahlung-NRF PSF the general slope and trend agrees very well with other experiments. However, it is found that the fluctuations of other experiments are stronger than the fluctuations observed for the present work, as the determined PSF is comparatively featureless and smoothly increases with energy. This deviation could hint at a possible violation of the Brink-Axel hypothesis.

The experimental method outlined in Section 2.3 allows for the simultaneous determination of downward and upward PSF from the performed NRF experiment. So far, only the downward PSF has been determined. With the described method, the determination of the upward PSF will be possible as well, by combining the ground-state decays observed integral spectroscopy with the observed decay of the 2^+_1 state. Thus, from a single NRF experiment, both the upward and the downward PSF will have been determined, allowing for a direct comparison and a comprehensive model-independent test of the Brink-Axel hypothesis as performed for ^{128}Te [129].

To normalize the resulting upward PSF, additional experimental data are required. In 2023, a bremsstrahlung-NRF experiment was performed at the γELBE setup at the ELBE facility at the Helmholtz-Zentrum Dresden-Rossendorf (HZDR) on ^{96}Mo, with an endpoint energy of 8 MeV. This experimental data can be combined with the experimental data of a previous measurement with an endpoint energy of 13.2 MeV already performed in 2006, which was used for the determination of the downward PSF in Ref. [143] without a state-to-state analysis. The combined dataset allows for the determination of the absolute photon flux for the HIγS experiment. Thus, the absolute scale of the upward PSF can be determined. This upward PSF can then be used to scale the downward PSF determined in this work, instead of using the Oslo-method data from Ref. [146].

7.2. Data acquisition systems

Two new DAQs were developed and commissioned for the experiments discussed in this work. A drasi-based system was developed for DHIPS that utilizes the Mesytec MDPP-16 digitizer. Since the commissioning beamtime in spring 2020, which included the ^{150}Nd bremsstrahlung measurement analyzed for this work, this system has been further developed for the subsequent 2022 and 2024 beamtimes.

The DHIPS DAQ system, as described in this work, has the downside of requiring a simultaneous synchronous readout of all connected detector signals. The digitizer is passing trigger information to the VULOM4B, which initiates the conversion process of the detected event, unless the DAQ system is busy (see Section 3.2.3). However, the trigger signal of the digitizer only provides trigger information for all channels or for a single channel of the digitizer. It is not possible to only selectively trigger on the HPGe detector signals but not on the BGO shield signals. Because their threshold has to be as low as possible for Compton suppression, the trigger rate of the BGO shields can in practice be up to ten times larger than the trigger rate of the HPGe detectors. Thus, the BGOs shields account for a majority of recorded data and significantly increase the dead time of the DAQ system.

To address the issue of high trigger rates, the Mesytec MDPP-16's ability to trigger on a single specific channel was utilized during the 2022 beamtime. The secondary energy outputs of the HPGe detectors were combined into a single signal that was connected to an unused channel of the digitizer. This channel was then used for the creation of the trigger signal. TFAs were used to adjust the gain of the energy signals such that the (single) energy threshold that is applied by the digitizer results in a consistent cutoff energy for all HPGe detectors. Alternatively, a dedicated analog CFD could have been used. The separate trigger branch significantly reduced the data rate and dead time of the system. However, it also required the manual setup of the dedicated analog trigger branch. This setup reduces the flexibility and reproducibility of the system, leading to several observed issues such as shifting cutoff energies.

The system was further developed for the 2024 beamtime. A second dedicated Mesytec MDPP-16 was added to the system, which is now used exclusively to process the BGO shield signals. Now, there are two separate trigger signals available for HPGe detectors and BGO shields. Only the HPGe detector trigger signal is used to trigger the data conversion and record data, resulting in low dead times and data rates. The

analog signal processing is eliminated, significantly reducing the time required to set up the DAQ. Furthermore, the second Mesytec MDPP-16 uses the QDC firmware, which is optimized for fast charge amplifying detectors and thus better suited for BGO shields. Thus, the preprocessing of the signals using TFA modules is no longer required. As a further benefit, dedicated scaler information are now available both for HPGe detectors and BGO shields.

For the ^{96}Mo experiment at HIγS, a hybrid system was put in place that combined the Mesytec VME DAQ system (mvme) already in use at the facility with a separate trigger branch based on Struck SIS3316 digitizers. This hybrid system was necessitated to accommodate for the special requirements of the γγ-coincidence experiment for ^{96}Mo. It was an interim solution specifically intended for the ^{96}Mo experiment, which took place during the COVID-19 pandemic, preventing the setup of a new dedicated drasi-based DAQ because of travel restrictions.

The originally planned drasi-based DAQ for the clover array setup was finally put in place and commissioned during the autumn 2022 HIγS beamtime. It employs several Struck SIS3316 digitizers read out via Ethernet, and rataclock-based timestamp distribution for high-resolution synchronized timestamps. This new system significantly increases the possible data and event rates and is better suited for the analysis of γγ coincidences as required for the present work and similar future experiments. It is triggerless, i.e., each channel is self-triggering, and high rates in one channel do not result in dead time for other channels of the digitizer.

To utilize synergy effects between the systems at DHIPS and the clover array, it is planned to develop a similar SIS3316-based DAQ to be used in Darmstadt. Struck SIS3316 digitizers are already in use at various other setups at the S-DALINAC, such as NEPTUN or QCLAM. All of them plan to use drasi in the future or already do so. A 16 bit-SIS3316 digitizer module optimized for the conversion of HPGe detector signals with a high energy resolution was already procured. Having similar systems in place at both the NRF setup in Darmstadt and the NRF setup operated at HIγS will improve the maintainability of the DAQ systems. Finally, it would also harmonize the data analysis for both setups. Analysis codes developed for one setup could be more easily adapted for the other one, making it easier and more efficient for students to analyze data from both experimental setups.

A. Experimental details

A.1. Detector configuration of γ^3 setup

Table A.1: Detector configuration of the γ^3 setup for the ^{150}Nd experiment. Distance refers to the distance between detector end cap and target center. The detector distances were changed throughout the experiment, The names Setup 4, 6, and 9, refer to the different configurations. In addition, detector positions and the thickness of shieldings attached to the front of the detectors are given.

Name	Serial Number	Position		Distance (mm)			Thickness (mm)	
		ϑ	φ	Setup 4	S. 6	S. 9	Cu filter	Pb filter
HPGe1	36-TN40663A	135°	315°	121	121	121	1.15	
HPGe2	36-TN30986A	90°	90°	83	96	127	1.15	1.20
HPGe3	36-TN31061A	135°	45°	123	123	123	1.15	
HPGe4[*]	43-TP31670A[†] P075689[‡]	90°	180°	91	111	136	1.15	1.20
LaBr1	A4149	90°	0°	76	76	76	1.15	1.20
LaBr2	A4932	90°	270°	76	76	76	1.15	1.20
LaBr3	A4933	135°	225°	114	114	114	1.15	
LaBr4	A4934	135°	135°	116	116	116	1.15	

[*] Defunct for run 385 to 392.
[†] Used until run 384. The detector had a bad energy resolution.
[‡] Used starting from run 393.

A.2. Detector configuration of clover array setup

Table A.2: Detector configuration of the clover array setup for the ^{96}Mo experiment. Distance refers to the distance between detector end cap and target center. In addition, detector positions and the thickness of shieldings attached to the front of the detectors are given. Both clover and coaxial detector types refer to HPGe detectors.

ID	Type	Serial Number	Position		Distance (mm)	Thickness (mm)	
			ϑ	φ		Cu filter	Pb filter
3	Clover	Duke	90°	90°	170	1.02	1.17
5	Clover	X	90°	180°	149	1.02	2.54
8	Clover	Yale 142051	90°	315°	162	1.02	1.17
B1	Clover	USNA 0016110391	135°	0°	197	1.02	1.17
B2[*]	Clover	ARL 4912I	125.2°	45°	197	1.02	1.17
B4[†]	Coaxial	42-TP41203A[‡] 43-TP31670A[§]	135°	135°	235	1.02	0.97
B5	Clover	ARL 4911I	125.2°	180°	203	1.02	1.17
L1	LaBr$_3$	Duke 165050	90°	0°	44		2.54
L7	LaBr$_3$	Duke 165052	90°	270°	60		2.54
LBI	LaBr$_3$	Duke 166247	135°	225°	121		2.54
LBM	LaBr$_3$	Duke 165051	135°	315°	114		2.54
B	CeBr$_3$	S2AB0346	90°	27.5°	203	1.02	
C	CeBr$_3$	S2AB0342	90°	45°	203	1.02	
D	CeBr$_3$	S2AB0343	90°	62.5°	203	1.02	
F	CeBr$_3$	S2AB0349	90°	117.5°	203	1.02	
G	CeBr$_3$	S2AB0351	90°	135°	203	1.02	
H	CeBr$_3$	S2AB0341	90°	152.5°	203	1.02	
K	CeBr$_3$	S2AB0350	90°	225°	146	1.02	
BD	CeBr$_3$	S2AB0345	135°	90°	165	1.02	

Table A.2:   (Continued)

ID	Type	Serial Number	Position ϑ	Position φ	Distance (mm)	Thickness (mm) Cu filter	Thickness (mm) Pb filter
BK	CeBr$_3$	S2AB0352	135°	270°	181	1.02	
0	Coaxial	Duke C120A	0°[¶]		2764		
Z	CeBr$_3$	S2AB0344	35°		1448		

[*] Saturated above 7.2 MeV to 7.5 MeV, depending on the clover leaf.
[†] Defunct for run 135 to 144.
[‡] Until run 134.
[§] Starting from run 145.
[¶] Swiveled into beam to measure beamprofile.

A.3. ^{150}Nd target

The ^{150}Nd target had a net weight of 11 582.8 mg and was in the form of Nd$_2$O$_3$ powder. It was enriched to 93.60(2) % ^{150}Nd. A cylindrical target container made from polyethylene with an outer diameter of $d = 25.4$ mm and a wall thickness of about 1 mm enclosed the powder.

A.4. ^{96}Mo target

The ^{96}Mo target had a net weight of 1949.0 mg and was in the form of metallic Mo powder. It was enriched to 95.90(1) % ^{96}Mo. The powder was pressed to a cylindrical pill with diameter of $d = 20$ mm which was embedded in a shrink-wrapped polyethylene foil with a mass of 50.8 mg.

A small hole was punched into the ^{150}Nd target container and ^{96}Mo polyethylene foil to allow for pressure equalization when placing the targets in the evacuated beam pipe.

A.5. ^{150}Nd HIγS beam energy settings

Table A.3: The beam-energy settings used for the ^{150}Nd experiment at HIγS. The beam-energy column refers to the nominal centroid energy of the quasi-monochromatic photon beam. The runs column refers to the run numbers for which the particular photon beam energy was used. The collimator radius specifies the radius of the collimator which was used to collimate the photon beam. The setup number indicates which detector distances specified in Table A.1 were used.

Beam energy (keV)	Runs	Collimator radius (mm)	Setup Number
2950	314, 315	9.525	4
3100	319	9.525	4
3200	318	9.525	4
3300	322	9.525	4
3400	323	9.525	4
3500	324	9.525	4
3600	325	9.525	4
3700	335	9.525	6
3800	336	9.525	6
3900	337	9.525	6
4000	338	8.0	6
4100	339	8.0	6
4200	340	8.0	6
4300	341	8.0	6
4400	342	8.0	6
4500	347	7.0	6
4600	348	7.0	6
4700	349	7.0	6
4800	350	7.0	6
4900	351	7.0	6

Table A.3:   (Continued)

Beam energy (keV)	Runs	Collimator radius (mm)	Setup Number
5000	352	6.0	6
5100	353	6.0	6
5200	354	6.0	6
5300	357	6.0	6
5400	358	6.0	6
5500	376	6.0	9
5600	483	6.0	9
5700	380	6.0	9
5750	484	6.0	9
5800	381, 401	6.0	9
5900	382, 485	6.0	9
6000	383, 384	5.0	9
6100	385	5.0	9
6100	402	6.0	9
6200	386	5.0	9
6300	391	5.0	9
6400	393	5.0	9
6500	394	5.0	9
6600	395	5.0	9
6700	396	5.0	9
6800	397, 398	5.0	9
6900	399	5.0	9
7000	400	5.0	9

A.6. ^{96}Mo HIγS beam energy settings

Table A.4: The beam-energy settings used for the ^{96}Mo experiment at HIγS. The beam-energy column refers to the nominal centroid energy of the quasi-monochromatic photon beam. The target column specifies the target that was placed at the target position. The polarization column indicates the polarization of the incident photon beam. The "run beamprofile" column gives the number of the run which was used to measure the spectral distribution of the photon beam. The "runs" column lists runs that were used to perform NRF experiments for the particular combination of beam energy, target and polarization.

Beam energy (keV)	Target	Polarization	Run beamprofile	Runs
3900	^{96}Mo	linear	7	8, 9, 10
4100	^{96}Mo	linear	11	12
4300	^{96}Mo	linear	13	14, 15, 18, 19
4500	^{96}Mo	linear	21	23, 24
4700	^{96}Mo	linear	26	27, 28, 29, 30
4900	^{96}Mo	linear	31	32, 33, 34
5020	^{11}B	linear	4	5, 6
5100	^{96}Mo	linear	36	37
5300	^{96}Mo	linear	38	39
5500	^{96}Mo	linear	40	41, 42, 43
5750	^{96}Mo	linear	44	45, 46, 47, 48
6000	^{96}Mo	linear	49	50, 51, 53, 54, 55, 56, 57
6250	^{96}Mo	linear	58	59, 60, 61, 62
6500	^{96}Mo	linear	63	64, 65, 66, 67
6750	^{96}Mo	linear	170	171, 172, 173, 176, 178
7000	^{96}Mo	linear	179	180, 181, 182, 183, 184
7250	^{96}Mo	linear	185	186, 187, 188, 189, 190

Table A.4: (Continued)

Beam energy (keV)	Target	Polarization	Run beamprofile	Runs
7500	^{96}Mo	linear	191	192, 193, 194, 195, 198
7750	^{96}Mo	linear	199	200, 201, 202, 203, 204
8000	^{96}Mo	linear	205	206, 207, 208, 209, 210
8125	^{32}S	circular	330	331, 332
8125	^{32}S	linear	326	327, 328, 329
8250	^{96}Mo	linear	211	212, 213, 214, 215, 216
8500	^{96}Mo	linear	217	219, 220, 221, 222, 223, 224, 226
8750	^{96}Mo	linear	237	239, 240, 241, 242, 244
8920	^{11}B	linear	245	246
9000	^{96}Mo	linear	155	164, 165, 166, 168, 169
9250	^{96}Mo	linear	227	228, 229, 232, 235, 236

Bibliography

[1]   R. H. Cyburt, B. D. Fields, K. A. Olive, and T.-H. Yeh, Rev. Mod. Phys. **88**, 015004 (2016).

[2]   E. M. Burbidge, G. R. Burbidge, W. A. Fowler, and F. Hoyle, Rev. Mod. Phys. **29**, 547 (1957).

[3]   S. E. Woosley, A. Heger, and T. A. Weaver, Rev. Mod. Phys. **74**, 1015 (2002).

[4]   D. D. Clayton, *Principles of stellar evolution and nucleosynthesis* (McGraw-Hill, New York, NY, USA, 1968), ɪsʙɴ: 978-0-0701-1295-7.

[5]   F. Käppeler, H. Beer, and K. Wisshak, Rep. Prog. Phys. **52**, 945 (1989).

[6]   F. Käppeler, R. Gallino, S. Bisterzo, and W. Aoki, Rev. Mod. Phys. **83**, 157 (2011).

[7]   M. Pignatari, R. Gallino, M. Heil, M. Wiescher, F. Käppeler, F. Herwig, and S. Bisterzo, Astrophys. J. **710**, 1557 (2010).

[8]   M. Arnould, S. Goriely, and K. Takahashi, Phys. Rep. **450**, 97 (2007).

[9]   T. Kajino, W. Aoki, A. B. Balantekin, R. Diehl, M. A. Famiano, and G. J. Mathews, Prog. Part. Nucl. Phys. **107**, 109 (2019).

[10]   J. J. Cowan, C. Sneden, J. E. Lawler, A. Aprahamian, M. Wiescher, K. Langanke, G. Martínez-Pinedo, and F.-K. Thielemann, Rev. Mod. Phys. **93**, 015002 (2021).

[11]   B. P. Abbott *et al.* (LIGO Scientific Collaboration and Virgo Collaboration), Phys. Rev. Lett. **119**, 161101 (2017).

[12]   S. Goriely, Eur. Phys. J. A **51**, 22 (2015).

[13]   G. Martínez-Pinedo and K. Langanke, Eur. Phys. J. A **59**, 67 (2023).

[14]   M. Reichert, C. Winteler, O. Korobkin, A. Arcones, J. Bliss, M. Eichler, U. Frischknecht, C. Fröhlich, R. Hirschi, M. Jacobi, J. Kuske, G. Martínez-Pinedo, D. Martin, D. Mocelj, T. Rauscher, and F.-K. Thielemann, *The nuclear reaction network WinNet*, version 1.0.2, 2023, arXiv:2305.07048 [astro-ph.IM], https://github.com/nuc-astro/WinNet.

[15]   A. Arcones and G. Martínez-Pinedo, Phys. Rev. C **83**, 045809 (2011).

[16] M. Hampel, R. J. Stancliffe, M. Lugaro, and B. S. Meyer, Astrophys. J. **831**, 171 (2016).

[17] A. Choplin, L. Siess, and S. Goriely, Astron. Astrophys. **667**, A155 (2022).

[18] M. Arnould and S. Goriely, Phys. Rep. **384**, 1 (2003).

[19] A. Zilges, V. Derya, D. Savran, A. Hennig, S. G. Pickstone, and M. Spieker, J. Phys. Conf. Ser. **580**, 012052 (2015).

[20] N. Pietralla, Eur. Phys. J. A **60**, 108 (2024).

[21] A. Bohr and B. R. Mottelson, *Nuclear structure: Single-particle motion*, 1st ed., Vol. 1 (Addison-Wesley, Reading, MA, 1969), ɪsʙɴ: 978-0-3183-5468-2.

[22] BIPM, *Le Système international d'unités / The International System of Units ('The SI Brochure')*, 9th ed. (Bureau international des poids et mesures, 2019), ɪsʙɴ: 978-92-822-2272-0, https://www.bipm.org/en/si/si_brochure/.

[23] J. D. Jackson, *Classical electrodynamics*, 3rd ed. (John Wiley & Sons, Inc., New York, 1999), ɪsʙɴ: 978-0-471-30932-1.

[24] J. Speth and A. van der Woude, Rep. Prog. Phys. **44**, 719 (1981).

[25] D. Savran, T. Aumann, and A. Zilges, Prog. Part. Nucl. Phys. **70**, 210 (2013).

[26] K. Heyde, P. von Neumann-Cosel, and A. Richter, Rev. Mod. Phys. **82**, 2365 (2010).

[27] W. Kuhn, Z. Phys. **33**, 408 (1925).

[28] F. Reiche and W. Thomas, Z. Phys. **34**, 510 (1925).

[29] J. S. Levinger and H. A. Bethe, Phys. Rev. **78**, 115 (1950).

[30] P. F. Bortignon, A. Bracco, and R. A. Broglia, *Giant resonances: Nuclear structure at finite temperature*, 1st ed., Vol. 10, Contemporary concepts in physics (Harwood Academic Publishers, Reading, UK, 1998), ɪsʙɴ: 978-90-5702-570-9.

[31] M. N. Harakeh and A. van der Woude, *Giant resonances: Fundamental high-frequency modes of nuclear excitation*, 1st ed., Vol. 24, Oxford studies in nuclear physics (Clarendon Press, Oxford, UK, 2001), ɪsʙɴ: 978-0-1985-1733-7.

[32] A. Bracco, E. G. Lanza, and A. Tamii, Prog. Part. Nucl. Phys. **106**, 360 (2019).

[33] D. Savran, M. Babilon, A. M. van den Berg, M. N. Harakeh, J. Hasper, A. Matic, H. J. Wörtche, and A. Zilges, Phys. Rev. Lett. **97**, 172502 (2006).

[34] E. G. Lanza, L. Pellegri, A. Vitturi, and M. V. Andrés, Prog. Part. Nucl. Phys. **129**, 104006 (2023).

[35] R. Mohan, M. Danos, and L. C. Biedenharn, Phys. Rev. C **3**, 1740 (1971).

[36] P.-G. Reinhard and W. Nazarewicz, Phys. Rev. C **81**, 051303 (2010).

[37] O. Bohigas, N. Van Giai, and D. Vautherin, Phys. Lett. B **102**, 105 (1981).

[38] A. Tamii, P. von Neumann-Cosel, and I. Poltoratska, Eur. Phys. J. A **50**, 28 (2014).

[39] X. Roca-Maza, M. Brenna, G. Colò, M. Centelles, X. Viñas, B. K. Agrawal, N. Paar, D. Vretenar, and J. Piekarewicz, Phys. Rev. C **88**, 024316 (2013).

[40] X. Roca-Maza, X. Viñas, M. Centelles, B. K. Agrawal, G. Colò, N. Paar, J. Piekarewicz, and D. Vretenar, Phys. Rev. C **92**, 064304 (2015).

[41] C. J. Horowitz and J. Piekarewicz, Phys. Rev. Lett. **86**, 5647 (2001).

[42] E. Litvinova, P. Ring, V. Tselyaev, and K. Langanke, Phys. Rev. C **79**, 054312 (2009).

[43] M. Weinert, M. Spieker, G. Potel, N. Tsoneva, M. Müscher, J. Wilhelmy, and A. Zilges, Phys. Rev. Lett. **127**, 242501 (2021).

[44] U. Kneissl, N. Pietralla, and A. Zilges, J. Phys. G Nucl. Part. Phys. **32**, R217 (2006).

[45] W. Andrejtscheff, C. Kohstall, P. von Brentano, C. Fransen, U. Kneissl, N. Pietralla, and H. H. Pitz, Phys. Lett. B **506**, 239 (2001).

[46] D. Bohle, A. Richter, W. Steffen, A. E. L. Dieperink, N. Lo Iudice, F. Palumbo, and O. Scholten, Phys. Lett. B **137**, 27 (1984).

[47] D. Bohle, A. Richter, U. E. P. Berg, J. Drexler, R. D. Heil, U. Kneissl, H. Metzger, R. Stock, B. Fischer, H. Hollick, and D. Kollewe, Nucl. Phys. A **458**, 205 (1986).

[48] N. Lo Iudice and F. Palumbo, Phys. Rev. Lett. **41**, 1532 (1978).

[49] F. Iachello, Nucl. Phys. A **358**, 89 (1981).

[50] A. Richter, Prog. Part. Nucl. Phys. **34**, 261 (1995).

[51] M. Krtička, F. Bečvář, J. Honzátko, I. Tomandl, M. Heil, F. Käppeler, R. Reifarth, F. Voss, and K. Wisshak, Phys. Rev. Lett. **92**, 172501 (2004).

[52] A. Schiller, A. Voinov, E. Algin, J. A. Becker, L. A. Bernstein, P. E. Garrett, M. Guttormsen, R. O. Nelson, J. Rekstad, and S. Siem, Phys. Lett. B **633**, 225 (2006).

[53] M. Guttormsen, L. A. Bernstein, A. Bürger, A. Görgen, F. Gunsing, T. W. Hagen, A. C. Larsen, T. Renstrøm, S. Siem, M. Wiedeking, and J. N. Wilson, Phys. Rev. Lett. **109**, 162503 (2012).

[54] A. Voinov, E. Algin, U. Agvaanluvsan, T. Belgya, R. Chankova, M. Guttormsen, G. E. Mitchell, J. Rekstad, A. Schiller, and S. Siem, Phys. Rev. Lett. **93**, 142504 (2004).

[55] M. Guttormsen, R. Chankova, U. Agvaanluvsan, E. Algin, L. A. Bernstein, F. Ingebretsen, T. Lönnroth, S. Messelt, G. E. Mitchell, J. Rekstad, A. Schiller, S. Siem, A. C. Sunde, A. Voinov, and S. Ødegård, Phys. Rev. C **71**, 044307 (2005).

[56] J. E. Midtbø, A. C. Larsen, T. Renstrøm, F. L. Bello Garrote, and E. Lima, Phys. Rev. C **98**, 064321 (2018).

[57] M. Wiedeking, L. A. Bernstein, M. Krtička, D. L. Bleuel, J. M. Allmond, M. S. Basunia, J. T. Burke, P. Fallon, R. B. Firestone, B. L. Goldblum, R. Hatarik, P. T. Lake, I.-Y. Lee, S. R. Lesher, S. Paschalis, M. Petri, L. Phair, and N. D. Scielzo, Phys. Rev. Lett. **108**, 162503 (2012).

[58] A. C. Larsen, N. Blasi, A. Bracco, F. Camera, T. K. Eriksen, A. Görgen, M. Guttormsen, T. W. Hagen, S. Leoni, B. Million, H. T. Nyhus, T. Renstrøm, S. J. Rose, I. E. Ruud, S. Siem, T. Tornyi, G. M. Tveten, A. V. Voinov, and M. Wiedeking, Phys. Rev. Lett. **111**, 242504 (2013).

[59] A. Simon, M. Guttormsen, A. C. Larsen, C. W. Beausang, P. Humby, J. T. Harke, R. J. Casperson, R. O. Hughes, T. J. Ross, J. M. Allmond, R. Chyzh, M. Dag, J. Koglin, E. McCleskey, M. McCleskey, S. Ota, and A. Saastamoinen, Phys. Rev. C **93**, 034303 (2016).

[60] E. Litvinova and N. Belov, Phys. Rev. C **88**, 031302 (2013).

[61] A. C. Larsen, J. E. Midtbø, M. Guttormsen, T. Renstrøm, S. N. Liddick, A. Spyrou, S. Karampagia, B. A. Brown, O. Achakovskiy, S. Kamerdzhiev, D. L. Bleuel, A. Couture, L. C. Campo, B. P. Crider, A. C. Dombos, R. Lewis, S. Mosby, F. Naqvi, G. Perdikakis, C. J. Prokop, S. J. Quinn, and S. Siem, Phys. Rev. C **97**, 054329 (2018).

[62] A. C. Larsen and S. Goriely, Phys. Rev. C **82**, 014318 (2010).

[63] S. Goriely, S. Hilaire, S. Péru, and K. Sieja, Phys. Rev. C **98**, 014327 (2018).

[64] K. L. Malatji, K. S. Beckmann, M. Wiedeking, S. Siem, S. Goriely, A. C. Larsen, K. O. Ay, F. L. Bello Garrote, L. C. Campo, A. Görgen, M. Guttormsen, V. W. Ingeberg, P. Jones, B. V. Kheswa, P. von Neumann-Cosel, M. Ozgur, G. Potel, L. Pellegri, T. Renstrøm, G. M. Tveten, and F. Zeiser, Phys. Rev. C **103**, 014309 (2021).

[65] M. Danos, Nuclear Physics **5**, 23 (1958).

[66] K. Okamoto, Phys. Rev. **110**, 143 (1958).

[67] R. F. Casten, Nat. Phys. **2**, 811 (2006).

[68] B. Pritychenko, M. Birch, B. Singh, and M. Horoi, Atom. Data Nucl. Data **107**, 1 (2016), [Erratum: Atom. Data Nucl. Data **114**, 371 (2017)].

[69] K. Yoshida, Phys. Rev. C **80**, 044324 (2009).

[70] K. Yoshida and T. Nakatsukasa, Phys. Rev. C **83**, 021304 (2011).

[71] K. Yoshida and T. Nakatsukasa, Phys. Rev. C **88**, 034309 (2013).

[72] P. M. Goddard, N. Cooper, V. Werner, G. Rusev, P. D. Stevenson, A. Rios, C. Bernards, A. Chakraborty, B. P. Crider, J. Glorius, R. S. Ilieva, J. H. Kelley, E. Kwan, E. E. Peters, N. Pietralla, R. Raut, C. Romig, D. Savran, L. Schnorrenberger, M. K. Smith, K. Sonnabend, A. P. Tonchev, W. Tornow, and S. W. Yates, Phys. Rev. C **88**, 064308 (2013).

[73] P. Carlos, H. Beil, R. Bergère, J. Fagot, A. Leprêtre, A. Veyssière, and G. V. Solodukhov, Nucl. Phys. A **258**, 365 (1976).

[74] M. Tamkas, E. Açıksöz, J. Isaak, T. Beck, N. Benouaret, M. Bhike, I. Boztosun, A. Durusoy, U. Gayer, Krishichayan, B. Löher, N. Pietralla, D. Savran, W. Tornow, V. Werner, A. Zilges, and M. Zweidinger, Nucl. Phys. A **987**, 79 (2019).

[75] O. Papst, V. Werner, J. Isaak, N. Pietralla, T. Beck, C. Bernards, M. Bhike, N. Cooper, B. P. Crider, U. Friman-Gayer, J. Kleemann, Krishichayan, B. Löher, F. Naqvi, E. E. Peters, F. M. Prados-Estévez, R. S. Ilieva, T. J. Ross, D. Savran, W. Tornow, and J. R. Vanhoy, Phys. Rev. C **102**, 034323 (2020).

[76] P. Carlos, H. Beil, R. Bergere, A. Lepretre, and A. Veyssiere, Nucl. Phys. A **172**, 437 (1971).

[77] L. M. Donaldson, C. A. Bertulani, J. Carter, V. O. Nesterenko, P. von Neumann-Cosel, R. Neveling, V. Y. Ponomarev, P.-G. Reinhard, I. T. Usman, P. Adsley, J. W. Brummer, E. Z. Buthelezi, G. R. J. Cooper, R. W. Fearick, S. V. Förtsch, H. Fujita, Y. Fujita, M. Jingo, W. Kleinig, C. O. Kureba, J. Kvasil, M. Latif, K. C. W. Li, J. P. Mira, F. Nemulodi, P. Papka, L. Pellegri, N. Pietralla, A. Richter, E. Sideras-Haddad, F. D. Smit, G. F. Steyn, J. A. Swartz, and A. Tamii, Phys. Lett. B **776**, 133 (2018).

[78] R. Krücken, B. Albanna, C. Bialik, R. F. Casten, J. R. Cooper, A. Dewald, N. V. Zamfir, C. J. Barton, C. W. Beausang, M. A. Caprio, A. A. Hecht, T. Klug, J. R. Novak, N. Pietralla, and P. von Brentano, Phys. Rev. Lett. **88**, 232501 (2002).

[79] W. Hauser and H. Feshbach, Phys. Rev. **87**, 366 (1952).

[80] N. Bohr, Nature **137**, 344 (1936).

[81] R. Capote, M. Herman, P. Obložinský, P. G. Young, S. Goriely, T. Belgya, A. V. Ignatyuk, A. J. Koning, S. Hilaire, V. A. Plujko, M. Avrigeanu, O. Bersillon, M. B. Chadwick, T. Fukahori, Z. Ge, Y. Han, S. Kailas, J. Kopecky, V. M. Maslov, G. Reffo, M. Sin, E. S. Soukhovitskii, and P. Talou, Nucl. Data Sheets **110**, 3107 (2009).

[82] A. J. Koning, S. Hilaire, and M. C. Duijvestijn, in Proceedings of the International Conference on Nuclear Data for Science and Technology – ND2007, edited by O. Bersillon, F. Gunsing, E. Bauge, R. Jacqmin, and S. Leray (2008), pp. 211–214.

[83] A. J. Koning and D. Rochman, Nucl. Data Sheets **113**, 2841 (2012).

[84] Koning, Arjan, Hilaire, Stephane, and Goriely, Stephane, Eur. Phys. J. A **59**, 131 (2023).

[85] M. Herman, R. Capote, B. V. Carlson, P. Obložinský, M. Sin, A. Trkov, H. Wienke, and V. Zerkin, Nucl. Data Sheets **108**, Special Issue on Evaluations of Neutron Cross Sections, 2655 (2007).

[86] H. A. Bethe, Phys. Rev. **50**, 332 (1936).

[87] T. Ericson, Nucl. Phys. **11**, 481 (1959).

[88] A. Gilbert and A. G. W. Cameron, Can. J. Phys. **43**, 1446 (1965).

[89] T. von Egidy and D. Bucurescu, Phys. Rev. C **80**, 054310 (2009).

[90] National Nuclear Data Center (NNDC), *Evaluated nuclear structure data file (ENSDF)*, version 2024-05 (Brookhaven National Laboratory, Upton, NY, USA), https://www.nndc.bnl.gov/ensdf/ (visited on 2024-05-19).

[91] D. Abriola and A. A. Sonzogni, Nucl. Data Sheets **109**, 2501 (2008).

[92] S. K. Basu and A. A. Sonzogni, Nucl. Data Sheets **114**, 435 (2013).

[93] T. von Egidy and D. Bucurescu, Phys. Rev. C **72**, 044311 (2005), [Erratum: Phys. Rev. C **73**, 049901(E) (2006)].

[94] T. Ericson, Adv. Phys. **9**, 425 (1960).

[95] S. Goriely, A.-C. Larsen, and D. Mücher, Phys. Rev. C **106**, 044315 (2022).

[96] G. A. Bartholomew, E. D. Earle, A. J. Ferguson, J. W. Knowles, and M. A. Lone, "Gamma-ray strength functions", in *Advances in Nuclear Physics*, Vol. 7, edited by M. Baranger and E. Vogt (Springer Science and Business Media LLC, New York, NY, USA, 1973) Chap. 4, pp. 229–324, ISBN: 978-1-4615-9046-0.

[97] S. Goriely, P. Dimitriou, M. Wiedeking, T. Belgya, R. Firestone, J. Kopecky, M. Krtička, V. Plujko, R. Schwengner, S. Siem, H. Utsunomiya, S. Hilaire, S. Péru, Y. S. Cho, D. M. Filipescu, N. Iwamoto, T. Kawano, V. Varlamov, and R. Xu, Eur. Phys. J. A **55**, 172 (2019).

[98] M. Wiedeking and S. Goriely, Phil. Trans. R. Soc. A **382**, 20230125 (2024).

[99] E. P. Wigner, Ann. of Math. **62**, 548 (1955).

[100] F. J. Dyson, J. Math. Phys. **3**, 140 (1962).

[101] F. J. Dyson, J. Math. Phys. **3**, 157 (1962).

[102] F. J. Dyson, J. Math. Phys. **3**, 166 (1962).

[103] C. E. Porter, *Statistical theories of spectra: Fluctuations*, Perspectives in physics (Academic Press, New York, 1965), ISBN: 978-0125623506.

[104] H. A. Weidenmüller and G. E. Mitchell, Rev. Mod. Phys. **81**, 539 (2009).

[105] A. Altland and M. R. Zirnbauer, Phys. Rev. B **55**, 1142 (1997).

[106] M. Gaudin, Nucl. Phys. **25**, 447 (1961).

[107] E. P. Wigner, SIAM Rev. **9**, 1 (1967).

[108] M. V. Berry and M. Tabor, Proc. R. Soc. London Ser. A **356**, 375 (1977).

[109] N. Rosenzweig and C. E. Porter, Phys. Rev. **120**, 1698 (1960).

[110] C. E. Porter and R. G. Thomas, Phys. Rev. **104**, 483 (1956).

[111] K. Hagino and G. F. Bertsch, Phys. Rev. E **104**, L052104 (2021).

[112] A. Pandey, Ann. Physics **134**, 110 (1981).

[113] Y. Alhassid, J. N. Hormuzdiar, and N. D. Whelan, Phys. Rev. B **58**, 4866 (1998).

[114] R. U. Haq, A. Pandey, and O. Bohigas, Phys. Rev. Lett. **48**, 1086 (1982).

[115] A. A. Adams, G. E. Mitchell, and J. F. Shriner, Jr, Phys. Lett. B **422**, 13 (1998).

[116] J. F. Shriner, C. A. Grossmann, and G. E. Mitchell, Phys. Rev. C **62**, 054305 (2000).

[117] P. E. Koehler, Y. M. Gledenov, T. Rauscher, and C. Fröhlich, Phys. Rev. C **69**, 015803 (2004).

[118] P. E. Koehler, J. L. Ullmann, T. A. Bredeweg, J. M. O'Donnell, R. Reifarth, R. S. Rundberg, D. J. Vieira, and J. M. Wouters, Phys. Rev. C **76**, 025804 (2007).

[119] P. E. Koehler, F. Bečvář, M. Krtička, J. A. Harvey, and K. H. Guber, Phys. Rev. Lett. **105**, 072502 (2010).

[120] H. A. Weidenmüller, Phys. Rev. Lett. **105**, 232501 (2010).

[121] P. E. Koehler, Phys. Rev. C **84**, 034312 (2011).

[122] G. L. Celardo, N. Auerbach, F. M. Izrailev, and V. G. Zelevinsky, Phys. Rev. Lett. **106**, 042501 (2011).

[123] P. E. Koehler, R. Reifarth, J. L. Ullmann, T. A. Bredeweg, J. M. O'Donnell, R. S. Rundberg, D. J. Vieira, and J. M. Wouters, Phys. Rev. Lett. **108**, 142502 (2012).

[124] A. Volya, H. A. Weidenmüller, and V. Zelevinsky, Phys. Rev. Lett. **115**, 052501 (2015).

[125] E. Bogomolny, Phys. Rev. Lett. **118**, 022501 (2017).

[126] D. M. Brink, "Some aspects of the interaction of light with matter", PhD thesis (Oxford University, 1955).

[127] P. Axel, Phys. Rev. **126**, 671 (1962).

[128] M. Guttormsen, A. C. Larsen, A. Görgen, T. Renstrøm, S. Siem, T. G. Tornyi, and G. M. Tveten, Phys. Rev. Lett. **116**, 012502 (2016).

[129] J. Isaak, D. Savran, B. Löher, T. Beck, M. Bhike, U. Gayer, Krishichayan, N. Pietralla, M. Scheck, W. Tornow, V. Werner, A. Zilges, and M. Zweidinger, Phys. Lett. B **788**, 225 (2019).

[130] M. Markova, P. von Neumann-Cosel, A. C. Larsen, S. Bassauer, A. Görgen, M. Guttormsen, F. L. Bello Garrote, H. C. Berg, M. M. Bjørøen, T. Dahl-Jacobsen, T. K. Eriksen, D. Gjestvang, J. Isaak, M. Mbabane, W. Paulsen, L. G. Pedersen, N. I. J. Pettersen, A. Richter, E. Sahin, P. Scholz, S. Siem, G. M. Tveten, V. M. Valsdottir, M. Wiedeking, and F. Zeiser, Phys. Rev. Lett. **127**, 182501 (2021).

[131] J. M. Blatt and V. F. Weisskopf, *Theoretical nuclear physics*, 1st ed. (John Wiley & Sons, Nashville, TN, 1952), ISBN: 978-0-471-08019-0.

[132] L. C. Campo, M. Guttormsen, F. L. B. Garrote, T. K. Eriksen, F. Giacoppo, A. Görgen, K. Hadynska-Klek, M. Klintefjord, A. C. Larsen, T. Renstrøm, E. Sahin, S. Siem, A. Springer, T. G. Tornyi, and G. M. Tveten, Phys. Rev. C **98**, 054303 (2018).

[133] M. D. Jones, A. O. Macchiavelli, M. Wiedeking, L. A. Bernstein, H. L. Crawford, C. M. Campbell, R. M. Clark, M. Cromaz, P. Fallon, I. Y. Lee, M. Salathe, A. Wiens, A. D. Ayangeakaa, D. L. Bleuel, S. Bottoni, M. P. Carpenter, H. M. Davids, J. Elson, A. Görgen, M. Guttormsen, R. V. F. Janssens, J. E. Kinnison, L. Kirsch, A. C. Larsen, T. Lauritsen, W. Reviol, D. G. Sarantites, S. Siem, A. V. Voinov, and S. Zhu, Phys. Rev. C **97**, 024327 (2018).

[134] F. Bečvář, J. Honzátko, M. Krtička, S. Pašić, G. Rusev, and I. Tomandl, Nucl. Instrum. Meth. B **261**, The Application of Accelerators in Research and Industry, 930 (2007).

[135] A. Voinov, S. M. Grimes, C. R. Brune, M. Guttormsen, A. C. Larsen, T. N. Massey, A. Schiller, and S. Siem, Phys. Rev. C **81**, 024319 (2010).

[136] P. Scholz, M. Guttormsen, F. Heim, A. C. Larsen, J. Mayer, D. Savran, M. Spieker, G. M. Tveten, A. V. Voinov, J. Wilhelmy, F. Zeiser, and A. Zilges, Phys. Rev. C **101**, 045806 (2020).

[137] C. T. Angell, S. L. Hammond, H. J. Karwowski, J. H. Kelley, M. Krtička, E. Kwan, A. Makinaga, and G. Rusev, Phys. Rev. C **86**, 051302 (2012), [Erratum: Phys. Rev. C **91**, 039901 (2015)].

[138] J. Isaak, D. Savran, M. Krtička, M. W. Ahmed, J. Beller, E. Fiori, J. Glorius, J. H. Kelley, B. Löher, N. Pietralla, C. Romig, G. Rusev, M. Scheck, L. Schnorrenberger, J. Silva, K. Sonnabend, A. P. Tonchev, W. Tornow, H. R. Weller, and M. Zweidinger, Phys. Lett. B **727**, 361 (2013).

[139] L. Netterdon, A. Endres, S. Goriely, J. Mayer, P. Scholz, M. Spieker, and A. Zilges, Phys. Lett. B **744**, 358 (2015).

[140] J. Kopecky and M. Uhl, Phys. Rev. C **41**, 1941 (1990).

[141] K. Sieja, Eur. Phys. J. A **59**, 147 (2023).

[142] C. W. Johnson, Phys. Lett. B **750**, 72 (2015).

[143] G. Rusev, R. Schwengner, R. Beyer, M. Erhard, E. Grosse, A. R. Junghans, K. Kosev, C. Nair, K. D. Schilling, A. Wagner, F. Dönau, and S. Frauendorf, Phys. Rev. C **79**, 061302 (2009).

[144] D. Martin, P. von Neumann-Cosel, A. Tamii, N. Aoi, S. Bassauer, C. A. Bertulani, J. Carter, L. Donaldson, H. Fujita, Y. Fujita, T. Hashimoto, K. Hatanaka, T. Ito, A. Krugmann, B. Liu, Y. Maeda, K. Miki, R. Neveling, N. Pietralla, I. Poltoratska, V. Y. Ponomarev, A. Richter, T. Shima, T. Yamamoto, and M. Zweidinger, Phys. Rev. Lett. **119**, 182503 (2017).

[145] H. Utsunomiya, S. Goriely, T. Kondo, C. Iwamoto, H. Akimune, T. Yamagata, H. Toyokawa, H. Harada, F. Kitatani, Y.-W. Lui, A. C. Larsen, M. Guttormsen, P. E. Koehler, S. Hilaire, S. Péru, M. Martini, and A. J. Koning, Phys. Rev. C **88**, 015805 (2013).

[146] J. E. L. Larsson, "Statistical properties of Mo-96 and Mo-100", MSc thesis (Universitetet i Oslo, 2023), https://www.duo.uio.no/handle/10852/103513 (visited on 2024-05-06).

[147] H. Beil, R. Bergère, P. Carlos, A. Leprêtre, A. De Miniac, and A. Veyssière, Nucl. Phys. A **227**, 427 (1974).

[148] P. Obložinský, *Reference input parameter library (RIPL-1), Handbook for calculations of nuclear reaction data*, tech. rep. IAEA-TECDOC-1034 (International Atomic Energy Agency (IAEA), Vienna, Austria, 1998).

[149] P. E. Koehler, Phys. Rev. C **105**, 054306 (2022).

[150] M. Markova, A. C. Larsen, G. M. Tveten, P. von Neumann-Cosel, T. K. Eriksen, F. L. Bello Garrote, L. Crespo Campo, F. Giacoppo, A. Görgen, M. Guttormsen, K. Hadynska-Klek, M. Klintefjord, T. Renstrøm, E. Sahin, S. Siem, and T. G. Tornyi, Phys. Rev. C **108**, 014315 (2023).

[151] M. Zweidinger, "Kernstrukturuntersuchungen in mittelschweren Atomkernen mit der Methode der Kernresonanzfluoreszenz", PhD thesis (Technische Universität Darmstadt, 2016), https://tuprints.ulb.tu-darmstadt.de/id/eprint/5615.

[152] C. Romig, J. Beller, J. Glorius, J. Isaak, J. H. Kelley, E. Kwan, N. Pietralla, V. Y. Ponomarev, A. Sauerwein, D. Savran, M. Scheck, L. Schnorrenberger, K. Sonnabend, A. P. Tonchev, W. Tornow, H. R. Weller, A. Zilges, and M. Zweidinger, Phys. Rev. C **88**, 044331 (2013).

[153] F. R. Metzger, Prog. Nucl. Phys. **7**, 54 (1959).

[154] U. Kneissl, H. H. Pitz, and A. Zilges, Prog. Part. Nucl. Phys. **37**, 349 (1996).

[155] A. Zilges, D. L. Balabanski, J. Isaak, and N. Pietralla, Prog. Part. Nucl. Phys. **122**, 103903 (2022), [Corrigendum: Prog. Part. Nucl. Phys. **133**, 104059 (2023)].

[156] H. A. Bethe and G. Placzek, Phys. Rev. **51**, 450 (1937).

[157] G. Breit and E. Wigner, Phys. Rev. **49**, 519 (1936).

[158] C. M. Davisson, *Interaction of γ-radiation with matter*, edited by K. Siegbahn, Vol. 1, Alpha- Beta- and Gamma-ray Spectroscopy (North-Holland Publishing Company, 1965) Chap. II, ISBN: 978-0-4441-0695-7.

[159] S. Kahane, R. Moreh, and O. Shahal, Phys. Rev. C **28**, 1519 (1983).

[160] P. Rullhusen, U. Zurmühl, W. Mückenheim, F. Smend, M. Schumacher, and H. G. Börner, Nucl. Phys. A **382**, 79 (1982).

[161] E. G. Fuller and E. Hayward, Nucl. Phys. **30**, 613 (1962).

[162] J. S. Levinger, Phys. Rev. **84**, 523 (1951).

[163] C. Romig, D. Savran, J. Beller, J. Birkhan, A. Endres, M. Fritzsche, J. Glorius, J. Isaak, N. Pietralla, M. Scheck, L. Schnorrenberger, K. Sonnabend, and M. Zweidinger, Phys. Lett. B **744**, 369 (2015).

[164] C. Romig, "Investigation of nuclear structure with relative self-absorption measurements", PhD thesis (Technische Universität Darmstadt, 2015), ISBN: 978-3-8439-2021-6, https://tuprints.ulb.tu-darmstadt.de/id/eprint/4446.

[165] G. Alaga, K. Alder, A. Bohr, and B. R. Mottelson, Dan. Mat. Fys. Medd. **29** (1955).

[166] R. M. Steffen and K. Alder, "Angular distribution and correlation of gamma rays", in *The electromagnetic interaction in nuclear spectroscopy*, edited by W. D. Hamilton (North-Holland, Amsterdam, NL, 1975) Chap. 12, pp. 505–582, ISBN: 978-0-4441-0519-6.

[167] K. S. Krane, R. M. Steffen, and R. M. Wheeler, Atom. Data Nucl. Data **11**, 351 (1973).

[168] A. P. Tonchev, S. L. Hammond, J. H. Kelley, E. Kwan, H. Lenske, G. Rusev, W. Tornow, and N. Tsoneva, Phys. Rev. Lett. **104**, 072501 (2010).

[169] U. Gayer, T. Beck, M. Bhike, J. Isaak, N. Pietralla, P. C. Ries, D. Savran, M. Schilling, W. Tornow, and V. Werner, Phys. Rev. C **100**, 034305 (2019).

[170] M. Scheck, V. Y. Ponomarev, T. Aumann, J. Beller, M. Fritzsche, J. Isaak, J. H. Kelley, E. Kwan, N. Pietralla, R. Raut, C. Romig, G. Rusev, D. Savran, K. Sonnabend, A. P. Tonchev, W. Tornow, H. R. Weller, and M. Zweidinger, Phys. Rev. C **87**, 051304(R) (2013).

[171] B. Löher, D. Savran, T. Aumann, J. Beller, M. Bhike, N. Cooper, V. Derya, M. Duchêne, J. Endres, A. Hennig, P. Humby, J. Isaak, J. H. Kelley, M. Knörzer, N. Pietralla, V. Y. Ponomarev, C. Romig, M. Scheck, H. Scheit, J. Silva, A. P. Tonchev, W. Tornow, F. Wamers, H. Weller, V. Werner, and A. Zilges, Phys. Lett. B **756**, 72 (2016).

[172] M. Wiedeking, M. Guttormsen, A. C. Larsen, F. Zeiser, A. Görgen, S. N. Liddick, D. Mücher, S. Siem, and A. Spyrou, Phys. Rev. C **104**, 014311 (2021).

[173] A. Schiller, L. Bergholt, M. Guttormsen, E. Melby, J. Rekstad, and S. Siem, Nucl. Instrum. Meth. A **447**, 498 (2000).

[174] A. Görgen, M. Guttormsen, A. C. Larsen, S. Siem, E. Adli, N. F. J. Edin, H. Gjersdal, G. Henriksen, E. Malinen, V. Modamio, B. Schoultz, P. A. Sobas, T. A. Theodossiou, and J. C. Wikne, Eur. Phys. J. A A **136**, 181 (2021).

[175] M. Guttormsen, A. Bürger, T. E. Hansen, and N. Lietaer, Nucl. Instrum. Meth. A **648**, 168 (2011).

[176] F. Zeiser, G. M. Tveten, F. L. Bello Garrote, M. Guttormsen, A. C. Larsen, V. W. Ingeberg, A. Görgen, and S. Siem, Nucl. Instrum. Meth. A **985**, 164678 (2021).

[177] M. Guttormsen, T. Ramsøy, and J. Rekstad, Nucl. Instrum. Meth. A **255**, 518 (1987).

[178] L. Henden, L. Bergholt, M. Guttormsen, J. Rekstad, and T. S. Tveter, Nucl. Phys. A **589**, 249 (1995).

[179] S. Bassauer, P. von Neumann-Cosel, and A. Tamii, Phys. Rev. C **94**, 054313 (2016).

[180] A. Tamii, Y. Fujita, H. Matsubara, T. Adachi, J. Carter, M. Dozono, H. Fujita, K. Fujita, H. Hashimoto, K. Hatanaka, T. Itahashi, M. Itoh, T. Kawabata, K. Nakanishi, S. Ninomiya, A. B. Perez-Cerdan, L. Popescu, B. Rubio, T. Saito, H. Sakaguchi, Y. Sakemi, Y. Sasamoto, Y. Shimbara, Y. Shimizu, F. D. Smit, Y. Tameshige, M. Yosoi, and J. Zenhiro, Nucl. Instrum. Meth. A **605**, 326 (2009).

[181] M. Fujiwara, H. Akimune, I. Daito, H. Fujimura, Y. Fujita, K. Hatanaka, H. Ikegami, I. Katayama, K. Nagayama, N. Matsuoka, S. Morinobu, T. Noro, M. Yoshimura, H. Sakaguchi, Y. Sakemi, A. Tamii, and M. Yosoi, Nucl. Instrum. Meth. A **422**, 484 (1999).

[182] A. Tamii, I. Poltoratska, P. von Neumann-Cosel, Y. Fujita, T. Adachi, C. A. Bertulani, J. Carter, M. Dozono, H. Fujita, K. Fujita, K. Hatanaka, D. Ishikawa, M. Itoh, T. Kawabata, Y. Kalmykov, A. M. Krumbholz, E. Litvinova, H. Matsubara, K. Nakanishi, R. Neveling, H. Okamura, H. J. Ong, B. Özel-Tashenov, V. Y. Ponomarev, A. Richter, B. Rubio, H. Sakaguchi, Y. Sakemi, Y. Sasamoto, Y. Shimbara, Y. Shimizu, F. D. Smit, T. Suzuki, Y. Tameshige, J. Wambach, R. Yamada, M. Yosoi, and J. Zenihiro, Phys. Rev. Lett. **107**, 062502 (2011).

[183] I. Poltoratska, P. von Neumann-Cosel, A. Tamii, T. Adachi, C. A. Bertulani, J. Carter, M. Dozono, H. Fujita, K. Fujita, Y. Fujita, K. Hatanaka, M. Itoh, T. Kawabata, Y. Kalmykov, A. M. Krumbholz, E. Litvinova, H. Matsubara, K. Nakanishi, R. Neveling, H. Okamura, H. J. Ong, B. Özel-Tashenov, V. Y. Ponomarev, A. Richter, B. Rubio, H. Sakaguchi, Y. Sakemi, Y. Sasamoto, Y. Shimbara, Y. Shimizu, F. D. Smit, T. Suzuki, Y. Tameshige, J. Wambach, M. Yosoi, and J. Zenihiro, Phys. Rev. C **85**, 041304 (2012).

[184] C. A. Bertulani and G. Baur, Phys. Rep. **163**, 299 (1988).

[185] T. N. Taddeucci, C. A. Goulding, T. A. Carey, R. C. Byrd, C. D. Goodman, C. Gaarde, J. Larsen, D. Horen, J. Rapaport, and E. Sugarbaker, Nucl. Phys. A **469**, 125 (1987).

[186] R. G. T. Zegers, T. Adachi, H. Akimune, S. M. Austin, A. M. van den Berg, B. A. Brown, Y. Fujita, M. Fujiwara, S. Galès, C. J. Guess, M. N. Harakeh, H. Hashimoto, K. Hatanaka, R. Hayami, G. W. Hitt, M. E. Howard, M. Itoh, T. Kawabata, K. Kawase, M. Kinoshita, M. Matsubara, K. Nakanishi, S. Nakayama, S. Okumura, T. Ohta, Y. Sakemi, Y. Shimbara, Y. Shimizu, C. Scholl, C. Simenel, Y. Tameshige, A. Tamii, M. Uchida, T. Yamagata, and M. Yosoi, Phys. Rev. Lett. **99**, 202501 (2007).

[187] J. Birkhan, H. Matsubara, P. von Neumann-Cosel, N. Pietralla, V. Y. Ponomarev, A. Richter, A. Tamii, and J. Wambach, Phys. Rev. C **93**, 041302 (2016).

[188] M. Mathy, J. Birkhan, H. Matsubara, P. von Neumann-Cosel, N. Pietralla, V. Y. Ponomarev, A. Richter, and A. Tamii, Phys. Rev. C **95**, 054316 (2017).

[189] I. Poltoratska, R. W. Fearick, A. M. Krumbholz, E. Litvinova, H. Matsubara, P. von Neumann-Cosel, V. Y. Ponomarev, A. Richter, and A. Tamii, Phys. Rev. C **89**, 054322 (2014).

[190] Y. Kalmykov, T. Adachi, G. P. A. Berg, H. Fujita, K. Fujita, Y. Fujita, K. Hatanaka, J. Kamiya, K. Nakanishi, P. von Neumann-Cosel, V. Y. Ponomarev, A. Richter, N. Sakamoto, Y. Sakemi, A. Shevchenko, Y. Shimbara, Y. Shimizu, F. D. Smit, T. Wakasa, J. Wambach, and M. Yosoi, Phys. Rev. Lett. **96**, 012502 (2006).

[191] I. Usman, Z. Buthelezi, J. Carter, G. R. J. Cooper, R. W. Fearick, S. V. Förtsch, H. Fujita, Y. Kalmykov, P. von Neumann-Cosel, R. Neveling, I. Poltoratska, A. Richter, A. Shevchenko, E. Sideras-Haddad, F. D. Smit, and J. Wambach, Phys. Rev. C **84**, 054322 (2011).

[192] N. Pietralla, Nucl. Phys. News **28**, 4 (2018).

[193] K. Sonnabend, D. Savran, J. Beller, M. A. Büssing, A. Constantinescu, M. Elvers, J. Endres, M. Fritzsche, J. Glorius, J. Hasper, J. Isaak, B. Löher, S. Müller, N. Pietralla, C. Romig, A. Sauerwein, L. Schnorrenberger, C. Wälzlein, A. Zilges, and M. Zweidinger, Nucl. Instrum. Meth. A **640**, 6 (2011).

[194] H. R. Weller, M. W. Ahmed, H. Gao, W. Tornow, Y. K. Wu, M. Gai, and R. Miskimen, Prog. Part. Nucl. Phys. **62**, 257 (2009).

[195] H. R. Weller, M. W. Ahmed, and Y. K. Wu, Nucl. Phys. News **25**, 19 (2015).

[196] B. Löher, V. Derya, T. Aumann, J. Beller, N. Cooper, M. Duchene, J. Endres, E. Fiori, J. Isaak, J. Kelley, M. Knörzer, N. Pietralla, C. Romig, M. Scheck, H. Scheit, J. Silva, A. P. Tonchev, W. Tornow, H. Weller, V. Werner, and A. Zilges, Nucl. Instrum. Meth. A **723**, 136 (2013).

[197] A. D. Ayangeakaa, U. Friman-Gayer, and R. V. F. Janssens, *The clover array for nuclear structure studies at HIγS*, (2021) https://www.innovationnewsnetwork.com/nuclear-structure/10491/ (visited on 2024-06-03), archived at https://web.archive.org/web/20240603222221/https://www.innovationnewsnetwork.com/nuclear-structure/10491/ on 2024-06-03.

[198] N. Pietralla, H. R. Weller, V. N. Litvinenko, M. W. Ahmed, and A. P. Tonchev, Nucl. Instrum. Meth. A **483**, 556 (2002).

[199] N. Pietralla, M. W. Ahmed, C. Fransen, V. N. Litvinenko, A. P. Tonchev, and H. R. Weller, AIP Conf. Proc. **656**, 365 (2003).

[200] B. Löher, "Probing the decay characteristics of the pygmy dipole resonance in the semi-magic nucleus ^{140}Ce with γ-γ coincidence measurements", PhD thesis (Johannes Gutenberg-Universität Mainz, 2014).

[201] J. Adamczewski-Musch, H. G. Essel, and N. Kurz, *GSI Multi-Branch System reference manual*, version 7.0, GSI Helmholtzzentrum für Schwerionenforschung (2022).

[202] *SIS3316 – 16 channel VME digitizer – user manual*, version 1.22, SIS GmbH (2019).

[203] F. Lüke, *mvme – mesytec VME data acquisition*, version 3.4.1, mesytec GmbH & Co. KG, 2022, https://github.com/flueke/mvme.

[204] *MDPP-16 QDC manual*, version 00.05, mesytec GmbH & Co. KG (2021).

[205] *MDPP-16 SCP/RCP manual*, version 00.20, mesytec GmbH & Co. KG (2021).

[206] *MVME datasheet*, mesytec GmbH & Co. KG (2021).

[207] J. Postel, *User Datagram Protocol*, RFC 768 (RFC Editor, 1980), pp. 1–3.

[208] H. T. Johansson, *TRLO II – flexible FPGA trigger control*, 2021, https://fy.chalmers.se/~f96hajo/trloii/ (visited on 2024-03-06), archived at https://web.archive.org/web/20240204062924/https://fy.chalmers.se/~f96hajo/trloii/ on 2024-02-04.

[209] T. Aumann, Prog. Part. Nucl. Phys. **59**, 3 (2007).

[210] H. T. Johansson and B. Löher, *[drasi] – data acquisition*, 2017, https://fy.chalmers.se/~f96hajo/drasi/ (visited on 2023-07-01), archived at https://web.archive.org/web/20230212122342/https://fy.chalmers.se/~f96hajo/drasi/ on 2023-02-12.

[211] B. Löher and H. T. Törnqvist, *NUstar ReaDout LIBrary – Nurdlib*, 2017, https://web-docs.gsi.de/~land/nurdlib/ (visited on 2023-07-01), archived at https://web.archive.org/web/20230212120817/https://web-docs.gsi.de/~land/nurdlib/ on 2023-02-12.

[212] H. T. Törnqvist *et al.*, *nurdlib – NUstar ReaDout LIBrary*, 2024, https://github.com/nustardaq/nurdlib (visited on 2024-06-07).

[213] H. T. Törnqvist, H. Simon, and B. Löher, *r3bfuser*, 2024, unpublished.

[214] M. Munch, J. H. Jensen, B. Löher, H. Törnqvist, and H. T. Johansson, IEEE T. Nucl. Sci. **66**, 575 (2019).

[215] H. T. Johansson, *The UCESB unpacker generator, long write-up – documentation and manual*, (2010) https://fy.chalmers.se/~f96hajo/ucesb/ (visited on 2018-04-09).

[216] R. Brun and F. Rademakers, Nucl. Instrum. Meth. A **389**, 81 (1997).

[217] I. Antcheva, M. Ballintijn, B. Bellenot, M. Biskup, R. Brun, N. Buncic, P. Canal, D. Casadei, O. Couet, V. Fine, L. Franco, G. Ganis, A. Gheata, D. G. Maline, M. Goto, J. Iwaszkiewicz, A. Kreshuk, D. M. Segura, R. Maunder, L. Moneta, A. Naumann, E. Offermann, V. Onuchin, S. Panacek, F. Rademakers, P. Russo, and M. Tadel, Comput. Phys. Commun. **180**, 2499 (2009).

[218] B. Löher, *nupeline*, version 0.3, 2021.

[219] InfluxData, Inc., *InfluxDB*, version 1.11.1, 2023, https://www.influxdata.com/.

[220] VictoriaMetrics, *VictoriaMetrics*, version 1.101.0, 2024, https://www.influxdata.com/.

[221] Grafana Labs, *Grafana*, version 10.4.1, 2024, https://grafana.com/.

[222] J. Mayer, E. Hoemann, O. Papst, N. Warr, N. Braun, T. Kotthaus, and R. Schulze, *HDTV: Nuclear spectrum analysis tool*, version 24.01, 2007, https://github.com/janmayer/hdtv.

[223] O. Papst, *DHIPS DAQ documentation*, Technische Universität Darmstadt (2019).

[224] C. R. Harris, K. J. Millman, S. J. van der Walt, R. Gommers, P. Virtanen, D. Cournapeau, E. Wieser, J. Taylor, S. Berg, N. J. Smith, R. Kern, M. Picus, S. Hoyer, M. H. van Kerkwijk, M. Brett, A. Haldane, J. F. del Río, M. Wiebe, P. Peterson, P. Gérard-Marchant, K. Sheppard, T. Reddy, W. Weckesser, H. Abbasi, C. Gohlke, and T. E. Oliphant, Nature **585**, 357 (2020).

[225] A. Meurer, C. P. Smith, M. Paprocki, O. Čertík, S. B. Kirpichev, M. Rocklin, A. Kumar, S. Ivanov, J. K. Moore, S. Singh, T. Rathnayake, S. Vig, B. E. Granger, R. P. Muller, F. Bonazzi, H. Gupta, S. Vats, F. Johansson, F. Pedregosa, M. J. Curry, A. R. Terrel, Š. Roučka, A. Saboo, I. Fernando, S. Kulal, R. Cimrman, and A. Scopatz, PeerJ Comput. Sci. **3**, e103 (2017).

[226] P. Virtanen, R. Gommers, T. E. Oliphant, M. Haberland, T. Reddy, D. Cournapeau, E. Burovski, P. Peterson, W. Weckesser, J. Bright, S. J. van der Walt, M. Brett, J. Wilson, K. J. Millman, N. Mayorov, A. R. J. Nelson, E. Jones, R. Kern, E. Larson, C. J. Carey, İ. Polat, Y. Feng, E. W. Moore, J. VanderPlas, D. Laxalde, J. Perktold, R. Cimrman, I. Henriksen, E. A. Quintero, C. R. Harris, A. M. Archibald, A. n. H. Ribeiro, F. Pedregosa, P. van Mulbregt, and SciPy 1.0 Contributors, Nat. Methods **17**, 261 (2020).

[227] J. D. Hunter, Comput. Sci. Eng. **9**, 90 (2007).

[228] W. McKinney, in Proceedings of the 9th Python in Science Conference, edited by S. van der Walt and J. Millman (2010), pp. 56–61.

[229] The pandas development team, *pandas-dev/pandas: Pandas*, 2024, https://github.com/pandas-dev/pandas/.

[230] T. Kluyver, B. Ragan-Kelley, F. Pérez, B. Granger, M. Bussonnier, J. Frederic, K. Kelley, J. Hamrick, J. Grout, S. Corlay, P. Ivanov, D. Avila, S. Abdalla, C. Willing, and J. development team, in Positioning and Power in Academic Publishing: Players, Agents and Agendas, edited by F. Loizides and B. Scmidt (2016), pp. 87–90, https://eprints.soton.ac.uk/403913/.

[231] J. Salvatier, T. V. Wiecki, and C. Fonnesbeck, PeerJ Comput. Sci. **2**, e55 (2016).

[232] A.-P. Oriol, A. Virgile, C. Colin, D. Larry, F. C. J., K. Maxim, K. Ravin, L. Jupeng, L. C. C., M. O. A., O. Michael, V. Ricardo, W. Thomas, and Z. Robert, PeerJ Comput. Sci. **9**, e1516 (2023).

[233] T. Wiecki, J. Salvatier, R. Vieira, M. Kochurov, A. Patil, M. Osthege, B. T. Willard, B. Engels, O. A. Martin, C. Carroll, A. Seyboldt, A. Rochford, L. Paz, rpgoldman, K. Meyer, P. Coyle, O. Abril-Pla, M. E. Gorelli, V. Andreani, R. Kumar, J. Lao, T. Yoshioka, G. Ho, T. Kluyver, A. Andorra, K. Beauchamp, D. Pananos, E. Spaak, and B. Edwards, *pymc*, 2024, https://github.com/pymc-devs/pymc/.

[234] J. Pivarski, H. Schreiner, A. Hollands, P. Das, K. Kothari, A. Roy, J. Ling, N. Smith, C. Burr, and G. Stark, *uproot*, 2024, https://github.com/scikit-hep/uproot5.

[235] R. Kumar, C. Carroll, A. Hartikainen, and O. Martin, J. Open Source Softw. **4**, 1143 (2019).

[236] J. Bezanson, A. Edelman, S. Karpinski, and V. B. Shah, SIAM Rev. **59**, 65 (2017).

[237] T. Tantau, J. Graph Algorithms Appl. **17**, 495 (2013).

[238] S. Agostinelli *et al.* (Geant4 Collaboration), Nucl. Instrum. Meth. A **506**, 250 (2003).

[239] J. Allison *et al.* (Geant4 Collaboration), IEEE T. Nucl. Sci. **53**, 270 (2006).

[240] J. Allison *et al.* (Geant4 Collaboration), Nucl. Instrum. Meth. A **835**, 186 (2016).

[241] U. Friman-Gayer, J. Kleemann, and O. Papst, *utr: Geant4 simulation of the Upstream Target Room (UTR) at the HIγS facility*, version 2024.01, 2019, https://github.com/u-eff-gee/utr.

[242] G. Knoll, *Radiation detection and measurement*, 4th ed. (John Wiley & Sons, New York, NY, USA, 2010), isbn: 978-0-470-13148-0.

[243] U. Friman-Gayer, "Probing nuclear structure relevant for neutrinoless double-beta decay with nuclear resonance fluorescence", PhD thesis (Technische Universität Darmstadt, 2020).

[244] C. Robert and G. Casella, *Monte Carlo statistical methods*, Springer texts in statistics (Springer, New York, NY, 2010), ISBN: 978-1-4419-1939-7.

[245] O. Papst, *angcorrwat – Angular distributions code for γ spectroscopy*, 2019, https://github.com/op3/angcorrwat (visited on 2024-06-07).

[246] G. R. Gilmore, *Practical gamma-ray spectroscopy*, 2nd ed. (John Wiley & Sons, New York, NY, USA, 2008), ISBN: 978-0-470-86196-7.

[247] B. Jäckel, W. Westmeier, and P. Patzelt, Nucl. Instrum. Meth. A **261**, 543 (1987).

[248] B. Hesbacher, "Kernstrukturuntersuchungen an ^{96}Ru mittels Elektron-Gamma-Koinzidenz-Reaktionen am S-DALINAC", MSc thesis (Technische Universität Darmstadt, 2023), unpublished.

[249] J. Mayer, E. Hoemann, M. Müllenmeister, P. Scholz, and A. Zilges, Nucl. Instrum. Meth. A **972**, 164102 (2020).

[250] M. S. Basunia, Nucl. Data Sheets **127**, 69 (2015).

[251] H. Junde, H. Su, and Y. Dong, Nucl. Data Sheets **112**, 1513 (2011).

[252] E. Browne and J. K. Tuli, Nucl. Data Sheets **114**, 1849 (2013).

[253] E. Browne and J. K. Tuli, Nucl. Data Sheets **108**, 2173 (2007).

[254] M. J. Martin, Nucl. Data Sheets **114**, 1497 (2013).

[255] N. Pietralla, I. Bauske, O. Beck, P. von Brentano, W. Geiger, R.-D. Herzberg, U. Kneissl, J. Margraf, H. Maser, H. H. Pitz, and A. Zilges, Phys. Rev. C **51**, 1021 (1995).

[256] L. I. Schiff, Phys. Rev. **83**, 252 (1951).

[257] G. Roche, C. Ducos, and J. Proriol, Phys. Rev. A **5**, 2403 (1972).

[258] F. Salvat, J. D. Martínez, R. Mayol, and J. Parellada, Phys. Rev. A **36**, 467 (1987).

[259] E. Haug, Radiat. Phys. Chem **77**, 207 (2008).

[260] H. H. Pitz, R. D. Heil, U. Kneissl, S. Lindenstruth, U. Seemann, R. Stock, C. Wesselborg, A. Zilges, P. Von Brentano, S. D. Hoblit, and A. M. Nathan, Nucl. Phys. A **509**, 587 (1990).

[261] J. G. Skellam, J. R. Stat. Soc. **109**, 296 (1946).

[262] O. Klein and Y. Nishina, Z. Phys. **52**, 853 (1929).

[263] F. Santosa and W. W. Symes, SIAM J. Sci. Stat. Comp. **7**, 1307 (1986).

[264] R. Tibshirani, J. Roy. Stat. Soc. B Met. **58**, 267 (1996), (visited on 2024-05-31).

[265] A. Gelman, J. B. Carlin, H. S. Stern, D. B. Dunson, A. Vehtari, and D. B. Rubin, *Bayesian data analysis*, 3rd ed., Chapman & Hall/CRC Texts in Statistical Science (Chapman & Hall/CRC, Philadelphia, PA, 2013), ISBN: 978-1-439-84095-5.

[266] N. Metropolis, A. W. Rosenbluth, M. N. Rosenbluth, A. H. Teller, and E. Teller, J Chem. Phys. **21**, 1087 (1953).

[267] W. K. Hastings, Biometrika **57**, 97 (1970).

[268] S. Duane, A. D. Kennedy, B. J. Pendleton, and D. Roweth, Phys. Lett. B **195**, 216 (1987).

[269] M. D. Hoffman and A. Gelman, J. Mach. Learn. Res. **15**, 1593 (2014).

[270] O. Papst, *Dataset for photo response of ^{150}Nd* (Technische Universität Darmstadt, 2024), https://tudatalib.ulb.tu-darmstadt.de/handle/tudatalib/4262.

[271] U. Friman-Gayer and O. Papst, *nutr: new utr*, 2020, https://github.com/u-eff-gee/nutr.

[272] J. L. Bentley, Commun. ACM **18**, 509 (1975).

[273] J. L. Blanco and P. K. Rai, *nanoflann: a C++ header-only fork of FLANN, a library for Nearest Neighbor (NN) with KD-trees*, version 1.5.5, 2014, https://github.com/jlblancoc/nanoflann.

[274] D. Tsybulevskii, *pynanoflann: Unofficial python wrapper to the nanoflann k-d tree*, version 0.0.9, 2019, https://github.com/u1234x1234/pynanoflann.

[275] U. Friman-Gayer, *alpaca: a linearly-polarized angular-correlation application*, 2021, https://github.com/u-eff-gee/alpaca.

[276] L. C. Biedenharn, "Angular correlations in nuclear spectroscopy", in *Nuclear Spectroscopy: Part B*, edited by F. Ajzenberg-Selove, Pure and applied physics (Academic Press, 1960), p. 732, ISBN: 978-1-4832-3064-1.

[277] O. Papst, *AngularCorrelation.jl – Angular correlations and distributions code for γ spectroscopy*, version 1.0.0, 2024, https://github.com/op3/AngularCorrelation.jl.

[278] J. Postel, *Transmission Control Protocol*, RFC 793 (RFC Editor, 1981), pp. 1–91.

[279] T. Thomas, V. Werner, J. Jolie, K. Nomura, T. Ahn, N. Cooper, H. Duckwitz, A. Fitzler, C. Fransen, A. Gade, M. Hinton, G. Ilie, K. Jessen, A. Linnemann, P. Petkov, N. Pietralla, and D. Radeck, Nucl. Phys. A **947**, 203 (2016).

[280] O. Papst, *Dataset for photon strength function of ^{96}Mo* (Technische Universität Darmstadt, 2024), https://tudatalib.ulb.tu-darmstadt.de/handle/tudatalib/4263.

[281] D. Heck, N. Ahmed, U. Fanger, W. Michaelis, H. Ottmar, and H. Schmidt, Nucl. Phys. A **159**, 49 (1970).

[282] R. L. Workman *et al.* (Particle Data Group), Prog. Theor. Phys. **2022**, 083C01 (2022).

[283] J. Kleemann, T. Beck, U. Friman-Gayer, N. Pietralla, V. Werner, S. W. Finch, J. Kotila, Krishichayan, B. Löher, H. Pai, O. Papst, W. Tornow, M. Weinert, and A. Zilges, Phys. Rev. C **104**, L061302 (2021).

[284] J. W. Hammer, B. Fischer, H. Hollick, H. P. Trautvetter, K. U. Kettner, C. Rolfs, and M. Wiescher, Nucl. Instrum. Methods **161**, 189 (1979).

[285] A. Zilges, "Untersuchung niedrigliegender Dipolanregungen in den Kernen der Seltenen Erden", PhD thesis (Universität zu Köln, 1992).

[286] T. Beck, "Novel decay properties of positive-parity low-spin states of deformed gadolinium and dysprosium nuclei", PhD thesis (Technische Universität Darmstadt, 2021).

[287] F. Bečvář, Nucl. Instrum. Meth. A **417**, 434 (1998), [Erratum: Nucl. Instrum. Meth. A **935**, 240 (2019)].

[288] S. Goriely and V. Plujko, Phys. Rev. C **99**, 014303 (2019).

[289] M. Guttormsen, Y. Alhassid, W. Ryssens, K. Ay, M. Ozgur, E. Algin, A. Larsen, F. Bello Garrote, L. Crespo Campo, T. Dahl-Jacobsen, A. Görgen, T. Hagen, V. Ingeberg, B. Kheswa, M. Klintefjord, J. Midtbø, V. Modamio, T. Renstrøm, E. Sahin, S. Siem, G. Tveten, and F. Zeiser, Phys. Lett. B **816**, 136206 (2021).

[290] J. Isaak, private communication, 2024.

[291] J. L. Wood, K. Heyde, W. Nazarewicz, M. Huyse, and P. van Duppen, Phys. Rep. **215**, 101 (1992).

[292] A. N. Andreyev, M. Huyse, P. Van Duppen, L. Weissman, D. Ackermann, J. Gerl, F. P. Hessberger, S. Hofmann, A. Kleinböhl, G. Münzenberg, S. Reshitko, C. Schlegel, H. Schaffner, P. Cagarda, M. Matos, S. Saro, A. Keenan, C. Moore, C. D. O'Leary, R. D. Page, M. Taylor, H. Kettunen, M. Leino, A. Lavrentiev, R. Wyss, and K. Heyde, Nature **405**, 430 (2000).

[293] C. Fransen, N. Pietralla, Z. Ammar, D. Bandyopadhyay, N. Boukharouba, P. von Brentano, A. Dewald, J. Gableske, A. Gade, J. Jolie, U. Kneissl, S. R. Lesher, A. F. Lisetskiy, M. T. McEllistrem, M. Merrick, H. H. Pitz, N. Warr, V. Werner, and S. W. Yates, Phys. Rev. C **67**, 024307 (2003).

[294] G. Rusev, R. Schwengner, F. Dönau, S. Frauendorf, L. Käubler, L. K. Kostov, S. Mallion, K. D. Schilling, A. Wagner, E. Grosse, H. von Garrel, U. Kneißl, C. Kohstall, M. Kreutz, H. H. Pitz, M. Scheck, F. Stedile, P. von Brentano, J. Jolie, A. Linnemann, N. Pietralla, and V. Werner, Phys. Rev. Lett. **95**, 062501 (2005).

[295] W. Witt, V. Werner, N. Pietralla, M. Albers, A. D. Ayangeakaa, B. Bucher, M. P. Carpenter, D. Cline, H. M. David, A. Hayes, C. Hoffman, R. V. F. Janssens, B. P. Kay, F. G. Kondev, W. Korten, T. Lauritsen, O. Möller, G. Rainovski, G. Savard, D. Seweryniak, J. Smith, R. Stegmann, S. Zhu, and C. Y. Wu, Phys. Rev. C **98**, 041302 (2018).

[296] D. Gribble, C. Iliadis, R. V. F. Janssens, U. Friman-Gayer, Krishichayan, and S. Finch, Phys. Rev. C **106**, 014308 (2022).

Academic Curriculum Vitae

Name: Oliver Papst
Date of birth: *Removed in this digital version*
Place of birth: Offenbach am Main, Germany
ORCID iD: ⓘ https://orcid.org/0000-0002-1037-4183

Education

2019–2024   **Technische Universität Darmstadt, Darmstadt, Germany**
Doctoral studies at the Department of Physics
Institut für Kernphysik

2016–2019   **Technische Universität Darmstadt, Darmstadt, Germany**
Master studies in Physics
Degree: Master of Science
Thesis (supervisor Professor Dr. Dr. h. c. mult. Norbert Pietralla):
   Dipole strength distribution of the deformed nucleus ^{164}Dy

2013–2016   **Technische Universität Darmstadt, Darmstadt, Germany**
Bachelor studies in Physics
Degree: Bachelor of Science
Thesis (supervisor Professor Dr. Dr. h. c. mult. Norbert Pietralla):
   Zerfallsverhalten von $J = 1$-Zuständen von ^{92}Zr und ^{94}Zr

2004–2013   **Goetheschule Neu-Isenburg, Neu-Isenburg, Germany**
Degree: Abitur

2010   **John Abbott College, Sainte-Anne-de-Bellevue, Canada**
Term abroad

Peer-Reviewed Publications

[A1] T. Beck, C. Costache, R. Lică, N. Mărginean, C. Mihai, R. Mihai, **O. Papst**, S. Pascu, N. Pietralla, C. Sotty, L. Stan, A. Turturică, V. Werner, J. Wiederhold and W. Witt, Nucl. Instrum. Methods Phys. Res. A **951**, 163090 (2020).

[A2] J. Sinclair, M. Scheck, S. W. Finch, Krishichayan, U. Friman-Gayer, W. Tornow, G. Battaglia, T. Beck, R. Chapman, M. M. R. Chishti, C. Fransen, R. Gonzales, E. Hoemann, J. Isaak, R. V. F. Janssens, D. A. Jaroszynski, S. Johnson, M. D. Jones, J. M. Keatings, N. Kelly, J. Kleemann, D. Little, B. Löher, K. R. Mashtakov, M. Müscher, D. O'Donnell, **O. Papst**, E. E. Peters, D. Savran, M. Schilling, R. Schwengner, P. Spagnoletti, M. Spieker, V. Werner, J. Wilhelmy, O. Wieland, S. W. Yates and A. Zilges, Eur. Phys. J. A **56**, 105 (2020).

[A3] T. Beck, V. Werner, N. Pietralla, M. Bhike, N. Cooper, U. Friman-Gayer, J. Isaak, R. V. Jolos, J. Kleemann, Krishichayan, **O. Papst**, W. Tornow, C. Bernards, B. P. Crider, R. S. Ilieva, B. Löher, C. Mihai, F. Naqvi, S. Pascu, E. E. Peters, F. M. Prados-Estevez, T. J. Ross, D. Savran, J. R. Vanhoy and A. Zilges, Phys. Rev. Lett. **125**, 092501 (2020).

[A4] **O. Papst**, V. Werner, J. Isaak, N. Pietralla, T. Beck, C. Bernards, M. Bhike, N. Cooper, B. P. Crider, U. Friman-Gayer, J. Kleemann, Krishichayan, B. Löher, F. Naqvi, E. E. Peters, F. M. Prados-Estévez, R. S. Ilieva, T. J. Ross, D. Savran, W. Tornow and J. R. Vanhoy, Phys. Rev. C **102**, 034323 (2020).

[A5] R. Schwengner, R. Massarczyk, M. Scheck, W. Tornow, G. Battaglia, T. Beck, D. Bemmerer, N. Benouaret, R. Beyer, M. Butterling, F. Fiedler, S. W. Finch, C. Fransen, U. Friman-Gayer, A. Frotscher, R. Gonzalez, M. Grieger, A. Hartmann, T. Hensel, E. Hoemann, H. Hoffmann, R. V. F. Janssens, S. Johnson, M. D. Jones, A. R. Junghans, N. Kelly, J. Kleemann, Krishichayan, D. R. Little, F. Ludwig, S. E. Müller, D. O'Donnell, **O. Papst**, E. Pirovano, J. Sinclair, M. P. Takács, S. Turkat, S. Urlaß, A. Wagner, V. Werner, O. Wieland and J. Wilhelmy, Phys. Rev. C **103**, 024312 (2021).

[A6] K. E. Ide, T. Beck, V. Werner, M. Berger, S. W. Finch, U. Friman-Gayer, J. Kleemann, Krishichayan, B. Löher, **O. Papst**, N. Pietralla, D. Savran, W. Tornow, M. Weinert, J. Wiederhold and A. Zilges, Phys. Rev. C **103**, 054302 (2021).

[A7] J. Kleemann, T. Beck, U. Friman-Gayer, N. Pietralla, V. Werner, S. W. Finch, J. Kotila, Krishichayan, B. Löher, H. Pai, **O. Papst**, W. Tornow, M. Weinert and A. Zilges, Phys. Rev. C **104**, L061302 (2021).

[A8] D. Savran, J. Isaak, R. Schwengner, R. Massarczyk, M. Scheck, W. Tornow, G. Battaglia, T. Beck, S. W. Finch, C. Fransen, U. Friman-Gayer, R. Gonzalez, E. Hoemann, R. V. F. Janssens, S. R. Johnson, M. D. Jones, J. Kleemann, Krishichayan, D. R. Little, D. O'Donnell, **O. Papst**, N. Pietralla, J. Sinclair, V. Werner, O. Wieland and J. Wilhelmy, Phys. Rev. C **106**, 044324 (2022).

[A9] A. Tamii, L. Pellegri, P.-A. Söderström, D. Allard, S. Goriely, T. Inakura, E. Khan, E. Kido, M. Kimura, E. Litvinova, S. Nagataki, P. Neumann-Cosel, N. Pietralla, N. Shimizu, N. Tsoneva, Y. Utsuno, S. Adachi, A. Bahini, D. Balabanski, B. Baret, J. A. C. Bekker, S. D. Binda, E. Boicu, A. Bracco, I. Brandherm, M. Brezeanu, J. W. Brummer, F. Camera, F. C. L. Crespi, R. Dalal, L. M. Donaldson, Y. Fujikawa, T. Furuno, H. Haoning, Y. Honda, A. Gavrilescu, A. Inoue, J. Isaak, H. Jivan, P. M. Jones, S. Jongile, T. Kawabata, T. Khumalo, J. Kiener, J. Kleemann, N. Kobayashi, Y. Koshio, A. Kuşoğlu, K. C. W. Li, K. L. Malatji, R. E. Molaeng, H. Motoki, M. Murata, A. Netshiya, R. Neveling, R. Niina, J. Oliver, S. Okamoto, S. Ota, **O. Papst**, E. Parizot, T. Petruse, M. S. Reen, P. Ring, K. Sakanashi, E. Sideras-Haddad, S. Siem, M. Spall, T. Suda, T. Sudo, Y. Taniguchi, V. Tatischeff, H. Utsunomiya, H. Wang, V. Werner, H. Wibowo, M. Wiedeking, O. Wieland and Y. Xu, (PANDORA Collaboration), Eur. Phys. J. A **59**, 208 (2023).

[A10] M. Müscher, E. Litvinova, R. Schwengner, T. Beck, D. Bemmerer, F. Fiedler, S. W. Finch, U. Friman-Gayer, S. Hammer, J. Isaak, R. V. F. Janssens, A. R. Junghans, N. Kelly, F. Kluwig, Krishichayan, S. E. Müller, **O. Papst**, K. Römer, D. Savran, M. Scheck, T. Schüttler, J. Sinclair, T. Szücs, W. Tornow, A. Wagner, J. Wilhelmy and A. Zilges, Phys. Rev. C **109**, 044318 (2024).

Conference Proceedings

[C1] V. Werner, U. Gayer, J. Kleemann, T. Beck, M. Bhike, V. Derya, J. Isaak, Krishichayan, B. Löher, L. Mertes, H. Pai, **O. Papst**, N. Pietralla, P. C. Ries, C. Romig, D. Savran, M. Schilling, W. Tornow, J. Wilhelmy and M. Zweidinger, J. Phys. Conf. Ser. **1056**, 012061 (2018).

[C2] U. Gayer, V. Werner, T. Beck, S. Finch, J. Kleemann, Krishichayan, B. Löher, **O. Papst**, N. Pietralla, P. C. Ries, D. Savran, M. Weinert and W. Tornow, EPJ Web Conf. **194**, 02004 (2018).

[C3] P. Koseoglou, M. L. Cortés, J. Isaak, V. Werner, **O. Papst**, J. Kleemann, M. Beuschlein, N. Pietralla, U. Ahmed, K. E. Ide, I. Jurosevic, C. Nickel, M. Spall, T. Stetz and R. Zidarova, HNPS Adv. Nucl. Phys. **28**, 154 (2022).

[C4] D. Savran, J. Isaak, A. Ayangeakaa, M. Beuschlein, S. Finch, D. Gribble, A. Gupta, J. Hauf, X. James, R. Janssens, S. Johnson, P. Koseoglou, T. Kowalewski, B. Löher, **O. Papst**, N. Pietralla, A. Saracino, N. Sensharma, W. Tornow and V. Werner, Il Nuovo Cimento C **47**, 1 (2024).

Datasets

[D1] **O. Papst**, *Dataset for photo response of ^{150}Nd* (Technische Universität Darmstadt, 2024), https://tudatalib.ulb.tu-darmstadt.de/handle/tudatalib/4262.

[D2] **O. Papst**, *Dataset for photon strength function of ^{96}Mo* (Technische Universität Darmstadt, 2024), https://tudatalib.ulb.tu-darmstadt.de/handle/tudatalib/4263.